Author:
Armstrong Green, Natalie C

Title:
Dynamic Response of Hygroscopic Pharmaceutical Aerosol on Inhalation

Dynamic Response of Hygroscopic Pharmaceutical Aerosol on Inhalation

by

Natalie C. Armstrong Green
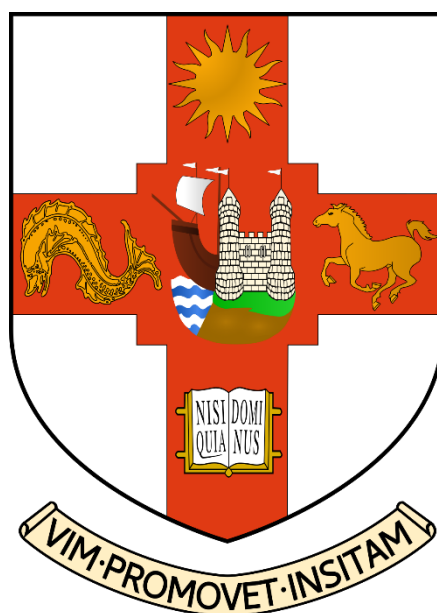
A dissertation submitted to the University of Bristol in accordance with the requirements of the degree of Doctor of Philosophy in the School of Chemistry, Faculty of Science

November 2021

Abstract

Drug delivery to the lungs using aerosol is a well-established route for treating a wide range of respiratory and systemic diseases. However, the physicochemical processes that transform aerosol between generation and deposition are poorly understood. Control over time-dependent aerosol properties, such as size and composition, could improve the efficacy of inhalation therapeutics by targeted delivery of an active pharmaceutical ingredient (API) to the disease site. Aerosol tools, developed for probing atmospheric aerosol processes, have been applied to study the dynamics of inhalation aerosol. This thesis will provide important insights into factors that govern the capacity and dynamics of hygroscopic growth, influencing where aerosol deposits in the respiratory tract.

This thesis describes laboratory-based techniques that were used to explore the dynamic aerosol processes occurring during and prior to inhalation. An advanced electrodynamic balance (EDB) was designed and developed to replicate the saturated environmental conditions within the lungs. Elastic light scattering methods were used determine the time-dependence of droplet size and phase on evaporation, condensation, crystallisation and dissolution. In addition to single particle measurements, a double ring EDB and falling droplet column (FDC) were used to collect dried aerosol samples prior to scanning electron microscopy (SEM) imaging.

Evaporation measurements on an EDB were used to infer the hygroscopic response of a range of APIs and excipients frequently used in inhalable drug formulations. The influence of environmental conditions, particle morphology, particle composition and particle size on dissolution kinetics of a crystalline particle were investigated. In addition, the effect of drying conditions on crystallisation kinetics of an aqueous droplet are explored. Importantly, it is shown that the time taken for complete dissolution of a crystalline particle is significantly reduced by an increase in particle size and a decrease in the gas phase RH. This thesis draws a comparison between aerosol phase and bulk phase dissolution measurements.

Acknowledgements

Studying for a PhD is by far the best decision I have ever made, and I have thoroughly enjoyed every minute. However, I am fully aware of how lucky I am to have had Bristol Aerosol Research Centre (BARC) as my research group and Prof Jonathan Reid as my supervisor. BARC is a very supportive research group and there are so many people to thank for their help and guidance over the years.

Firstly, a big thank you to Dr Allen Haddrell, it has been a pleasure learning from you over the past four years. Thank you to my EDBuddy Florence Gregson, what a great time we had in BARC together and I can't imagine my PhD Floless. A mention to the noodle gang, old and new, I hope this is a long-lasting tradition and I will make sure to be a frequent visitor. Thank you to colleagues at BARC who answered my regular aerosol science and current affairs questions, Dan, Malcolm, Henry, and Tom. Thank you to Jim and Justice for their invaluable support in the lab, and to Aleks and Grazia for leaving behind an incredible Electrodynamic Balance (EDB) legacy. I would also like to mention Mara, Lara and Lauren who have offered endless amounts of support, giggles, and cakes. A big thank you to Prof Jonathan Reid for giving me the opportunity to work in his research group and for all the support, guidance, and knowledge throughout my PhD.

I would like to thank my mum and brothers for their support throughout my PhD, often popping round with cupcakes during a stressful week. A special mention to Dom and Freddy, who have massively contributed to the last four years being the best years yet.

Author Declaration

I declare that the work in this dissertation was carried out in accordance with the requirements of the University's Regulations and Code of Practice for Research Degree Programmes and that it has not been submitted for any other academic award. Except where indicated by specific reference in the text, the work is the candidate's own work. Work done in collaboration with, or with the assistance of, others, is indicated as such. Any views expressed in the dissertation are those of the author.

SIGNED............N C Armstrong Green ....DATE... 17.11.2021..................

Contents

List of Symbols

Symbols

a – Activity

a_w – Water activity

A – Correction for Stefan flow

c – Concentration

cp – Specific heat capacity

$\bar{c}$ – mean molecular gas speed

d - diameter

D – Diffusion coefficient

f - Frequency

F - Force

H – Henry's law constant

I – Mass flux

J' – Molecular Flux

k – Evaporation rate

K – Thermal conductivity

L – Latent heat of vaporisation

J – Crystal nucleation rate

m – Mass

M – Molar mass

n – refractive index

p – Pressure

P – Probability of crystal nucleation

q - Charge

r – Radius

Ri – Molar refraction of a component

S - Saturation

T – Temperature

v – Gas speed

V – Volume

x – Mole fraction

Greek Alphabet symbols

α – accommodation coefficient

βM – Transitional correction factor for mass transfer

βT – Transitional correction factor for mass transfer

σ – Surface tension

λ – Wavelength

υk – kinematic viscosity

η - viscosity

ϑ - angle

ρ – density

μ - Chemical potential

γ – Activity coefficient

Subscript

a – Property at a droplet surface

e – Property of a mixture

i – Property of one component

∞ - Gas phase property far from the droplet

Fundamental Constants

R - Molar gas constant 8.314 J mol-1 K-1

kB - Boltzmann constant 1.38×10-23 J mol-1

g – Gravitational acceleration 9.81 m s-1

Chapter 1

Introduction to the Dynamic Processes of Aerosol in Drug Delivery to the Lungs

This thesis reports findings that examine the microphysics of the aerosol processes that transform aerosol from the point of generation through to inhalation potential. Lab based techniques were used to take measurements of single, pharmaceutically relevant, aerosol. In this chapter an introduction to aerosol science in the pharmaceutical industry is provided, alongside a detailed overview of drug production, inhaler devices and lung deposition. The kinetics of transformation of pharmaceutically relevant aerosol properties, such as hygroscopic growth and dissolution, will be explored. Furthermore, the development of the techniques and instruments used in this work are reviewed. To conclude the chapter, the aims and objectives of this thesis will be presented.

1.1   An Overview of Aerosol Applications in the Pharmaceutical Industry

Aerosols are a colloidal system containing solid particles or liquid droplets suspended in a gas phase. Aerosols play an important role in many aspects of life, such as their indirect and direct radiative forces influence on climate, their use in cosmetics and paints, dispersion of agricultural products and in the delivery of drugs. This thesis focuses on the role of aerosols in drug delivery to the lungs, with an emphasis on the particle dynamics occurring prior and during inhalation. Pulmonary drug delivery is a widely used method of respiratory treatment due to the large surface area and absorbing capabilities of the lungs. It is suggested that pulmonary delivery is also a successful method for systemic and local delivery of therapeutic agents, due to the high permeability of the lungs and large surface area.[1] As a growing method of medical treatment, drug delivery to the lungs requires continuous scientific research to optimise the delivery technique.

The efficiency of drug delivery for the desired treatment via the lungs is highly dependent on the quantity of drug that deposits to the target location. Thus, the overall pharmacological affect is governed by the regional deposition fraction of drug particles throughout the lung. To improve the efficiency of drug delivery to the lung there must be better predictors of drug deposition and accurate guidance for drug particle engineering. There has been slow progress in the efficacy of the treatment of respiratory diseases, suggesting a need for a multidisciplinary approach. The majority of research carried out on drug deposition is performed using bulk phase techniques or with polydisperse aerosol.[2] Measurements of monodisperse, individual aerosol allow exploration of the physical and chemical changes occurring

on a smaller scale. A thorough understanding of individual particle dynamics can then be applied to a larger scale, helping to establish the full picture.

The process of drug delivery to the lungs begins with the production of the drug formulation. Following the formulation manufacturing, a delivery device must be chosen to best suit the patient's needs and the required pharmaceutical affect. Upon inhalation, during which the drug particles are exposed to a rapid change in environmental conditions, physicochemical processes alter the particles properties. Once deposited, the pharmacokinetics govern the time course of drug adsorption and distribution. Drug delivery to the lungs is a very complex process, where the efficiency is influenced by many factors. This section introduces the stages of drug delivery to the lungs, from drug production to drug deposition.

1.1.1   Production of Inhalable Drug Formulations

This section outlines the main techniques used to produce drug formulations administered to patients via the lungs. An introduction to the physical properties of aerosolised particles is given, such as size, morphology, and phase state. Single particle studies are carried out in this thesis to explore the competition between crystalline and amorphous particle formation. Additionally, the factors in the drying process that govern final particle morphology are described.

Spray Drying Approaches

The spray drying approach converts a liquid solution into dried particles.[3] The liquid feed is atomised to a spray and exposed to a hot gaseous medium. A high temperature leads to rapid evaporation of the droplets, forming dried solid particles. The particles are separated from the gas using one of three techniques: a cyclone, electrostatic precipitator, or bag filter. Spray drying can be used in the production of materials for many applications as each of the atomisation, drying and separation techniques can be altered according to application. One example of a change in drying conditions is the spray freeze drying method which is described in the next subsection. Spray drying is a common technique for preparing active pharmaceutical ingredients (APIs) for pulmonary drug delivery applications due to the ability to manipulate and control particle size. Additionally, spray drying benefits from producing a narrow size distribution, spherical particles and controlled density.[4] A typical open cycle spray dryer is shown in Figure 1.1. In an open cycle dryer the drying gas is exhausted to the atmosphere rather than recycled, as is the case with a closed-cycle dryer. The drying gas, commonly air, is heated to the desired temperature and constantly monitored, e.g. with a thermocouple. Upon rapid drying of the atomised liquid droplets, coarse particles are collected at the bottom of the main chamber and fine particles are collected at the bottom of the cyclone chamber. The liquid feed poses a slight problem in the case of

APIs, which are commonly very insoluble in water. However, spray drying accommodates substances of low aqueous solubility, as the liquid feed can be made from organic solvents.
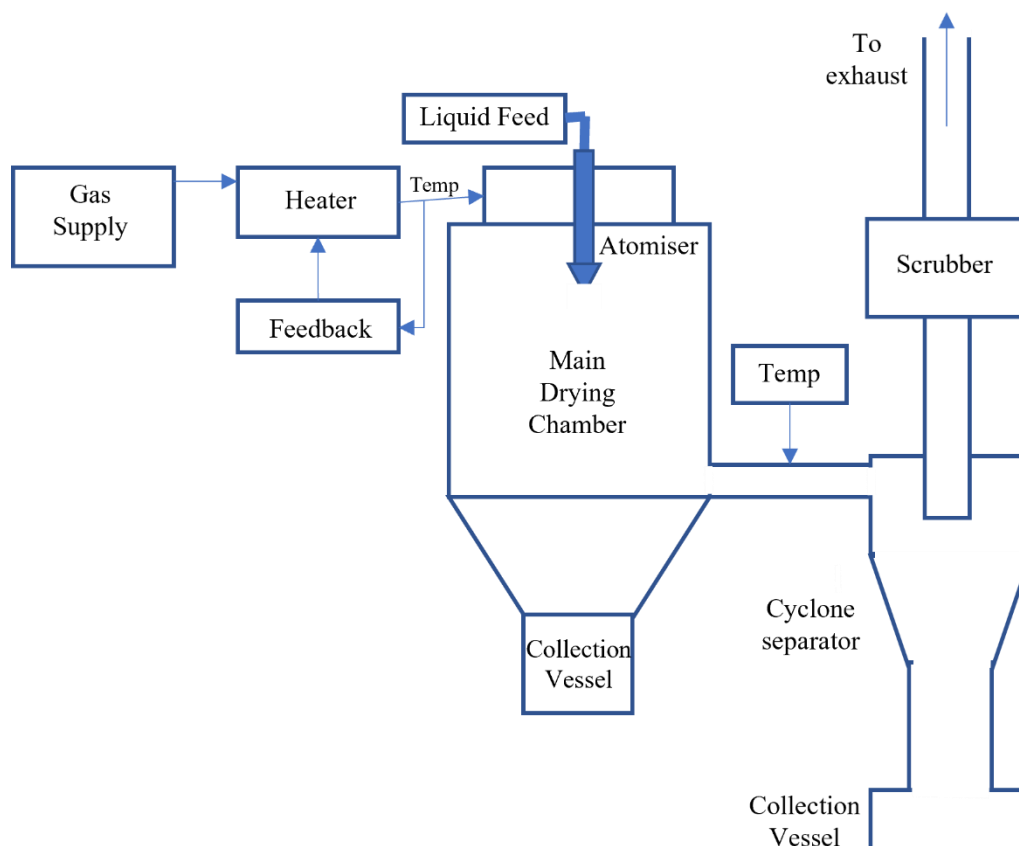
Figure 1.1. Schematic of an open-cycle spray-dryer.[3]

The initial droplet sizes are governed by the atomisation conditions and the final solid particle sizes are determined by the dynamic evaporation and substance properties. Research carried out in the 1950's identified the physical characteristics of the final solid particle and their dependence on the drying conditions.[3] For example, at a gas temperature below boiling point, a droplet with viscoelastic properties is likely to form a shrivelled dry particle. Whereas, at a gas temperature above boiling point a viscoelastic substance is likely to form an inflated, collapsed, deformed or spongy dry particle. A diagram of the potential particle morphologies that can be formed using a spray dryer is given in Figure 1.2. It is shown that spray drying can be used to produce particles with a controllable size and morphology, achieved by altering the drying conditions within the chamber. For example, the "dense particles" shown in the scanning electron microscopy (SEM) images were formed using a wall furnace temperature of 150 °C.[5] Widiyastuti et al. found that as the wall furnace increased from 150 to 700 °C the zirconia particles became more brittle and at 500 and 700 °C the spherical droplets fragmented.[5] The microencapsulated particle shown in Figure 1.2 was formed using a mixture of ZrO_2 and large SiO_2 particles.[6] Iskandar et al. produced encapsulated spherical or spheroidal particles by preparing powders using a mixture of ZrO_2 with large SiO_2 or small SiO_2 particles.[6] Drying kinetics and known physical

properties of the atomised substance can be used to control the final particle morphology. In the pharmaceutical industry, a spherical, porous, low-density particle is ideal for inhalation with rapid drug transport to the blood flow.
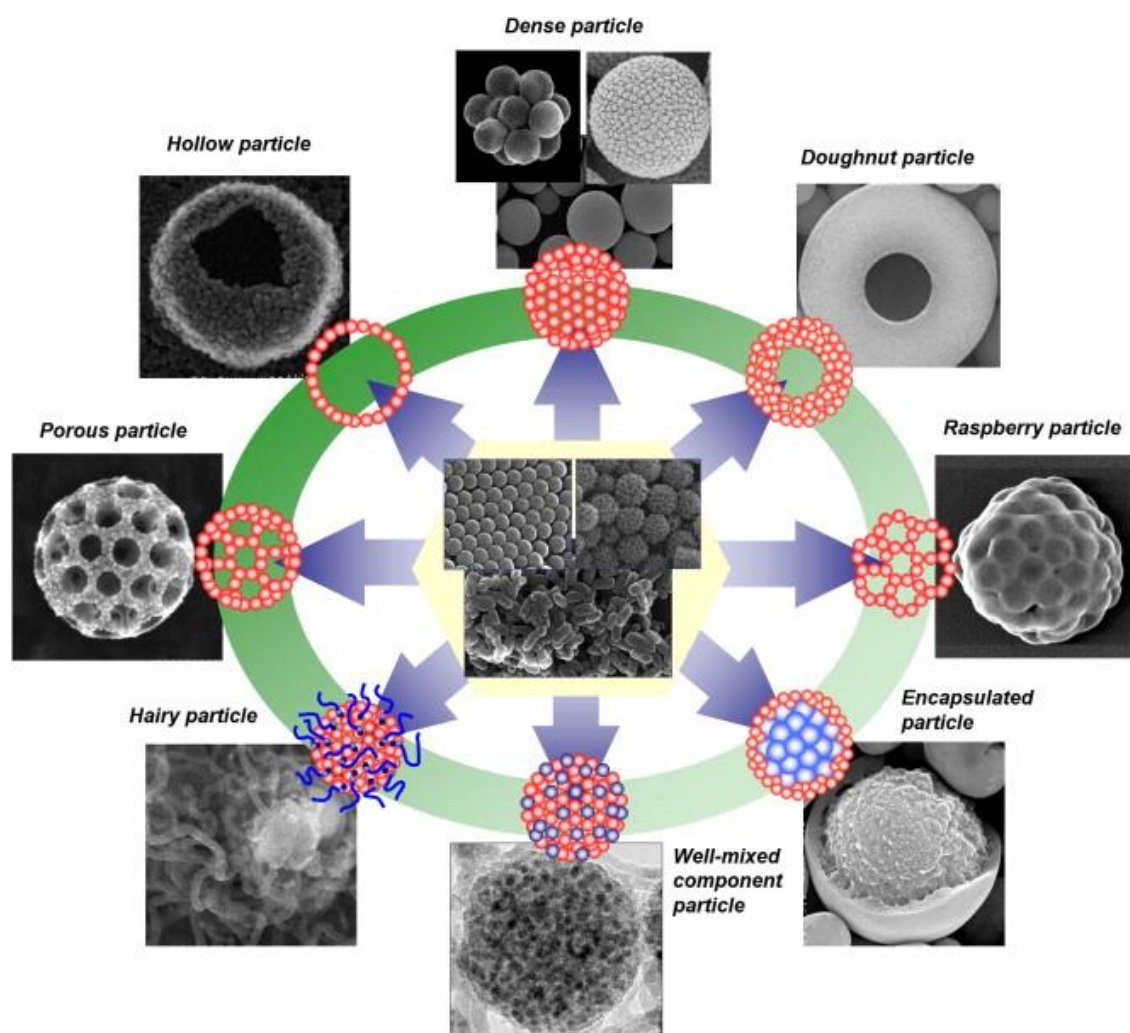
Figure 1.2. Particle morphologies that can be produced using the spray drying technique. Figure reprinted with permission from Nandiyanto et al.[7]

Spray Freeze Drying Method

Spray freeze drying has been used for pharmaceutical applications since the early 1990s. Some drugs and excipients have low melting and glass transition temperatures. Due to the formation of amorphous particles upon rapid evaporation, the glass transition temperature is vital in determining if spray drying is the correct approach. If the glass transition temperature of a substance is below the gas outlet temperature, then particles are likely to be in a supercooled, viscous state. In a supercooled particle, a saturated film is likely to form which leads to recrystallisation. A cyclone separator is not able to recover individual crystal particles.[3] Spray freeze drying offers a solution to the problem of crystal particles,

where liquid droplets are frozen rather than dried. It is an advanced particle engineering technique, combining two drying processes: spray-drying and freeze-drying. Unlike the use of hot gas in the main chamber for spray-drying, freeze drying is performed using liquid nitrogen. The drug solution is atomised into liquid nitrogen, where frozen droplets are collected in a vacuum chamber prior to lyophilisation (freeze-drying). The instrumental set up is similar to that in Figure 1.1, however there is a cooler attached to the main chamber and an additional liquid collection vessel.

Supercritical Fluid Technology

Inhalable particles are required to have a diameter less than 5 µm, which most spray drying techniques are able to produce. However, in the case of proteins, the high temperature required to evaporate the solvent causes the protein to denature.[3] Additionally, micronisation, reducing the average particle diameter, can cause damaging effects on the crystallinity and chemical stability of the particles.[3] Denaturing can be prevented by reducing the temperature of the surrounding gas and by operating in an inert atmosphere, reducing the possibility of oxidation. Additionally, lower temperatures tend to form more brittle particles, aiding the micronisation process for pharmaceutical materials. Furthermore, lyophilisation often produces a broad particle size distribution, reducing the efficacy of inhalable formulations. Therefore, there is great interest in developing another drying technique that addresses the issue of denaturing proteins. One popular method is to use supercritical fluids.

In a spray drying process, supercritical fluids or compressed fluids can be used as a recrystallisation solvent.[3] They can be added to a solution as an antisolvent, forcing the precipitation of the solute primarily from an organic solution.[8] Supercritical solvent and antisolvent micronisation techniques commonly use compressed gaseous, liquid or supercritical fluid carbon dioxide. Supercritical fluids have liquid like densities and viscosities in the transitional state between a gas and liquid. Small changes in temperature and pressure of a supercritical fluid result in large changes to the solvent's power. Thus, the solvent's influence on the formulation can be controlled across the whole drying process. The supercritical fluid region of a pure component is where the pressure and temperature are such that the liquid and gas phase boundary lines meet. At this point, the gas and liquid form have the same density and the component will appear as a single phase.[3] For pharmaceutical applications, CO_2 is the most common solvent due to its low critical temperature, 31 °C, nontoxic and non-flammable properties and low cost.[3]

1.1.2 Devices for Delivering Drugs to the Lungs

The development of drug inhalation via the lungs is dependent on many physical, biological, and chemical variables. The physical variables associated with inhalable particle generation, such as size distribution and particle velocity, are dependent on the delivery device. This section will outline the attributes of the four main delivery systems: the metered dose inhaler (MDI), the dry powder inhaler (DPI), the nebuliser and the soft mist inhaler (SMI).

Metered Dose Inhaler (MDI)

The MDI is the most frequently used device for delivering drugs to the lungs. Upon actuation, the MDI generates an aerosol plume of drug formulation, driven by a propellant. Prior to the Montreal Protocol in 1987, the propellant was commonly chlorofluorocarbons (CFC). However, due to the depletion of the ozone layer from the labile chlorine atoms in CFCs, a new propellant was introduced, hydrofluoroalkane (HFA). HFA-134a and HFA-227 are commonly used as alternatives to CFCs, they do not contain chlorine, thus have no impact on ozone. However, HFAs and CFCs do possess different physical and chemical properties. The jetting force and velocity of the aerosol spray are reduced with the use of HFAs compared with the old CFC formulations.[9] A reduction in velocity is likely to reduce particle deposition in the mouth region, a benefit of HFAs. Additionally, excipients were commonly used alongside CFCs to prevent aggregation of particles and to lubricate the metering valve. However, excipient solubility is reduced in HFAs.[10] Often, ethanol is used to dissolve drug and excipient components. The drug formulation is emitted through a nozzle at a high velocity, > 30 m s^{-1}.[11] A schematic of an MDI is shown in Figure 1.3a, and a photo of a Chiesi MDI is shown in Figure 1.3b. The canister is held within a plastic case, the metering valve and actuator at the bottom of the canister emit the drug dose as a high velocity spray.
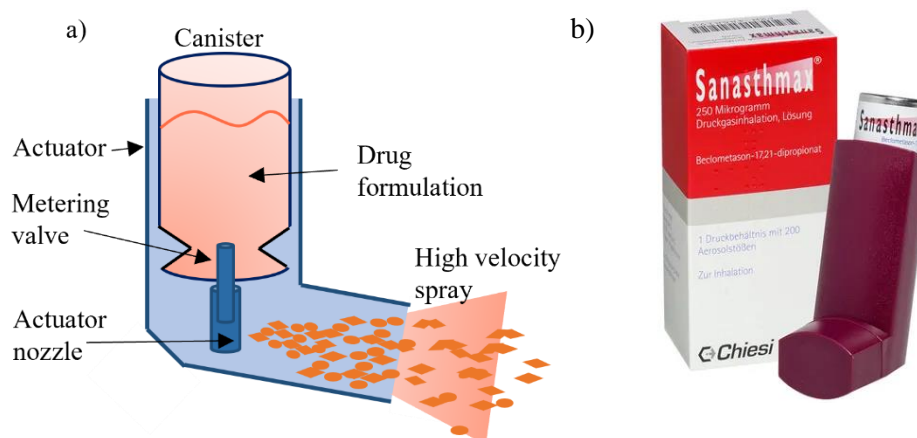
Figure 1.3. a) Schematic of an MDI. b) Sanasthmax, a Chiesi MDI device for beclometasone dipropionate (BDP).

MDIs have a very low drug delivery efficiency, only 10-20% of the emitted dose deposits in the lung. Newman et al. found that 50-80% of the emitted dose deposits in the oropharyngeal region due to high velocity and large particle size.[12] The dependency of deposition location on particle size is discussed in Section 1.1.4. Additionally, another cause of low efficiency is patient misuse, mainly with hand-mouth coordination. Crompton et al. found that 51% of patients were unable to co-ordinate actuation with inhalation and 24% of patients delayed inhalation upon drug dose emittance into the mouth.[13] Additionally, Crompton et al. found that 12% of patients inhaled through the nose rather than mouth.[13] The inspiration flow rate (IFR) of a patient influences the efficacy of an MDI. Bennet et al. found that deposition was most dependent on IFR for particles in the size range of 1-5 μm mass median aerodynamic diameter (MMAD).[14] They found that an increase in IFR lead to a decrease in deep lung, peripheral airways .[14] An increase in IFR results in a larger proportion of particle deposition in the upper lungs, conducting airway. A higher flow rate, > 60 L min^{-1}, leads to an increase in particle velocity, causing particles to deposit via impaction in the upper lungs and mouth. Newman et al. found that deposition via gravitational sedimentation in the deep lung increases with slow inhalation.[15] Additionally, it has been shown that a breath hold after inhalation allows more aerosol to reach and deposit in the deep lung, rather than being exhaled.[15]

Spacer tubes, valved holding tubes, were introduced to prevent patients inhaling aerosol below freezing temperatures. The Freon effect causes patients to stop inhaling when the aerosol are below freezing and the tube gives the aerosol time to increase in temperature.[11] It is known that the aerosol inhaled from a spacer tube is finer than when inhaled directly from an MDI. There is a decrease of about 25% in MMAD of particles from a spacer tube compared with direct inhalation from an MDI.[16] Finer aerosol is more likely to reach the deep lung, increasing drug delivery efficiency. However, it was found that for patients with obstructive pulmonary disease, a spacer tube had little effect on the percentage of deep lung deposition.[17]

Dry Powder Inhaler (DPI)

The DPI was introduced to address the patient error of hand to mouth coordination. Additionally, DPIs combat the issue of CFCs as they do not include a propellant, instead they are breath actuated. There are two common methods of drug formulation for DPIs; micronized drug particles attached to large course carrier particles (often lactose monohydrate), or carrier free spherical drug particles. All marketed DPIs are breath actuated, with two key variations in how the dose is loaded: a single-dose pack loaded by the patient or a multiunit dose pack that moves through the device.[18] A schematic of a single-dose DPI is shown in Figure 1.4a and a schematic of a multi-dose pack DPI in Figure 1.4b. A photo of a new DPI, NEXThaler (Chiesi) is shown in Figure 1.4c.
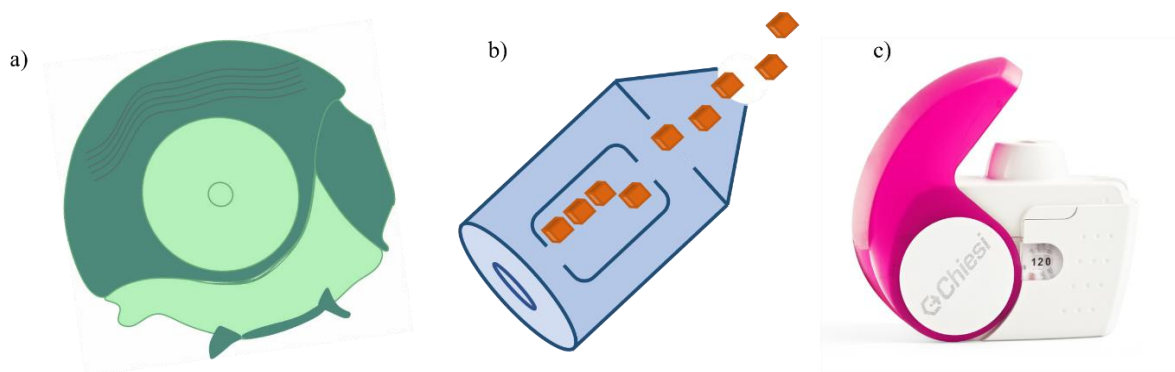
Figure 1.4. a) Schematic of a common DPI. b) Schematic of the inside of a DPI, highlighting the canister filled with dry powder particles. c) A photo of a new DPI, NEXThaler ®, developed by Chiesi.

DPIs have a slightly higher drug delivery efficiency than MDIs, with about 12-40% of the emitted dose depositing in the lung.[19] However, a large proportion of the drug formulation remains within the device, about 20-25%.[19,20] The MMAD of the dry particles influences their deposition fraction and is a function of the carrier particle size, density and shape.[18] The majority of particles generated from a DPI are too large to reach the deep lung due to the large carrier particles and formation of powder agglomerates. The formation of particles able to reach the lung is dependent on a turbulent air flow within the powder container.[11] A turbulent air flow helps to break up the aggregates, producing particles of adequate size to reach the deep lung, < 5 µm MMAD. Additionally, the air flow is required to separate the API particles from the large carrier particles. The air flow required differs between devices and is dependent on the IFR of the patient. High resistance devices require a larger IFR, and are known to have increased deep lung deposition.[16] A potential way to mitigate the dependence of deep lung deposition on IFR is to reduce the importance of a patient's inhalation ability. One method of aiding the IFR of a patient is by adding a battery-driven propeller to the DPI, or using compressed air to form a cloud of aerosol particles prior to inhalation.[16] Newhouse et al. found that a slow IFR, high relative humidity (RH) and a rapid change in temperature effect drug aggregation and thus, delivery effiency.[21] Additionally, Borgstrom et al. found that the total lung dose of an API increased with an increase of IFR from 35 to 60 L min^{-1} when using a Turbuhaler.[22] Unlike an MDI device, their research showed an increase of total lung dose of the API from 14.8% to 27.7% with an increase in IFR.[22]

Nebuliser

Since the transition from CFCs to HFAs there has been a growing interest in nebulisers due to the high cost of HFA formulations.[23] Additionally, patient error plays a large part in the inefficiency of drug delivery with MDIs, whereas nebulisers do not require any coordination. Furthermore, DPIs are breath actuated, causing problems for patients with respiratory limitations and infants. Nebulisers require no specific inhalation technique and are able to deliver large doses. There is a large variety of nebulisers available for the treat of asthma and other respiratory diseases.

A nebuliser is filled with a liquid solution or suspension of drug formulation and generates aerosol for inhalation. There are three basic types of nebulisers: jet, mesh, and ultrasonic. A jet nebuliser uses compressed gas (air or oxygen), which passes through an orifice causing a negative pressure around the outlet. Due to the low pressure, a film of drug solution is drawn up from the liquid reservoir, which is unstable and breaks into droplets in the gas stream.[23] An example of two commercially available mesh nebulisers is shown in Figure 1.5.[23] Mesh nebulisers are made with a mesh or plate that has many apertures, producing a plume of aerosol upon actuation. Batteries are needed to use a mesh nebuliser and an external gas flow is required. They provide treatment on a short time scale and are able to nebulise many different solutions and suspensions.[23] Ultrasonic nebulisers use a piezoelectric crystal to generate a stream of liquid inside a chamber. The crystal vibrates at a high frequency (1-3 MHz), and the higher the frequency, the smaller the droplets.

Figure 1.5. Commercially available mesh nebulisers, image from Pleasants et al.[23]

Although nebulisers are able to provide a large dose, and can be used for most drug solutions, treatment can be very time consuming. Additionally, there is large amount of drug wastage associated with nebulisers and about 50% loss with a continuous nebuliser such as a jet.[24] A large proportion of the drug remains within the device and only about 10% is deposited in the deep lung.[24] Recent developments have led to a new nebuliser that reduces drug waste and increases drug delivery efficiency. A novel method of monitoring the patient's breathing pattern allows for targeted aerosol delivery. An increase in aerosol output is achieved by directing auxiliary air through the nebuliser during inspiration only.[11]

The Halolite device was found to deposit 60% of the emitted dose in the lung, 37% in the mouth and only 3% was lost to the envrionemntt.[23,25] Additionally, in recent years many metered dose liquid inhalers have been developed, which produce a plume of liquid aerosol with the use of nozzles at the device outlets. These new technologies are described in the next sub-section.

Soft Mist Inhaler (SMI)

SMIs are similar to nebulisers, aerosolising a liquid solution or suspension. Unlike nebulisers, however, SMIs are portable, which is a huge advantage for patients and therefore SMIs have received vast interest. They are the newest type of inhaler in the market and often used with long-acting bronchodilators. A schematic and photo of Respimat® are shown in Figure 1.6. Respimat®, like nebulisers and DPIs, does not use a propellant and instead the drug formulation is pushed through a membrane.[23] The Respimat® device has been found to produce aerosol of MMAD appropriate for respiratory to the lung, ~ 2 µm.[26] The generated aerosol have been found to be homogenous in composition, releasing slowing from the device outlet, compared to the high velocity associated with MDIs.[27] The slow release action of Respimat® has two potential benefits. Long duration of dose release from Respimat® may address the lack of coordination often observed with actuation and inspiration in MDIs. Additionally, slower velocity of aerosol may reduce the amount of drug depositing in the mouth via impaction, thus resulting in higher deep lung deposition.[23] Chapter 4 explores the particle dynamics of each component associated with the Respimat® device.
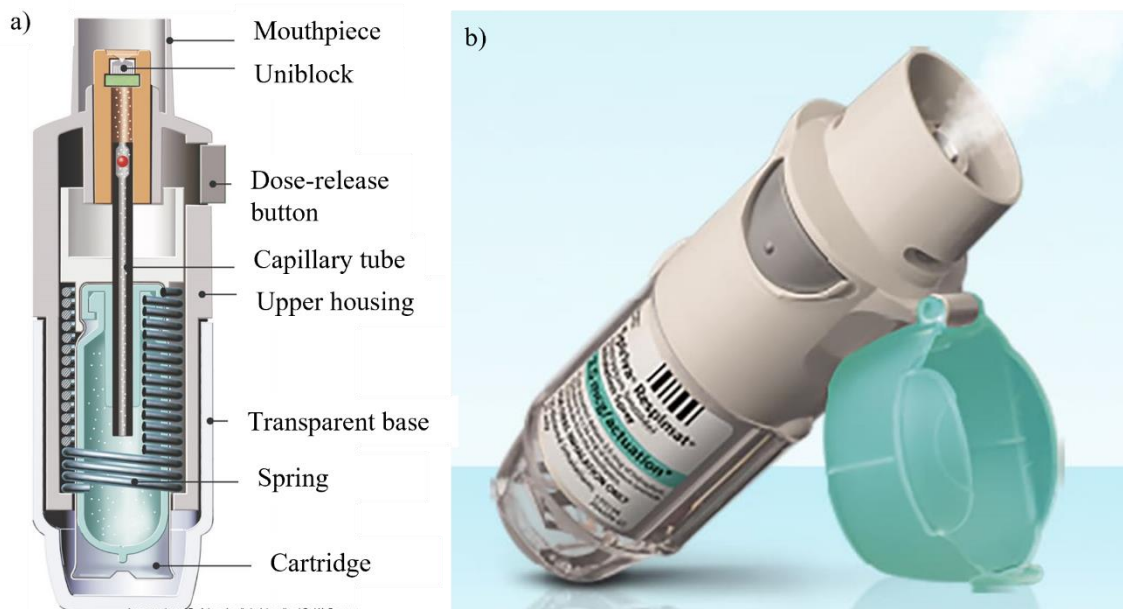
Figure 1.6. a) Schematic produced by Pleasants et al. of the inside of a soft mist inhaler.[23] b) Photo of the soft mist Respimat® device.[26]

1.1.3 Evaporation and Condensation Processes Transforming Particles Following Generation and Inhalation to the Lung

Aerosol offer direct delivery to a target site for treatment of a range of respiratory diseases and for administering drugs for systemic circulation. The dynamic aerosol processes occurring between the point of aerosol generation and deposition are rarely considered.[28] However, there are many studies on the drug formulation and the device used to generate and deliver the drug.[28] Additionally, there has been much research on the resulting deposition pattern in the lung, often explored using a cascade impactor, in which environmental conditions are rarely considered.[29] Particle dynamics in the aerosol phase in a humid environment, such as the lung, are key to optimising inhalation therapies. Pharmacokinetics of the inhaled medicine and the efficacy of the treatment also receive much interest.[28] Improving the efficiency of treatment is likely to be dependent on improving the ability to target lung deposition fraction, so that drugs can be delivered to specific regions.[30] Targeted deposition requires an understanding of the aerosol processes that occur during inhalation, as well as an understanding of the relationship between the physicochemical characteristics of a substance and the subsequent aerosol dynamics in a humid environment.

The four main devices used in drug delivery to the lung are outlined in Section 1.1.2. Solution, or suspension formulations are used in pMDIs, containing an API, ethanol (co-solvent), HFA (propellant) and with or without excipient. A dry powder mixture of micronized API particles attached to large course carrier particles (lactose monohydrate) is delivered with an DPI. Nebulisers/SMIs are used to deliver an aqueous based solution of API with or without excipient. The aerosol are generated from each device as either a liquid droplet, amorphous particle, or crystalline particle. A schematic of the transformations that occur between generation and inhalation is shown in Figure 1.7. In the case of an MDI, patient actuation forces liquid from the canister through an actuator to form a plume of monodisperse liquid droplets. The propellant and ethanol evaporate rapidly due to high volatility and high boiling point.[31] As the volatile components evaporate, the droplet temperature decreases, known as evaporative cooling. A decrease in temperature leads to water condensation from the gas phase. In a humid environment, such as the lung, water vapour is abundant and thus is not a limiting factor to the mass flux.[31] Upon water condensation, a droplet composed of water, API and excipient remains. The final droplet has potential to take the form of many phases: homogenous aqueous droplet, non-homogeneous aqueous droplet, amorphous particle, or crystalline particle. The final phase state of the particle is dependent on the physical properties of the API, such as hygroscopicity, the presence of an excipient and the timescale between generation and deposition, e.g., spacer tube or no spacer tube.
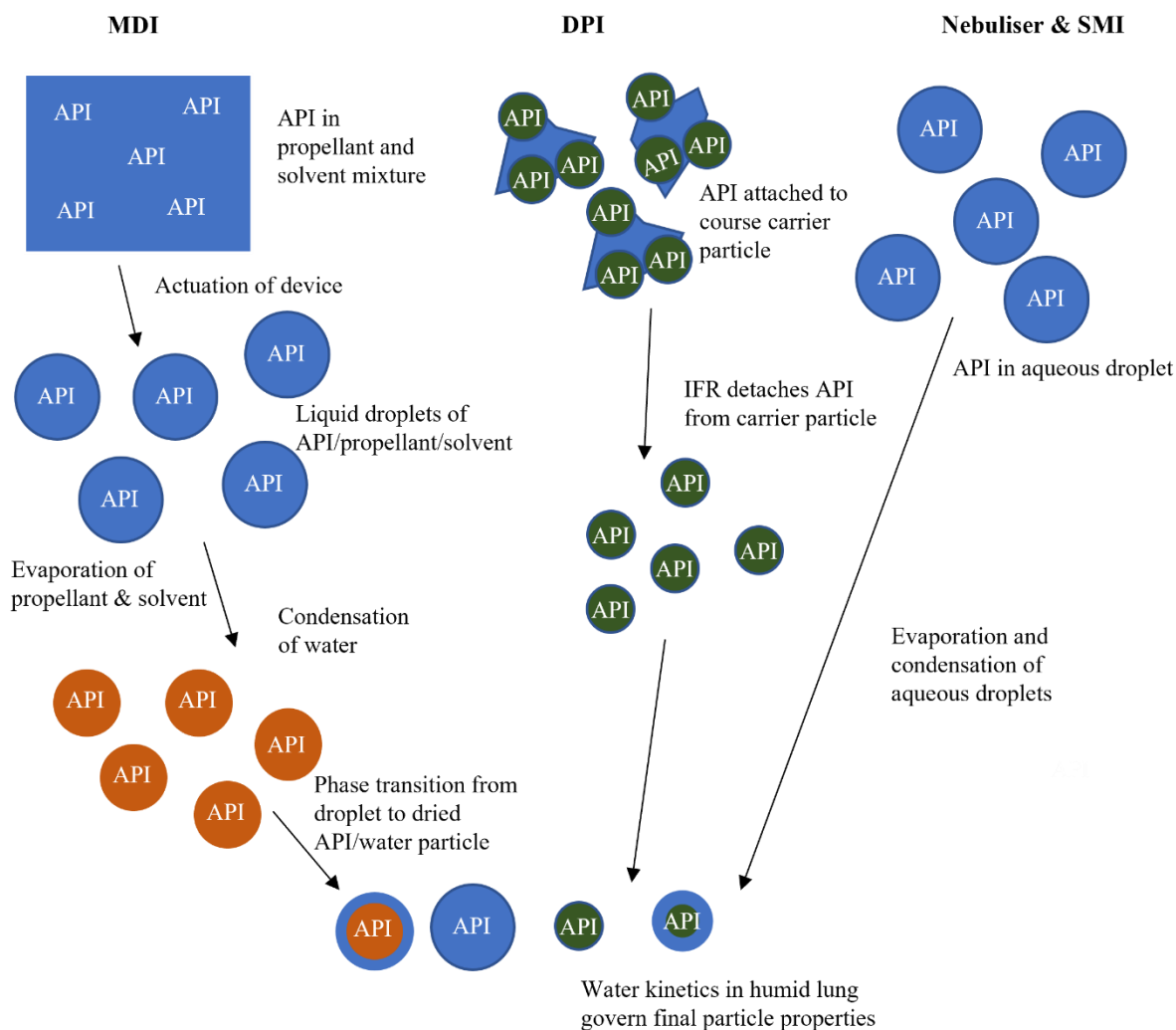
Figure 1.7. Dry and liquid aerosol production of MDIs, DPIs and nebuliser/SMIs. Followed by the dynamic aerosol processes occurring during inhalation.

A DPI device is breath actuated and produces a cloud of dried particles, composed of an API attached to large carrier particles. The formulation is commonly spray dried, resulting in the production of amorphous or crystalline particles. The API and carrier particles are separated in the mouth and upper airway due to the inspiratory flow. Carrier particles are too large to deposit in the deep lung, >5 µm diameter, and instead deposit in the mouth or upper airway via impaction. The micronised amorphous and crystalline drug particles, <2.5 µm diameter, travel through the humid airway before depositing in the deep lung. The final particle morphology and size may be influenced by water condensation kinetics during inhalation. A crystalline particle with a high solubility limit and is unlikely to take up water during the time of an inhalation, ~3 s. However, an amorphous, hygroscopic particle will undergo significant water condensation, influencing the final particle morphology and size. The water kinetics associated with the DPI particles will govern physical properties such as size, morphology, and phase. Particle size is known to influence deposition site, where as morphology and phase are known to

influence pharmacokinetics.[28] Understanding the relationship between the physical properties and particle dynamics of a DPI particle is vital to improve targeted drug delivery.

Nebulisers and SMIs systems are slightly simpler, in that there are no rapidly evaporating solvents. Instead, an aqueous solution is used to form a plume of aqueous droplets, composed of API, water and with or without excipient. The homogeneity of the droplets is dependent on the solubility of the API, and the mass flux of water between generation and inhalation. In the case of a very soluble API, a liquid droplet is likely to decrease in size upon generation to an ambient environment, while remaining a homogenous droplet. Subsequent droplet dynamics are then only dependent on the hygroscopic properties of the components within the droplet. In the case of a non-soluble API, it is likely that exposure to ambient RH will lead to formation of a non-homogeneous droplet, with undissolved API particles present. Here, droplet dynamics are dependent on the dissolution kinetics of the undissolved components. Followed by dependence on hygroscopic properties upon formation of a homogenous liquid droplet. The humidity of the respiratory tract is close to saturation, >99.9% RH, which will influence particle size with dependence on the hygroscopic properties of the substance.[28]

The dynamic processes occurring during generation to inhalation and on to deposition have influence on the efficiency of drug delivery if the timescale of events match that of an inhalation. The International Commission on Radiological Protection, ICRP, states that the average time of an inspiration flow to reach the deep lung is about 2-3 s.[32] Air residence times in the lung range from 2 to 5 s, depending whether the patient is stationary or exercising. The time scale of air residence and for flow to reach the deep lung is dependent on human biological features such as age, weight, gender, and respiratory health. Therefore, it is important to determine the time dependency of particle dynamics to accurately predict the phase and size of depositing particles. Additionally, it is common practice that particle deposition measurements, such as the Anderson cascade impactor, use dry particle size or a set relative humidity. This thesis aims to explore the effect of relative humidity on particle dynamics, while illustrating that development in deposition measurements is needed to accurately represent lung deposition.

1.1.4 Deposition Mechanics of Inhaled Pharmaceutical Particles in the Lung

Drug delivery to the lungs is a preferred route of treatment of lung disease due to the instant respiratory relief for the patient. Inhaled drug formulations travel through the oropharyngeal region (upper airway/mouth and nose), conducting zone (trachea and lower airway), and respiratory zone (deep lung). An outline of the three main regions is shown in Figure 1.8a. The lower airways and deep lung are affected by respiratory diseases, such as asthma and chronic obstructive pulmonary disease (COPD). Thus, the conducting zone and respiratory zone are the target sites for particle deposition when treating asthma and COPD. Figure 1.8a indicates the dependence of deposition location on particle radius, while the deposition mechanism dependence on size is shown in Figure 1.8b. A graph showing the dependence of lung deposition fraction and deposition region as a function of particle diameter is shown in Figure 1.8c. The highest total lung deposition is seen in the region of 0.001 to 0.01 µm and 2 to 5 µm. To ensure consistency, this thesis explores the influence of particle size on drug delivery to the lung using only optical particle radius and diameter as a measurement of the particle size. However, it is common in the pharmaceutical industry to use the aerodynamic diameter of a particle when referring to size. The aerodynamic diameter is defined as that of a sphere, whose density is 1 g cm $^{-3}$ (density of water), which settles in still air at the same velocity as the test particle, of non-spherical shape. Understanding particle dynamics during inhalation is key to predicting the deposition site and optimising pulmonary drug delivery.
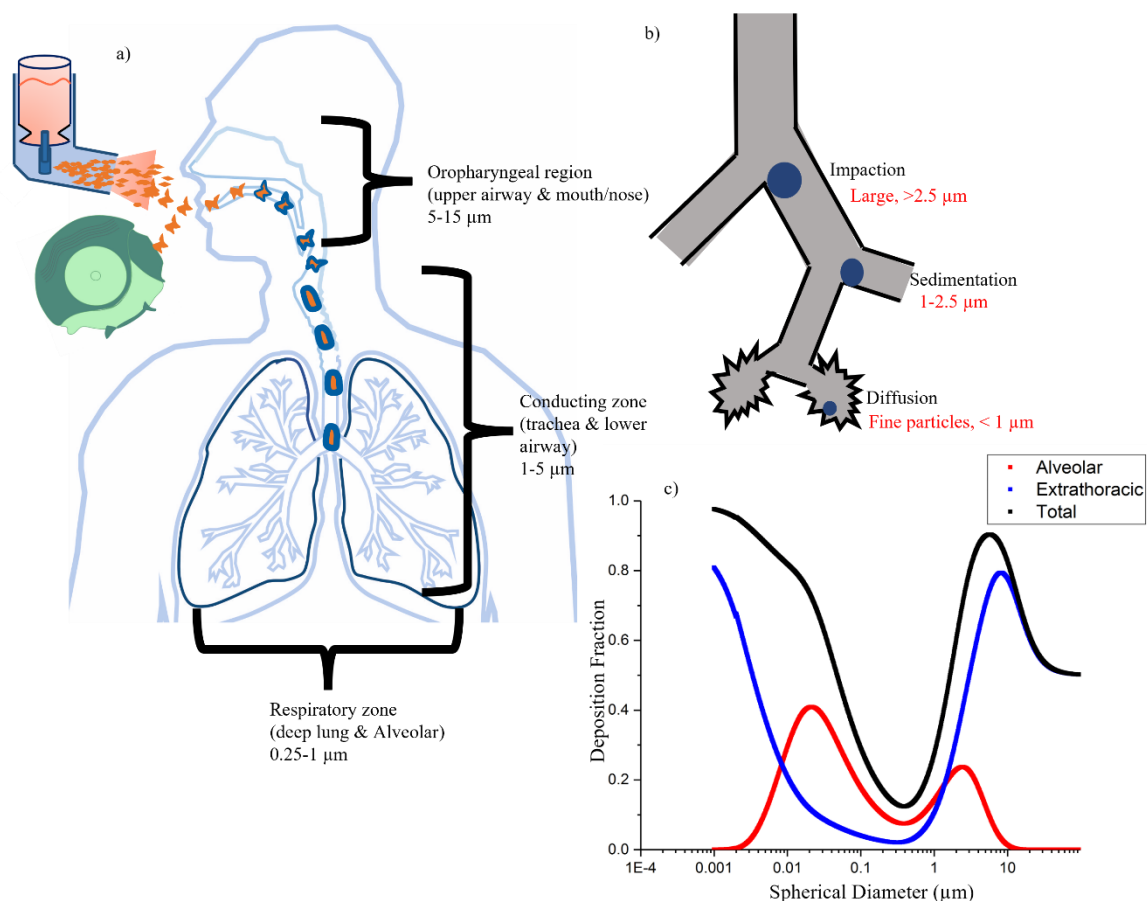
Figure 1.8. a) Schematic of an adult lung with predictions of deposition dependent on particle radius. b) Mechanisms of particle deposition in the upper airway, lower airway and deep lung.[23] c) Deposition fraction of inhaled particles as a function of diameter.[33]

There are three mechanisms of aerosol deposition: inertial impaction, gravitational sedimentation and diffusion.[34,35] Larger, <2.5 µm radius, fast moving particles are likely to deposit by inertial impaction in the oropharyngeal region or larger airways. Particles of sufficient mass and size, 1-2.5 µm radius, are likely to deposit via gravitational sedimentation.[3] The smallest particles, <1 µm radius, are likely to travel through the airways and deposit in the deep lung, including the alveoli and bronchioles.[36] The deposition mechanisms of drug deposition, dependent on particle size and velocity, are shown in Figure 1.8b. In the treatment of respiratory diseases, muscle receptors are the targeted site for drug deposition. Many inhaled APIs, such as salbutamol sulphate, are a β2-agonist bronchodilator and provide rapid relief to shortness of breath. The β receptors are spread throughout the airways and upon deposition the drug exerts its effects on the receptors within minutes.[23] The inhaled drug must reach the desired site to ensure the required pharmacological effect. Additionally, inhalation is a common method to administer drugs for systemic circulation. Such treatment requires the drug particles to reach the deep lung, where there is a large surface area, and the drug can reach the bloodstream rapidly.

Inhaled drug particles are most likely to reach the airways and deep lung, inducing a pharmacological effect, when particles are in the fine-particle fraction of 0.5-1 µm radius. Particles of radial size 0.25-1 µm behave as a gas and undergo Brownian diffusion, settling slowly on the lung surface. Additionally, fine particles and ultra-fine particles may also be exhaled, reducing the deposition fraction. Clearance of drug particles is dependent on air-flow obstruction within the lung, pharmacokinetic properties, and physicochemical properties such as molecular weight of the drug. During inhalation particles are introduced to a high RH, which affects the deposition due to hygroscopic growth. This thesis aims to explore particle size dynamics associated with water kinetics, to better predict final particle size and thus, control the deposition site.

1.2   Properties of Aerosol

This section introduces the aerosol properties which influence experimental measurements and the aerosol science associated with drug delivery to the lung. The optical properties are often exploited to characterise aerosol phase laboratory measurements and are used in this thesis. The thermodynamic and kinetic properties of aerosol play an important role in the overall process, and efficiency of pulmonary

drug delivery. The optical properties, thermodynamic properties, and the dissolution process of aerosol must all be understood to deduce their effect on each other.

1.2.1   Optical Properties of Aerosol

When the electric field of incident light interacts with the polarisable electrons composing molecules in an aerosol, the light can be elastically or inelastically scattered. Elastic light scattering from an aerosol can be described using Maxwell's equations,[37] with the emitted light and incident light having the same wavelength. However, elastically scattered light consists of emitted light that has an increased wavelength compared with the incident light. A schematic of the interaction mechanisms of incident light with a droplet is shown in Figure 1.9. The interaction mechanism is dependent on the optical properties of an aerosol. The size, shape, morphology, and refractive index (RI) of a particle all contribute to the optical response of a particle, and thus the amount of scattering and absorption observed during light and particle interaction.
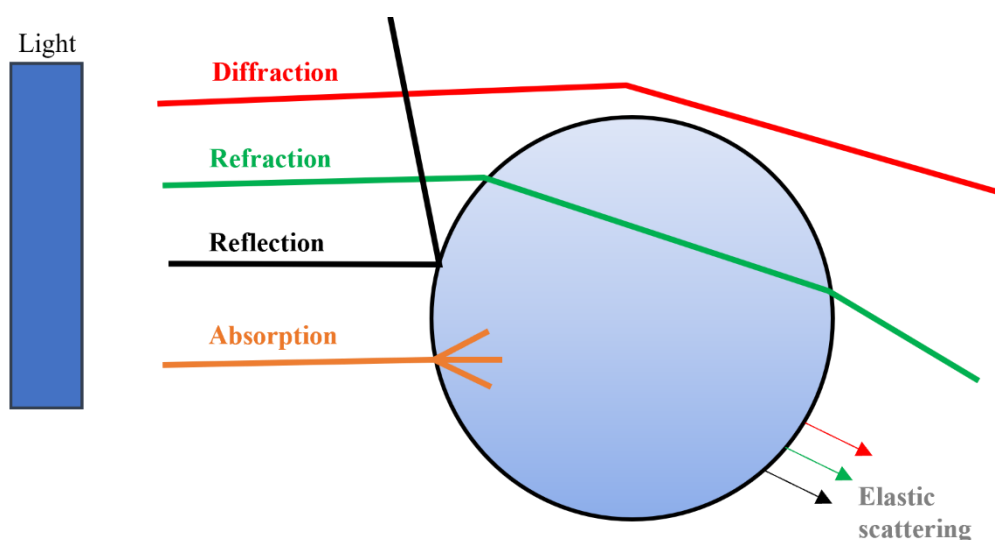
Figure 1.9. Schematic of the interaction mechanisms of light with a droplet.

The RI (n) is given in Equation 1.1. and is separated into a real (m) and imaginary (k) part. The real part of the RI governs the elastic scattering process and is dependent on the density and molecular polarizability of the substance. Furthermore, the real part is defined as the ratio between the speed of light through a substance and vacuum. The speed of light is less when travelling through a substance compared to a vacuum. The imaginary part of the RI governs the attenuation of light as it is absorbed by the substance.

$$n = m + i\,k$$

16

Mie theory was first introduced by Gustav Mie in 1908[38] and can provide an exact solution to the light scattering of a spherical droplet.[38] However, approximation of Mie theory can be used under limiting conditions to reduce computational cost. For small droplets, $\lambda \gg r$, where the wavelength is larger than droplet radius, light scattering can be approximated by Rayleigh scattering. In the case of $\lambda \ll r$, where the wavelength is less than the droplet radius, Geometric Ray Optics can be used to describe the light scattering.[39] In Rayleigh scattering, the radiation is uniformly scattered in all directions.[40] Light scattering can be used to infer the physical properties of aerosol. In this thesis, elastically scattered light is used to determine droplet size and phase state. The instrumental techniques for collecting and interpreting scattering light from particles are introduced in Section 1.3.1.

1.2.2 Hygroscopic Properties of Aerosol

Hygroscopicity is the ability of a substance to absorb moisture from the surrounding environment. The hygroscopic properties of pharmaceutical aerosol play a very important role in the efficiency of drug delivery via the lungs.[28] The RH of the lungs is close to saturation, resulting in the potential of large amounts of water absorption by particles and thus, large physical and chemical changes. Section 1.1.4 highlights the dependency of the deposition site of inhaled particles on particle size.

The amount of water uptake is governed by the hygroscopic response of a substance, which is different from compound to compound. Additionally, the magnitude of aerosol water uptake is dependent on the RH of the gas phase. The RH, often expressed as a percentage, is given by:

$$RH = (P_{H_2O}/P_{H_2O}^*) \times 100\%$$

Equation 1 - 2

where P_{H_2O} is the partial pressure of water and $P_{H_2O}^*$ is the equilibrium saturation vapour pressure of water. Changes in the RH lead to mass flux of water from or to a droplet, known as evaporation and condensation, respectively. Evaporation and condensation result in changes to the droplet size, composition, and RI, which all affect the light scattering characteristics and absorption properties of a particle.

Aerosol hygroscopicity is commonly presented as radial growth factor (RGF) with respect to water activity (a_w). At an RH of 100%, the water activity is equal to 1. The RGF, given in Equation 1-3, is the ratio between the wet particle radius (r_{wet}) and dry particle radius (r_{dry}):

$$RGF = \frac{r_{wet}}{r_{dry}}$$

Equation 1 - 3

The growth factor is a common way to represent hygroscopicity in environmental science, this thesis aims to highlight the important of RGF in pharmaceutical aerosol science. As outlined above, the deposition fraction of inhaled particles is a function of particle size. Furthermore, particle size is dependent on the ability of a substance to take water. Therefore, radial growth is an important parameter for predicting aerosol deposition for hygroscopic aerosol in the lung.[41] The hygroscopic response of sodium chloride, represented as RGF with respect to water activity, is shown in Figure 1.10. Lowering the gas phase a_w results in a decrease in droplet radius, which continues up to a point known as the efflorescence RH (ERH). For sodium chloride the ERH is 45%, at this point the a_w of the gas phase is too low to keep the solute in solution. Instead, the low RH leads to crystallisation of the sodium chloride and the droplet undergoes efflorescence. Interestingly, in the aerosol phase a solute is able to stay in solution beyond the bulk solubility limit. For sodium chloride, the bulk solubility is reached at a water activity equivalent to 75% RH. During the period between the bulk solubility limit, 75% RH, and the ERH, 45%, a saline droplet is described as supersaturated. Once a substance has effloresced, the RGF is equal to 1, indicating that the size is equal to the dry radius of the solute-only particle. Following an increase of the gas phase RH, water molecules will adsorb onto the surface of an effloresced particle. However, the gas phase RH must be taken to a value where the water activity of the dissolved solute would be equal or larger than the bulk solubility limit to transition back to a solution droplet. This RH is known as the deliquescence RH (DRH), which is 75% RH for sodium chloride. At this point, there is sufficient water in the gas phase for the dried sodium chloride to deliquesce and form a homogenous, saline droplet. The processes of efflorescence and deliquescence occur frequently during pulmonary drug delivery, from generation to inhalation and on to particle deposition. Techniques have been developed throughout this thesis which probe the efflorescence/deliquescence cycle of many pharmaceutically relevant compounds. The kinetic and thermodynamic properties associated with the mass flux outlined in Figure 1.10. are discussed thoroughly in Chapter 2.
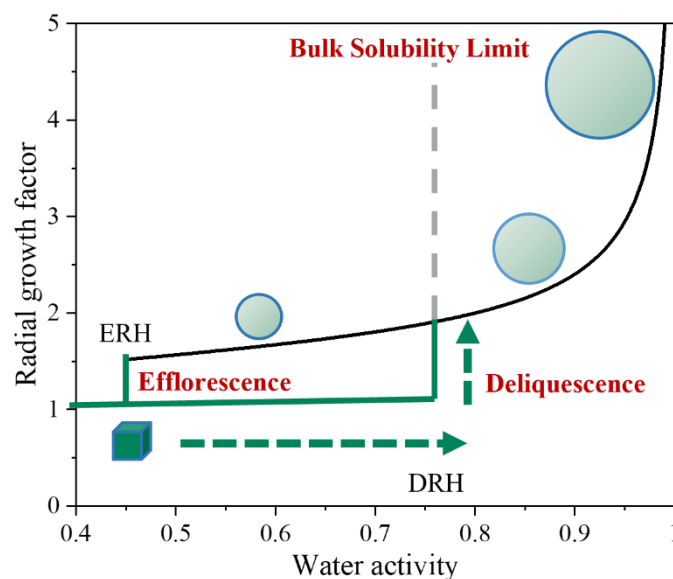
Figure 1.10. Radial growth factor as a function of water activity for sodium chloride.

1.2.3 Dissolution Properties of Aerosol

Deliquescence is a first order phase transition, where a solid transitions to a saturated liquid droplet at a certain RH, known as the DRH.[42] Dissolution takes place as a result of deliquescence, altering the chemical and physical properties of a particle. In drug delivery to the lungs, the patient often inhales amorphous or crystalline particles that have been delivered using a DPI.[4] As well, particles generated from an MDI experience rapid evaporation of HFA and the co-solvent, often resulting in a dried drug particle. Upon inhalation to a humid lung, a dried particle may experience significant water uptake. The phase state and final size of the deposited aerosol are influenced by the dissolution properties of the substance. Pharmacokinetics, the time scale of drug absorption and distribution into the body, are governed by the phase state of a particle and the point of deposition. Therefore, it is vital to probe the dissolution and deliquescence properties of pharmaceutically relevant aerosol to better control the physical properties of the deposited particle.

The DRH is influenced by the solubility of a substance, a highly soluble crystalline particle will begin deliquescence at a lower RH than that of a non-soluble particle. At the DRH, an aqueous droplet is the thermodynamically favoured phase, thus dissolution commences.[42] Below the DRH, a crystalline particle surrounded by water vapour is the thermodynamically favoured phase. There is a significant range in the DRH for pharmaceutical aerosol. For example, the DRH of sodium chloride is 75% compared with 96% for mannitol. The difference in DRH between sodium chloride and mannitol is a result of their different bulk solubility values. A substance with a high aqueous solubility value will

tend to have a lower DRH. Additionally, in the case of an upward relationship between temperature and solubility, the DRH will decrease at lower temperatures.

A schematic of the dissolution process of solid particle to aqueous droplet is shown in Figure 1.11. In ambient conditions, when the RH < DRH, water adsorbs on to the particle, but no dissolution is observed. For example, sodium chloride is known to adsorb 2-3 monolayers of walk prior to bulk dissolution.[42,43] As the ambient RH increases above the DRH, more water vapour adsorbs onto the particle and dissolution of the solute at the surface commences. A thin, saturated film of solute forms around the particle, which has a lower vapour pressure than that of pure water. Substances of highly water solubility are found to significantly reduce the water vapour pressure in the saturated film compared with pure water. Therefore, water condenses on to a particle at a lower RH for highly soluble substances due to the difference in vapour pressure in the saturated film and pure water.
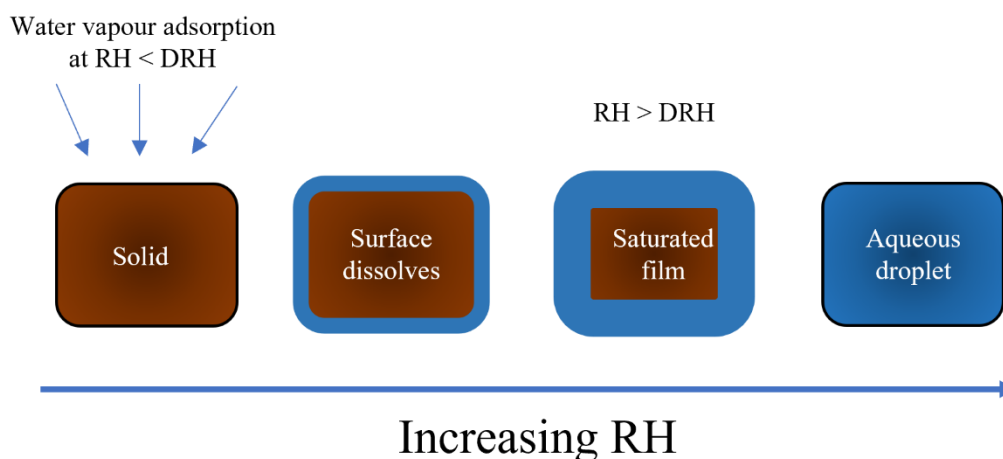
Figure 1.11. Schematic of the dissolution process of a solid to aqueous particle.

1.3   Overview of Single Aerosol Particle Measurement Techniques

In this thesis, particle measurements were solely performed using single particle techniques, with the exception of size distribution measurements on an aerosol particle sizer. Electrodynamic techniques were used to trap single particles, which enabled exploration of physical and chemical aerosol properties. Dynamic single aerosol measurements were undertaken while controlling environmental conditions, RH and temperature. An electrodynamic balance (EDB) was used to trap particles of a radius range 5-80 μm. This section provides an overview to common single particle measurements, with a focus on the development of electrodynamic levitation.

1.3.1.   Single Particle Measurements

The microphysical processes that effect the efficiency of drug delivery to the lung can be replicated using single particle measurements. Focusing on individual aerosol, removes the limitation associated with droplet-droplet interaction in ensemble measurements. The dynamic processes of single particles can be precisely controlled, with in-depth probing of the kinetic and thermodynamic processes associated with drug inhalation. In this thesis, an EDB was used to replicate the processes and conditions within the lung. A detailed introduction to electrodynamic levitation, and the history of the EDB, is given in Sections 1.3.2 and 1.3.3. Brief descriptions of three other common single particle measurements are outlined in this section; acoustic techniques, optical techniques and falling droplet column.

Acoustic Techniques

Acoustic techniques are used to trap single and multiple particles use sound waves at very high frequencies. It is a useful technique to levitate small liquid droplets and particles within an ultrasonic field.[44] The frequency of the stationary ultrasonic field influences the size of the levitated sample, commonly in the radial range of 0.1 to 5 mm. Droplets or particles are suspended in the pressure nodes of an ultrasonic field within acoustic tweezers. The environmental conditions can be controlled and monitored, for example Tuckerman et al., monitored droplet temperature using an infrared-thermography system.[44] A stationary sound wave within an acoustic levitator is generated by an ultrasonic radiator and a concave reflector. A droplet or particle is confined in the nodes of the stationary ultrasonic field. Acoustic techniques have been used to measure evaporation rates of water droplets and the influence of an organic surfactant.[45,44] Additionally, acoustic tweezers have been used for surface tension measurements of liquid droplets and to explore the process of ice nucleation.[46]

Optical Techniques

Ashkin first reported optical levitation in 1970 and he achieved levitation of a single micronised particle in the gas and liquid phase.[47] It was discovered that the radiation pressure of light scattering can apply a force on a droplet or particle. The optical trapping techniques involve a force acting on a droplet or particle that is generated from the scattering of a laser light.[48] A trap is formed as the laser beam is tightly focused through an objective of significant aperture. The scattering force of an incident light is used to confine individual droplets and particles. In 1987, Ashkin developed a gradient-force, three dimensional optical trap for single droplets, using an infrared (IR) laser.[49] Raman spectroscopy can be used to characterise the size, refractive index and composition of aerosol that are levitated using optical

tweezers. Particles of the size range 0.5 to 5 µm can be confined using optical tweezers, and their hygroscopic properties measured.[50] Additionally, the vapour pressure of semi-volatile compounds, rate of water evaporation and oxidative ageing of organic aerosol have all been measured using optical techniques.[51]

The Bessel beam trap is another optical technique that is often used in aerosol measurements. A spherically symmetrical beam is produced by passing a Gaussian laser bean through an axicon. The beam is perpendicular to the propagation direction and consists of a high intensity core.[52] The Bessel beam trap is often used to measure the vapour pressure of droplets using their water evaporation kinetics. A new development of the Bessel beam is its coupling with a cavity-ring down system, which allows particles in the size range 300-3000 nm to be probed.[52]

Optical trapping techniques provide accurate measurements on micrometre sized particles. However, an optical trap requires a large plume of aerosol to be generated into the chamber, resulting in the confinement of a single aerosol.[53] Often a nebuliser, similar to the device described in Section 1.1.2, is used to produce a plume of aerosol. A large volume of volatile and semi-volatile components within a trapping chamber can result in changes to the initial conditions of the single confined aerosol. Additionally, nebulisers can be limited by physical properties such as viscosity and surface tension of the substance. Although all compounds explored in this thesis are not harmful, in other areas of aerosol science many substances are toxic. Thus, nebulising such materials pose a safety risk, particularly with the required large plumes of aerosol. Electrodynamic levitation involves targeted delivery of a droplet to the trapping point, much research is focused on achieving the same for optical techniques.

Falling droplet column measurements

The disadvantage of the single droplet methods described above is the time taken to stabilise and trap each individual droplet. Additionally, the use of a laser beam to infer physical properties requires the trapped particles to remain homogenous and spherical throughout measurement. Falling droplet column measurements, also known as the droplet chain method, are often used to measure droplet evaporation in spray drying and other areas of microfluids.[54] A chain of monodispersed droplets is introduced into a controlled gas flow. Often, the monodispersed droplets are formed using a thermal dispenser, vibrating orifice or a piezoelectric dispenser (the method used in this work). Additionally, a droplet on demand piezoelectric dispenser produces droplets with a spacing larger than a droplet diameter, preventing droplet merging.[54] Baldelli et al. deduced models which provide a partial description of particle formation, they require a droplet to have a constant evaporation rate.[54] Their model has been developed to incorporate a change in evaporation rate over time and for a change in substance properties.[55]

A falling droplet column is made of three main sections: droplet generation, collection chamber and an optical source. In BARC, droplets are generated using a Microfab droplet on demand dispenser and often with an orifice of 30 µm. The dispenser produces uniform droplets with a distance between each one that prevents droplets colliding. A detailed description of the dispensing technique is outlined in Chapter 3. The droplets are dispensed into a vertical flow tube, Hardy et al. designed a glass chamber of 4 cm^2 inner area and 50 cm long.[56] The droplets are dispensed horizontally and fall vertically through the centre of the chamber, where they deposit on a glass slide at the collection point. The physical properties of the collected particles, such as morphology, structure, and density, can be further analysed using SEM. The droplets evaporate as they fall, the rate of which is dependent on the gas phase RH, reducing in aerodynamic diameter. To measure the size change during a droplet lifetime a propagating laser is strobed at the same frequency as the droplet dispenser. The droplets are illuminated, which produces the illusion of a static chain of droplets. An imaging system is used to measure the droplet size at various points along the chain. The falling droplet column is a closed system, where the gas phase RH and temperature in the chamber can be controlled.[55] The falling droplet column has been used to measure crystallisation rates, evaporation rates, viscosity and dynamic radial changes.[56,54]

1.3.2. Electrodynamic Levitation

Electrodynamic levitation is a popular technique for trapping individual aerosol due to no surface contact of the particle and good trapping stability. This method of droplet trapping was used throughout this thesis, and advancements on existing electrodynamic traps were made. Electrodynamic levitation was used in this work due to the stable trapping of individual particles, which can be physically analysed using light scattering techniques. The instruments described in this section are known as an EDB.

An electrodynamic trap consists of a set of electrodes which form an electric field and spatially confine a charged particle. A high alternating current (AC) and direct current offset (DC) are applied to the electrodes. An EDB is able to trap particles on the size range of $1 - 100$ µm, depending on the electrode configuration and the droplet dispenser. The droplets must be charged prior to entering the trap, often a DC voltage is applied to a needle which causes a Coulombic explosion, resulting in a charged droplet.[57] A vibrating orifice is used to generate liquid droplets and is combined with the inductive charging. Solid particles, such as pollen, have been delivered to an EDB with the use of a metal rod and a high voltage. Davis et al. attached pollen particles to a metal rod, upon application of a high voltage the particles on the rod detached and were introduced to an EDB.[58] The experiments in this thesis used an induction charge technique.[59] Unlike optical trapping, droplets can be introduced to an EDB individually, reducing the effects associated with a plume of aerosol.[59]

If only an AC voltage is applied to a trapping cell, a charged droplet will oscillate around a central null point due to the gravitational forces acting vertically on the droplet. Therefore, a combination of an AC and DC field is applied to counteract the gravitational force, leading to stable trapping of the droplet precisely in the centre of instrument. Stable trapping allows for accurate analysis of the size, mass, and morphology of the trapped particle.

1.3.3. Development of the Electrodynamic Balance

Development of the electrodynamic balance began with Millikan's desire to measure the elemental charge on an electron.[60] In 1909, Millikan used an oil drop experiment to measure the charge of an electron, receiving a Nobel prize for his work in 1923. The oil drop experiment was based on earlier by Wilson, who confined a cloud of water droplets between two charged plates which were connected to a battery. An electric field was applied to the plates, when switched off the rate of fall of the droplets was measured. Wilson's measurements were used to measure the charge on an electron; however the experiment had low reproducibility and produced a value of charge of 1.034E-19 C.[40] Unlike the water droplet in Wilson's experiment,[61] Millikan used oil droplets, eliminating errors associated with evaporation. The experimental set up of Millikan's oil drop experiment is shown in Figure 1.12a. A stream of oil droplets enters the top of the electrode chamber, parallel to the plate electrodes. In 1913, Millikan measured the rate of fall of droplets with and without an electric field and he determined a value of 1.433E-19 C of the charge on an electron. Following the measurements of falling droplets, Millikan recognised that some alterations to the experimental would allow for prolonged

electrodynamic levitation of charge particles. The addition of a DC voltage compensates for the gravitational force acting downwards on the droplet.

Figure 1.12. Schematics of the EDB development.

Straubel used the principal of Millikan's experiment and the newly discovered knowledge of stably held ions in a quadrupole ion trap by Paul and Raether.[62] It was shown that a quadrupole trap could stably confine ions by applying an AC voltage to a hyperboloidal electrode setup. Combining the AC voltage set up of a hyperboloidal electrode and a DC voltage that compensates the gravitational force, the first electrodynamic balance (EDB) was introduced, Figure 1.12b. A disk-electrode applying an AC voltage was positioned around the centre of the trap. The DC plate electrodes, as per Millikan's experiment, were positioned above and below the disk electrode. Straubel was able to trap charged droplets of ~10
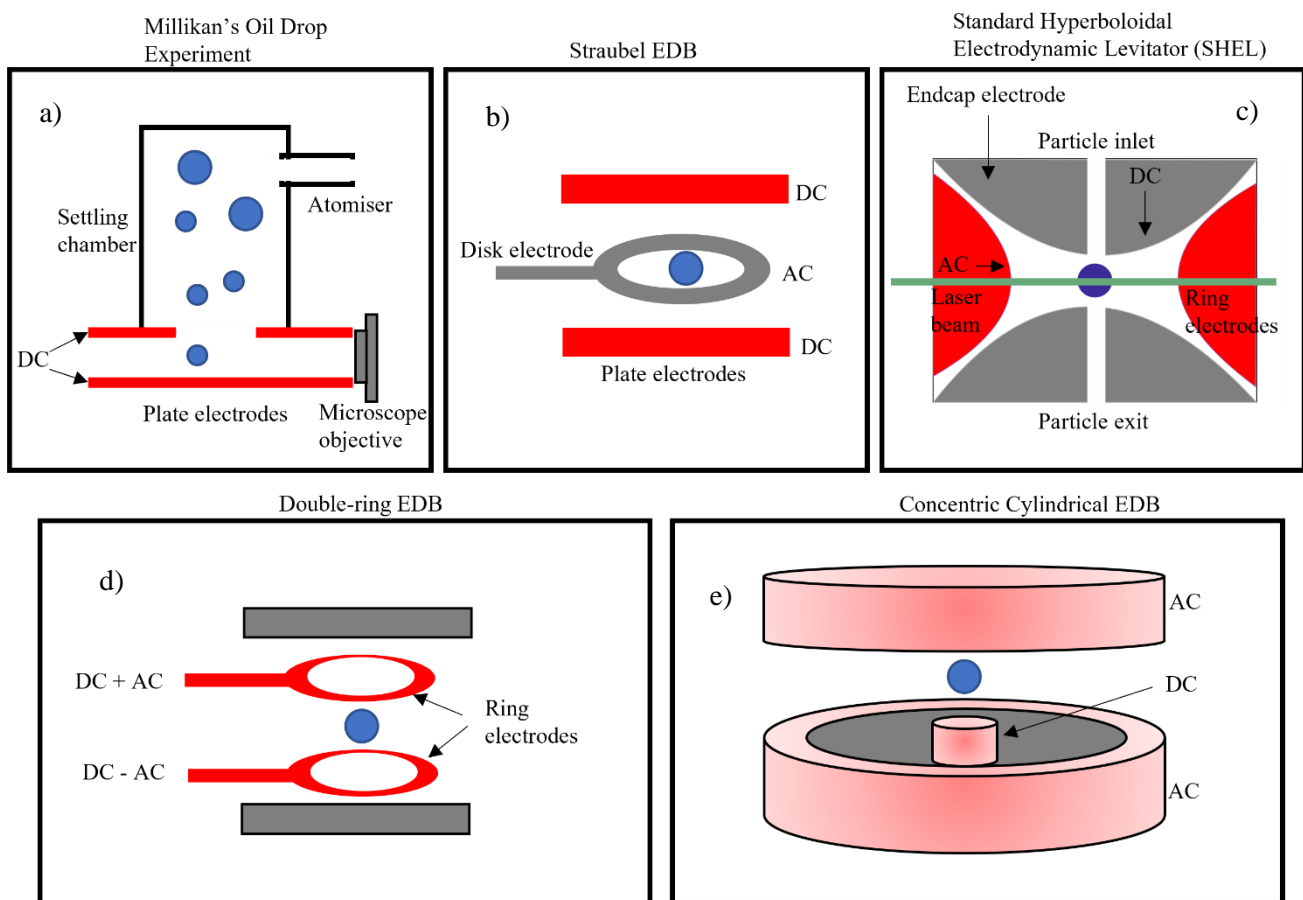
µm using AC frequencies of 100 Hz.

In 1959 Wuerker et al. adapted the quadrupole ion trap, and introduced the standard hyperboloidal electrodynamic levitator (SHEL), Figure 1.12c.[63] In addition to vertical and lateral stability of a trapped droplet using an AC and DC field, optical light scattering was also accessible with SHEL. Figure 1.12c shows how the instrument is used to trap a single particle in the centre of the chamber, whilst illuminating the particle with a laser beam. The scattering light can be collected and used to study the

dynamic process of particles, such as evaporation. In 1970, Davis et al. developed SHEL for use in the field of aerosol science.[64]

Since the development of SHEL there have been many variations of the EDB. The double ring electrode, shown in Figure 1.12d, was first introduced by Ray and Souyri. The instrument shown in Figure 1.12d is a popular set up of a double ring electrode, due to the viewing access of the trapped particle.[65] An instrument used to measure the longevity of levitated aerosol containing bacteria was developed at BARC and it was used in thesis to collect dried samples.[66,67] Following the double ring electrode developed by Ray and Souyri, a concentric cylindrical EDB was designed and introduced.[40] The concentric cylindrical EDB is shown in Figure 1.12e and the electrodes are mounted vertically opposite one another. Each electrode contains an AC and DC field to ensure stable trapping of the particle. The set up in Figure 1.12e was first introduced by Heinisch et al. and found to be a suitable instrument to measure the hygroscopic properties of aerosol.[59]

1.4.   Thesis Objectives, Aims and Instrumental Summary

The evaporation, condensation, and dissolution dynamics of aerosol during and prior to inhalation effect the deposition fraction and phase state of the final particle. It is known that targeted deposition, dependent on particle size, is required to ensure patients receive the necessary pharmacological effect. Using single particle measuring techniques to study particle dynamics allows exploration of the kinetic and thermodynamic properties of pharmaceutical aerosol. This thesis aims to investigate the dynamics of pharmaceutically relevant aerosol in conditions representative of the environments throughout drug delivery to the lungs. To achieve conditions representative of the deep lung, where the RH > 99%, a new EDB was developed that allows for particle measurements in a saturated gas phase. Single particle measurements provide an insight to the microphysics of pulmonary drug delivery, which are compared to bulk phase measurements collected by collaborators. A combination of aerosol phase and bulk phase measurements offers knowledge on the full picture of drug delivery to the lungs.

The key aims in this thesis are as follows:
- Study the hygroscopic response of APIs, excipients and mixtures of APIs and excipients commonly used in drug delivery to the lungs in the treatment of respiratory diseases. Furthermore, apply the hygroscopic response of a drug formulation to a deposition fraction simulator, replicating measurements of a cascade impactor.
- Develop an EDB to be used for measurements of the generation and inhalation of rapidly evaporating propellant (HFA) and co-solvent (ethanol) found in MDIs. Low temperatures are

required in the generation stage of measurements, followed by saturated conditions of the gas phase inside the chamber during droplet trapping.

- Combine aerosol phase and bulk phase measurements of particle dynamics of MDI formulations with and without an excipient. Exploring the crystallisation and dissolution processes of MDI droplets and further analysing dried particles using SEM.

- Investigating the dissolution dynamics of dried crystal particles, with a focus on the model system sodium chloride. To determine the variables effecting dissolution dynamics and to provide knowledge on how dissolution can be controlled and predicted in drug delivery to the lungs.

Instrumental Setup	Chapter(s)
Comparative-kinetics electrodynamic balance (CK-EDB)	4,6
Double ring electrodynamic balance (EDB)	5
Single particle levitation at saturated conditions (SPLASH)	5,6
Scanning electron microscope (SEM)	5,6
Falling droplet column (FDC)	5,6

Chapter 2

Droplet Evaporation and Condensation: Thermodynamic Principles and Kinetic Processes

The thermodynamic properties and environmental conditions determine the equilibrium physical state of an aerosol. In dry conditions, a droplet will exhibit transformational processes as it proceeds towards thermodynamic equilibrium that are kinetically distinct from the rates of processes under humid environmental conditions. The equilibrium partitioning of chemical components between the gas and particle phases is governed by thermodynamic principles, while the energy and compositional differences between the gas and particle phase drives the kinetic processes of mass and heat transfer. This chapter discusses how the thermodynamic and kinetic properties of a system influence the mass/water transport of liquid droplets, along with the reasons why a liquid droplet may form a solid particle or why a solid particle may form a liquid droplet.

2.1   Equilibrium Thermodynamics of Solution Droplets

2.1.1. Vapour Pressure

The vapour pressure of a solvent is an important parameter in the context of aerosol as it determines the relative proportions of a substance in the gas (vapour) and condensed (liquid) phases. Vapour is defined as a gas that can condense at the given temperature; thus, the terms gas and vapour can be used interchangeably. In atmospheric aerosol literature, the term gas is used to distinguish inert gases from condensable gases, referred to as vapours; in this thesis the same classification is used.[68] When gas and liquid phases coexist, the gas molecules constantly collide with the liquid surface and can become incorporated, i.e. condensation. Meanwhile, molecules in the liquid phase can leave and become part of the gas phase, i.e. evaporation. At equilibrium, the rates of evaporation and condensation are balanced. At this state of equilibrium, the pressure of the gas phase above a pure liquid surface at a given temperature is known as the vapour pressure of the liquid. The partial pressure in the gas phase above the pure liquid surface is also called the saturation vapour pressure, which increases strongly with temperature as the liquid molecules have more thermal energy and so more molecules are able to partition to the gas phase.[68] To rationalise this dependence of the vapour pressure of a substance on temperature, it is first necessary to describe the fundamental thermodynamic relationships, starting with the Gibbs energy, G:[69]

$$G = H - TS$$

<div align="right">Equation 2 - 1</div>

where H is enthalpy, T is the temperature and S is the entropy. It is important to note the definition of enthalpy, H, as the sum of internal energy, U, and pressure multiplied by volume, pV. In addition, the First Law of Thermodynamics, $dU = Q - W$, where change in internal energy is equal to the difference of heat transfer into a system, Q, and the work done by a system, W, can also be used to denote the following:

$$H = U + pV \qquad dU = Q + W = TdS - pdV$$

Following this, the change in G for a system with a change in temperature or pressure can be represented as:

$$dG = V\ dp - S\ dT$$

When two phases are in equilibrium with one another, such as a sealed box containing a substance in equilibrium with both liquid and vapour phases, then their molar Gibbs energy must be equal, $(dG_{liquid} = dG_{Vapour})$. Using Equation 2-3, it can be written that:

$$V_{liquid}\ dp - S_{liquid}dT = V_{vapour}dp - S_{vapour}dT$$

This equilibrium leads to the derivation of the Clapeyron equation,[70] where the difference in molar entropy for the phase transition, ΔS, and the difference in molar volumes of the liquid and vapour, ΔV, can be related to the gradient of the slope in the pressure-temperature phase diagram at the boundary separating the two phases:

$$\frac{dp}{dT} = \frac{S_{liquid} - S_{vapour}}{V_{liquid} - V_{vapour}} = \frac{\Delta S}{\Delta V}$$

At equilibrium, the difference in Gibbs energy between the liquid and vapour phases is equal to zero, i.e. Equation 2-3 is equal to zero:

$$\Delta G_{liquid-vapour} = V_{liquid}\ dp - S_{liquid}dT = V_{vapour}dp - S_{vapour}dT = 0$$

allowing for the Clapeyron equation to be written as:

$$\frac{dp}{dT} = \frac{\Delta H}{T \Delta V}$$

where the ΔH is equal to the enthalpy of vaporisation, describing the phase transformation of molecules between the liquid and gas phase, $\Delta H_{vaporisation} = H_{gas} - H_{liquid}$. Assuming that the change in molar volume from a liquid to a gas phase is large, then it can be written that $\Delta V = V_{gas} - V_{liquid} \approx V_{gas}$. Additionally, under the assumption that the gas phase is an ideal system, it can be written that $V_{gas} = \frac{RT}{p}$ substituted into Equation 2-7 gives the Clausius-Clapeyron Equation:

$$\frac{d \ln p}{dT} = \frac{\Delta H}{RT^2}$$

while using the approximation of $\frac{dp}{p} \sim d(lnp)$. The Clapeyron equation can be integrated between temperatures T_{ref} and $T_{standard}$, assuming that the enthalpy of vaporisation is independent of temperature, to give an expression for the vapour pressure, p_i:

$$p_i(T) = p_i^0 \exp\left[\frac{\Delta_{vap}H}{R}\left(\frac{T_{ref} - T_{standard}}{T_{ref}T_{standard}}\right)\right]$$

where p_i^0 is the standard vapour pressure at a standard temperature, $T_{standard}$, of a substance, i. Vapour pressure is a measure of the tendency of a substance to transfer into the gas phase and is useful for describing the evaporation of liquid droplets. The saturation vapour pressure of water as a function of temperature is shown in Figure 2.1. Simply, a molecule of a substance with a higher vapour pressure is more likely to exist in the gas phase at a given temperature and pressure than one with a lower vapour pressure.
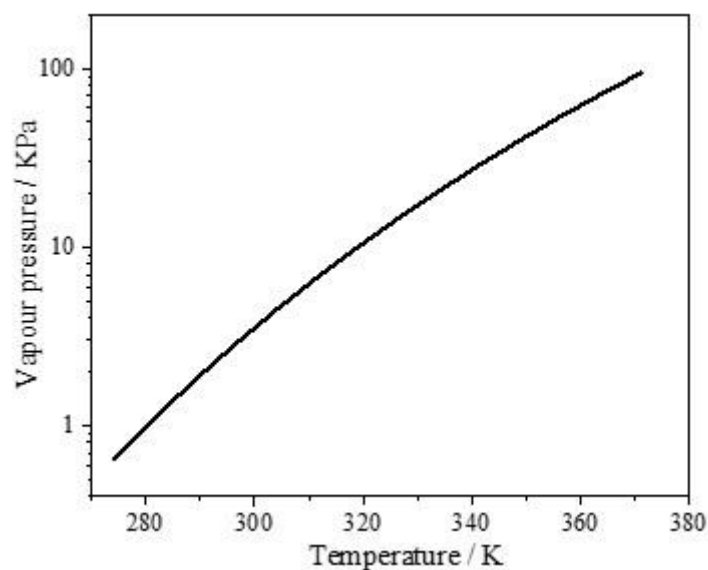
Figure 2.1. The saturation vapour pressure of water with respect to temperature according to the Antoine equation.

2.1.2. Vapour-Liquid Phase Equilibrium of a Binary Mixture

Introducing a second substance, a solute, to a liquid droplet to form a binary mixture influences certain thermodynamic properties of the solution. A second substance lowers the vapour pressure of the solvent (often water in aerosols), increases the boiling point and reduces its freezing point.[69] Raoult's and Henry's laws, combined with chemical potentials expressed in terms of mole fraction, can be used to calculate the effect of a solute on the thermodynamic properties of a liquid droplet. Additionally, the chemical potential can be expressed as an activity, which can be measured for individual substances. If a solute is contained within a solution, the vapour pressure of the solvent is reduced as the solvent concentration at the surface is reduced, dependent on the amount of dissolved solute. The chemical potential is used to relate the gas phase concentration of substance i to its concentration in the liquid phase. It is defined as the partial molar Gibbs energy, which is the gradient of the Gibbs energy change (∂G) with the molar mount of substance i in a closed system, where there is a constant temperature and pressure:

$$\mu_i = \left(\frac{\partial G}{\partial x_i}\right)_{p,T,x}$$

Equation 2 - 10

The chemical potential, μ_i, is the partial molar Gibbs energy of substance i and x is component mole fraction. It follows that the total Gibbs energy of a binary mixture of components A and B is:

$$G = x_A \mu_A + x_B \mu_B$$

Equation 2 - 11

31

where μ_A and μ_B are the chemical potentials of substances A and B, respectively. It can be stated that the chemical potential of a substance in a mixture is its molar contribution to the total Gibbs energy of the mixture. So far, the chemical potential of a solute in a mixture has been discussed, the chemical potential of a solvent in a mixture can be written as:[48]

$$\mu_A = \mu_A^0 + RT\ln p_A$$

where μ_A^0 is the chemical potential of *A* in a pure liquid state. A French chemist, Francois Raoult, found that the ratio of the partial vapour pressure of A in a mixture and that in a pure liquid is approximately equal to the mole fraction, x_A, which is known as Raoult's law:

$$p_A = x_A p_A^0$$

Raoult's law only applies for ideal solutions and can be used for mixtures of components that have similar structures, e.g. benzene and methylbenzene, two substances that were included in the serious of experiments performed by Raoult. A mixture of glycerol and water is given as an example in Figure 2.2, where the partial pressure of both components deviates from Raoult's law, indicating that it is not an ideal solution. Additionally, Raoult's law is a good approximation only for the properties of the solvent if the solutes are dilute, departing significantly from Raoult's law at points farthest away from the pure component. Following this finding, the English chemist William Henry performed experiments for non-ideal, dilute solutions, and found that the vapour pressure of the solute was proportional to its mole fraction:[69]

$$p_B = x_B H_B$$

where x_B is the mole fraction of the solute and H_B is a Henry's law constant for solute *B* in units of pressure. The constant is calculated by fitting a line tangential to the experimental data of vapour pressure with respect to mole fraction *B* for measurements at low solute concentrations with $x_B \to 0$. An ideal-dilute solution is a mixture for which the solute follows Henry's law and the solvent obeys Raoult's law.
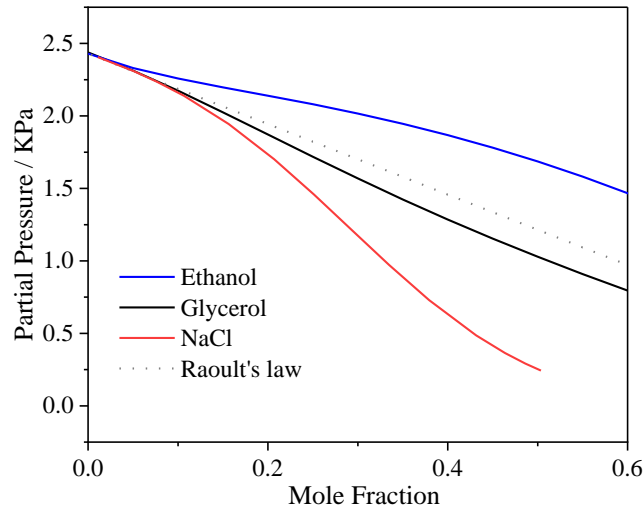
Figure 2.2. Mole fraction against partial pressure of water above ethanol, glycerol, and sodium chloride, modelled using AIOMFAC and E-AIM at 298.15K.[71,72,73] All components deviate from Raoult's law, indicating non-ideal systems and are systems studied in this thesis.

The deviation from ideality, or Raoult's law, can be written in terms of an activity (a_i), which is the mole fraction (x_i) of the substance multiplied by an activity coefficient (γ_i). The vapour pressure of component *i* above the mixture is given as:

$$p_i = \gamma_i x_i p_i^0 = a_i p_i^0$$

<div align="right">*Equation 2 - 15*</div>

The vapour pressure for each component in Figure 2.2 shows a deviation from Raoult's law and thus ideality at 298.15 K. Interestingly, ethanol shows a deviation above Raoult's law, indicating that the addition of ethanol to water increases the vapour pressure of water and, therefore, water molecules are more likely to equilibrate into the vapour phase. Glycerol and NaCl decrease the vapour pressure below the ideal limit, therefore reducing the drive for water molecules to transfer into the gas phase.

2.1.3. Defining Relative Humidity

In a purely water-based system, both vapour and liquid phase, the ratio between the partial pressure of water vapour in equilibrium above an aqueous solution and the saturation vapour pressure of water is known as the saturation ratio, S_w, at a given temperature. This can be expressed as a percentage and is referred to as the relative humidity (RH):

$$\frac{p_w}{p_w^0} \times 100 = s_w \times 100 = Relative\ Humidity$$

where p_w is the partial pressure of water and p_w^0 is the vapour pressure of water at the temperature of the gas phase. The RH is an important environmental condition and impacts on the physical properties of aerosol. The dependence of particle phase on RH is particularly examined throughout this work. In Equation 2-16 the saturation ratio (S_w) is equal to the droplet water activity (a_w) at equilibrium above a solution of a well-defined equilibrium composition and is equivalent to the gas phase relative humidity percentage (RH).

2.1.4. The Solute Effect

Aerosol hygroscopicity, defined as the ability of a substance to take up and hold water molecules, is determined by the water activity (a_w) of a solution, with a given concentration of the components. Pure water has a water activity of 1, where the vapour pressure at the droplet surface is equal to the saturation vapour pressure, Equation 2-16. In an environment where the relative humidity (RH) is less than 100%, a pure water droplet will evaporate entirely; if there is a solute present then the water activity is reduced according to Equation 2-15 and an equilibrium between the solution and gas phases can be established under sub-saturated conditions. This is known as the solute effect. An aqueous solution droplet will evaporate until the water activity in the droplet is equal to the RH, thus achieving equilibrium. The process of evaporation causes an increase in mole fraction of solute and change in water activity. The variation in droplet composition is used in this work to measure the hygroscopicity of new compounds.

Hygroscopicity can be presented in different ways, but the mass fraction of solute (MFS) as a function of a_w is common, reporting the change in equilibrium solution composition with change in vapour pressure of water. An example of MFS as a function of a_w for sodium chloride and glycerol is shown in Figure 2.3b. Additionally, hygroscopicity can be presented in terms of a radial growth factor (GF$_r$), which is the ratio of the size of a "wet" droplet at a given RH and the "dry" particle. A dry particle is assumed to be a homogeneously, solid sphere with bulk density. The dry radius is commonly used throughout this PhD, as the focus on drug delivery to the lungs is more suited to particle size rather than particle mass.

$$(GF_r = \frac{r_{wet}(RH)}{r_{dry}})$$

The consequences of the solute effect are shown in Figure 2.3a, where the evaporation profiles of sodium chloride and glycerol deviate from that of pure water, with both solutes starting at an MFS of

0.1. It should be noted that the model is performed using concentration of solute (g/L), which is calculated by multiplying the starting MFS (0.1) by the equivalent density of a solution of that MFS. The binary mixtures are seen to equilibrate once the water activity in the droplet is equal to that in the gas phase. Additionally, Figure 2.3b presents the hygroscopicity curves of sodium chloride and glycerol, it shows that sodium chloride is more hygroscopic than glycerol, i.e., a single ion pair of Na+ and Cl- will hold on to more water than a single molecule of glycerol. The hygroscopicity is presented in terms of mass fraction of solute and radial growth factor with respect to water activity.
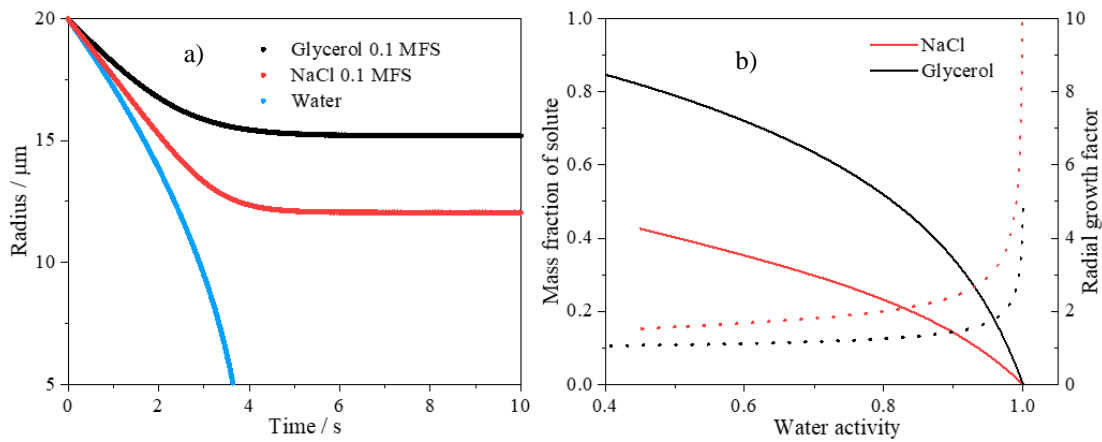
Figure 2.3. a) Evaporation profiles of water, sodium chloride and glycerol, the latter two both at 0.1 MFS at 60% RH and 293.15 K, modelled using AIOMFAC,[72] where starting density was calculated from experimental data. b) Hygroscopic growth curves for sodium chloride and glycerol, presented in terms of MFS (solid) and radial growth factor (dashed), modelled using AIOMAC.[72]

The Kelvin equation shows that the vapour pressure over a curved surface is greater than that over a flat surface.[74] This is because the molecules on a curved surface experience weaker interaction with neighbouring molecules compared with those on a flat surface. The effect of curvature is only significant for particles of radius less than 0.1 μm. Therefore, the Kelvin effect is not considered when discussing liquid droplet vapour pressures in this thesis as the radial size range is ~5 -35 μm.

2.1.5. Köhler Equation and Theory

Köhler theory is a combination of the solute effect and Kelvin effect, defining the saturation ratio of water surrounding a liquid droplet containing an aqueous solute:[75]

$$\frac{p_w}{p_w^0} = \frac{RH}{100} = s_w = a_w exp \frac{2\sigma M_w}{RT\rho_w r}$$

<div align="right">*Equation 2 - 18*</div>

35

The first three terms are taken from Equation 2-16 and the last from the Kelvin Equation, where the molecular mass of water and density are denoted by M_w and ρ_w, respectively, and σ is the surface tension of water. The Kohler equation considers the influence of surface curvature on water evaporation from a droplet containing a solute in a water droplet. The Kelvin effect describes how a liquid droplet has a higher vapour pressure than that of a flat surface, assuming radius is small. However, an aqueous-solution droplet will also experience the solute effect. In this case, the two factors influencing droplet vapour pressure are in competition, leading to a maximum of the equilibrium Kohler curve at a supersaturation and particle size that corresponds to a critical radius. The Kelvin effect will dominate the Kohler curve for a dilute aqueous droplet but leads to a very minor correction and very low critical supersaturation for particles >1 μm in diameter. Instead, the solute effect dominates the characteristics of the equilibrium growth curve even when the aqueous droplet is near the solubility limit.

2.1.6. Thermodynamic Hygroscopicity Models

So far in this section, two thermodynamic models have been used to simulate equilibrium solution properties: the Extended-Aerosol Inorganics Model (E-AIM)[76] and the Aerosol Inorganic-Organic Mixtures Functional Groups Activity Coefficients model (AIOMFAC).[71] Hygroscopicity models can be used to predict the hygroscopic response of solutes by calculating the equilibrium composition of an aqueous-solute droplet with varying water activity.

E-AIM was developed at the University of East Anglia by Clegg and Wexler,[73,77] and is available online at: http://www.aim.env.uea.ac.uk/aim/aim.php.[78] The model is based on experimental data for the activity coefficients and is used to minimise the Gibbs free energy of an inorganic solution droplet which has a defined volume, pressure and temperature to calculate the equilibrium properties. It can be used to calculate the magnitude of partitioning at equilibrium between the vapour and liquid phase for a chemical system. E-AIM calculations report values of molality, molarity, and partial pressures of the components in a droplet in the vapour phase as a function of the RH. The user can define the RH, chemical composition, and temperature range of the system, which is then used to output the phase ratio of vapour to liquid of the components at equilibrium. It is used in Chapter 4 to compare against experimentally calculated hygroscopic properties of pharmaceutically relevant aerosol.

AIOMFAC was developed at ETH Zurich, Caltech and McGill University by Andreas Zuend and co-workers,[79,71,80] and is available at http://www.aiomfac.caltech.edu/.[72] Analogous to E-AIM, the equilibrium concentration of aerosol droplets containing a mixture of organic and inorganic solutes can be estimated with the organic solutes represented by a functional group activity model. The user provides the model with the functional groups of each chemical species that are present in the aerosol phase, as well as the environmental conditions of RH and temperature. The model then predicts the

mass fraction, mole fraction, molality, activity coefficient and vapour pressure for each component when the system is at equilibrium. AIOMFAC was used in this chapter to simulate evaporation profiles and in Chapter 4 to generate hygroscopic data of aerosol mixtures and their activity coefficients.

2.2   Kinetics of Evaporation and Condensation

Differences in the saturation ratio of a component in the vapour phase far from the droplet and close to the droplet surface drive mass and heat transport to and from the droplet. The key processes governing the rate of evaporation for a volatile or semi-volatile component are shown in Figure 2.4. First, molecules must diffuse to the surface through the bulk phase of the liquid-droplet and then transfer over the phase boundary. Finally, molecules diffuse away from the droplet surface through the gas phase. The reverse of this process is condensation. This Section considers heat and mass transport and the limitations associated with each. Mass transport kinetics of the continuum regime are limited by gas phase diffusion, The transport of molecules across the gas-surface phase boundary limits the kinetics in the continuum regime. Finally, the limitations of bulk and surface diffusion of molecules on mass transport is discussed. In summary, the three types of kinetics discussed in this chapter are bulk phase limited, surface limited and gas-phase limited regimes.
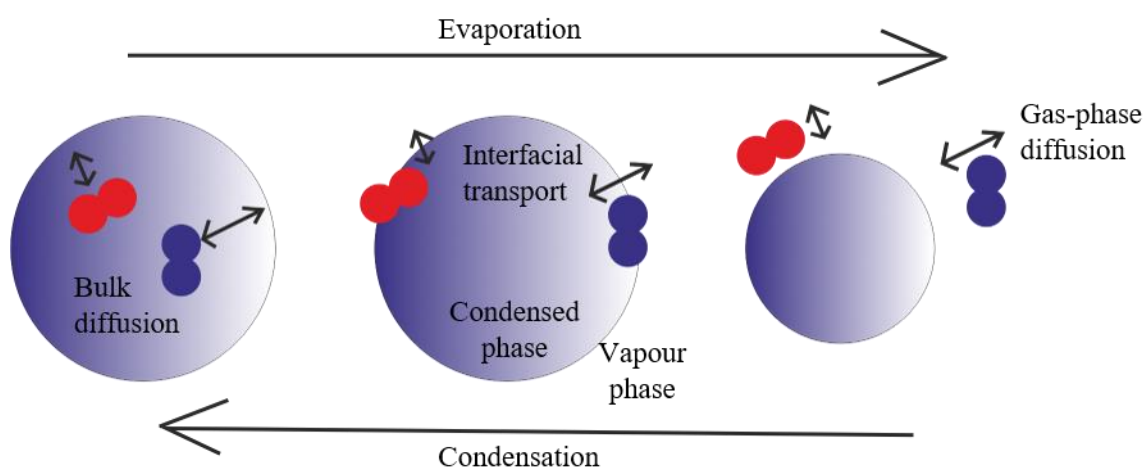
Figure 2.4. Molecular transport processes between the condensed and vapour phase. Evaporation consists of bulk diffusion within the droplet, interfacial transport across the droplet surface and gas-phase diffusion away from the droplet, the transport process would be reversed for condensation.

2.2.1. Aerosol Kinetics Regimes

The regime limiting the kinetics of evaporation and condensation depends on the relative size of the droplet and the distance between molecules in the vapour phase. The Knudsen number, a dimensionless number, can be used to define the regimes between a droplet and surrounding vapour phase and is the ratio between the mean free path of the vapour (λ) and the droplet radius (r):

$$K_n = \frac{\lambda}{r}$$

λ is the average distance that a gas molecule will travel before colliding with another. There are three gas-particle regimes that can be defined using the Knudsen number, Figure 2.5. In the continuum regime the droplet size is larger than the mean free path and thus K_n tends to zero. Here, the large droplet experiences continuous collisions with small gas molecules, behaving as a continuous fluid around the particle. In the free-molecule regime the droplet radius is smaller than the mean free path and so $K_n \gg$ 1. Finally, an intermediate regime known as the transition regime, $K_n \sim 1$, must be considered when the droplet size is on the same order of magnitude as the mean free path of the gas molecules.

a) Continuum regime   b) Transition regime   c) Free-molecule regime
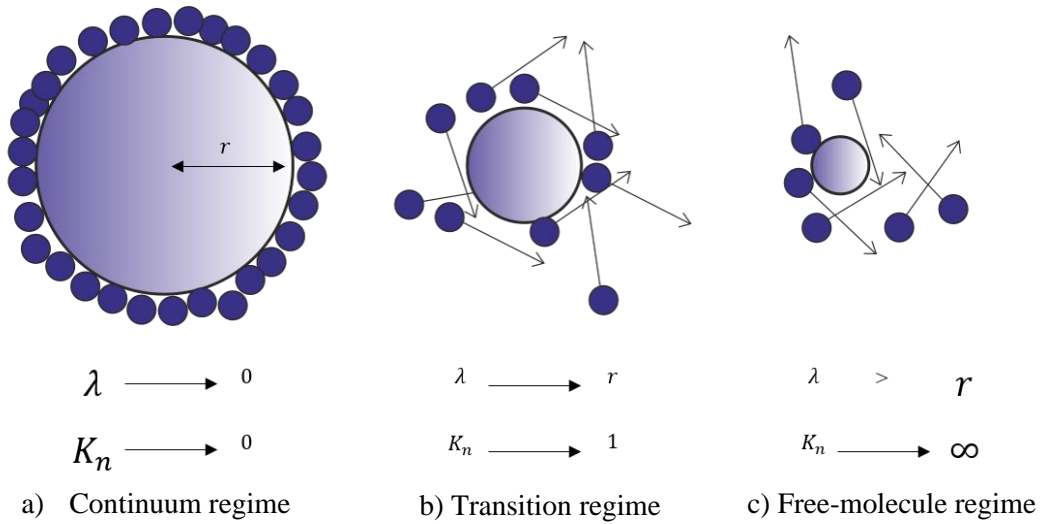
Figure 2.5 A schematic of the three regimes of gas-particle interactions. a) The continuous regime where the droplet radius is larger than the mean free path (K_n tends to 0). b) The transition regime where the droplet radius and mean free path are of the same order of magnitude (K_n tends to 1). c) The free-molecule regime where the droplet radius is smaller than the mean free path ($K_n \gg 1$).

2.2.2. Mass Transport in the Continuum Regime

The work in this thesis takes place in the continuum regime, where the droplet radius (5-80 μm) is larger than the mean free path (68 nm at 293 K, 1013 hPa). In the continuum regime the gas phase may be considered as a continuous fluid, where the evaporation and condensation rates are governed by the rate of mass diffusion of the component through the gas phase above the surface of the droplet. The

equations which describe mass transport in the continuum regime were first published by James Clerk Maxwell in 1877 in the Encyclopedia Britannica. The laws of diffusions were derived by Adolf Fick in 1855. The first law, steady diffusion, is given by the following equation:[69]

$$J' = D\frac{c}{RT}\frac{\partial \mu}{\partial x}$$

where J' is the molecular flux in terms of molecules per unit area per time, c is the molecular number density, μ is the chemical potential at position x. Fick's law can be related to the concentration gradients and diffusion coefficient to give:

$$J' = D\frac{\partial c}{\partial x}$$

Fick's second law describes the time-dependent change in concentration for unsteady diffusion in an ideal solution, given by:

$$\frac{\partial c}{\partial t} = \frac{\partial J'}{\partial x} = -D\frac{\partial^2 c}{\partial^2 x}$$

The Laplace operator, ∇^2, can be used to replace the partial differential with respect to x^2, generalising Fick's laws to three-dimensions:

$$\frac{\partial c}{\partial t} = -D\nabla^2 c$$

Equation 2-23 can be converted into spherical coordinates for a spherically symmetric system (e.g., an evaporating droplet) by noting that the Laplace operator is described as $\frac{\partial}{\partial x} + \frac{\partial}{\partial y} + \frac{\partial}{\partial z}$:

$$\frac{\partial c}{\partial t} = D\left(\frac{\partial^2 c}{\partial r^2} + \frac{2}{r}\frac{\partial c}{\partial r}\right)$$

where the concentration will only change in the radial direction. Several initial and boundary conditions can be imposed on Equation 2-24 of mass transport to or from a spherical droplet. Firstly, the gas phase surrounding the droplet has a fixed initial vapour concentration, c_i, at an infinite distance from the droplet and around the surface of the droplet. Secondly, the gas phase is at a fixed concentration at infinite distance from the particle. Finally, the concentration of the gas phase immediately above the surface is kept fixed.

The first condition defines steady evaporation and was studied by Maxwell. The Maxwell equation,[81] which describes the mass flux, I, shows that slow evaporation of single-component liquid droplets is

proportional to the diffusion coefficient, D, and the difference in vapour concentration (c_i) at the droplet surface ($i = a$) and far from the droplet ($i = \infty$):

$$I = \frac{d\,m}{d\,t} = -4\,\pi\,r\,D\,(c_a - c_\infty)$$

where r is the droplet radius. Substituting $r = \sqrt[3]{m / (\frac{4}{3}\,\pi\,\rho)}$, where m is the droplet mass and p is the droplet density, and assuming ideal vapours with concentration $c_i = p_i(T)\frac{M_i}{R\,T}$, Equation 2-25 can be integrated between r_o and r_t with respect to mass to give the r^2 law:

$$r_t^2 = r_0^2 - \frac{2\,D\,M_i\,t}{\rho\,R\,T}\,(p_a(T) - p_\infty(T))$$

where t is the time, R is the molar gas constant, M_i is the molar mass of the evaporating component, ρ is the liquid density, where $p(T)$ is the temperature dependent vapour pressure. Equation 2-26 applies to evaporation and condensation that is gas-phase diffusion-limited, where the flux of vapour travelling away or towards the droplet surface governs the evaporation/condensation rate. Evaporation in the continuum regime becomes unsteady if the droplet surface recedes faster than the vapour concentration above the droplet surface can stabilise, particularly when there is a large evaporative mass flux. In this case, Equation 2-26 cannot be used to describe the mass flux away from the droplet. Additionally, heat transport must also be considered when determining evaporation or condensation processes. Temperature influences the evaporation and condensation rates and the transfer of heat between droplet and gas phase. Heat transport will be discussed in the next section.

2.2.3. Heat Transport in the Continuum Regime

A droplet will cool in temperature as volatile components evaporate, whereas heat is generated during condensation and the droplet temperature increases. This is due to the enthalpy changes associated with vaporisation and condensation. Only when the heat fluxes to and from the droplet are equal can a steady gas-phase temperature profile be achieved. The unsteady gas-phase temperature equation is of a similar form to that of mass diffusion in Equation 2-24:[60]

$$\frac{\partial T}{\partial t} = \frac{K}{c_{p,gas}\,\rho_{gas}}\left(\frac{\partial^2 T}{\partial r^2} + \frac{2}{r}\frac{\partial T}{\partial r}\right)$$

where K is the thermal conductivity, $c_{p,gas}$ is the specific heat of the gas phase and ρ_{gas} is the density of the gas phase. There will be a difference in temperature between the droplet and gas phase during

evaporation or condensation. The direction of this gradient is dependent on the competing rates of heat transport: for example, in evaporation, heat is transferred away from the droplet as molecules evaporate and heat is also transferred from the gas to the droplet, due to the temperature gradient. In the case of rapid evaporation, the heat transferred away from the droplet is greater than the heat transferred towards the droplet, thus resulting in temperature suppression of the droplet. Here, the vapour pressure of the evaporating component is reduced and therefore the mass transport, Equation 2 – 24, and heat transport, Equation 2 – 27, must be solved together.[60]

2.2.4. Coupled Heat and Mass Transport in The Continuum Regime

Kulmala et al. derived a semi-analytic treatment for coupling heat and mass transport for droplets within in a gas flow in the continuum regime.[82] Equation 2-28 defines the condensational growth and evaporation loss of a substance (i) to and from the droplet. The mass flux (I) of a volatile component (i) away from the surface of a homogenous droplet, with radius r, is given by:

$$I_i = -4\,\pi\,r\big(S_{i,\infty} - S_{i,a}\big)\left[\frac{R\,T_\infty}{M_i\,\beta_M D_i p_i^0(T_\infty)A} + \frac{S_{i,a}L_i^2 M_i}{R\beta_T K T_\infty^2}\right]^{-1}$$

where $S_{i,\infty}$ is the saturation ratio of substance i in the gas phase. In this thesis, the substance is assumed to be water unless noted otherwise. $S_{i,a}$ is equivalent to water activity at the droplet surface, R is the ideal gas constant, T_∞ is the gas phase temperature, M_i is the molar mass of the evaporating liquid, β_M and β_T are transitional correction factors for the mass and heat transfer, respectively. D_i is the diffusion coefficient of the diffusing species, $p_i^0(T_\infty)$ is the saturation vapour pressure at gas phase temperature, L_i is the latent heat of vaporisation of i, K is thermal conductivity of the gas phase. A is a correction factor to account for Stefan flow and is given by:[83]

$$A = 1 + p_i^0(T_\infty)\frac{(S_{i,\infty} - S_{i,a})}{2\,p}$$

where p is the total gas pressure.

The Kulmala equation was derived using an approximation for the vapour pressure at the droplet surface, $p_i^0(T_\infty)$, which is dependent on temperature.[82] The Clapeyron Equation, Equation 2-9, scaled by the saturation at the droplet surface, is given by:

$$p_{i,a}(T_a) = S_{i,a}p_i^0(T_\infty) \exp\left[\frac{L_i M_i}{R}\left(\frac{T_a - T_\infty}{T_a\, T_\infty}\right)\right]$$

Equation 2 - 30

where the temperature difference, $T_a - T_\infty$, is estimated by considering an energy balance of the mass and heat flux between the droplet and the gas phase, where the value of each temperature parameter must be similar for the approximation to hold true.[82] The expression for the temperature difference is given by:

$$T_a - T_\infty = -\left[\frac{L_i\, I_i}{4\,\pi\, r\, K}\right]$$

Equation 2 - 31

The exponential term in equation 2-30 can be approximated using a first-order Taylor expansion:

$$p_{i,a}(T_a) \approx S_{i,r}p_i^0(T_\infty)\left[1 + \frac{L_i M_i}{R}\left(\frac{T_a - T_\infty}{T_a\, T_\infty}\right)\right]$$

Equation 2 - 32

where a indicates a parameter at the droplet surface and ∞ is an infinite distance from the droplet surface. The term $p_i^0(T_\infty)$ is temperature dependent, which is underestimated if the droplet temperature, T_a, cools significantly during evaporation, and vice versa during rapid condensational growth.[39] The error in vapour pressure at the droplet surface increases as the temperature difference between gas and droplet increases. In this thesis, Equation 2-28 is only used to simulate evaporation or condensation kinetics where the mass flux leads to a difference in temperature no more than 3 K.[39] The difference in temperature is calculated using Equation 2-31.

The evaporation profiles of sodium chloride droplet, MFS = 0.1, simulated using Equation 2-28, at 80%, 70% and 60% RH are shown in Figure 2.6a. The droplets have an initial radius of 30 µm at a temperature of 293 K. The mass flux is simulated using the Kulmala model and is then used to estimate the droplet temperature using Equation 2-31.[82] The associated temperature of each droplet is shown in Figure 2.6b, where the droplet at 60% RH is seen to experience a $\Delta T > 3\,K$, and the Kulmala equation cannot accurately model the mass flux. In this case, any data points where ΔT is above the 3 K threshold would be removed from the data set prior to further analysis when retrieving the hygroscopic response of the droplet. The temperature of each droplet decreases suddenly at the start of the evaporation curve before steadily equilibrating with the gas phase temperature. In Figure 2.6c the evaporation profiles of water droplets are simulated using the Kulmala equation. The associated temperature change for each droplet in Figure 2.6d shows almost no change and the approximation in Equation 2-30 holds. The water

droplets remain at a steady temperature, where the heat loss through evaporation is equal to the heat conducted through the gas.
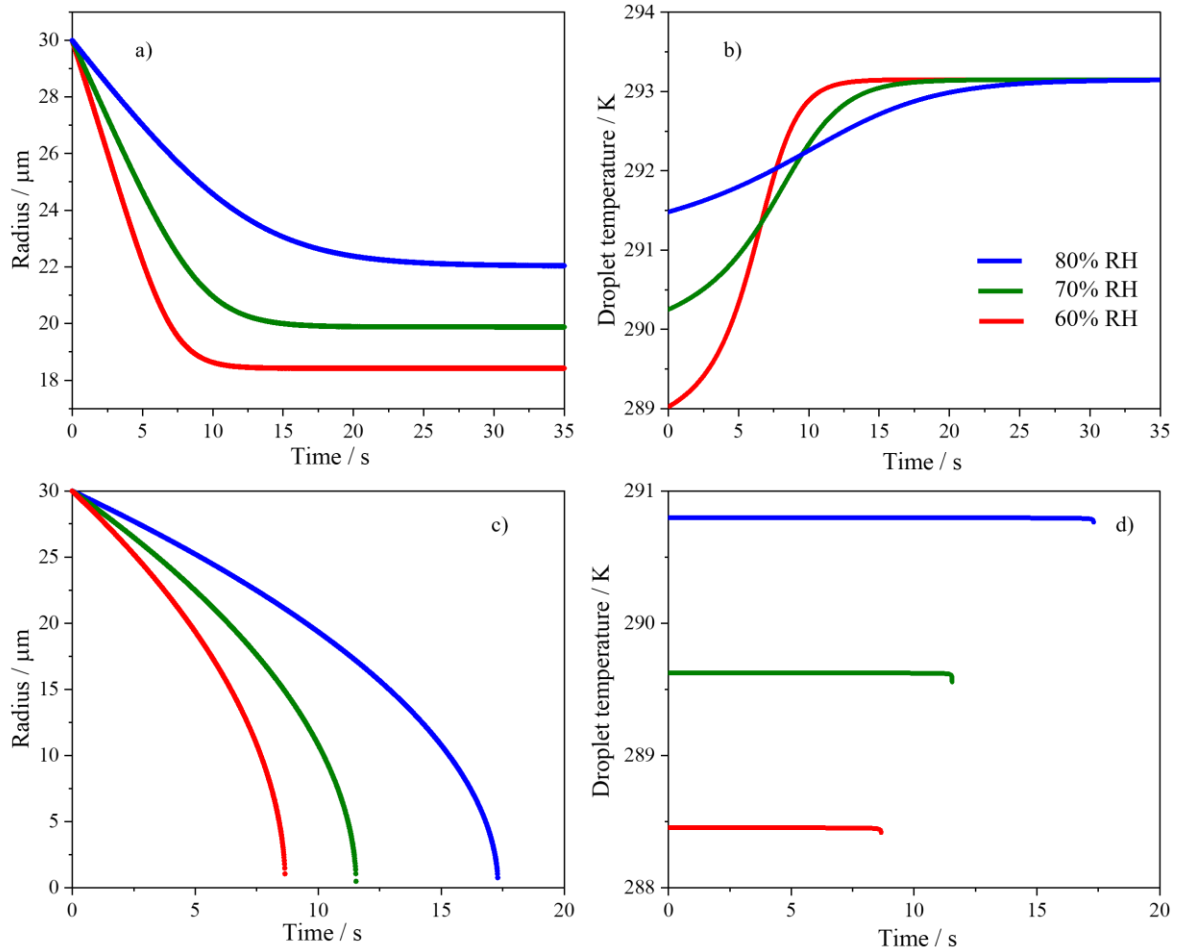
Figure 2.6. a) and c) Sodium chloride (MFS = 0.1) and water droplets, respectively, evaporating into 80%, 70% and 60% RH at 293 K, with initial radius of 30 μm. b) and d) The associated temperature of each evaporating sodium chloride and water droplet, respectively, calculated using the mass flux and Equation 2-31.

2.2.5. The Free-Molecule Regime

In the case where $Kn \gg 1$, the free-molecule regime, macroscopic gas diffusion cannot accurately describe the mass transport dynamics of very small droplets.[84] Instead, the kinetics are determined by the random motion of molecules using the Maxwell-Boltzmann equations. The rate, $\frac{dm}{dt}$ where m is the mass of the evaporating component, at which a gas diffuses in time across an area A is given by:[84]

$$\frac{dm}{dt} = \frac{A_g}{4} \rho_g \bar{c}$$

where ρ_g is the gas density and $\bar{c}$ is the mean molecular speed which is given by:

$$\bar{c} = \sqrt{\frac{8 \, k_B \, T}{\pi \, M_g}}$$

in which k_B is Boltzmann's constant and M_g is the molecular mass of the diffusing gas. Hence, the rate of gas molecule collisions with a surface per unit time per unit area can be written as:[84]

$$z = \frac{n \, \bar{c}}{4}$$

The molecular flux across a surface layer above the droplet surface is given as:[40]

$$J = \pi \, a^2 \, \bar{c} \, a_M \, (c_\infty - c_a)$$

where a_M is the mass accommodation coefficient, which describes the fraction of molecules that are able to be adsorbed into the droplet as they land at the interface. It is accepted that the reverse may be applied between evaporation and condensation, where an equivalent evaporation coefficient is denoted by γ, such that $\gamma = a_M$.[85] The free molecule regimes is suitable for small droplets (< 100nm) and the continuum regime treatment is suitable for large droplets (>1000 nm). For droplets in the range of 100 – 1000 nm, the transition regime treatment is introduced. This treatment applies a correction to the expression of continuum kinetics which accounts for the free molecule kinetics.

2.2.6. The Transition Regime

In the case where $Kn \sim 1$ and the droplet size is the same order of magnitude as the mean free path, droplets are considered in the transition regime. All experimental work presented in this thesis involves droplets in the continuum regime. However, simulations presented in Chapter 4 of droplet dynamics take place in the transition regime. The mass transport is governed by a mixture of diffusion and heat transport kinetics, where droplets experience both the continuum and free-molecule regime. Thus, a correction factor must be applied to the continuum regime method, Equation 2-28, when calculating the

mass flux. In this thesis, the approach of Fuchs and Sutugin is used, where the correction for mass transfer, β_M, is:[86]

$$\beta_M = \frac{1 + kn}{1 + \left[\left(\frac{4}{3a_M} + 0.337\right) \times Kn\right] + \left[\left(\frac{4}{3a_M}\right) kn^2\right]}$$

The transitional correction factor for heat transfer, β_T, is the same as equation 2-37, using the thermal Knudsen number, Kn_r, and thermal accommodation coefficient, a_r. In the continuum regime, where Equation 2-28 is used to calculate mass flux, Kn tends to zero, β_M and β_T are equal to one and have no contribution to the equation. The mass flux of smaller droplets falls into the transition regime, therefore the β correction factors allow Equation 2-28 to be used to simulate evaporation and condensation kinetics.

2.2.7. Bulk Limitations to Mass Transport

Droplets that are homogenous in composition experience a limitation in mass flux from only gas phase diffusion, which is the assumption made in Kulmala equation. Therefore, evaporation or condensation profiles that are a result of additional limitations to the mass flux differ from simulations using Equation 2-28. One common limitation considered in this thesis is bulk phase diffusion, which is often limited by an increase in viscosity, i.e. non homogeneity in the concentration of solutes and solvents within the droplet. In a viscous droplet there is a kinetic limitation to mass transport in the bulk,[87] affecting the time taken for water molecules to diffuse to the surface for evaporation and for water molecules to diffuse to the centre for dissolution.[88] Droplet viscosity (η) is related to the diffusion coefficient (D) using the Stokes-Einstein Equation:

$$D = \frac{k_B T}{6 \pi \eta r_{mol}}$$

where k_B is the Boltzmann constant, T is the temperature and r_{mol} is the molecular radius of the diffusion molecule. The timescale (s) for diffusional mixing is calculated by:

$$\tau = \frac{r^2}{\pi^2 D}$$

where r is the droplet radius. An example of timescale for diffusional mixing at a given radius is given in Figure 2.7, where the diffusing molecule is water (r_{mol} = 0.135 nm) at 293 K, over a range of viscosities from 0.1 Pa s to 10000 Pa s. A small, non-viscous droplet has a short mixing time, whereas a large, viscous droplet has a long mixing time. For example, a droplet with r = 2 µm and a viscosity of 0.1 Pa s has a mixing time of ~0.023 s, where as a droplet with r = 25 µm and viscosity 10000 Pa s has a mixing time of ~93.5 hours, requiring considerable time to reach an equilibrium moisture composition with the surrounding gas phase.
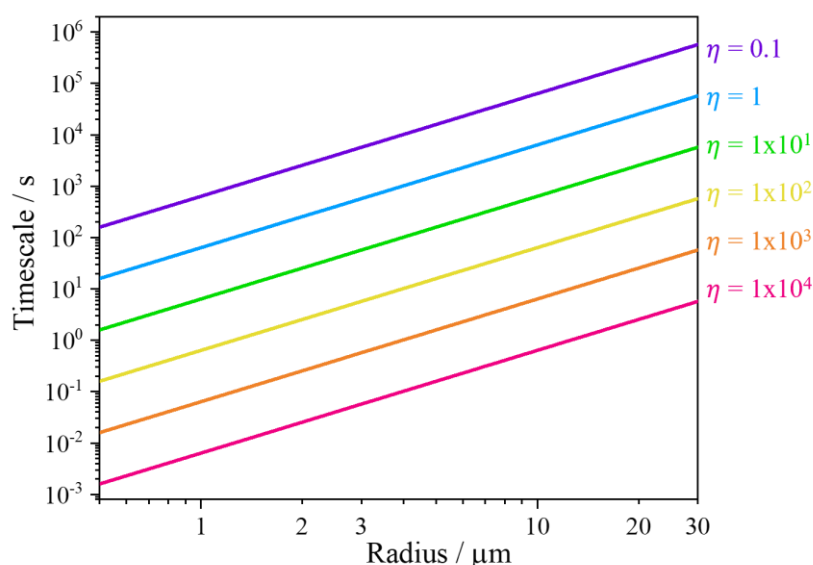
Figure 2.7. Timescale (s) for diffusional mixing of water within an aerosol particle as a function of droplet radius (µm) while varying the viscosity (Pa s). The timescale is calculated using Equation 2-39, where the diffusion coefficient is derived from Equation 2-38.

Often excipients and drug carriers, such as lactose monohydrate, form viscous or amorphous particles during drying techniques.[89] Upon inhalation, dried particles are introduced to almost saturated conditions in the lung (99.9 % RH), where water transport can be limited by bulk phase mixing.

2.3   Water-Solid Interactions: Efflorescence and Deliquescence

So far, only the evaporation and condensation kinetics of liquid droplets, both homogenous and non-homogenous, have been discussed. However, in drug delivery to the lungs the patient is often inhaling dried particles, which may be an indirect product of metered dose inhalers post ethanol evaporation or directly generated from dry powder inhalers. Upon inhalation the dried particles experience a rapid increase in RH (>99.5% RH), where water uptake occurs and the magnitude of which depends on the chemical composition and phase state of the particles. This presents itself as a cycle of liquid droplets, dried particles and many intermediate phases in between, which takes the form of the well-known

efflorescence and deliquescence cycle.[90,91,92] In this section the theory of droplet crystallisation, efflorescence, and particle dissolution, deliquescence, is discussed.

2.3.1. Overview of The Efflorescence and Deliquescence Cycle

In the bulk phase, components will crystallise at the point of achieving the saturation concentration. However, in the aerosol phase the droplet can remain aqueous at solute concentrations far in excess of the solubility limit. For example, sodium chloride will crystallise in the bulk phase at an MFS = 0.26 but can remain as a liquid droplet up to an MFS of 0.45 at 293 K, Figure 2.8. Supersaturated droplets are able to form because there is no solid surface around the liquid droplet which would lead to heterogeneous nucleation. In the aerosol phase it is possible for initial crystallisation to be homogeneous. Efflorescence is the process of crystal nucleation and growth in the aerosol phase, where the solute is sufficiently saturated that homogeneous nucleation occurs spontaneously. The RH at which this occurs is known as ERH. The response in the size of a sodium chloride droplet to changes in RH is illustrated in Figure 2.8, where the solute passes the bulk phase solubility at $a_w < 0.75$ and becomes supersaturated. At a water activity of 0.45, the droplet will reach critical supersaturation and thus effloresce, forming a sodium chloride crystal.
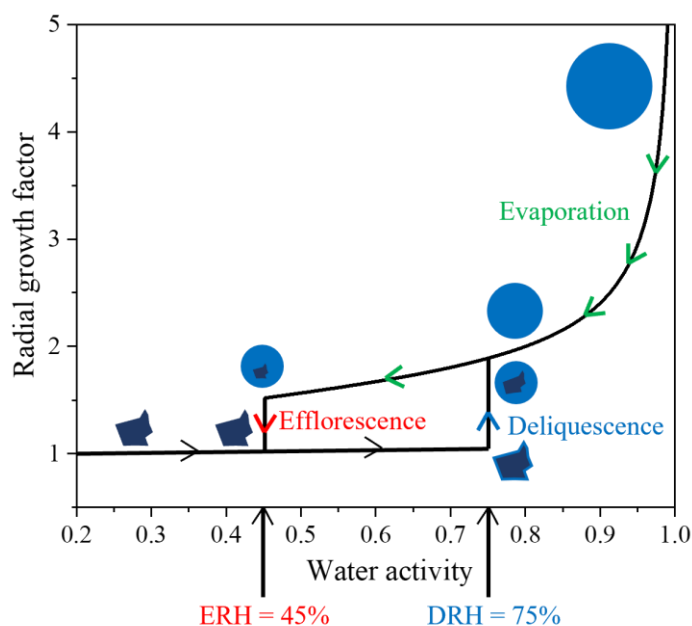
Figure 2.8. Radial growth factor for NaCl with respect to water activity, where aw = 1 is equivalent to 100% RH. Efflorescence occurs at 45% RH and deliquescence occurs at 75% RH at 293 K.

If a dried particle is exposed to a high RH, the process of deliquescence commences leading to spontaneous water uptake and complete dissolution of the crystalline particle. Complete deliquescence results in the formation of an aqueous solution droplet, where the size is governed by the equilibration of water activity in the droplet with the gas phase. Dissolution only occurs at an RH at or above the

deliquescence RH (DRH) of the solute. For sodium chloride, Figure 2.8, the DRH is 75% RH and equivalent to the water activity of the bulk solubility limit.[90] The DRH is different for every compound and a particle containing multiple components often has a lower DRH than that of the individual compounds, known as deliquescence lowering.[42] The cycle presented in Figure 2.8 is applicable to most compounds discussed in this thesis. However, some solutes do not effloresce and instead they form amorphous, but dried, particles. Additionally, some extremely insoluble compounds, such as active pharmaceutical ingredients, may not take up water at all, even at RHs close to saturation, 100% RH, instead remaining as a solid particle.

2.3.2. Crystal Nucleation Kinetics

Drug delivery to the lungs often consists of dried particles in the range of 0.1 to 5 microns to be inhaled by the patient and subsequently deposit in the lungs. The depositing dried particles have either been formed prior to packaging (dry powder inhalers - DPIs) or during generation and inhalation (metered dose inhalers - MDIs).[93] The environmental conditions and droplet properties, such as size and composition, involved with each delivery device differ significantly. All these factors influence the crystallisation kinetics, where the competition between the rate of crystal growth and solvent evaporation can govern crystal size, degree of crystallinity and crystal morphology.[94,54] Dry particle morphology and crystallinity play a key role in the efficiency of drug delivery, for example, carrier particles with high roughness powder are known to improve dispersibility.[54] Additionally, dried drug formulations can exist in different states: amorphous, crystalline or a mixture of phases. The phase state has implications on properties such as dissolution rate, thermodynamic stability, and the pharmacokinetics. Although there is a strong interest in drug delivery to the lungs, little is known about the properties of the dried microparticles and their influence on delivery efficiency and efficacy.[95]

Single particle measurement techniques were used in this thesis to explore the crystallisation behaviour of pharmaceutically relevant substances, observing a homogenous nucleation process in the aerosol phase. In the case of a highly concentrated droplet, the components will be driven to a more thermodynamically stable state, leading to crystal nucleation. A schematic is shown in Figure 2.9a.
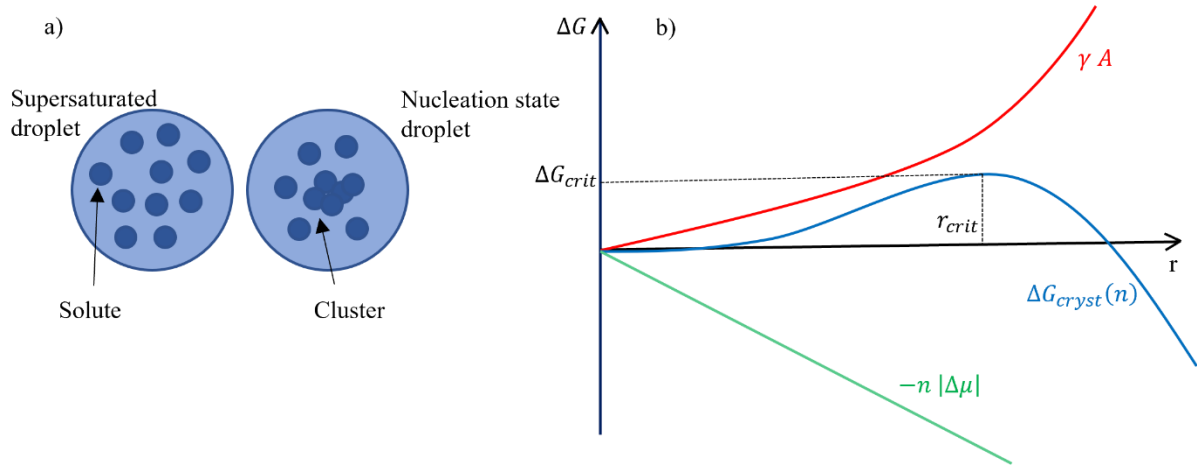
Figure 2.9. a) Schematic of a supersaturated droplet allowing for crystal nucleation. b) Change in Gibbs free energy, blue line, in transitioning from a supersaturated droplet to crystal nucleation, determined by two functions, red and green lines. Based on Equation 2-40, where r_{crit} is related to the number of solute molecules in a cluster.

A crystal nuclei can form in a supersaturated droplet at any time. At the point of crystallisation there is an enthalpic change, ΔH_{cryst}, which is opposite to the enthalpy of dissolution, ΔH_{diss}. The Gibbs free energy, G, is used to determine the change in energy between solution and crystal phase. The change in Gibbs free energy is the competition between the energy released from forming a cluster of solute and the energy gained by the creation of a phase boundary, or surface, between the cluster and solution:[96]

$$\Delta G_{cryst}(n) = -n\,|\Delta\mu| + \gamma\,A$$

where n and $|\Delta\mu|$ are the number of solute molecules in a cluster and the chemical potential change between solution and crystal, respectively. γ is the surface tension between a cluster and solution and A is proportional to $n^{2/3}$ and related to the dimensions of the cluster. The first term on the right-hand side in Equation 2-40 represents the free energy released due to the formation of thermodynamically favourable solute-solute interactions, increasing as more solutes ions are included in the cluster, green line in Figure 2.9b. The second term represents the energy gained by the creation of a phase boundary or surface between the cluster and the solution, red line in Figure 2.9b. The resulting $\Delta G_{cryst}(n)$, blue line, is initially positive with n, which is related to the radius of the cluster, as the solute interactions do not outweigh the unfavourable formation of a phase boundary between the cluster and solution. At the point ΔG_{crit} there is a maximum, after which an increase in radius leads to a decrease in Gibbs free energy and crystal growth. If the clusters form a sphere, the maximum change in Gibbs free energy, ΔG_{crit}, occurs at a critical radius, r_{crit}.

The Arrhenius equation is used to denote the nucleation rate of crystals out of solution per unit volume per unit time, J:[96]

$$J = K \exp\left[\frac{-\Delta G_{crit}}{k_B T}\right]$$

where K is the pre-exponential parameter taking diffusive transport and other kinetic factors into account, k_B is the Boltzman constant and T is the equilibrium temperature.

2.3.3. Thermodynamics and Kinetics of Deliquescence

It is common that dry powder formulations come in to contact with residual moisture while they are packaged, leading to many significant changes in physical and chemical properties.[42] Additionally, as clouds of dry powder produced directly from a DPI or indirectly from a MDI are inhaled into a very humid lung, these changes become even more apparent. High water activity in the gas phase has an impact on the lung deposition fraction, efficiency, and efficacy.[28] Water molecules interact with solids using several major mechanisms,[42] and this thesis focuses on capillary condensation, vapour absorption and deliquescence. There is much work around water absorption onto amorphous and dry particles.[87] However there is little knowledge about the influencing factors of deliquescence.[97]

A schematic of the deliquescence process is shown in Figure 2.10., where a solid particle experiences a phase change to a liquid droplet. Deliquescence occurs when the ambient RH (RH_i) is greater than or equal to the substance specific DRH. For example, the DRH for sodium chloride at 293 K is 75% RH, shown previously in Figure 2.8. When the ambient RH is below the DRH, water interacts with the solid via adsorption and, in general, highly crystalline solids will adsorb a few molecular layers of water.[42] Sodium chloride has been observed to adsorb 2-3 monolayers before bulk dissolution is seen.[43] Once the RH has increased above the DRH, water vapour is adsorbed at the surface of the solid particle, where a thin film of saturated solution surrounds the particle. The film has a lower vapour pressure than that of pure water, driving more water vapour from the gas phase onto the solid particle.[98]
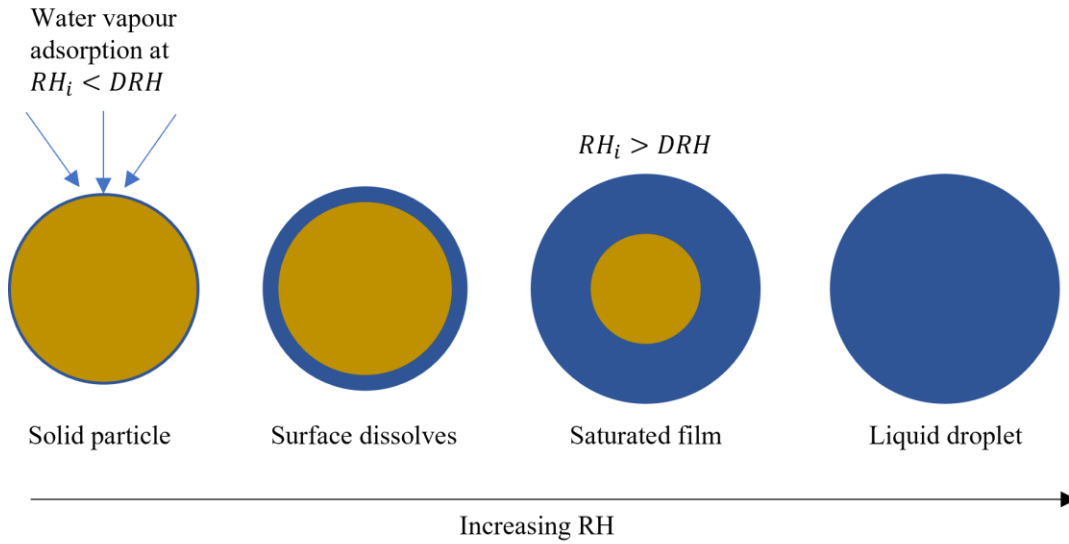
Figure 2.10. Schematic of the deliquescence process of a solid particle to liquid droplet.

The difference in chemical potential between water in solution, μ_{sol}, and pure water, μ_{pure}, can be written as:

$$\mu_{sol} - \mu_{pure} = R \, T \ln \left(\frac{p_{sol}}{p_0} \right)$$

Equation 2 - 42

where R is the gas constant, T is the temperature, p_{sol} is the vapour pressure of water in the saturated solution and p_0 is the vapour pressure of pure water at temperature T. In the case when p_{sol} is less than p_0 there is a driving force for condensation of water onto the droplet. As water condenses onto the film p_{sol} increases to that of the surrounding water vapour, p_0. The vapour pressure decreases back to DRH as further solid is dissolved and saturation is reached. Condensation and dissolution continues until all the solid dissolves, where the droplet reaches equilibrium with the gas phase upon complete dissolution.[99]

Van Campen et al. showed that the kinetic rate of deliquescence increases as the RH increases above DRH.[99,100,101] Van Campen et al. modelled the kinetics of water uptake in a single component deliquescent solid systems, demonstrating an excellent agreement with their experimental studies.[99] The work of Van Campen et al. was reported in a series of three articles. In their first article they presented a heat transport model which quantitatively describes water sorption kinetics above DRH in an atmosphere of pure water vapour. In simplest form, the equation for the sorption rate, W_h', can be written as:

$$W_h' = (C + F) \ln\left(\frac{RH_o}{DRH}\right)$$

where C is the conductive term and F is the radiative term, both found to contribute equally to heat transport.[99]. It is assumed that a deliquescent solid retains a saturated film around the particle when DRH > RH_0 .[99] Equation 2-43 highlights the dependence of dissolution rate on the ratio between the DRH and gas phase RH, a relationship that is explored thoroughly on this thesis. Additionally, Equation 2-43 indicates that as RH_o approaches DRH the kinetics will be slow, and when RH_o= DRH then the sorption rate is zero.[42] In the second article by Van Campen et al. the applicability of the heat transport model, Equation 2-43, was tested for various alkali halides and sugar.[100] Excellent agreement was found between experimental and calculated values of W_h'.[42] The final article by Van Campen et al. tested the heat transport model in 1 atmosphere of air, where they assumed only mass transport occurs. Following this, Van Campen et al. expressed the final mass-heat transport model.[101] This thesis aims to test their findings of the dependence of dissolution on DRH, while exploring other factors that influence dissolution rates of solid particles.

2.4   Chapter 2: Summary

This chapter has introduced the thermodynamic and kinetic processes that govern evaporation and condensation of liquid droplets. The influence of vapour pressure and the presence of a solute on the chemical potential of the solvent was discussed. Three regimes were described, in which the droplet size differs, each experiencing different kinetics of mass flux. The focus of this work is on the continuum regime, where the droplet size range is relevant to experiments carried out in this thesis. The coupled heat-mass transfer equation was introduced, where limitations and assumptions such as temperature suppression were described. Additionally, the kinetics of mass flux for non-homogenous particles were discussed, by first introducing the efflorescence and deliquescence cycle. The theory of crystal nucleation was examined, leading to the kinetics of deliquescence of dried particles.

Chapter 3

Experimental Techniques and Methodologies: The Electrodynamic Balance and Advanced Derivatives, The Falling Droplet Column, and Imaging of Dried Particles

In this chapter, the experimental techniques and methods used for the findings in this thesis will be presented. This work was mainly carried out using an electrodynamic balance (EDB) which is a single particle measuring technique, where individual droplets or particles (5-30 µm radius) are suspended in an electric field. A green laser (532nm) illuminates the trapped droplets, the elastically scattered light is collected and can be used to infer the radial size and physical state of the droplet. Over the years there has been much development of the EDB. Three key derivatives to this work are described in this section, each possessing specialised components. Throughout my PhD I aided with the development of several EDBs. Contributions included rebuilding of an instrument, addition of measurement capabilities and addition of environmental capabilities. EDBs can be used to collect data on evaporation kinetics, condensation kinetics, dissolution dynamics, mass measurements and a droplet's dried morphology or physical state.

In addition to the EDBs, particle imaging was carried out on collected dried samples. This was performed using a scanning electron microscope (SEM), where the dried particles had been collected using one of the EDB derivatives or a falling droplet column (FDC), dependent on the environmental conditions that were required. This section describes the progression of the electrodynamic balances within BARC. First, a double ring electrode configuration, next a comparative-kinetics electrodynamic balance (CK-EDB) and most recently, the single particle levitation at saturated conditions (SPLASH). The ring electrode applies only a DC voltage, developed for bio-aerosol measurements, and is referred to as "Controlled Electrodynamic Levitation and Extraction of Bioaerosol onto a Substrate" (CELEBS).[66]

3.1   Introduction to The Electrodynamic Balance

The development of the electrodynamic balance came from the ambition to measure the elemental charge on an electron. Millikan measured the charge on an electron in 1910 using the Millikan oil drop experiment. It is a non-intrusive method to levitate particles, which can be used in the micrometre or sub-micrometre range. Since then, there has been significant advances in the ability to confine a single particle using an electric field and carry out measurements on the physical properties of aerosol. The

hyperboloidal electrodynamic balance was the first instrument that used both AC and DC voltages to increase trapping stability. The AC voltage gives transverse stability in the horizontal plane. The standard hyperboloidal electrodynamic balance (SHEL), shown in Figure 3.1a, was developed by Wuerker et al.[63] as a powerful tool for studying processes in droplets. Although SHEL levitated droplets stably, the visual access was limited as the electrodes surrounded the particle. In 1980 E. James Davis and A. K. Ray designed an electrodynamic balance, Figure 3.1a, which is the backbone of the work carried out during my PhD. Davis. J. measured evaporation rates of single droplets of dibutyl sebecate (DBS), where the droplet sizes were in the micron and submicron range.[64] The electrodynamic balance consisted of two hyperboloidal endcap electrodes which created the DC field, and a central ring electrode with an applied AC voltage, with the particle confined at the null point of the field.[64] Once a charged particle had been trapped it was possible to probe it's physical properties with the use of an illuminating laser. The droplet radius, as a function of time, could be inferred from the light-scattering using Mie theory and the mass could be determined from the DC voltage applied across the electrodes balancing out the gravitational force.
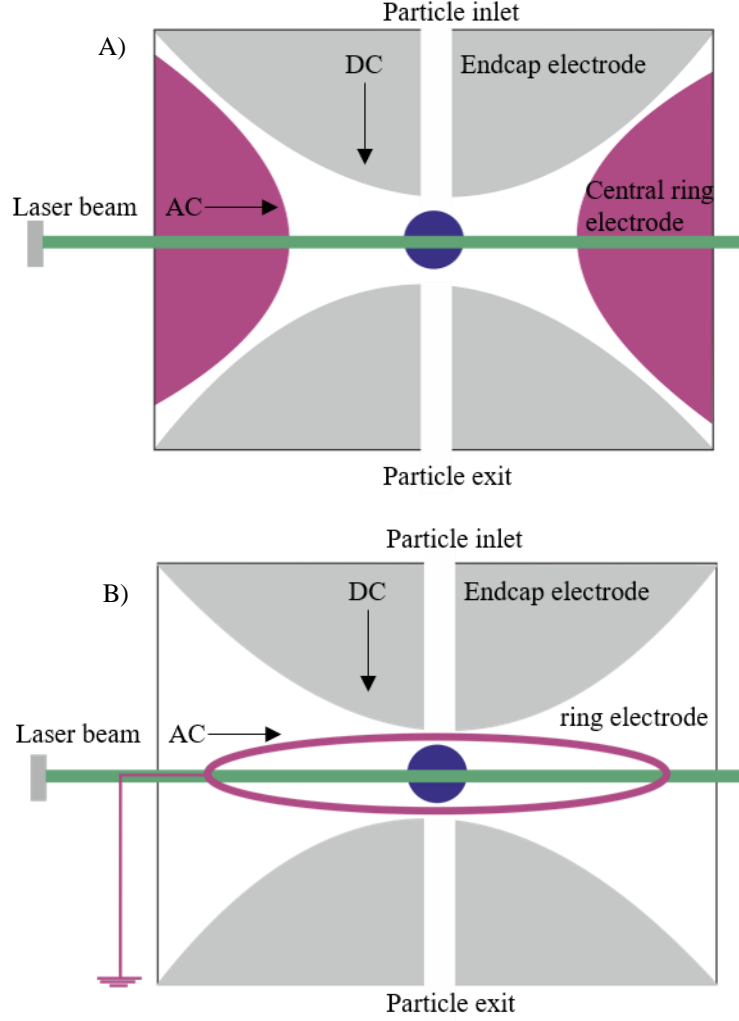
Figure 3.1. a) Cross-sectional view of a standard hyperboloidal electrodynamic balance (SHEL).[63] b) Cross-sectional view of an electrodynamic balance designed by James Davis and A. K. Ray.[64]

In an electrodynamic balance, the electric field resulting from the AC voltage exerts a periodic force on a confined particle in the vertical and radial directions, proportional to its distance from the centre of the trap, where the electric field approaches zero. The oscillatory AC voltage locally stabilises the particle and a DC voltage applies an electrostatic force to balance any net forces on the particle, such as gravity. The equation of vertical motion in an EDB is given by:[102,103]

$$m\frac{d^2z}{dt^2} = -3\pi a\eta\frac{dz}{dt} + F_z - mg - qC_0\frac{V_{dc}}{Z_0} - \left(2qC_1\frac{V_{ac}}{Z_0^2}\cos\omega t\right)z$$

Equation 3 - 1

m is the mass of the particle, z is the vertical distance from the midplane of the balance, t is time, a is the particle radius (assuming sphericity), and η is the gas viscosity. F_z is the force parameter, which includes external forces on the particle, such as Stokes drag caused by a continuous gas flow and radiation force of a laser beam, and the gravitational force is given by mg. The forces due to the AC and

DC voltages involve q, the coulombic charge, the DC and AC potentials, V_{dc} and V_{ac}, the AC circular frequency, ω, and geometrical constants z_0, C_0, and C_1. The DC and AC balance constants, C_0 and C_1 respectively, depend on the electrode configuration for the EDB. Usually $C_0 < 1$ for the Millikan apparatus with effectively infinite DC electrodes, and for a general EDB set up both constants are less than one. The AC frequency, $f = \frac{\omega}{2\pi}$, where ω is the angular frequency includes a time-dependent term and is usually varied. A trapped particle will oscillate in the electric field when it is moved from the null point, due to the drag force, such that net force of the DC voltage balances gravity and the external force. A particle will reach a stable state without any oscillations with the following requirement:

$$F_z - mg = qC_0 \ \frac{V_{dc}^*}{Z_0}$$

When gravity is the only external force ($F_z = 0$), then Equation 3.2 can be simplified to a standard force balance equation applied to the EDB:

$$mg = -qC_0 \frac{V_{dc,0}}{Z_0}$$

where $V_{dc,0}$ is the DC voltage required to balance the gravitational force. This allows for the EDB to be used for gravimetric analysis as $V_{dc,0}$ is directly proportional to the particle mass.

The estimated mass can be calculated from the applied DC voltage that is applied to counteract the gravitational force, in order to calculate the radius or physical phase state of a droplet or particle, light scattering techniques offer an accurate solution.

3.2 Ring Electrode Configuration

The ring electrode balance, i.e. CELEBS, was used in this work to collect dried aerosol samples prior to imaging. A recent version of CELEBS is shown in Figure 3.2a. The instrument consists of a metal, or 3D printed, chamber encasing the ring electrodes. Sample collection is not the usual purpose of the instrument, it was designed to study bioaerosol survival as a function of relevant environmental conditions. Droplet on demand dispensers are used to produce an array of droplets that become trapped between the ring electrodes. The array of droplets are levitated within a controlled environmental chamber and later deposited on a substrate after a desired period.[66] The droplets are levitated until crystallisation, about 10-20 s depending on the gas phase RH.
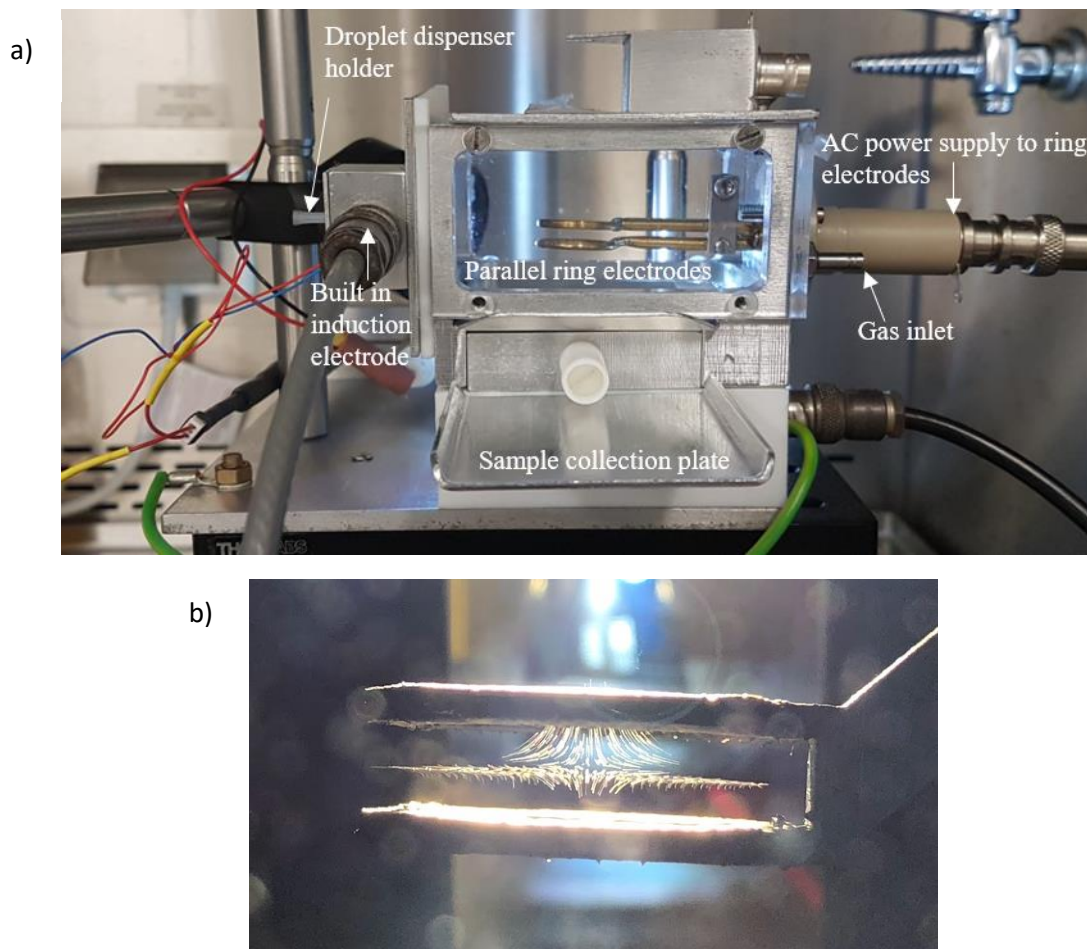
Figure 3.2. a) A photograph of a recent version of CELEBS with an attached droplet dispenser on the side. b) A photograph of an array of droplets confined between two ring electrodes on CELEBS.

The system does not use an illuminating laser beam, as the purpose of CELEBS is not to measure radial sizing. However, a Light-Emitting Diode, LED, allows visual inspection of the array of droplets, Figure 3.2b. The system consists of two ring electrodes which are encased in a plastic chamber, of which the structure has been 3D printed out of plastic filament. A thorough description of the instrumental set up can be found in the literature,[66] while this thesis will cover the methods of droplet generation, trapping between ring electrodes, RH and temperature control and sample collection on CELEBS.

3.2.1 Droplet Generation and Charging

Droplets containing a chosen solution are generated on demand using a commercial piezoelectric droplet-on-demand (DoD) dispenser (Microfab MJ-ABP-01), which is placed outside of the chamber in front of a small aperture. The standard dispenser orifice diameter used in this work was 30µm, however different sizes were used when a variation in droplet radius was required, with an increase up to 80µm possible. Piezoelectric dispensers are commonly used in inkjet printing and are selected over other droplet generating devices, such as nebulisers, due to the reproducible droplet size. Additionally,

DoDs allow for single droplet generation, whereas nebulisers produce a cloud of aerosol, which for some measuring instruments is the desired outcome, such as optical tweezers.[104]

The droplet dispenser is set up outside the chamber, there is a small capillary tube , ~2 mm diameter, attached to the non-orifice end, a solution is pipetted into the reservoir using a micropipette (Pipetman, Gilson). To actuate the dispenser, a pulse voltage is applied controlled by a LABVIEW programme which outputs a square wave form to a Data Acquisition (DAQ) card and onto a 10× voltage amplifier. The recommended voltage limit to apply to a Micro-Fab dispenser is 70 volts. When dispensing a low viscosity substance, such as water, the required pulse voltage is low. However, when working with a high volatility solvent, such as ethanol, the voltage required is often 70 volts. Increasing the pulse amplitude increases the droplet velocity which ensures the droplet reaches the trap before too much mass has been lost.

Once a pulse voltage is sent to the micro dispenser a piezoelectric crystal is actuated, generating a pressure wave in the capillary tube that forces a small volume of the solution out of the orifice at the tip of the dispenser. The jet of liquid subsequently breaks down into multiple droplets, where ideally a stable generation minimises formation of small satellite droplets, as shown in Figure 3.3a. The pulse width of the voltage affects droplet size; often 20-50 µs is appropriate to produce droplets that can be reliably trapped and close to the orifice size. The standard voltage and pulse width input signals often produce a droplet of about 25 µm starting size when using a 30 µm orifice. Additionally, these signals can be tailored to control the starting droplet size. For example, a higher pulse width often leads to a larger droplet, and vice versa. A 30 µm orifice dispenser can be used to produce droplets ranging from 19 to ~29 µm.
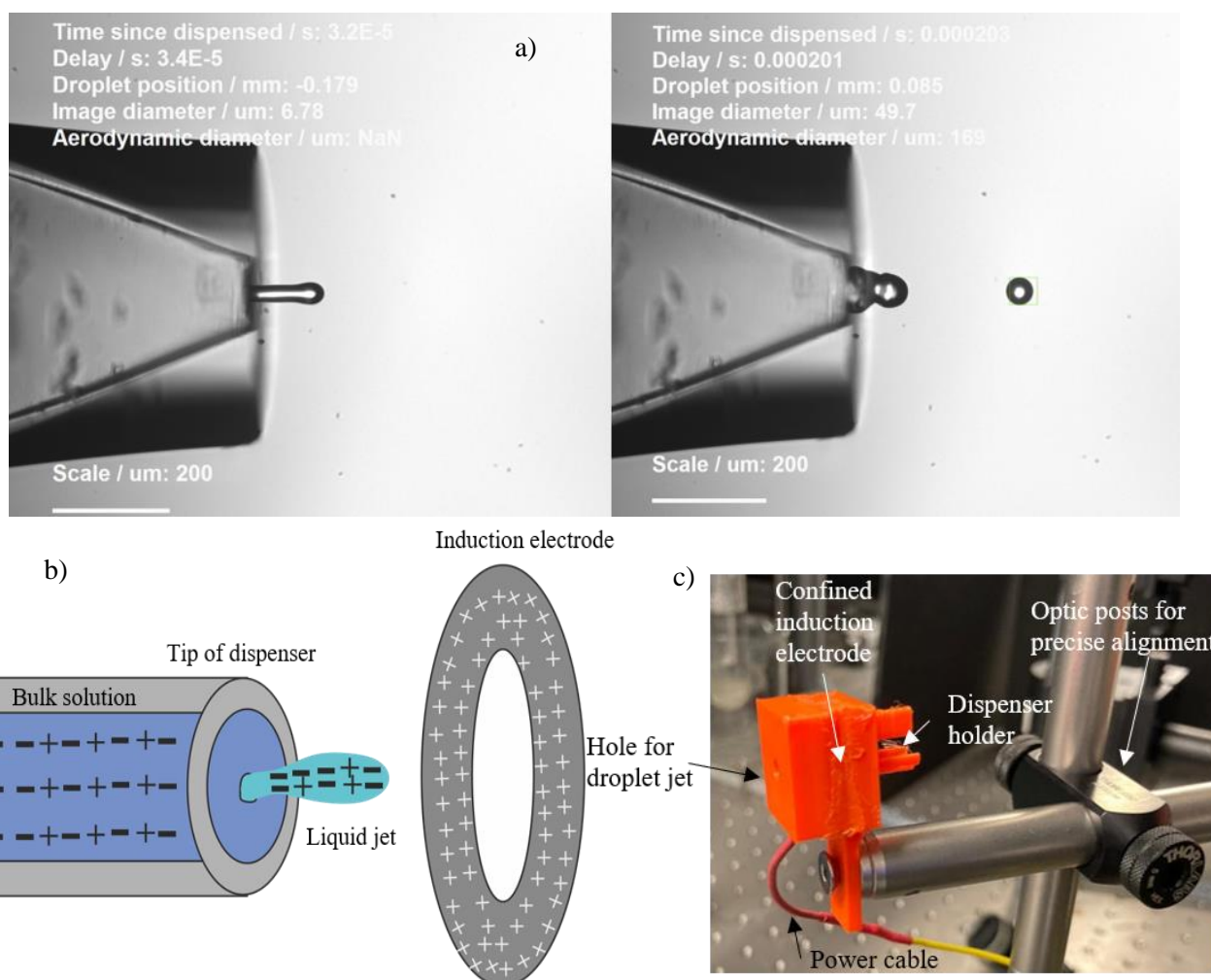
Figure 3.3. a) Images of a liquid jet leaving the tip of a dispenser followed by the formation of a single primary droplet and several smaller satellite droplets to follow, *images taken by Daniel Hardy, a BARC colleague*. b) A schematic of inducing a charge on a droplet using a high voltage induction electrode. c) The droplet dispenser holder with a confined induction electrode.

A high voltage induction electrode induces a charge upon droplets as they are generated, Figure 3.3b. The induction electrode is a conductive ring held at the front of the dispenser holder, completely encased by a 3D printed box, Figure 3.3c. The charge ensures that the droplets can be confined within the electric field of the EDB. Originally, an induction electrode was attached to the side of the EDB chamber and the dispenser holder contained only the dispenser. There were two main issues with this set up: an exposed highly charged electrode creates a user safety risk. Additionally, a dispenser that makes contact with an induction electrode damages the droplet dispenser driver boxes. The distance between the droplet and the induction electrode affects the charge imbalance acquired by the droplet on generation. The separation between the electrode holder and electrode itself varies, this leads to a change in the charge imparted on the droplet. A variation in droplet charge impacts on mass measurements when using the DC offset, as the relationship between the two involves the droplet charge. A potential of 100-700 V is applied to the conductive ring using a Stanford Research Systems Inc high voltage power

supply (Model PS350/5000V-25W). The power supply induces a mirror charge on the droplet as it forms at the tip, Figure 3.3b. The electric field generated between the induction electrode and the tip of the dispenser induces a separation of ionic species within the liquid jet following actuation of the dispenser. When the jet separates into small droplets they retain a net charge with a polarity opposite to that of the induction electrode. The induction electrode is positive for all EDBs as described in Figure 3.3. It is possible to estimate the charge on droplets,[105] previous work suggests droplets from a micro dispenser incur a charge on the order of 5 – 50 fC.[105] The droplet charge is not estimated in this work.

3.2.2 Trapping a Droplet in an Electrodynamic Field Between Double Ring Electrodes

An AC voltage is applied to the double ring electrodes in CELEBS using a LabVIEWsoftware, which simulates a sine wave. The signal is generated with a resolution of about 5 µs and passed to a National Instrument multifunction device (NI USB-6001). A voltage amplitude with a range of 1000 to 2700 V is generated by the DAQ card and is amplified by a high voltage amplifier (Matsusada AP-1B3). The voltage signal is sent to the ring electrodes. The maximum AC voltage on CELEBS is much higher than that of the other EDBs used in this work, 2700 V vs 1000 V respectively. CELEBS is an open system with a larger distance between the double electrodes, thus it requires a larger voltage to trap a droplet. The double ring electrode instrument (CELEBS) does not use a DC voltage in addition to the AC voltage.[66] This is due to two reasons. First, it is not the purpose of CELEBS to trap individual droplets in an electric field with position stability, which is the primary reason for adding a DC voltage to an electrodynamic trap. Second, colleagues in BARC discovered that the introduction of a DC voltage to their system negatively affected the ability to collect the sample of charged droplets after the experiment on a plastic petri dish situated below the rings.[67] Instead, using an AC field alone, it is possible to stably trap up to 200 droplets between the parallel rings, while the electrostatic repulsions among the array of positively charged droplets prevents coalescence.[66] Light from an LED with a wavelength of 580 nm illuminates the population of droplets, while a charged couple device (CCD) camera is placed above the chamber so the user can monitor the location and stability of the droplets in the trap. The user can control the electric field to ensure that droplets are confined at the null point for the required time, changing the frequency and voltage as needed. This prevents premature deposition on to the substrate or glass slide. In this thesis a glass slide was used to collect the dried sample. Other EDBs used in this work do not have sample collection capabilities.

3.2.3 RH and Temperature Control Between the Double Ring Electrodes

The environmental conditions within the CELEBS chamber are controlled slightly differently to the other EDBs used in this work. Although there is no temperature control in CELEBS, the instrument is situated in a fume hood which helps maintain a steady room temperature (~293 K). The temperature

and RH are measured continuously using a probe (Humidity and Temperature Meter HMT331, Vaisala, UK), immediately before the gas inlet to the EDB chamber, highlighted in Figure 3.2a.

The plastic chamber, or metal in the later version show in in Figure 3.3a, isolates the trapped droplets from the surrounding air flows and ambient laboratory conditions. While the droplets are suspended, a gas flow through the inlet is used to control the RH of the chamber, ranging from 10% to 90% RH. The gas flow is easily adjusted by the mixing of two flows, humidified and dry air, and delivered by an air purifier (Precision Air Compressor, Peak Scientific, UK) using two flow controllers.

3.2.4   Collecting a Sample of Particles from the Ring Electrode Trap

After the desired time, the sample collection plate and the trap are connected by removing the safety plate, the white handle shown in Figure 3.3a. The droplets are extracted from the EDB by gradually lowering the amplitude of the waveform applied to the ring electrodes and the droplets land on the substrate in short period of time (1-3 s).[66] Prior to particle extraction, a plastic petri dish was placed in the sample collection tray, while a small circular glass slide was placed in the centre of the dish. A small glass slide is used to allow for easy accessibility to the sample when performing subsequent electron microscopy imaging, further details on this are described in section 3.3.9. Additionally, it was found effective to rub a cotton cloth around the base of the petri dish prior to removing the safety plate. Rubbing a cotton cloth induces static charge on to the dish allowing for very effective sample deposition of the charged droplets. Sample collection on CELEBS is suggested to have 100% efficiency.[66]

3.3   Comparative-Kinetics Electrodynamic Balance (CK-EDB)

The following three subsections describe the in-house built instrument referred to as a Comparative-Kinetics Electrodynamic Balance (CK-EDB). Three CK-EDBs were used in this work, each used interchangeably depending on their strengths, such as RH stability or distance of dispenser from trap. The methods of droplet generation and charging are almost identical to the procedures described above. However, there are some small differences or advancements when working with a single particle trapping EDB compared to a multiple droplet trapping EDB, i.e., CELEBS. The instrumental set up to control the RH is different on the CK-EDB and, in addition, there is the ability for temperature control.

3.3.1   Instrumental Setup of The Comparative-Kinetics Electrodynamic Balance (CK-EDB)

The Comparative-Kinetics Electrodynamic Balance (CK-EDB) instrumental set up is shown in Figure 3.4, as a top-down view. The instrument is contained within a large, elevated laser box, which has doors

on all four sides and allow for easy access to the CK-EDB. During an experiment, the doors remain closed preventing laboratory air current to affect the measurements, while also supporting operation at a sustained steady temperature (particularly the temperature of the water bubblers, which are used to control the RH of the chamber). The CK-EDB consists of two sets of concentric cylindrical electrodes, above and below one another. The electrodes are set in place but the distance between them differs slightly between instruments, ranging across 2 - 5 mm. The space between the cylindrical electrodes is where the individual charged droplets are trapped. The CK-EDB chamber is an octagonal shape, with two viewing windows, a laser entrance, two apertures for droplet injection, a laser exit and two windows for camera access.
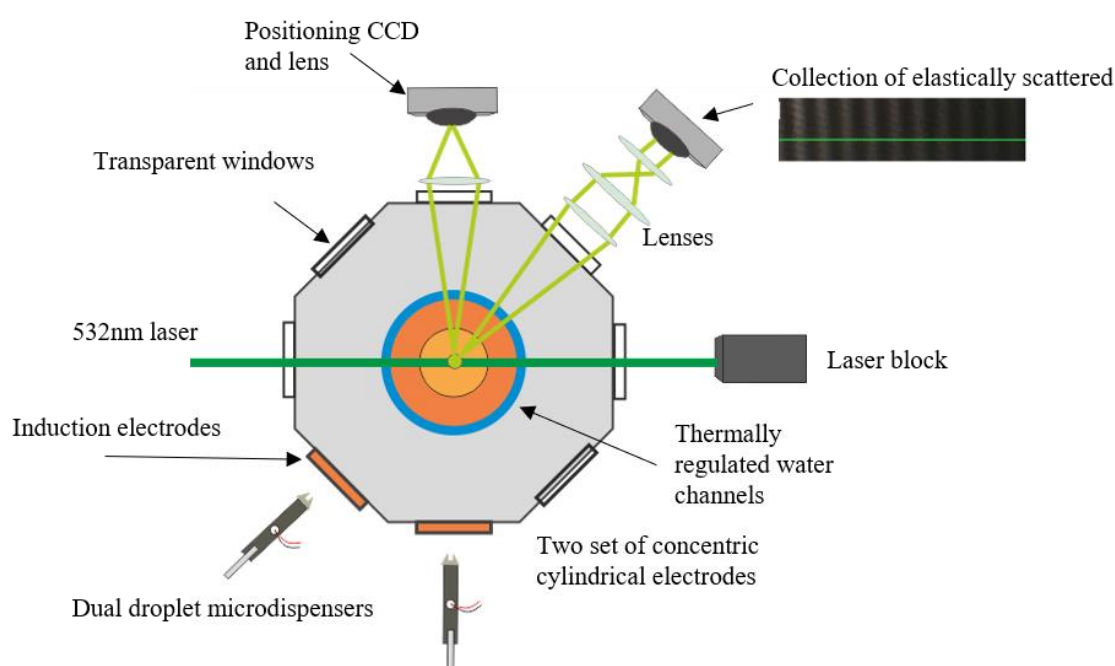
Figure 3.4. A schematic of the CK-EDB from a perspective above the instrument.

A 532 nm continuous wave laser is directed parallel to the optics bench and aligned through the centre of the trap, exiting through an aperture to a laser block. As the laser interacts with the trapped droplet, a light scattering pattern is generated that is collected and imaged by a series of lenses onto a CCD. There are two CCDs mounted onto the chamber. One camera is used to collect elastically scattered light in the form of a phase function in the near-forward scattering direction, which is subsequently used for estimating the size of a trapped droplet. The other camera collects near-back scattered light and produces a focused image of the droplet used to identify the vertical position of a trapped droplet.

The temperature and relative humidity (RH) in the chamber can be controlled, using a polyethylene glycol liquid flow through the electrode assemblies and a humidified-N_2 gas flow, respectively. The circulating coolant passes through the electrodes and the gas flow passes through the cylindrical electrode channels. Initially, CK-EDBs had only one gas flow with updated versions including two

independent flows, one through the top and a second through the bottom electrode assembly. This allows for rapid switching between RH conditions and is further described in the next section.

3.3.2 Trapping a Droplet in an Electrodynamic Field Between Cylindrical Electrodes

The CK-EDB was used in this work to explore physical properties of single particles. Thus, the voltage pulse sequence applied to the droplet on demand dispenser was tailored to prevent an array of droplets becoming trapped in the chamber during measurements, unlike experiments performed on CELEBs. The same Microfab droplet on demand dispensers were used on CELEBs and the CK-EDBs. To achieve single particle confinement, the dispenser is aligned whilst in "continuous" mode, often with a pulse voltage of 40 -70 V at a width of 30 – 80 μs applied at a frequency of 10 Hz. Once the droplets can be seen passing through the centre of the electrodes, the control software sets the dispenser to operate in "automatic" mode, and the user can begin trapping single droplets. The LabView software recognises when a droplet is captured by the trap from the appearance of light scattering recorded by the CCD camera. At this point, a reduced pulse voltage is applied to the dispenser ensuring that fresh solution constantly replenishes the tip of the dispenser for subsequent droplet measurements while not generating droplets with sufficient momentum to reach the trap location. This constant pulse sequence ensures that evaporation of the solvent does not affect the solute concentration at the orifice and the voltage is usually 10 V below the voltage required to dispense a droplet into the trapping zone. Once the droplet falls out of the trap, or the user discards it, the change in light scattering signal initiates the generation of a fresh droplet to load the trap. The instrument can only record the radius of the droplet once it is trapped in the instrument, so the radius at t=0 s can only be determined by extrapolating back through the first 0.1 s.

Droplets are charged upon generation in the same way as described above. An induction electrode is built into the droplet dispenser holder charged to a voltage of 200 – 700 V. As the droplets are charged and the dispenser set to "continuous" mode, the droplets enter the chamber and are aligned to pass into the trapping region between the cylindrical electrodes. At this point the electrodynamic field is turned on, applying an AC voltage across the four electrodes in the EDB, which traps the droplet in the centre. The implementation of the cylindrical electrode design is discussed in the earlier work of Heinisch et al.,[59] and Figure 3.5 is reproduced from their article. The figure shows the calculated absolute value of the electric field in the space around the cylindrical electrodes, corresponding to a potential of 1 kV on the inner electrode and 0 V on the outer electrode.

An AC voltage is applied to the cylindrical electrodes in the same way as described above for CELEBS. In addition to an AC voltage the CK-EDB is also coupled with a DC offset, which is applied between the bottom and top electrodes. Applying only an AC voltage to the trap causes the droplet to oscillate

due to the combined effects of the electrodynamic, gravitational and drag forces. A DC voltage is applied to counteract the downward forces and support the particle levitation. The initial AC voltage applied to the electrodes is around 600 – 700 V at a frequency of 90 – 120 Hz and this varies depending on the charge on the droplet. Once multiple droplets are confined the dispensing is set to "automatic" mode, after which single droplets are confined in the trap. In order to keep the droplet trapped for a significant period, or until equilibrium, the AC voltage and frequency must be varied in relation to the changes in droplet size. This can be achieved manually, often when droplets experience rapid large radial size changes, or automatically use the following expressions:

$$V(a) = V_0 - \frac{dV}{1 - \frac{a}{a_0}}$$

$$f(a) = f_0 - \frac{df}{1 - \frac{a}{a_0}}$$

<div align="right">Equation 3 - 4</div>

where V_0 and f_0 are the initial voltage and frequency, and dV and df are parameters which change the voltage and frequency according to the ratio of the radius, a, to an initial radius, a_0, which is manually entered. The values for V_0 and f_0 differ between experiments but are in the ranges 0 to 4 V and 100 to 400 Hz, respectively. A simple rule is rapid droplet evaporation leads to rapid change in droplet radius and values of V and f must change accordingly. It was shown that combining AC and DC fields led to stable trapping of a water droplet in the trapping chamber, with droplets not moving further than 1 µm from the equilibrium position within the centre of the EDB.[59]
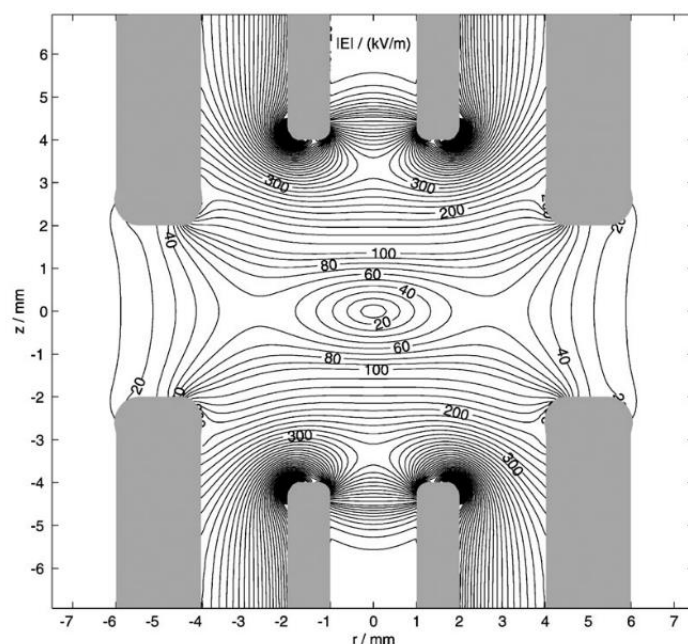
Figure 3.5. Reproduced from Heinisch et al.,[59] figure showing cross section of the cylindrical electrodes of the EDB, with calculated value of the electric fields for a potential of 1 kV at the inner electrodes and 0 V at the outer electrodes.

3.3.4   RH and Temperature Control in the CK-EDB

A steady relative humidity is achieved by the mixing of a humidified flow and dry nitrogen gas flow, where the ratio governs the final RH. The aerosol laboratory is connected to the School of Chemistry's mains nitrogen gas supply, in the event that this is not available there is a store of nitrogen cylinders (BOC or Air Liquide cylinders) that can be used to supply gas to the mass flow controllers (MFCs). There are two MFCs (MKS 1179A Mass- Flow, rated for 500 sccm N_2) connected to each gas inlet on the top and bottom electrodes. One MFC controls the gas flow through the water bubbler and the other controls the flow of the dry nitrogen, as shown in Figure 3.6. In majority of CK-EDBs, the MFCs are controlled by a MKS power supply (247D), which is connected to the computer using a DAQ card (NI USB 6001). The DAQ card enables the user to monitor the RH using a LabView interface.

In order to generate a steady RH flow in to the EDB chamber, a humidified flow and dry N_2 flow is required. A dry N_2 flow is passed through a MFC which controls the volumetric flow rate of gas passing through a water boat. Evaporation of water leads to a saturated gas phase with respect to water vapour and the N_2 gas flow leaves the boat at close to 100% RH. The humidified flow mixes with the dry flow, which has a flow rate set by a further MFC. The resulting mixed flow is sent into the EDB chamber via the top or bottom electrode depending on the EDB set up. The ratio of the humidified and dry flows is set using the MKS control units with the ratio of the two flows governing the RH, i.e. when set 1:1,the RH should equal about 50%; when set 0:1 (dry : wet), the RH should be close to 100%. The total gas

65

ratio is set to equal a flow-rate of 200 sccm (cm^3 min^{-1}), i.e. 1:1 = 100 sccm : 100 sccm, , with a gas speed of 3 cm s^{-1} previously established in the trapping region.[40] In a humidified flow of 100% wet air the RH will never reach saturation, the highest achievable RH is around 95 to 96%. An RH below saturation is due to many reasons; most important being the transport of the wet flow through the tubing, which is exposed to ambient temperature prior to entering the chamber. However, in section 3.4.2 it is explained how saturation can be achieved in an EDB using a new method of RH control.
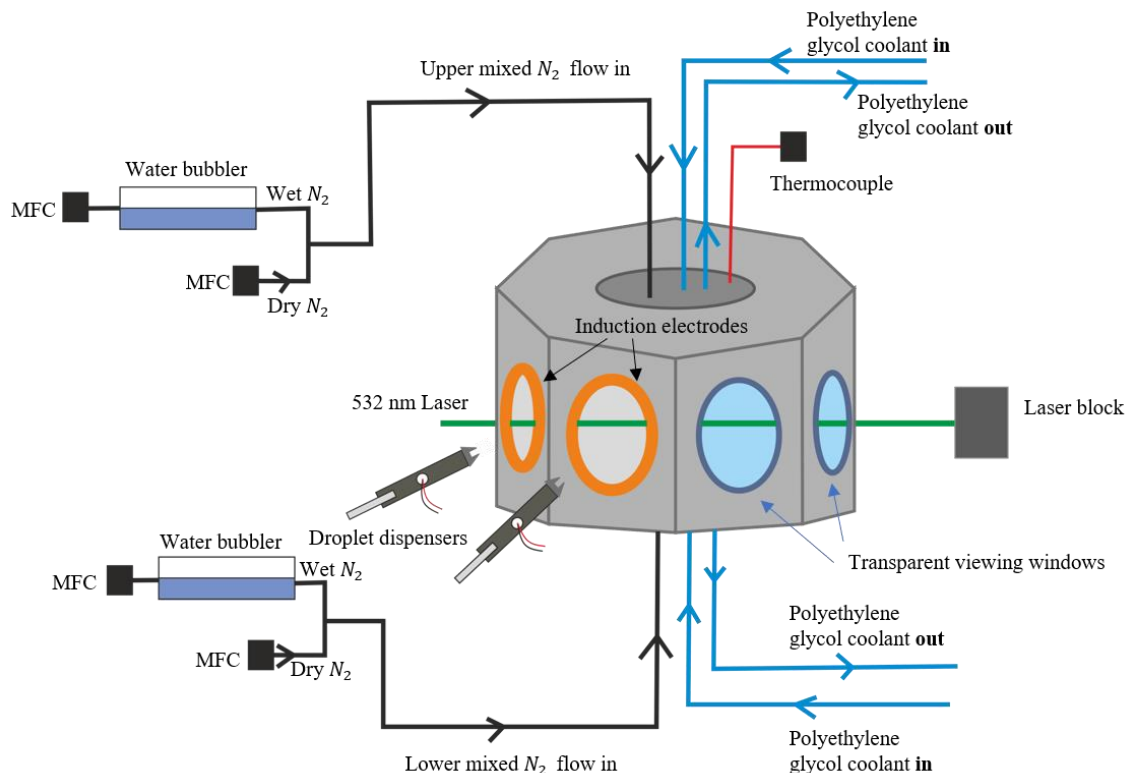
Figure 3.6. A side view schematic of a CK-EDB, with a description of the RH and temperature control inside the chamber, using N$_2$ gas flows and polyethylene glycol coolant, respectively.

The temperature in the CK-EDB can be set between 273 and 323 K and is controlled by circulating a polyethylene glycol coolant through the upper and lower electrode assemblies. The temperature of the coolant is controlled using a chiller (F32-ME, Julabo) and recorded using a thermocouple (National instruments, NI-USB-TC01 with K-type probe) close to the gas flow. The readings are sent to the LabView interface and can be recorded every 0.01 s.

It is shown in Figure 3.6 that there are two points of entry for the RH gas flow, upper and lower. It is possible to set the upper and lower gas flows to different RHs, e.g., 95% vs 10% RH. The user can instantaneously switch between the two rates using the LabView interface. This allows for sudden changes in RH and simulation of processes such as inhalation, from a dry to a very wet environment. The trapped particle experiences a large change in RH instantly. Figure 3.7 reports the evaporation rate for a water droplet exposed to two sudden changes in RH at T0 and T1, from 60% to 80% and then 80% to 60%, respectively. The change in the droplet evaporation rate is almost instantaneous, < 0.1 s.[87] This

method has been used in the work reported in this thesis to replicate water condensation and evaporation during inhalation to a humid lung.
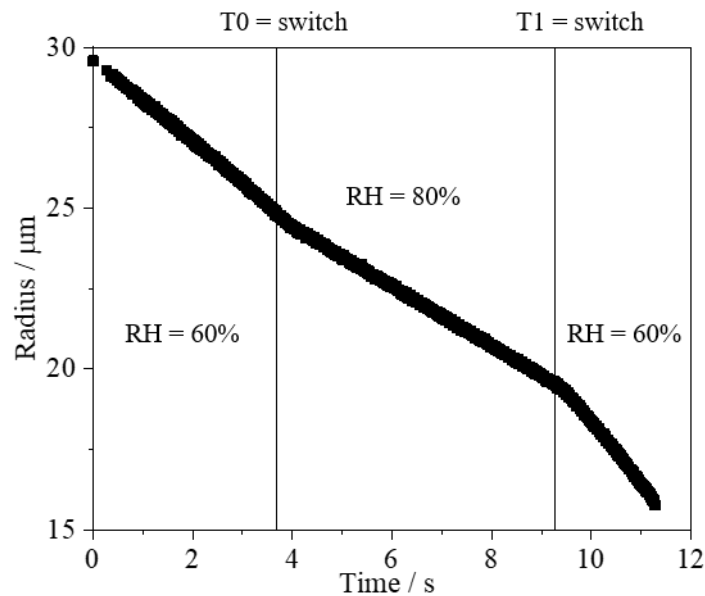
Figure 3.7. An evaporation profile of a water droplet in a CK-EDB, where the RH is switched between 60% and 80%, showing the instant change in evaporation rate of the water droplet after T0 and T1.

3.4   Single Particle Levitation at Saturated Humidity (SPLASH)

The single particle levitation at saturated humidity (SPLASH) instrument was designed, constructed, and benchmarked by Dr Allen Haddrell. Details of SPLASH have not been published and a detailed description is provided here.

3.4.1   Instrumental Setup of The Single Particle Levitation at Saturated Humidity

SPLASH was designed to enable simulation of the process that aerosol particles experience upon inhalation to the lung. A schematic is shown in Figure 3.8. The key function of SPLASH is the ability to reach super saturated gas phase conditions, consistent the high RH found in the lung. SPLASH is not built to perform hygroscopic growth measurements; thus, it is not the appropriate system to produce accurate quantitative aerosol radial size data. Moreover, it is to be used alongside CK-EDB measurements to collect relative qualitative data of particle dynamics, such as dissolution and crystallisation, also facilitating accurate dynamic mass measurements. As such, comparative measurements of sequential pairs of probe and sample droplets are not performed in SPLASH and, thus, there is no requirement to configure the instrument with two micro droplet on demand dispensers.
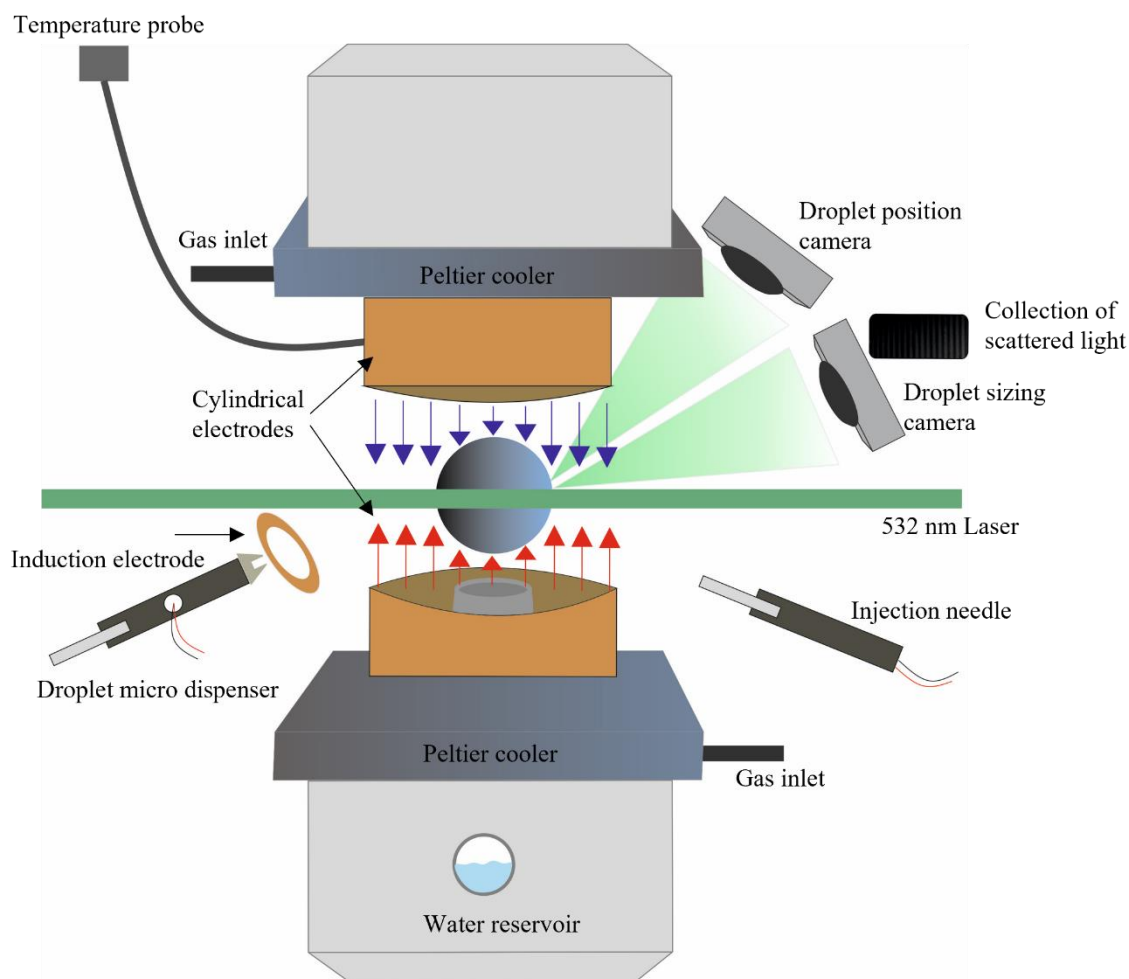
Figure 3.8. A side view schematic of the instrumental set up of SPLASH. The size camera and droplet position camera collect elastically scattered light in the horizontal plane.

The instrumental set up of SPLASH is similar to the CK-EDB, but there are some key differences. Firstly, it is an open system, Figures 3.8 and 3.9 show there are no sides surrounding the centre of the trap, it is an open chamber. A main benefit to an open system is the ability for the user to place the droplet on demand dispenser close to the centre of the trap. A short distance between the dispenser and trap is essential when working with substances of high volatility, such as ethanol-based drug mixtures. Highly volatile substances often do not travel sufficiently far to reach the null point on a CK-EDB. Additionally, SPLASH allows easy access for a dry powder injection needle to be moved close to the electric field. The dry powder injection needle method is described later in this section. There are two CCD cameras, one for positional measurements with varying DC voltage, and one for sizing the particle using the scattered laser light.
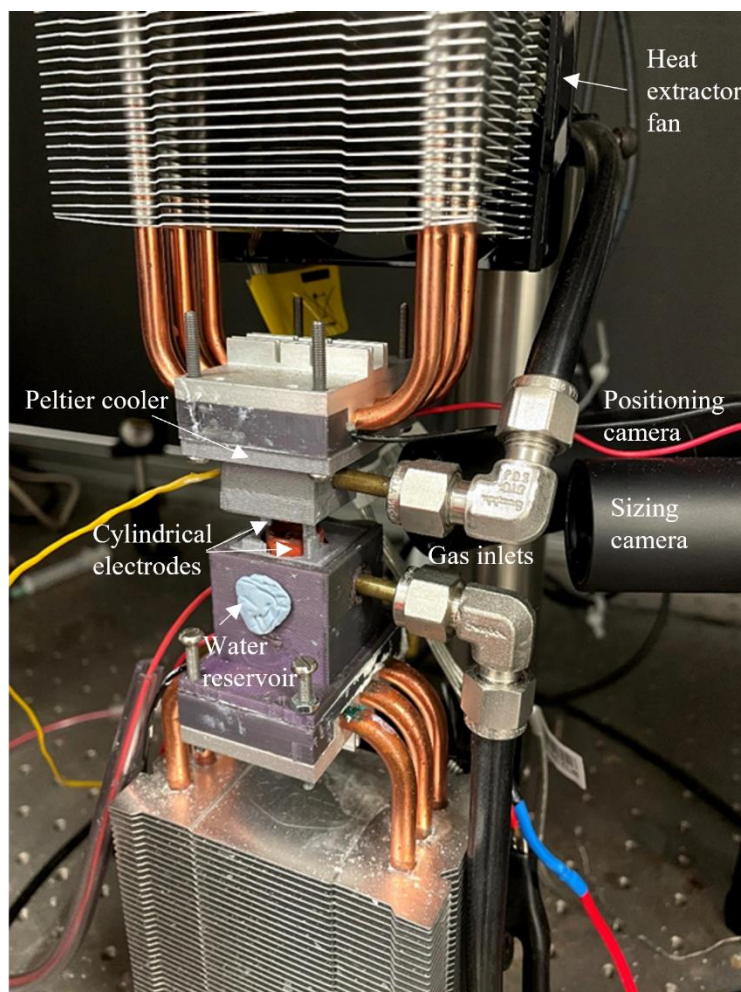
Figure 3.9. A photo of SPLASH.

The temperature of the electrodes is controlled by two Peltier coolers which are enclosed in a 3D printed holder. The Peltier coolers are attached to the bottom and top cylindrical electrodes, as shown in Figure 3.8. The Peltier coolers are controlled using a DC power supply and provide a temperature range of about -10 °C up to 70 °C, and each Peltier cooler can be set to a different temperature, e.g. top at 0 °C and bottom at 25 °C. The Peltier coolers can be used to create a temperature gradient between the electrodes. A temperature gradient is used to increase the relative humidity of the gas phase surrounding the droplet and allows the user to access a supersaturated regime. The approach for achieving super saturated conditions in SPLASH will be discussed further in the next section. Peltier coolers require excess heat to be removed to decrease the temperature of the gas phase. The large metal grills seen in Figure 3.9 have a fan connected at the rear, which draws the heat away from the Peltiers so they can work efficiently. However, when levitating micro sized droplets any air current in the gas phase causes significant disruption to the trapping. Therefore, the fans cannot be used to remove the excess heat. Instead, dry ice is placed on top of the metal grill and above the top electrodes. With the use of dry ice it is possible to maintain a temperature on the top electrode of -5 °C for about 20-30 mins. Half an hour is ample time to collect saturation measurements as the electrodes become too wet after 30 mins and

levitation is no longer possible. A thermocouple, the yellow cable in Figure 3.9, is attached to the top electrode and the temperature is displayed on the LabVIEW interface. The user can alter the DC power to increase or decrease the temperature.

3.4.2   Reaching Super Saturated Conditions in SPLASH

The temperature of each electrode is independently controlled using the Peltier coolers and this enables the formation of a temperature gradient between them. This gradient can be used to access a supersaturated relative humidity at the location of the trapped droplet. The vapour phase is saturated when there are an equal number of molecules condensing to and evaporating from a pure water droplet. At the point of saturation, the pressure of the vapour is called the saturated vapour pressure and increases with an increase in temperature. Figure 3.10a shows that at a higher temperature more water can be held in the vapour phase.

The relative humidity in the lungs is >99.5%RH. Therefore, to replicate physical processes that occur during inhalation it is vital that the instrument can reach the same conditions. Relative humidity is defined as $\frac{p_w}{p_w^0} \times 100 = s_w \times 100 = RH$, where the amount of water vapour present in air is expressed as a percentage of the amount needed for saturation at the same temperature. An example of RH dependence on temperature is shown in Figure 3.10b. For an actual vapour pressure of water of 1.06658 kPa at a temperature of 20 °C with a vapour pressure of 2.33847 kPa at saturation, the RH is 1.06658/2.33847, which equals 45.61% RH. As temperature decreases, saturation vapour pressure also decreases, resulting in an increase in saturation for a constant absolute pressure. For example, at 5 °C the saturation vapour pressure of water is 0.87193 kPa, thus the RH at 5 °C with the same partial pressure of water would equal 1.06658/0.87193 = 122.3% RH. The relationship between temperature and saturation vapour pressure is utilised in SPLASH. The partial pressure of water is set and then the temperature between the trapping electrodes is altered. The humidified gas flow is formed in the same way as described previously for a CK-EDB, by passing nitrogen gas over a water bubbler. The humidified gas flow is the passed through tubing until it reaches the trap. The temperature of the wet gas flow is ambient, often between 19 – 21 °C. Despite the formation of a gas flow using a ratio of wet to dry at 200:0, it is never fully saturated. Therefore, the gas flow introduced to SPLASH never exceeds 95% RH, as with the CK-EDB. A temperature gradient is established between the bottom and top electrodes: the gas flow travels through the bottom electrode at room temperature, while the upper electrode is set to 0 °C. The temperature at the null point of the trap is halfway between the temperatures of the two electrodes. The temperature drop experienced by an almost saturated gas flow enables the gas phase surrounding the trapped particle to surpass saturation at the local temperature of the droplet. It is possible for the trap to remain at saturation for about 20 mins, after this time water begins condensing on to the metal electrodes and impacts the capabilities of the instrument to infer the droplet

size. At the point of significant condensation on the electrodes, the experiment is stopped, dry nitrogen gas is pumped through the trap and the experiment can begin again.
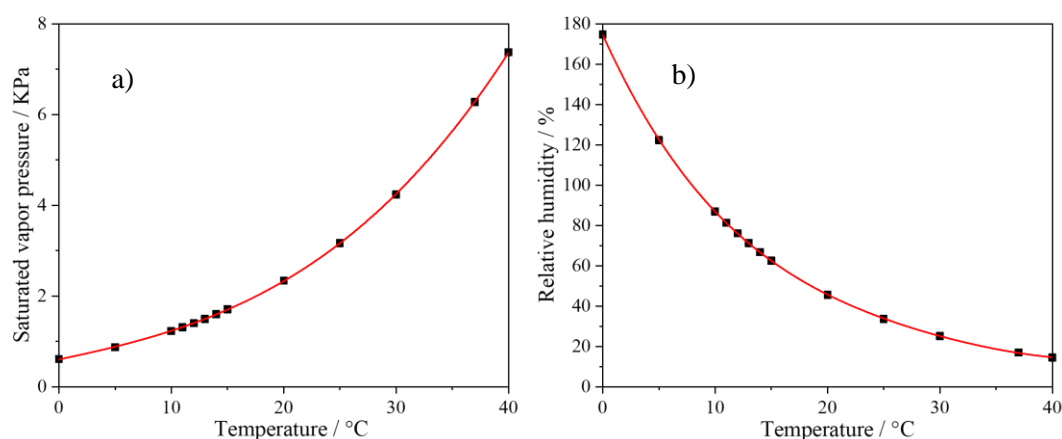
Figure 3.10. a) Saturated vapour pressure for water as a function of temperature. b) Relative humidity [(actual vapour pressure/ saturated vapour pressure) * 100] as a function of temperature, where the actual vapour pressure is set at 1.06658 KPa as an example.

Additionally, a water reservoir in the bottom electrode aids with the process of reaching saturation, shown in Figures 3.8 and 3.9. The wet gas flow passes over the reservoir immediately before entering the trap and increases the amount of water in the vapour phase. The reservoir can be seen in Figure 3.9, it is covered with BlueTac which can be removed to refill reservoir using a glass pipette prior to starting experiment. In essence, it is a second water bubbler directly before the trap, which the gas flow to passes over prior to entering the trapping cell. The addition of the water reservoir combined with the temperature gradient enables SPLASH to reproducibility reach saturation. A series of water droplets ranging from 80% to >100% RH is shown in Figure 3.11. Once a temperature gradient is introduced the droplets experience saturated conditions and can be seen to equilibrate with the gas phase and grow in radius. In Figure 3.11, the light blue line that appears horizontal, indicates that the RH of the trap is around 100% RH, where little to no condensation or evaporation is observed, and the water droplet is in equilibrium with a water activity of 1. Following this, a further decrease of the top electrode's temperature on SPLASH results in the growth of a water droplet. An increase in radius is shown by the top blue line, supersaturation has been reached and water molecules condense onto a water droplet with a water activity of more than 1. Here, the top electrode was set to ~ -1°C, which allowed for a rapid increase in RH above the saturation limit. Over a period of 100 s the radius increased from 25 µm to 40 µm. After this period, the electrodes became too wet to continue trapping the water droplet and ice started to form on the top electrode, otherwise, in theory, the droplet would just keep growing.
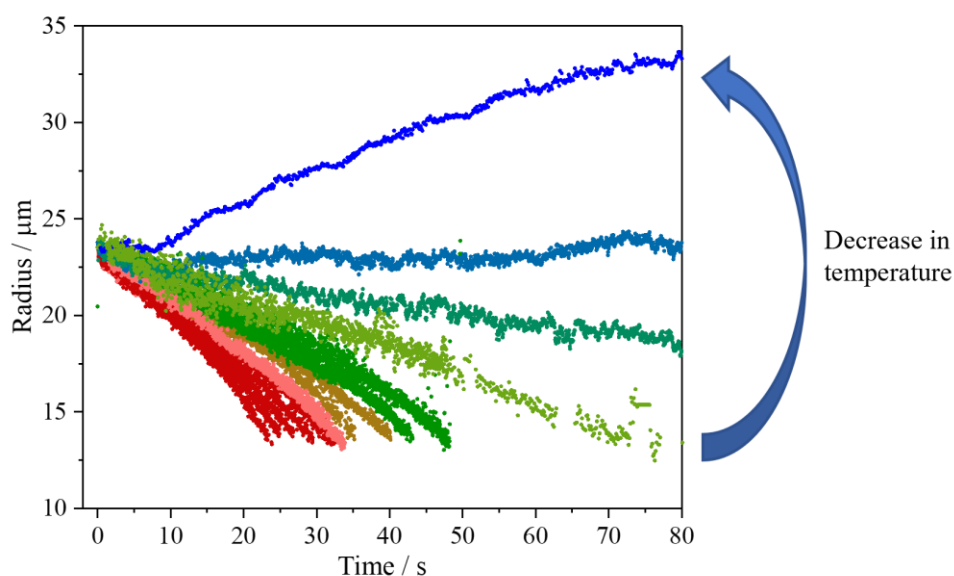
Figure 3.11. A series of water droplets trapped in SPLASH while the gas flow is set to fully wet, and the temperature of the top electrode is reduced gradually to ~ -1°C. At the lowest temperature a water droplet will grow, here the gas phase is super saturated. The RH ranges from about 80% to > 100%.

3.4.3   Motorised Back Pressure and Low Temperature Control for Volatile Solutions

The main component of meter dose inhalers (MDIs) is Hydrofluoroalkane (HFA)-134a – 1,1,1,2-Tetrafluoroethane, a propellant that makes up about 80-97% of the formulation in the canister, along with ethanol. The active pharmaceutical ingredient (API) and occasionally an excipient, such as glycerol for particle size control, make up the remainder of the mixture. An example of canisters used in this work is shown in Figure 3.12 on the right with the formulations made of HFA 86%, ethanol 13% and glycerol 1%. As HFA is the main component of the canister, SPLASH needs to be set up so that it can accommodate the dramatic changes in physical properties that occur due to the low boiling point of the propellant. HFA-134 has a boiling point of -26.3 °C, compared with 78.37 °C for ethanol and 100 °C for water. Considering that ambient room temperature is around 20 °C this causes serious complications for the measurement if using a standard CK-EDB instrumental set up. Therefore, several additions to SPLASH were designed to mitigate the issues of HFA boiling off prior to trapping and the pressure changes in the dispenser capillary tube which results in no solution being dispensed.

Without preventative measures in place, the HFA will boil off through the tip of the dispenser or out of the back of the capillary tubing. This causes the pressure in the capillary tubing to vary and forms a pressure gradient behind the micro dispenser and, due to the mechanics of the piezo electric system, this stops any solution from being dispensed. Therefore, a system that ensures the liquid solution is constantly being pushed through the tubing and not escaping from the back is essential. Additionally,

72

pressure is needed to ensure that the tubing remains equally filled, i.e. no air bubbles, allowing continuous dispensing. The pressure gradient is formed because HFA is boiling off, and therefore is the primary process to mitigate using a cooling procedure.

The experiment begins with all required components stored in an insulated dry ice box, Figure 3.12, including canisters, syringe, vials, solution and dispensers. Firstly, the canisters of HFA are stored in dry ice for at least 30 mins, ensuring the HFA remains in its liquid phase. Secondly, a canister piecer, seen at the bottom of Figure 3.12, is used to make two small holes in the canister, the HFA can then be poured into a cooled glass vial. Next, a cooled glass syringe, which has been stored in dry ice as two separate parts, is attached to a 10-15 cm length of cooled capillary tubing. The glass syringe is reassembled using cooled ethanol as a lubricant and filled up and emptied multiple times with ethanol. This ensures that the inside of the syringe is close in temperature to the dry ice that everything is stored in, in order to prevent HFA boiling. Once all the tubing and syringe is at the same temperature, the liquid HFA can be suctioned up. Immediately, the syringe is placed back under dry ice and left for 10-20 mins. If any bubbles form in the syringe, the syringe and solution are too warm and the HFA will boil off. The procedure must then be restarted.

Figure 3.12. Photographs of the dry ice storage for dispenser, tubing, canisters, solutions, and syringe.

At the point when the HFA appears stable in the syringe, i.e. no bubbles are seen, then the syringe can be quickly moved to the 3D printed case which holds the motor, this can be seen in Figure 3.13. The top, bottom and side of the solution are surrounded by dry ice, which should produce a sufficiently low gas phase temperature to prevent HFA from boiling inside the syringe. It should be noted, as the tubing attached to the syringe out lengths the 3D case, another source of suspended dry ice is needed to cool the air surrounding the tubing, which can be seen in Figure 3.13 on the left. When the solution remains stable in the 3D case, then the cooled dispenser can be attached to the metal syringe tip, which is subsequently placed in the dispenser holder close to the trap. Once this point has been reached, then the motor can be switched on to push through the solution of HFA, down the tubing and to the dispenser.
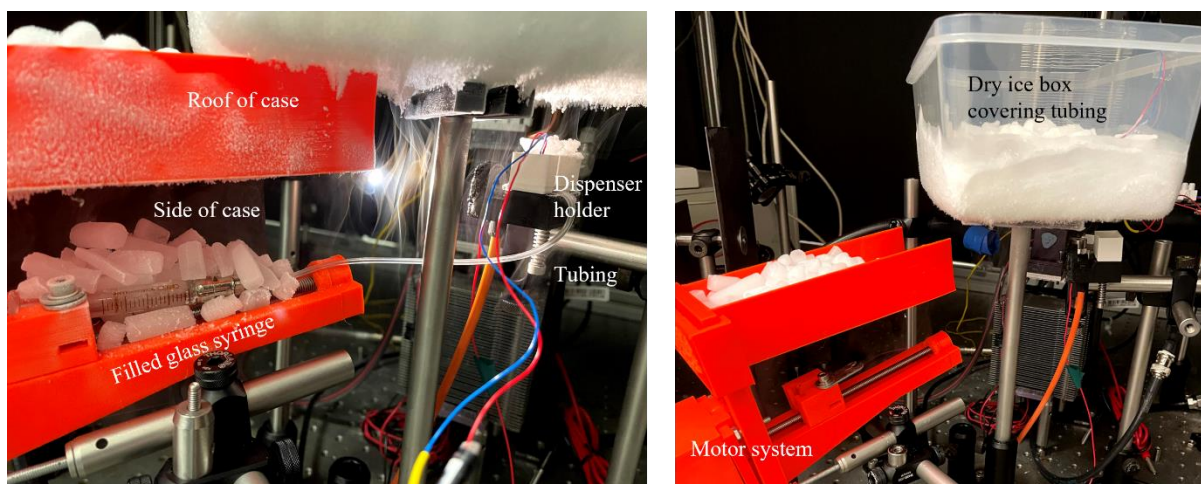
Figure 3.13. Photographs showing the glass syringe positioned in the 3D printed case, which is built around the motor and suspends dry ice above and around the solution. Capillary tubing, covered by addition dry ice, leads to the dispenser in the holder closer to the trap.

The 3D printed case in Figure 3.14 holds a stepper motor, in addition to serving as a dry ice holder. The plunger part of the syringe is locked in and, as the motor turns, it drives the plunger in, using an attached rotating screw, and pushes HFA liquid along the tubing and through the dispenser. The stepper motor (Permanent Magnet Stepper Motor, 2.8 V, 5 mm Shaft) is connected to a National Instrument (NI) NI DAQ card so that it can be controlled by the LabVIEW interface. The speed and direction of the motor can be controlled. It was found that pushing the HFA through the tubing quickly works best. Rapid transport of cooled HFA through the tubing potentially helps rapidly cool inside the tubing and prevent any HFA boiling off. Once HFA begins to spray from the dispenser tip, then the motor can be stopped. At this point the dispenser is turned on and a voltage and frequency are applied using the LabVIEW interface. As the HFA has a very low boiling point, there is no doubt that some HFA will boil off at the tip whilst the DoD is dispensing. In order to mitigate the effect this has on the pressure inside the tubing, the motor is used to apply a gentle back pressure to keep the tubing constantly filled with solution and the dispenser tip supplied with HFA.
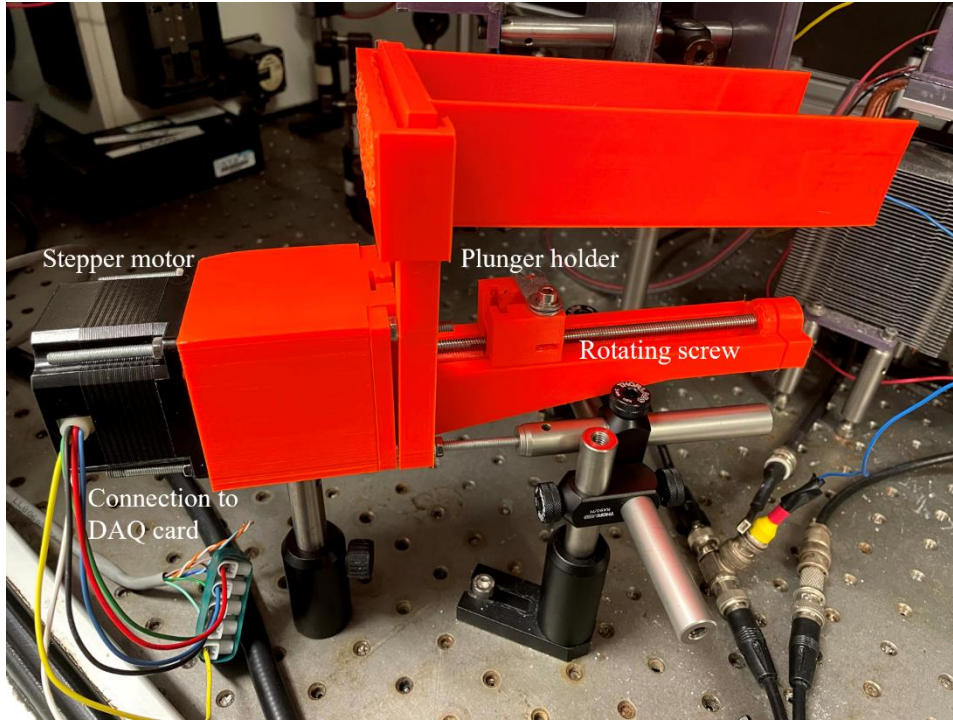
Figure 3.14. Photograph of the stepper motor used on SPLASH to supply back pressure to syringe, tubing, and dispenser.

3.5 Data Analysis

3.5.1. Determining Droplet Size

The process of estimating droplet size is the same for data collected on a CK-EDB or SPLASH. As shown in Figures 3.4 and 3.8, the green laser beam is aligned through the centre of the trapping cell so that the trapped droplet is illuminated. As the light interacts with the droplet it is refracted and reflected in and around the droplet. A scattering pattern is produced because of interaction between a droplet and laser beam and is collected in the form of a phase function. A phase function is formed from constructive and destructive interference. The elastically scattered light is collected at 45 ° over an angular range of ~ 27 ° in the forward direction using a CCD. The lenses within and connected to the camera are arranged over a distance of ~ 175 mm, with focal lengths of 25, 50 and 100 mm, so to collect the scattered light.

The wavelength of the light radiation, λ, and the particle size, r, govern the way the particle interacts with the light source. Rayleigh theory can be used to interpret scattering patterns when the particle is much smaller than the wavelength, $r < \frac{\lambda}{20}$. Mie theory can be applied to all size ranges but is the only accurate treatment when $r \sim \lambda$. However, Mie theory is computationally expensive and is usually avoided where possible. In this work the particle radius is significantly larger than the wavelength, $r > 532\ nm$, and a geometric optics approximation to Mie theory is used to interpret the scattering patterns. The scattering pattern produced by the particle from the 532 nm laser illumination takes the form of a

phase function (pf). When the particle is liquid, spherical and homogenous, the fringes are regularly spaced with an intensity that decays uniformly over the angular range, this can be seen in the top of Figure 3.15. This phase function can be used to form a plot of intensity vs scattering angle, shown in the bottom of Figure 3.15.
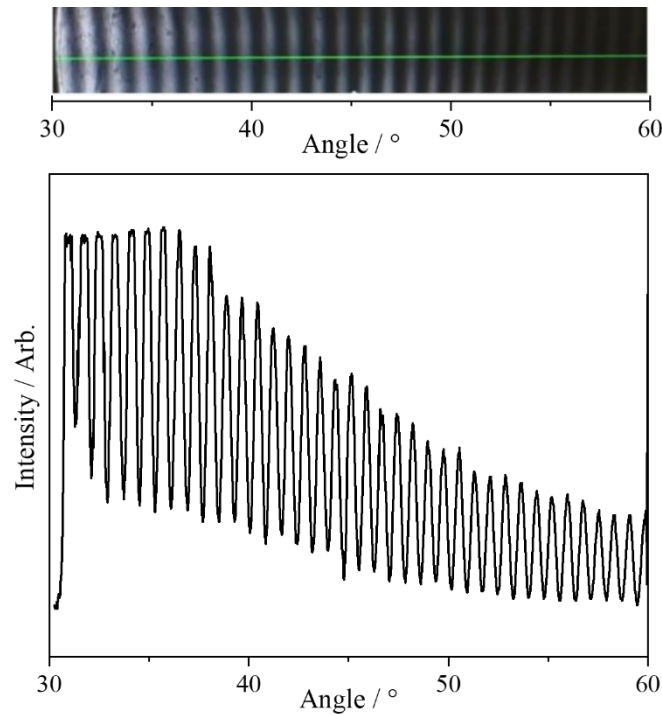
Figure 3.15. Top shows a raw phase function for a homogeneous droplet, where brightness if constructive interference and dark is destructive. Below is an intensity plot of the scattered light as a function of the collection angle, the distance between the peaks is used to calculate the droplet radius.

The geometric optics approximation can be used to estimate the droplet radius, r, in real-time with an accuracy of $\pm$ 100 nm, and is given by:

$$r = \frac{\lambda}{\Delta\vartheta} \left(\cos\left(\frac{\vartheta}{2}\right) + \frac{n\sin\left(\frac{\vartheta}{2}\right)}{\sqrt{1 + n^2 - 2\,n\cos\left(\frac{\vartheta}{2}\right)}} \right)$$

where $\Delta\vartheta$ is the angular spacing between the peaks in the scattering pattern, n is the real part of the droplet refractive index and ϑ is the central viewing angle. The radius is estimated using equation 3-5 in real time, where the refractive index is taken as that of water at 532 nm, 1.335. Thus, during subsequent refinement of the analysis the refractive index must be corrected as the droplet is not pure water. As an aqueous droplet evaporates, the concentration of the contained solute increases, causing the radius in Equation 3-5 to become more inaccurate. Additionally, the density of an aqueous droplet

increases during evaporation and this must be corrected when outputting the hygroscopic response of a substance. This is discussed further in the next two sections.

3.5.2. Parameterising the Density Solutions

An accurate parametrisation of the density (g/cm³) of an aqueous solution, of water (i) and solute (ρ_e), across the concentration range is needed to correct for the change in refractive index. The method used depends upon the bulk solubility of the solute.[106] If bulk solubility is greater than 0.4 as a mass fraction of solute (MFS), then a range of densities up to the solubility limited is collected using a density meter (Mettler, Toledo). After which, the density measurements are plotted against the square root of MFS and fitted with a 3rd order polynomial,[106] which can be used to estimate from extrapolation the pure component density at a MFS = 1.

If the bulk solubility is less than 0.4 MFS, then the pure component melt density, ρ_s, is estimated using the ideal mixing rule:

$$\frac{1}{\rho_e(1 - MFS)} = \frac{MFS}{(1 - MFS) * \rho_s} + \frac{1}{\rho_w}$$

Equation 3 - 6

where ρ_e is the density of the aqueous solution and ρ_w is the density of pure water. This equation can be interpreted simply as $y = mx + c$, where $y = \frac{1}{\rho_e(1-MFS)}$ and $x = \frac{MFS}{(1-MFS)}$, with an intercept at $\frac{1}{\rho_w}$, forming a straight line where the inverse gradient is equal to ρ_s. This method produces a much lower uncertainty than density estimations deduced from the polynomial function method, only if the solubility limit is low. An example of each density parametrisation methods are shown in Figure 3.16 for trehalose which is a common excipient used in drug formulations. The solubility of aqueous trehalose at 293 K is 0.372 MFS. Figure 3.16a shows a 3rd order polynomial function fitted to bulk data for density with respect to MFS$^{1/2}$. A 95% confidence band highlights the error associated with the extrapolation to the pure component density, ρ_s. The method presented here gives a value of $\rho_s = 1.416 \pm 0.043$, compared with a bulk value for trehalose of 1.58 g/cm³.[107]

A linear function is fitted to the bulk data in Figure 3.16b, where the uncertainty is clearly seen to be much less. The gradient of the line is 0.651 ± 0.00003, which produces a pure component density if $\rho_s = 1.654 \pm 0.00005$. The smaller error associated with this method coverts to a much smaller error in the refractive index of pure melt trehalose.
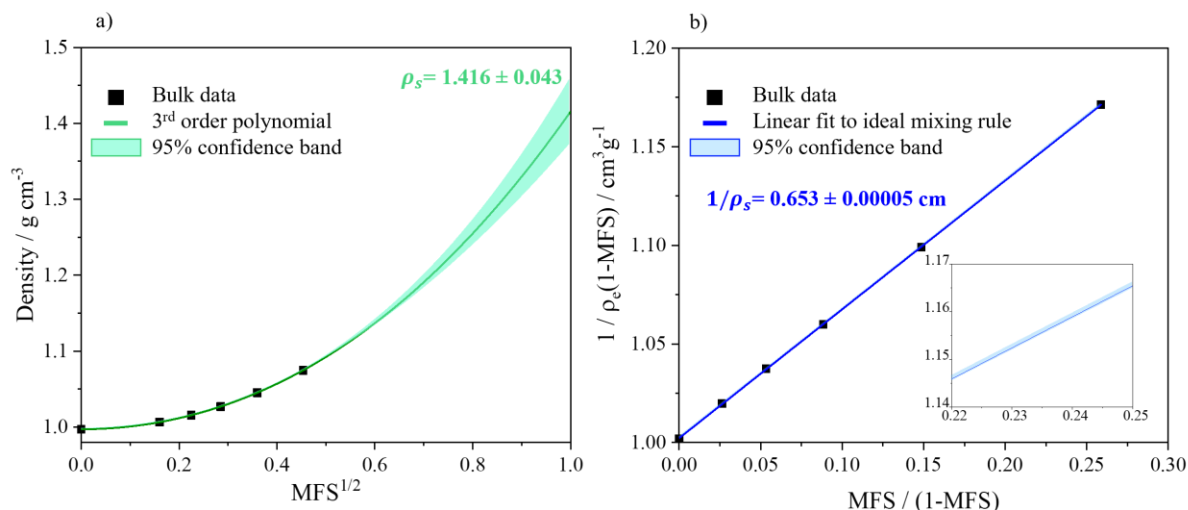
Figure 3.16. a) The bulk density of aqueous trehalose measured using a density meter. The black data points are experimental measurements, and the green line is a 3rd order polynomial fit to the data with a 95% confidence band. b) A linear fit, blue line, to the ideal mixing rule data, black points, with a 95% confidence band.

It is not possible to experimentally estimate the ρ_s of solute. However, the above values can be compared to the pure crystalline density of trehalose, 1.58 g cm^{-3}. The value calculated using the ideal mixing method is closer in value than the 3rd order polynomial method. This indicates that at low solubility, < 0.4 MFS, the polynomial method produces an underprediction of the pure component density and a value with a much larger uncertainty. Therefore, the ideal mixing method was used in this work wherever possible, which was for almost all the solutes in this thesis.[106] After density parameterisation, the refractive index can be calculated, before correcting the raw data for a change in refractive index. The refractive index of solute is calculated across the entire concentration range, followed by an in-house LabVIEW software which iterates through each time step of the experimental data.

3.5.3. Correcting Raw EDB Data for a Change in Refractive Index

The radius of a trapped droplet is estimated using equation 3-5 in real time assuming the refractive index is equal to that of water. During post analysis of the data, the refractive index can be estimated from the inferred time-dependent solute concentrations in the droplet using the molar refraction mixing rule.[106] The mixing rule is an accurate model for treating the refractive index of mixtures for a range of inorganic and organic solutes. It states that the molar refraction of a solute, R_e, is a mole fraction (x_i) weighted sum of the molar refraction of each component in the mixture. In the case of water and a solute i, it can be written as:

$$R_e = x_i R_i + x_{water} R_{water}$$

where R_i is defined as:

$$R_i = \frac{(n_i^2 - 1)M_i}{(n_i^2 + 2)\rho_i}$$

n_i is the pure component melt refractive index, M_i is the molecular weight of the substance and ρ_i is the pure component melt density. The effective refractive index of solution, n_e, can be solved using the following equation:

$$R_e = \frac{(n_e^2 - 1)M_e}{(n_e^2 + 2)\rho_{es}}$$

where M_e is the effective molecular weight, R_e is the effective molar refraction and ρ_{em} is the effective density of the solution. Equation 3-8 can be rearranged to solve for refractive index, n_e, by :

$$n_e^2 = \frac{\left(\frac{2\rho_{es}R_e}{M_e}\right) + 1}{1 - \left(\frac{\rho_{es}R_e}{M_e}\right)}$$

which leads to equation 3-10 when top and bottom of equation 3-9 are multiplied by $\frac{M_e}{\rho_{es}}$:

$$n_e = \left(\frac{2R_e + \frac{M_e}{\rho_{es}}}{\frac{M_e}{\rho_{es}} - R_e}\right)^{\frac{1}{2}}$$

This allows estimation of the refractive index of a solution of components across a concentration range. At $t = 0\ s$, the initial radius of a trapped droplet can be estimated from the raw data, $r_{0,raw}$, as well as the starting MFS. Therefore, the initial refractive index, density and mass are also known, $n_0, \rho_0\ \&\ m_0$ respectively. The initial radius is corrected using equation 3-5 and the initial refractive index, n_0, producing a corrected radius at $t = 0\ s$, $r_{0,corrected}$. At the next time step, t_1, water has either condensed or evaporated from the droplet depending on the gas phase RH, so there is a new raw radius,

$r_{1,corrected}$. Here, as the time steps are very small (typically < 0.01 s), the new mass, m_1, can be estimated using the density for the composition in the step before. Next, the MFS of t_1 can be calculated using m_1, given that any change in mass is due to a change in concentration of the solute in the aqueous droplet. The new MFS can be used to give an improved estimation of the density at t_1, which can then be used to better estimate the mass at t_1. After which, another attempt to calculate the mass change during t_1 results in a better determination of the concentration, density, and refractive index at t_1. Simply, there are two iterations to estimate the density at each time step, allowing for an accurate value of refractive index to be calculated. The radius from the raw data can then be corrected. In the case of water evaporation and with a solute that has a pure component refractive index greater than that of water, 1.335, the corrected droplet radius will increase from the raw data value. An example of raw and corrected radial data for an evaporating NaCl droplet is shown in Figure 3.17, where the initial concentration of the droplet was 0.1019 MFS. The relative humidity of the gas phase consistent with the equilibrated size can be estimated to be 73% RH at 293 K as the water evaporates the refractive index of the saline droplet increases as the MFS of droplet increases.
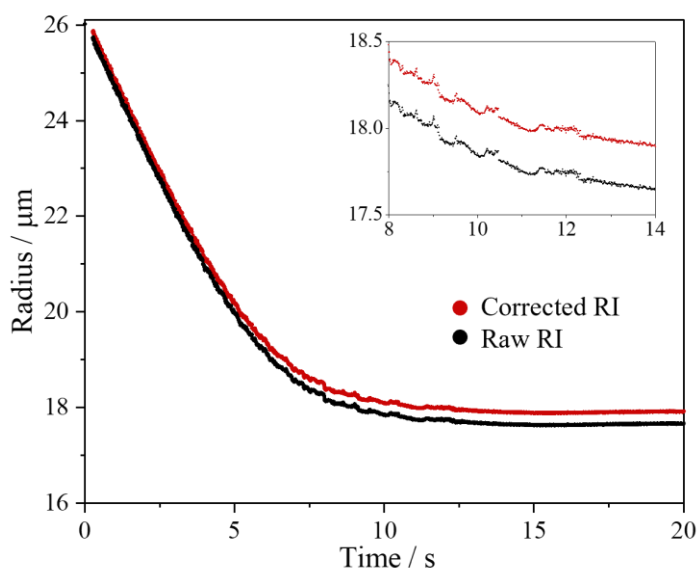
Figure 3.17. The evaporation of a sodium chloride droplet before (black) and after (red) correcting for the change in refractive index. Initial MFS of droplet is 0.1019 in 73% RH at 293 K.

3.5.4. Determining the Gas Phase RH using a Probe Droplet

Accurate retrieval of the gas phase RH is a vital step in determining the hygroscopic response of a substance. Once the RH has been accurately determined, the hygroscopic properties of a substance can be explored and is explored further in the following section. The evaporation of a probe droplet is compared to the Kulmala model, so the surrounding gas phase RH can be retrieved and paired with a

subsequent sample droplet. An any instantaneous measurement of evaporation/condensation, the mass flux can be used to determine the water activity of a droplet with radius, r:

$$I = -2\,Sh\,\pi\,r\,(S_\infty - a_w)\left(\frac{R\,T_\infty}{M\,\beta_M\,D\,p^0\,(T_\infty)\,A} + \frac{a_w\,L^2\,M}{R\,\beta_T\,K\,T_\infty^2}\right)^{-1}$$

Equation 3 - 11

Sh is the Sherwood number which represents the mass transfer coefficient and is the ratio between mass transfer by convection and mass transfer by diffusion. S_∞ is the saturation ratio of water in the gas phase (i.e., RH) and a_w is the droplet water activity. R is the ideal gas constant, T_∞ is the gas phase temperature, M is the molar mass of water, β_M is the transitional correction factor for mass, D is the mass diffusion coefficient of water vapour, $p^0\,(T_\infty)$ is the saturation vapour pressure of water at T_∞ and A is a correction for Stefan Flow. L is the latent heat of vaporisation of water, β_T is the transitional correction factor for heat and K is the thermal conductivity of the gas phase. Examples of a sodium chloride and water probe droplet evaporation measurements are shown in Figure 3.18 A simulation of the evaporation kinetics is estimated using Equation 3-11.
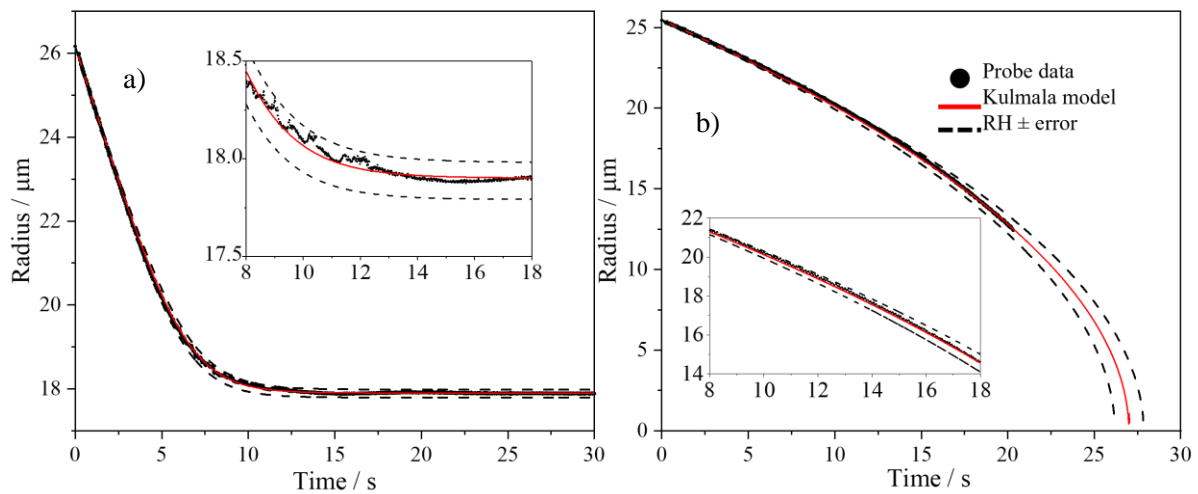
Figure 3.18. An example of a sodium chloride probe (a) and water probe droplet (b) at 293 K, with the Kulmala model, red line, fitted to calculate the RH of the gas phase. The dashed lines indicate the upper and lower error associated with the RH. The evaporation kinetics of the sodium chloride droplet are consistent with an RH of 72.8% and the water droplet an RH of 90.8%.

The above example was performed at 293 K. At 293 K at water droplet is used as the probe droplet for conditions > 80% RH and sodium chloride for an RH below 80%. The Kulmala equation accurately estimates the mass flux of a droplet evaporating under quasi-isothermal conditions, i.e., slow evaporation and a steady droplet temperature.[108] The model assumes that the droplet temperature remains close to the gas phase temperature, ± 3 K. In the case of rapid evaporation, the droplet

temperature will rapidly decrease due to the latent heat loss during liquid to vapour conversion. The mass flux can be used to estimate the droplet temperature:

$$T_{droplet} - T_{gas} = \frac{-I\,L}{4\,\pi\,\beta_T\,K\,r}$$

The Kulmala equation can only be used to simulate water droplet evaporation above 80% RH, where temperature suppression does not exceed ±3 K as per Equation 3-12. Below 80% RH results in a water droplet cooling beyond what can be accurately modelled using equation 3-11.[109] At an RH < 80%, the equilibrated size of a sodium chloride droplet is used to estimate the RH, left Figure 3.18. Determination of the RH from an equilibrated sodium chloride droplet is performed using the initial radius and MFS to calculate for the dry radius of NaCl in the droplet, r_{dry}. The radial growth factor (GF_r), which is the ratio between the wet and dry radius, can then be used to determine the RH.

$$GF_r = \frac{r_{wet}}{r_{dry}}$$

The GF_r is used alongside the E-AIM model, which accurately correlates the equilibrated size of the NaCl probe droplet with RH.[73]

An error associated with estimating the RH using a water comes from an error in the radius. There is an error association with estimating the radius using the geometric optics approximation and from the extrapolation to determine the initial radius. There has been much work that concludes that the use of a probe droplet to determine the RH in an EDB is a sound method.[110] Additionally, there are errors associated with estimating the RH from a sodium chloride probe, such as the density of saline droplets and the hygroscopic growth of NaCl across a range of RHs. These parameters are taken from the E-AIM model and previous work in the BARC group has shown a very good agreement between the model and EDB hygroscopicity measurements.[73,76] Additionally, it was found that the error in radius also contributes to an error in RH when using an NaCl probe droplet.[48] The upper and lower errors in determining the RH using a water probe are given by:[39]

$$RH_w error^+ = -((0.169 \times RH_w^2) - (0.364 \times RH) + 0.194)$$

$$RH_w error^- = (-0.02 \times RH) + 0.021$$

The upper and lower errors in determining RH when using an NaCl probe droplet are given by:

$$RH_{NaCl}error^+ = \left(-0.0199 \times RH^2_{NaCl}\right) + (0.013 \times RH) + 0.0063$$

$$RH_{NaCl}error^- = \left(-0.0266 \times RH^2_{NaCl}\right) + (0.0086 \times RH) + 0.0017$$

The dashed lines in Figure 3.18 correspond to the errors described in Equations 3 -14 to 17. For example, at an RH of 90%: $RH_w error^+ = 0.33$, $RH_w error^- = 0.3$, $RH_{NaCl} error^+ = 0.19$ and $RH_{NaCl} error^-$ = 0.12.

3.5.5. Hygroscopicity Measurements of Solutes using the CK-EDB

A comparative -kinetics technique is applied to measurements taken with an EDB and used to determine the hygroscopic properties of a compound. This technique consists of sequentially measuring the evaporation kinetics of a probe droplet followed by the sample droplet, where the probe is used to determine the RH of the gas phase. An example data set collected on a CK-EDB is shown in Figure 3.19, a similar graph is also shown in Chapter 4, with a water droplet as the probe (red) and sodium chloride as the sample (black), initial MFS 0.0571. The evaporation profile of a single sodium chloride droplet in the experiment is shown in Figure 3.20a. The parametrisation for the density of aqueous sodium chloride is used to calculate the total mass and MFS with respect to time in Figures 3.20b and 2.30c, respectively.
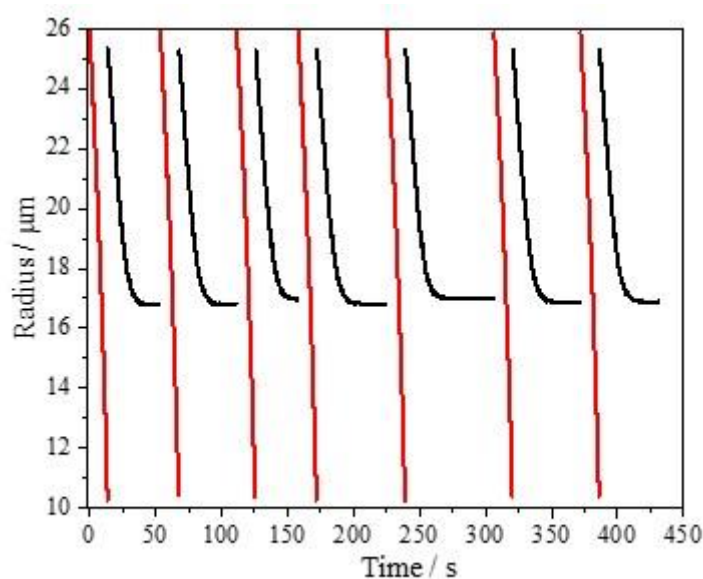
Figure 3.19. Comparative kinetic measurements taken on a CK-EDB for sodium chloride (black) using a water probe (red) to calculate the RH of each sample droplet. RH > 80%.

The mass flux of a volatile component, e.g., water in Figure 3.20d, away from the droplet surface is defined in equation 3-11, where the MFS is known throughout the experiment using the method described in section 3.5.3. The transient water activity of the droplet at a particular time can be determined by rearranging equation 3-11:

$$a_w = S_\infty - \left[\frac{I \, R \, T_\infty}{2 \, Sh \, \pi \, r \, M \, \beta_M \, D \, p^0 \, (T_\infty) A} \right] * \left[1 + \frac{I \, L^2 \, M}{K \, R \, \beta_T \, T_\infty^2} \right]^{-1}$$

Equation 3 - 18

where the gas phase RH, S_∞, is estimated from the evaporation kinetics of the probe droplet. Thus, with knowledge of the gas phase RH, and mass flux of the sample droplet, the water activity, a_w, at the sample droplet surface at each time step can be calculated using equation 3-18, shown in Figure 3.20e. Then Figure 3.20c can be used alongside a_w vs time to calculate the hygroscopic response of the sample droplet, in the form MFS vs a_w which is shown in Figure 3.20f. This final figure represents the equilibrium solution behaviour determined from a kinetic evaporation measurement.
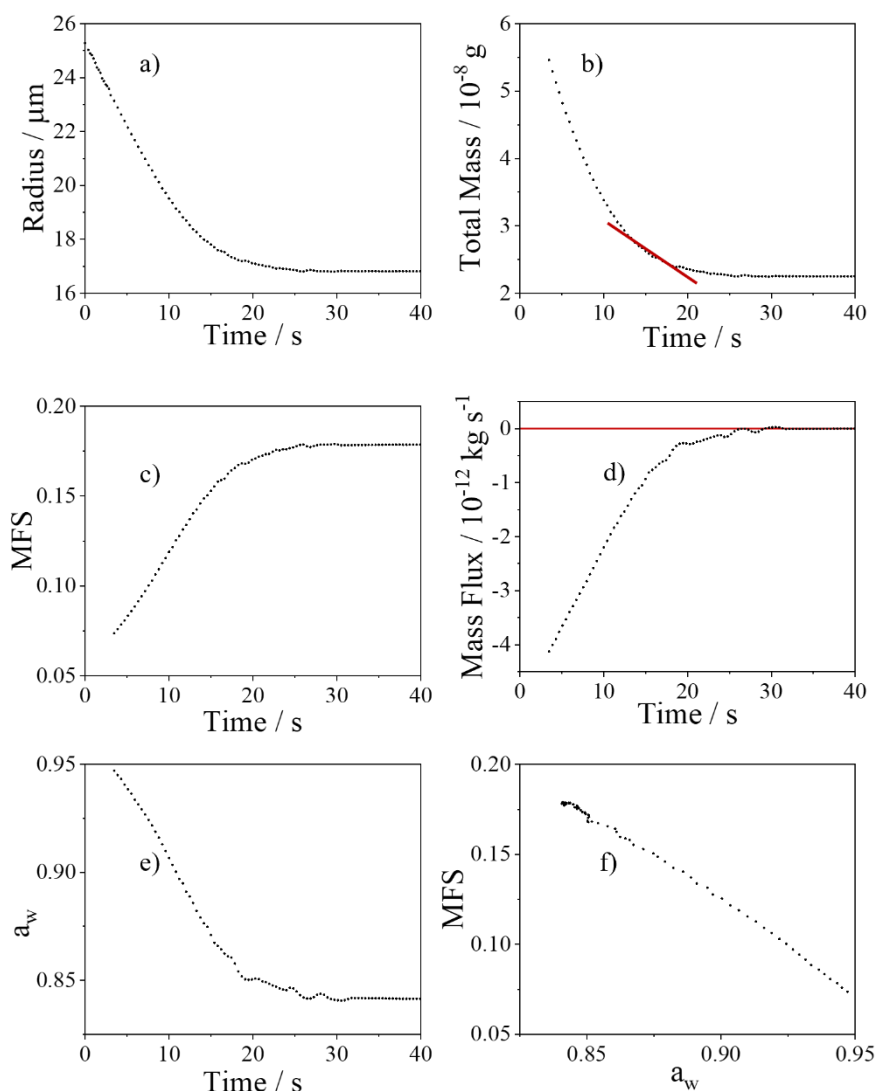
Figure 3.20. a) Evaporation profile of a sodium chloride droplet, initial MFS 0.0571, at 84.2% RH 293K. b) Mass of droplet as a function of time, gradient used to calculate mass flux in d). c) MFS during droplet evaporation. d) Change in mass of droplet, assumed to be only water evaporation, with respect to time. e) Water activity of droplet calculated from d). f) The hygroscopic response of the sodium chloride droplet.

The droplet temperature is estimated using equation 3-12. During aqueous droplet evaporation, the temperature is lower than that of the gas phase. After some time, as the mass and evaporative heat flux decrease, the temperature of the droplet reaches that of the gas phase. In the example data set presented in Figure 3.20 it was not necessary to remove any data points, as none fell beyond the $\Delta K > 3$ criteria, Figure 3.21 shows that the largest difference in temperature was -1.4 K. It is common, during rapid evaporation, that a sample droplet experiences a temperature suppression beyond 3 K, in this case any data points in that region are discarded. This approach has been extensively validated and tested in previous work.[39]
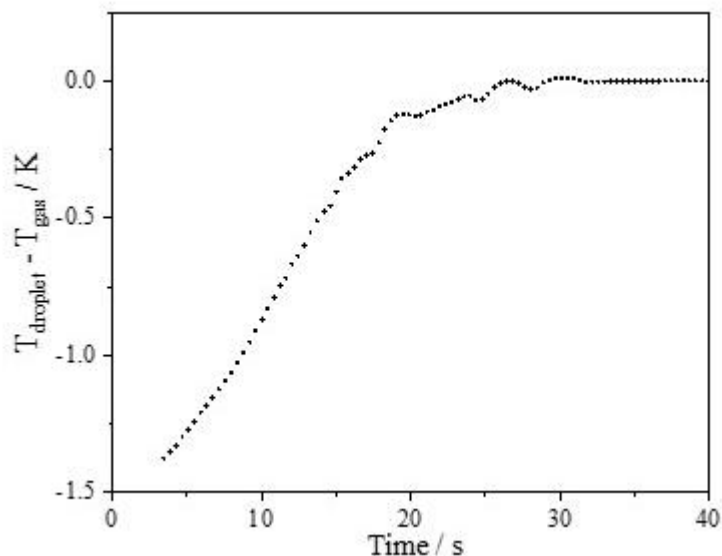
Figure 3.21. Difference in temperature for between sample droplet and the gas phase with respect to time.

Temperature suppression that leads to discarded data points occurs due to too rapid droplet evaporation and are nearly always at the early times after droplet evaporation when the droplet of low MFS, high a_w, is evaporating into a low RH, low a_w. Therefore, to determine the hygroscopic response of a solute, several evaporation experiments into a range of steady RHs are required, often starting at a low MFS at a high RH and ending with a high initial MFS at a low RH. The hygroscopic response of sodium chloride from 0.5 to 0.99 water activity is shown in Figure 3.22, where the different colour data sets represent the separate experiments performed so to maintain no more than a 3 K droplet-gas phase temperature difference. Additionally, the data sets in Figure 3.22 clearly overlap, validating the procedure and supporting previous work.[39] The black line is the E-AIM model for sodium chloride,[73] which shows good agreement with the experimental data collected on the EDB.
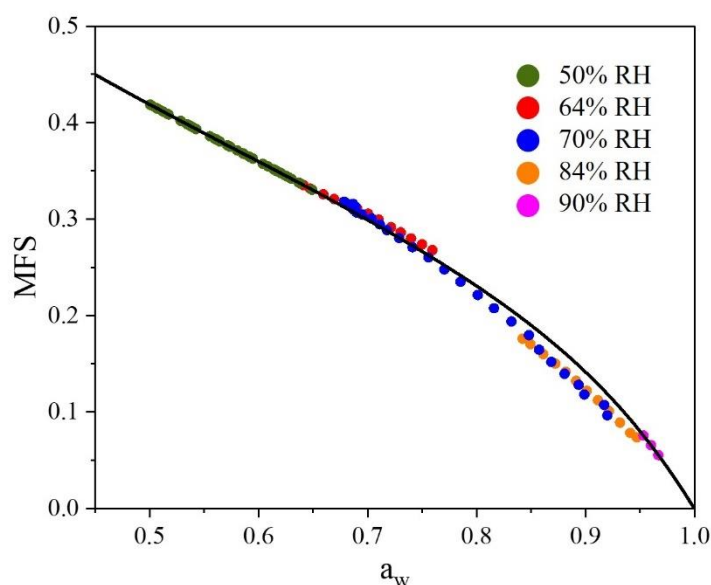
Figure 3.22. The complete hygroscopic response of sodium chloride presented using five separate datasets, collected over a range of RHs in the EDB at 293 K. Black line is model data from E-AIM.[73]

3.5.6. Determining Particle Phase State

In the above sections it is described how elastic light scattering can be used to estimate the radius of a droplet and, in addition, light scattering can be used to determine the phase state of the droplet or particle. The method of particle phase state analysis is outlined in this section and is based on the paper published by Haddrell et al.[111] The regularly spaced fringes seen in Figure 3.15 are the result of constructive and destructive light scattering as a 532nm laser interacts with a spherical, homogenous droplet. However, the particles used in the inhaled drug formulation for drug delivery to the lungs are very often not homogenous or spherical. Therefore, phase analysis is required to identify what form the aerosolised drug particles are in as they deposit on the surface of the lung. The phase state of the particle has an impact on the pharmacokinetics that follow deposition, and therefore is key to optimising drug delivery to the lung.

In the case of a non-homogenous or non-spherical droplet, the phase function can become irregular and accurate radius estimations are no longer possible. However, the characteristics of the irregular phase function, caused by the non-homogeneity of the droplet or particle, can instead be used to infer the morphology. There are four particle morphologies, shown in Figure 3.23, that can be identified by light scattering in the EDB: homogeneous sphere (a), inclusion droplet (b), crystal/non-homogenous (c) and core shell/concentration gradient (d). The morphology of a particle at each time point is inferred using the regularity of spacing between the peaks and the relative amplitude of the peaks in each phase function. Haddrell et al.[111] designed an algorithm, shown in Figure 3.24, that can differentiate between

particle morphologies based on the characteristics of the light scattering peaks. The initial condition in the algorithm is the relative standard deviation (RSD) of the spacing between the peaks in a phase function. After this, the goodness of fit of the angular variation in the amplitude of the peaks in the phase function to either a polynomial or quadratic function is considered. The order of polynomial is based on the number of peaks in the phase function; a 6th order polynomial is used when there is fewer than 18 peaks and the order is 1/3 of the number of peaks when there are more than 18 peaks in the phase function. For example, in Figure 3.23a there are 36 peaks, so a 12th order polynomial was fitted to the peaks.
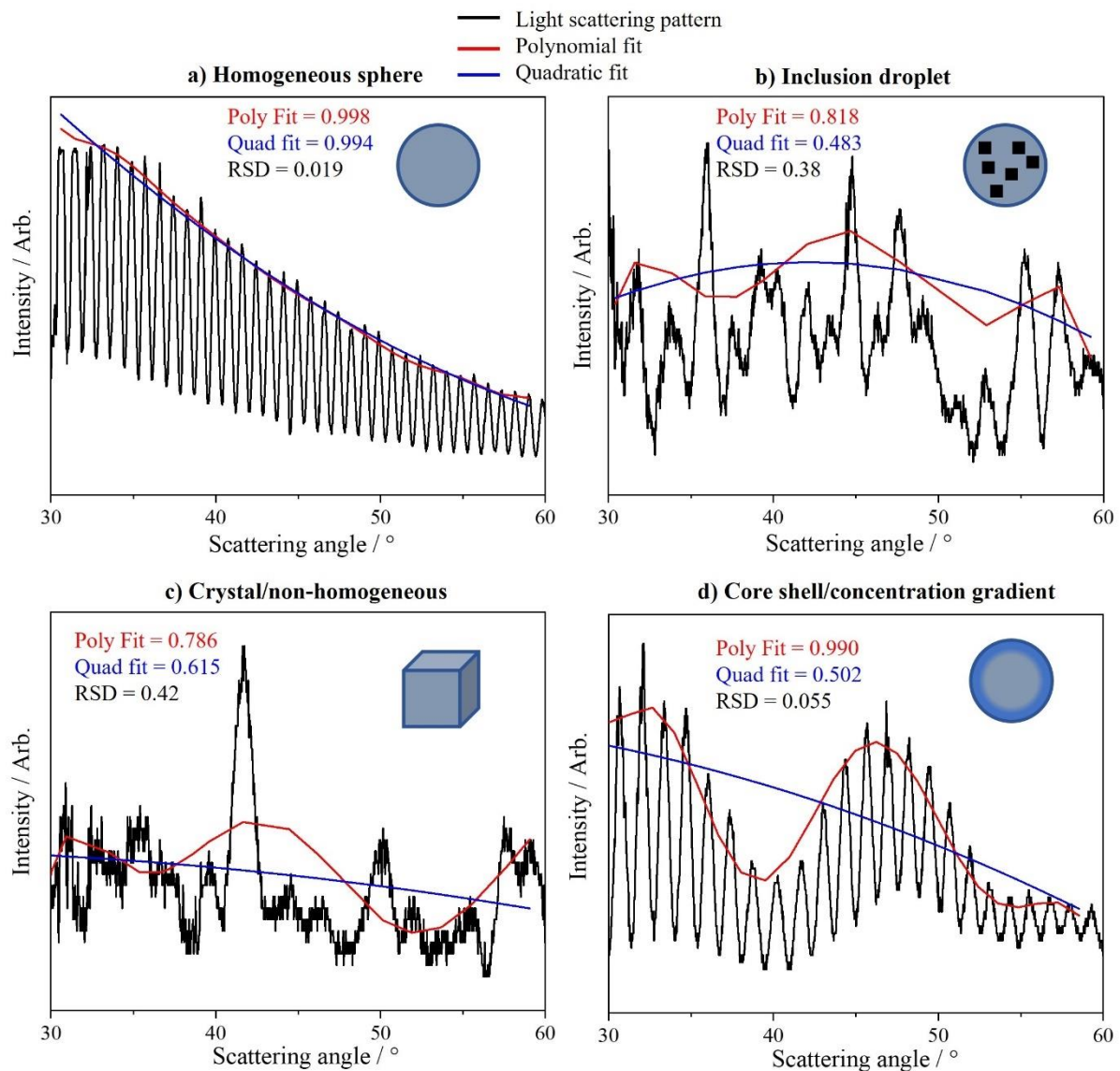
Figure 3.23. Example phase functions for four particle morphologies. a) A homogenous sodium chloride droplet. b) An inclusion phase function for a sodium chloride droplet that contains small nuclei but has not fully crystallised. c) A crystalline phase function for a sodium chloride crystal that has dried in the EDB. d) A decanol-water-ethanol droplet trapped at 50% RH in the EDB that has formed a core shell droplet.
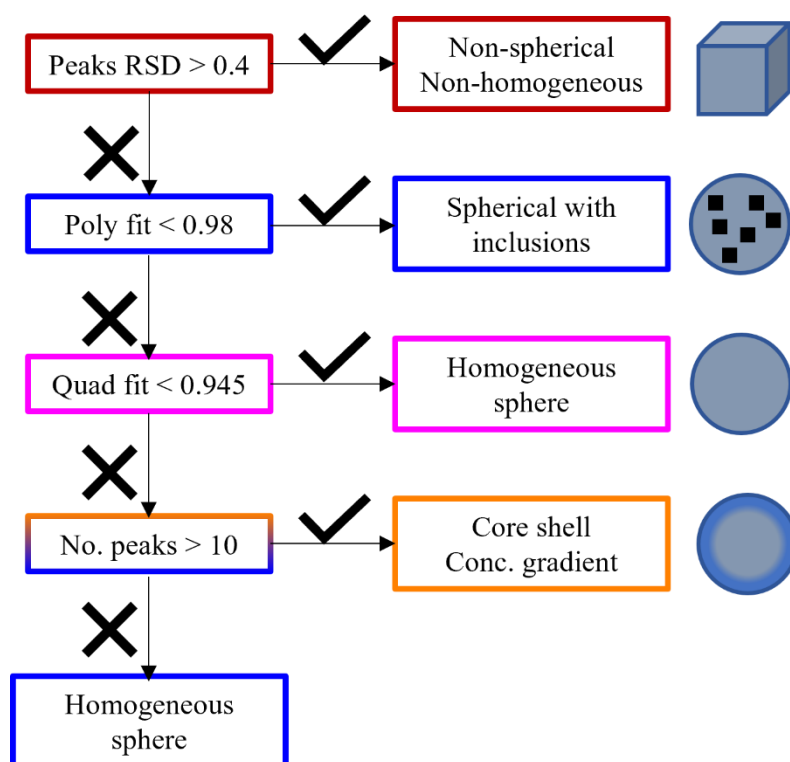
Figure 3.24. A flow chart of the algorithm used to differentiate between particle types.[111] At the top, if the given condition in the box is true then the particle is labelled as non-spherical/non-homogenous, if false then the next parameter is considered. If none are true, then the droplet is described as a homogenous sphere.

A non-spherical or non-homogenous particle is detected when RSD > 0.4.[111] However, in some of the work presented in this thesis the condition is RSD > 0.35. A lower value for the RSD can be assigned after visual analysis of the phase functions show characteristics of a crystal. If the RSD condition is false then the particle must be one of the other morphologies shown in Figure 3.24. At the next condition, if the polynomial fit is not good ($R^2 < 0.98$), then the droplet is labelled as spherical with inclusions. The phase function for an inclusion droplet is characteristically made of regular peak spacings but with significant peak-to-peak fluctuations in amplitude that are distinct from a homogenous sphere. If the polynomial fit is good then a quadratic fit is considered and this separates the remaining two morphologies, spherical homogenous and core-shell. Both homogenous and core-shell droplets have low RSD values and a good match to a polynomial fit. A spherical-homogenous droplet shows a much closer fit to a quadratic function, $R^2 < 0.945$, than a core-shell droplet. In the case of a phase function containing less than 10 peaks, corresponding to a radius of under ~ 6 μm, the droplet is assigned as homogeneous as there are not enough features present to infer the morphology. The thresholds presented here were determined by correlating fits with peak positions for over one million phase functions from experimental data, where the particle morphology was known.[111] The phase function is recorded with a high time resolution, ~ 0.01 s, to account for any background noise or droplet movement.

Additionally, the morphology label of each phase function is averaged over several data points to improve the accuracy.

3.5.7. Dissolution Measurements of Solutes using the EDB and SPLASH

Dissolution measurements for a range of pharmaceutically relevant substances were carried out on the CK-EDBs, Figure 3.4, and on SPLASH, Figure 3.8. The experimental and analytical procedures follow the same steps as those discussed above, however there are some additional stages for a dissolution measurement. Firstly, a solution droplet of known initial MFS and radius is trapped within the electric field, in this thesis the solvent is always water unless stated otherwise. The trapped droplet is subject to dry conditions, < 5% RH at 293 K, causing water evaporation and nucleation of the solute, followed by the formation of a dried particle. It should be noted that the dry gas phase RH can be higher than 5% RH and still cause crystallisation. However, the lower RH must be less than the efflorescence RH of the solute. For example, sodium chloride effloresces at 45% RH, this means from 0% to 45% RH at 293 K a sodium chloride droplet will crystallise, the effect on the final particle of different drying conditions is discussed in Chapter 7. The dry radius can be calculated with the knowledge of initial MFS and initial radius, with the assumption that the particle is spherical and homogeneous. It is assumed that the particle is not porous which, in reality, is often not the case. However, "dry radius" is a reproducible method of determining crystal size across all experimental data. As the laser beam interacts with the dried particle, the scattering becomes very erratic and estimation of droplet size is no longer possible. However, due to distinct changes in phase function characteristics, it is possible to determine the exact time step that the liquid droplet transformed to a dried particle or crystal.
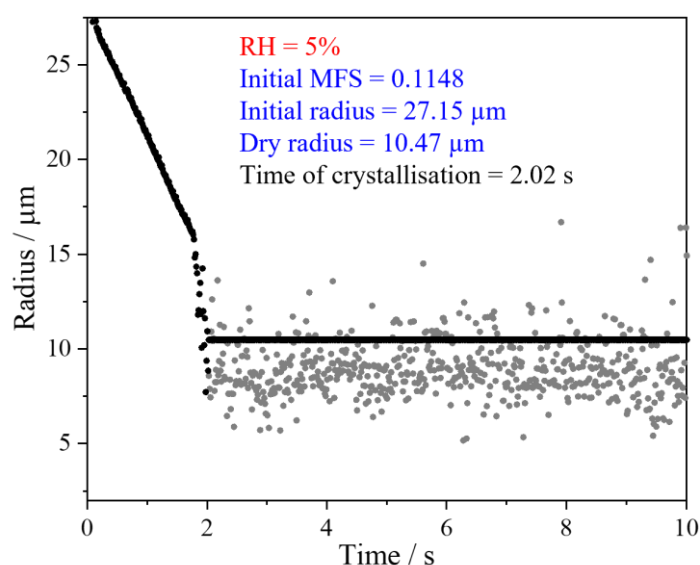
Figure 3.25. Crystallisation of a sodium chloride droplet in the EDB at 5% RH, 293 K. The dry radius can be calculated from initial radius and MFS, while crystallisation time is determined by a change in phase functions.

In the crystallisation process, the RH is set to dry air, replicating the initial stage of aerosol generation or storage in a DPI, MDI, or nebuliser. The next step of drug delivery to the lungs is inhalation, where the aerosol rapidly moves from a dry to humid environment and the same RH transition is needed within the EDB chamber. As explained earlier in this chapter, the EDBs and SPLASH used in this work are built with two gas inlets leading to the chamber. It is possible to set one gas flow to dry air, < 5% RH, and the other to humid air, > 90% RH, and instantaneously switch between the two, Figure 3.26. This allows for replication of inhalation to the lung, where the time taken for the droplet to experience the change in RH in the EDB has been shown to be ~0.2 s.[87] However, the dried particle is seen to stay crystalline for some time after the switch, indicated by the noisy data in Figure 3.26, before slowly returning to a homogenous state and finally equilibrating with the gas phase RH.
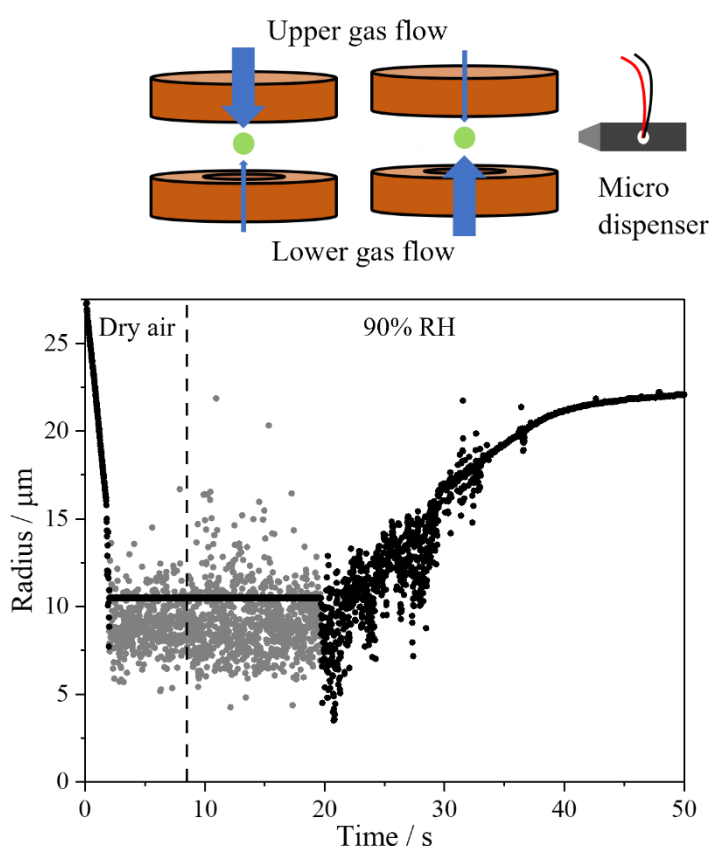
Figure 3.26. The gas flow can be switched instantaneously in the EDB to replicate inhalation, where aerosol move from low to high RH. The bottom graph is an example of a complete dissolution measurement for sodium chloride, where the dashed line indicates where the gas flow has switched from dry to wet.

To better understand the dissolution dynamics of a substance, a thorough analytical procedure was introduced, which infers the time taken for a dried particle to fully dissolve and highlights the phase transitions throughout the process. A phase analysis LabVIEW programme, which uses the algorithm described in Figure 3.24, was heavily used throughout this work to quantitatively compare dissolution dynamics of various substances in a range of environmental conditions. Figure 3.27 shows an

experimental dissolution profile for sodium chloride, where the dashed line indicates the switch from dry to wet RH. The RSD, polynomial and quadratic fit of the amplitude and spacing of the peaks in the phase function are all used in accordance with the algorithm in Figure 3.24 to infer when the particle transitions from crystal to homogenous droplet. The exact time of each phase transition is known, and therefore can be used to accurately determine the dissolution dynamics of that substance in those environmental conditions. In the example given in Figure 3.27, the sodium chloride crystal takes 28.5 s to fully dissolve after the RH switch. This procedure was performed for many substances, where factors such as crystal size, crystal morphology, upper RH, lower RH and solvent were varied to determine their influence of the dissolution dynamics.
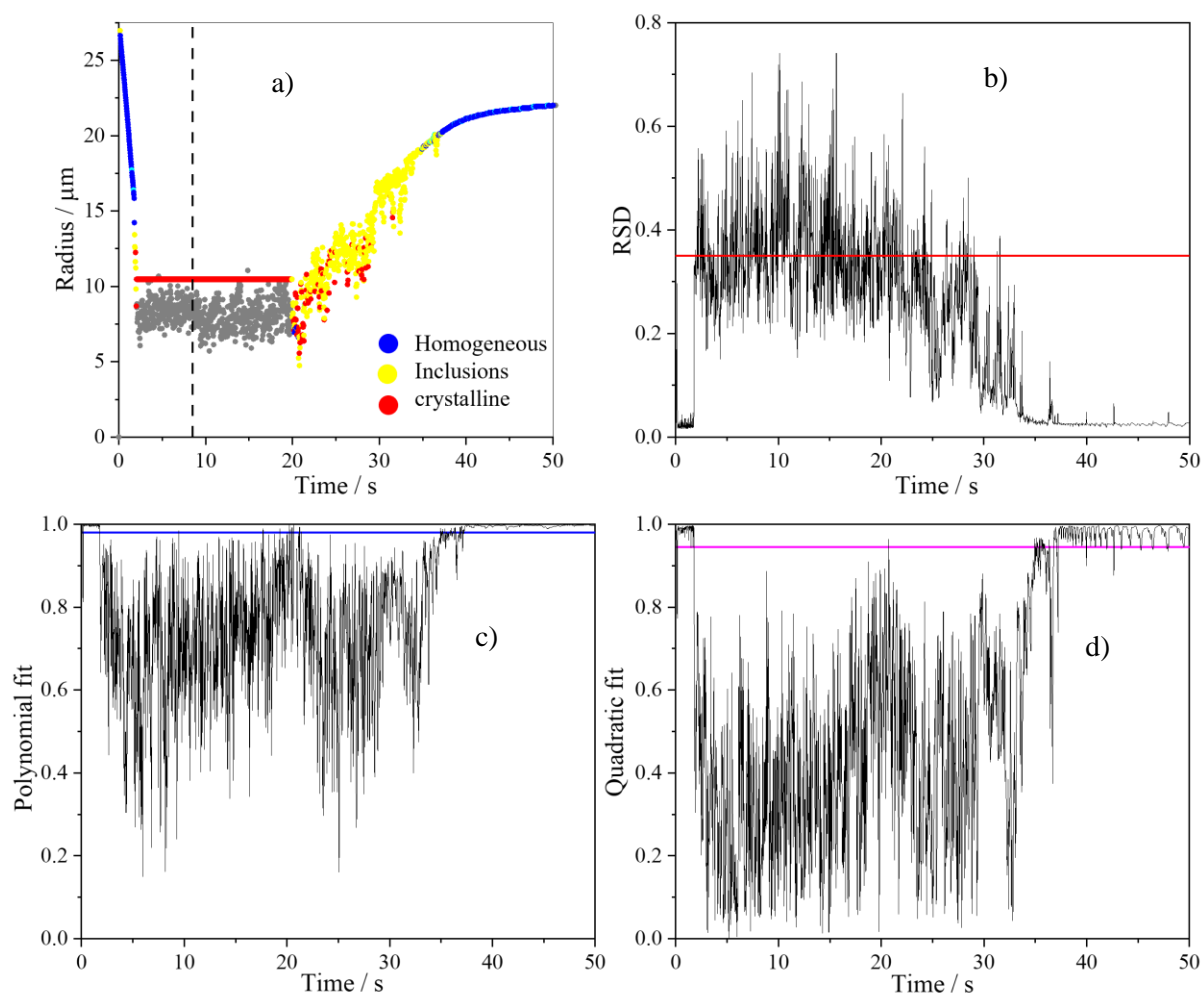
Figure 3.27. Phase analysis for a sodium chloride dissolution experiment performed on an EDB (a), where the RSD (b), polynomial fit (c) and quadratic fit (d) of the amplitude of the peaks in the phase functions are analysed to determine the particle morphology; homogeneous (blue), inclusion (yellow) or crystalline (red). The algorithm used is described in Figure 3.24.[111]

3.5.8. Determining Changes in Particle Mass

The mass of a spherical, homogenous particle can be calculated using methods described above, where accurate knowledge of the radius is available. However, in the case of non-homogenous or non-spherical particles it is not possible to determine the radius as the elastically scattered light produces erratic phase functions, such as those in Figures 3.23 b, c & d. An alternative method can be applied to these particles where the DC voltage and mass relationship is used.[102] This method was used during dissolution experiments after the switch to a high RH. Between the time of RH switch and time that a homogenous droplet is formed, there is an intermediate inclusion phase as the crystalline solute dissolves. Here, the droplet radius cannot be determined and mass measurements can instead be used, indicating how much water has adsorbed onto the particle. The experiment starts the same way as described in the above section; a particle is trapped and dried in an EDB, and the RH is switched to wet. It is at this point that the electric field is held constant and the DC offset is set to vary accordingly to keep the droplet trapped at a fixed position in the trap. The DC offset is essentially counteracting gravity, so as the droplet increases in size, the force needed to keep it levitated also increases. The upper and lower limits of measurable particle radius on an EDB are lower when using only DC offset for trapping, compared with full electric field parameters. Therefore, the DC offset can only be used individually when the change in particle size is about ±3 µm. For example, it is not possible to use only DC offset to trap a droplet from t=0 in dry air with an initial radius of ~20 µm, the droplet would fall out immediately.

The DC offset and mass relationship is calibrated using a homogenous droplet. In Figure 3.28 a sodium chloride droplet is trapped in the EDB at about 60% RH and once stable the electric field is turned off and the DC offset is set to alternate. The mass is calculated using the initial radius, dry radius, growth factor, and density. The RH is increased to ~75%, so to ensure the size change is not too large, and the DC offset decreases to ensure the droplet remains trapped. The process of increasing and decreasing the RH is repeated to ensure that the DC offset is not presenting any lag. The data points from an increase and subsequent decrease can be seen to overlap in Figure 3.28b, indicating that the droplet is stable and an accurate relationship between the two parameters can be calculated. Once a linear relationship has been inferred, then it is possible to trap a non-spherical or non-homogeneous particle in the EDB and alternate only the DC offset to keep it trapped. The linear relationship can be applied to the non-homogenous data and a change in mass can be calculated. This method does not consider a difference in density between substances. However, as the change in size is limited it would have very little effect on the calculated mass. Additionally, this method requires that sequential particles receive a constant charge from the induction electrode and the non-homogenous droplet must be held in the same trap position as the calibrated droplet.
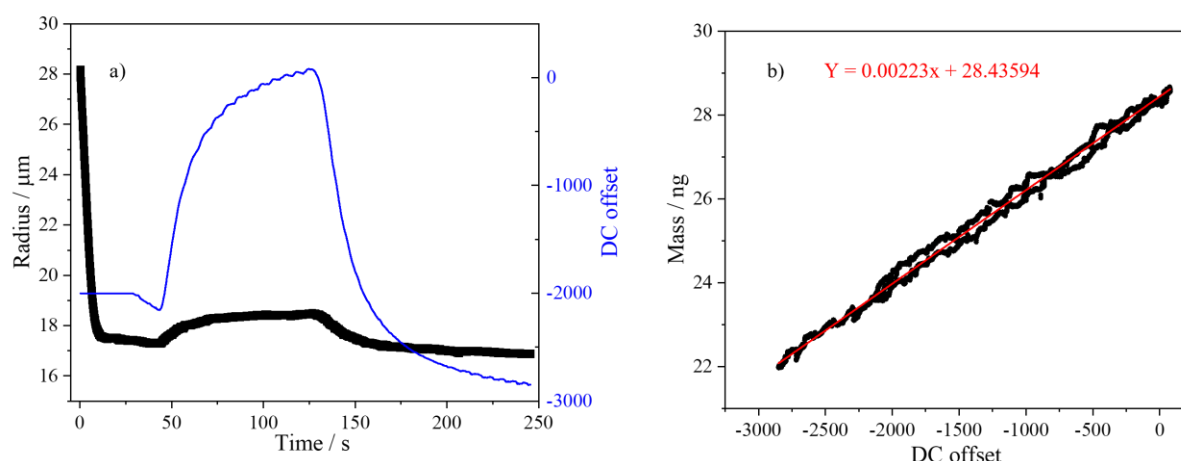
Figure 3.28. a) Radius and DC offset as a function of time for a sodium chloride droplet trapped in an EDB where the RH ranges from ~60% to 75%. b) A linear relationship between DC offset and mass to calibrate the mass change during non-homogeneous or non-spherical experiments.

Once the instrument, either SPLASH or an EDB, has been calibrated using a homogenous droplet, such as that in Figure 3.28, or a homogenous section of an experiment, then mass changes can be calculated for non-spherical or non-homogeneous data. The linear relationship can be applied to the alternating DC offset required to trap the non-homogenous particle, and a change in mass can be calculated. Initially when trapping a droplet for DC offset calibration the size dependent fields are used as the size change at the start is too large for only DC offset. For example, in Figure 3.28a the initial size change is 10 microns before the droplet becomes equilibrated with the gas phase. Once the droplet has equilibrated then the size dependent fields are turned off, which is after about 40 s in Figure 3.28a, and the DC offset is set to alternate as the RH is varied ± 15%.

3.5.9. Imaging of Samples

The phase analysis software described above is an appropriate way to differentiate between particle morphology during a dissolution experiment using light scattering. Further investigation is needed to determine the reasons behind the process of dissolution and why the dynamics vary so much between compounds and the surrounding environmental conditions. Therefore, imaging of the particles was carried out to allow for further exploration on the morphology and structure of the particles. The CK-EDBs and SPLASH do not have the capabilities to trap and then collect a particle. However, there are two other instruments in the BARC laboratory, CELEBS and the falling droplet column (FDC). CELEBS has been discussed earlier in section 3.2 and a detailed description can be found in the literatre.[66] The FDC is a new instrument that has been developed and is based on work by Vehring and Baldelli.[55,54] The FDC was used to collect samples of particles under the same conditions as the CK-EDB work. It is a glass column, square in cross-section, standing ~50 cm tall. The same micro dispenser used on the CK-EDB was used here, and the initial sizes of droplets were consistent with CK-EDB

measurements. Environmental conditions were consistent between both instruments; the temperature remained at 293K and the RH could be set to either dry (0%) or ambient (~45%). The RH was measured using a probe that was placed at the bottom of the column and was controlled using only a dry air flow, which was either on or off: 0% or 45%. The droplets fell through the column and deposited on a glass slide, which was kept in a desiccator before electron microscopy.

CELEBS was also used to collect dried samples. However, it is possible on CELEBS to control environmental conditions and trap a droplet up to 85% RH. The collected particles must be dry before imaging as liquid droplets burst under electron imaging. Many of the substances forming the dried particles that were collected for imaging are very insoluble and it was common that they would produce a dry particle despite being trapped at such a high RH. A salt such as sodium chloride however would form a liquid droplet which could not be imaged. Once the dried particles had been collected, they were imaged using a scanning electron microscope (SEM, Joel IT300 SEM), using a 15 mm working distance, 15.0kV acceleration voltage and magnificent of 100-2000x. A sputter coater was used to apply a silver coating of ~15nm (sputter coater, Agar Scientific) to the particles and substrate before placing them under the microscope.

3.6   Chapter 3: Summary

The chapter has described the setup of each instrument that was used to collect experimental data for this thesis, as well as describing the analytical procedures carried out on raw data. The CK-EDB was used to elevate droplets and particles in order to determine the hygroscopic response of a substance and to investigate dissolution dynamics. CELEBS and FDC were used to collect dried particles where the environmental conditions matched those of the dissolution measurements carried on the CK-EDB, which could then be imaged using SEM. Lastly, a new EDB named SPLASH was designed, developed, and used to explore how particles and droplets react to a supersaturated gas phase.

Chapter 4

The Equilibrium Hygroscopicity of Pharmaceutically Relevant Components for Inhalation

4.1　Hygroscopicity and Drug Delivery to the Lungs

The inhalation of aerosolised drug formulations has become a well-established route for treating a range of respiratory and systemic diseases such as asthma and diabetes. The drug deposits in the lung or respiratory tract, where there is a large surface area and full cardiovascular output offering effective delivery. The deposition mechanism, which is influenced by the aerosol size, governs where in the lung the drug is deposited. The preferred site of delivery is different depending on the disease being treated, thus the aerosol must be of appropriate size to ensure the highest deposition fraction at the target site. Despite the dependence of deposition fraction and location on particle size, the physico-chemical processes governing the dynamic size change of the aerosol between generation and inhalation are poorly understood.[112] In this work, an electrodynamic balance (EDB) was used to explore the dynamic size change of single particles as the relative humidity (RH) in the surrounding gas phase varied. Hygroscopic curves for a selection of compounds that are commonly used in drug formulations were produced. These studies provide important insights into factors that govern the capacity and dynamics of hygroscopic growth, influencing where aerosol deposits in the lung.

The deposition fraction of aerosol in the lungs is a function of the radius of the droplet. Therefore it is important to understand the rate and magnitude of the mass flux of water to the droplet during inhalation to understand the dynamic changes in size that influence the deposition pattern.[113] There are many models that predict the deposition fraction of aerosol as a function of the initial aerosol size, where the aerosol has been targeted to a specific region of the lung.[114,115] It is extremely difficult to include all variables effecting the deposition fraction. Often models simplify the inhalation process and overlook key processes, such as hygroscopicity. Additional biological and physical factors increase the complexity of drug efficacy, e.g. patient breathing patterns and the aerosol deposition mechanism, respectively.[116] Additionally, the influence of pre-inhalation environmental conditions on the aerosol is not included when modelling the deposition pattern, and the hygroscopic properties of a compound are absent from many models, where the hygroscopic growth of a compound is determined by its chemical composition.

The size of the aerosol particles in their surrounding environment is dynamic and governed by the RH in the gas phase and the imbalance between the water activity in the droplet and the RH. The absolute

size change is dependent on the chemical composition of the droplet and the difference in RHs that the aerosol transitions between during generation and inhalation.[117] The radial growth factor (RGF) reported as a function of water activity for sodium chloride is shown in Figure 4.1a, where a water activity of 1 is equivalent to an RH of 100%. The mass and heat flux govern the time taken for an aerosol particle to reach equilibrium with the gas phase. In Figure 4.1b the final RH for equilibration is 80%, and the droplet reaches equilibrium within 4 s, for each initial RH. Whereas, at an upper RH of 95%, Figure 4.1c & d, the time taken for the aerosol to reach equilibrium is significantly longer, ~30 s, as the droplet reaches a larger final radius. It is important to understand the thermodynamic properties of an aerosol, influencing the rate of change. As well as the kinetic processes, influencing the magnitude of change.

Aerosolised drug formulations are exposed to a sudden change in RH during inhalation. When using a dry powder inhaler (DPI) aerosol are exposed to an ambient RH initially (~45% RH), followed by a very wet environment as aerosol enters the humid lung (>99% RH). A rapid change in water concentration in the gas phase, results in a rapid change in droplet radius.[118] In ambient conditions, the concentration and size of the aerosol are controlled by the water activity in the gas phase. Water vapour availability influences the ability for the droplet to take up water once inhaled. In Figure 4.1e the droplet is initially at 50% RH before increasing in radius when introduced to an environment to 80%. In Figure 4.1f the aerosol initially experiences an RH of 70%. At a lower starting RH, the aerosol has a greater capacity to absorb water. Thus, the droplet experiences a larger change in radius, compared with a droplet of the same initial radius with a higher initial RH. The time taken for a droplet to reach its final radius is dependent on the initial radius.
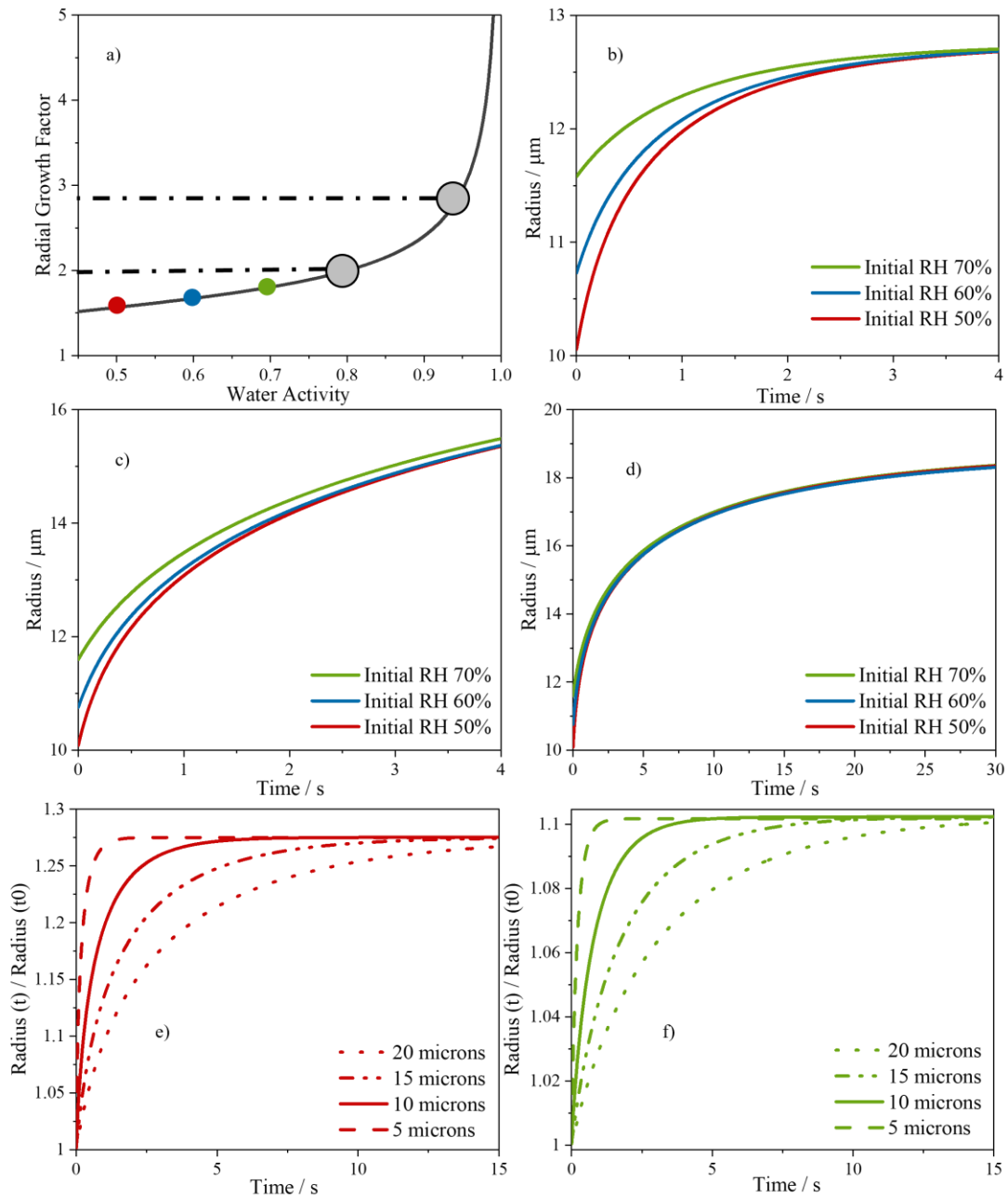
Figure 4.1. a) Hygroscopic growth curve of NaCl represented using radial growth factor. b) Droplet growth for a dried particle of radius 6.38 µm, at starting RHs of 50%, 60% and 70%. All equilibrating at 80% RH and growth shown by the difference between coloured dots and first dashed line in a. c & d) Droplet growth for particles of same dried radius as a) and same starting RHs, all equilibrating at 95% RH, growth shown by the second dashed line, time taken to reach equilibration is 30 s vs 4 s in b. e & f) The relative growth of NaCl aerosol of various initial radii, equilibrating at 80%RH , with starting RHs of 50% and 70% RH, respectively.

Dynamic size change of an aerosol is influenced by its hygroscopic properties, along with other characteristics such as morphology and chemical composition. The mechanisms of aerosol deposition

onto the lung surface are described in Figure 4.2. Particles > 2.5 µm in radius will impact on to the surface, sedimentation occurs for particles > 0.5µm and for small particles, <0.1 µm, the observed deposition mechanism is diffusion.[119] Additionally, large, particles with high inertia are likely to deposit via impaction in the upper respiratory tract. The upper and lower lung is often the desired target site for treating respiratory diseases. Conversely, small particles are likely to travel to the deep regions of lung, alveoli, which is the chosen deposition site when administering drugs for systemic circulation. A figure of the deposition fraction as a function of particle size is shown in Figure 4.2 and described thoroughly in Section 1.1.3, where it is explained that particles of 300 nm have the lowest deposition in all regions of the lung.
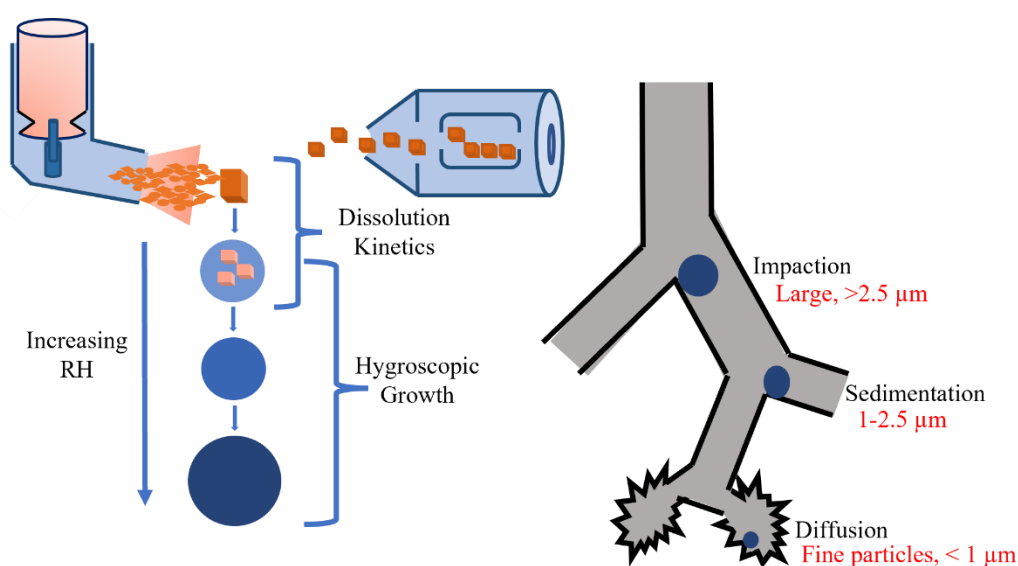
Figure 4.2. A schematic of particle deposition dynamics during drug delivery to the lungs using a metered dose inhaler (MDI), left, and a dry powder inhaler (DPI), right.

Initially, water adsorbs onto inhaled dry aerosol resulting in dissolution. This is followed by hygroscopic growth once an aqueous droplet has formed. Prior to deposition the phase state of the aerosol is governed by the initial phase state of the drug mixture. For example, aerosol generated from an MDI, DPI, or nebuliser, and the subsequent dissolution kinetics, the first stage shown in Figure 4.2. Dissolution kinetics will be discussed in detail in Chapters 5 & 6. In the case of a DPI, the patient actuates the device with a breath and inhales a cloud of dry particles. At this point the dried aerosol migrate from ambient to very wet conditions. A steady inhalation is considered to be at a rate of 6.0 L/min (inhalation of 10 times/min, and a volume of 0.6 L per inhalation), where a single breathing cycle lasts for ~6.0 s and the average value for one breath cycle is 14.4 L/min.[120] These values are heavily dependent on gender, age, weight, height and most importantly, the impact of any respiratory health conditions.[114] However, for the purpose of discussion throughout this thesis, it will be assumed that an average breathing cycle lasts for 6.0 s, unless stated otherwise. The deposition fraction of inhaled aerosol is time dependent, and the dissolution kinetics of dried particles vary in time between substances.

Upon complete dissolution, hygroscopic growth (second stage in Figure 4.2) governs the particle size. The time taken for a droplet to reach an equilibrated size is influenced by the initial droplet size and final RH and may not be reached depending on the deposition timescale. For example, if a patient inhales a cloud of dried particles, where the active pharmaceutical ingredient (API) requires 9 s to fully dissolve in the aerosol phase, then upon deposition the API will be non-homogenous. The particle phase state will affect the pharmacokinetics that follow deposition and are influenced by the bulk dissolution properties of the substance. Whereas, if an aerosol plume is inhaled using a nebuliser, where the drug mixture is formed into aqueous droplets, then the droplets will experience hygroscopic growth prior to deposition, assuming API remains in solution. To summarise, it is vital that the time dependent processes of dissolution and hygroscopic growth are analysed in detail as this will help to better predict the deposition fraction and pattern. Indeed, it must also be recognised that different aerosol formulations and delivery devices lead to different journeys through the respiratory tract.

This chapter aims to assess the impact of aerosol hygroscopicity on deposited aerosolised drug formulations by exploring the mass flux of water and the effect it has on the dynamics of particle size. The environmental conditions prior to and during inhalation influence the deposition pattern as a result of particle size change. Relative humidity is found to have a significant impact on the deposition pattern, which is discussed fully in this chapter.[113]

4.2 Hygroscopicity Measurements using a CK-EDB

4.2.1 Representations of Hygroscopicity

There are six common ways to represent hygroscopic growth as a function of water activity or RH: Mass Fraction of Solute (MFS), a kappa parameter, RGF, Mass GF and the osmotic coefficient with respect to sqrt molality. MFS and Radial GF versus water activity were used throughout this work and will be discussed in further detail in this section, while the other methods of representation will be briefly explained here.

Kappa, κ, was first introduced by Petters and Kreidenweis, allowing the representation of the hygroscopicity of an aerosol by a single parameter that can vary between 0.1 for non-hygroscopic species and 1.4 for very hygroscopic species, such as inorganic salts.[121] The intended purpose of κ was to aid with aerosol hygroscopicity data applied to atmospheric models covering complex regional and global areas. The Mass GF is the ratio between the wet droplet mass and the dry particle mass. It is used for applications that directly measure droplet mass rather than droplet diameter. At a low water activity, the Mass GF will tend to a value of 1. Experimental N_{water} divided by N_{solute} is a similar way to

represent hygroscopicity to Mass GF, however when plotted as a log function, it minimises the effect that data tending a value of 1 has on the ability to visualise the data accurately.

Figure 4.3 shows RGF on the right y-axis and MFS on the left y-axis for sodium chloride, both as a function of water activity, where 100% RH is equivalent to a water activity of 1. These are both commonly used in literature when discussing aerosol dynamics during drug delivery to the lung. The efficiency of drug delivery to the lung is fundamentally dependent on the amount of dose that the patient receives and is best represented by mass fraction of solute. MFS as a function of water activity is comparable between compounds. The MFS of a compound equals 1 at a water activity of 0 and the MFS equals 0 at a water activity of 1. Values of MFS can be directly compared to other data sets. The MFS of solute A is described by equation 4.1, where m_A is the mass of solute and m_B is the mass of solvent.

$$MFS\,(A) = \frac{m_A}{m_A + m_B}$$

The radial growth factor is denoted in equation 4-2 by the ratio between the wet droplet radius (or diameter) and dry particle radius, where the dried particle size is a theoretical spherical equivalent radius equivalent to the true volume of the particle. In our EDB measurements, we can estimate it from the starting concentration and radius of the droplet. RGF is often used as the single particle instruments used in this work measure particle size by its radius. A pure component density is used to calculate the dry droplet size. Additionally, as explained in Section 4.1, Figure 4.2, aerosol deposition is dependent on particle size, thus best represented by the radial growth factor variable. A more hygroscopic component will have a higher radial growth factor at a set water activity, than a less hygroscopic component which is able to hold onto less water molecules.

$$GF_r = \frac{wet_r}{dry_r}$$
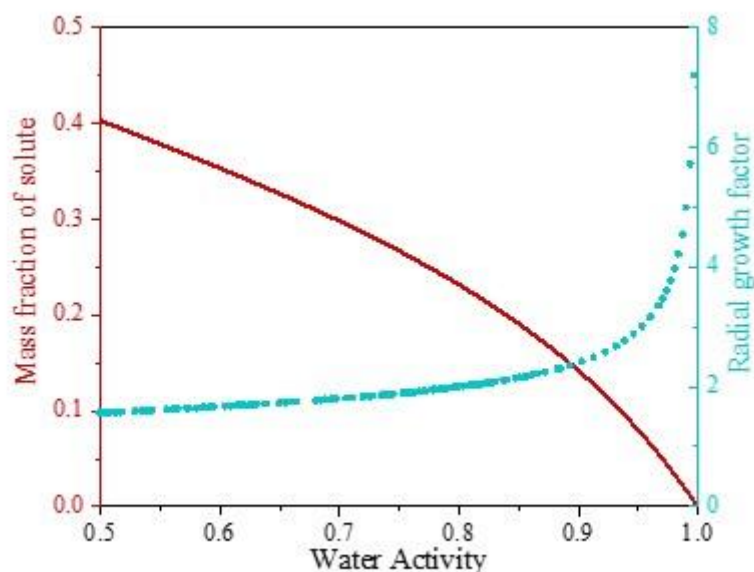
Figure 4.3 A plot showing two common ways of representing hygroscopic growth of sodium chloride. Turquoise – radial growth factor, red – mass fraction of solute, where both curves are a function of water activity and tend to one as water activity tends to zero.

4.2.2 Comparative Kinetics Measurements

Hygroscopic measurements of a compound require accurate determination of the RH that the sample droplets are exposed to. It is possible to measure the RH of the chamber using a probe, such as Vaisala, UPSI or Honeywell, however there is significant error associated with such probes. This error arises from the accuracy in the reported RH, the time taken to respond to a change in RH and the minimum and maximum limits of the probe. Most importantly, the accuracy of reported RH commonly ranges from ±1 to ±5% between 10 and 90% RH and worsens at RHs greater than 90%. To determine the hygroscopic response of a new substance, a more accurate method of determining the RH is provided by the Comparative Kinetics procedure by J F Davies during his PhD.[40] It will briefly be described here.

The comparative kinetics method is described in Chapter 3 of this thesis. The CK-EDB consists of two droplet dispensers, which send droplets into the chamber one after another. Figure 4.4 shows an example dataset of the probe-sample approach, where each water droplet was used to determine the RH for each sample droplet, in this case, sodium chloride.
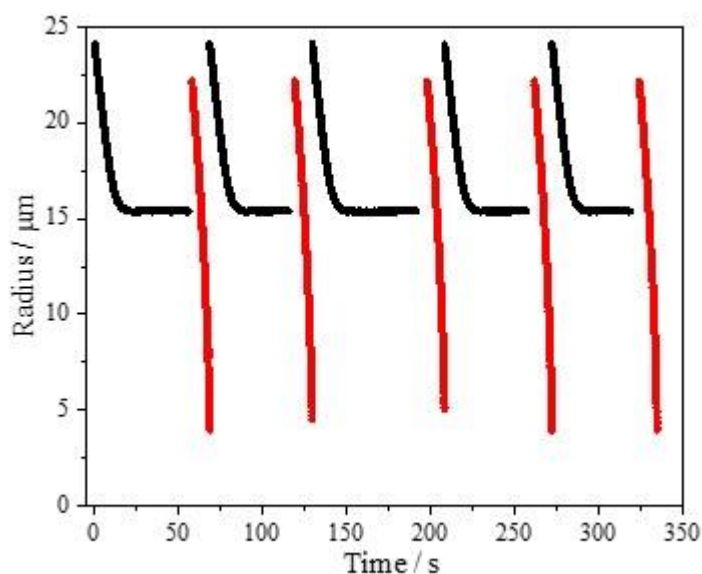
Figure 4.4. Comparative kinetic measurements taken on a CK-EDB for sodium chloride (black) using a water probe (red) to calculate the RH of each sample droplet. RH > 80%.

The hygroscopicity of a range of aerosol is discussed, including that of active pharmaceutical ingredients (APIs) and drug delivery excipients, where their mass flux kinetics are compared to that of the probe to produce hygroscopic growth curves, presented as RGF or MFS with respect to water activity.

4.2.3   Viscosity as a Potential Source of Error in Hygroscopic Response

This section explores the error associated with the hygroscopic response of a substance due to an increase in viscosity within an evaporating droplet as the water content drops and the concentration of solutes rises. In drug delivery to the lungs, many excipients and APIs become viscous at low RHs, such as trehalose, which has a viscosity of about 10^4 Pa s at 60% RH.[87] Viscosity is a kinetically limiting property, in terms of mass flux, for water transport in many pharmaceutically relevant aerosol. An increase in viscosity impacts bulk diffusional mixing within the droplet, and thus effects the hygroscopic response of the substance.[87] Therefore, corrections to hygroscopic measurements of viscous substances must be discussed. In this work, deviations from the hygroscopic curve were observed during experiments which indicated the presence of high viscosity.

The Kulmala model,[82] discussed thoroughly in Chapter 2, was used extensively in this work to analyse and simulate hygroscopic measurements. An assumption of the model is that the mass flux is only gas-phase diffusion limited, i.e., evaporation occurs in the absence of a bulk-phase limitation. Additionally, the particle is assumed to be spherical and homogenous. The hygroscopic growth curves for a) sodium

104

chloride and b) lactose monohydrate are shown in Figure 4.5. Aqueous sodium chloride is a non-viscous, solution which remains as a liquid droplet down to 0.45 aw, meeting the requirements of the Kulmala model and so can be used a probe. The data in Figure 4.5a are presented for multiple data sets, collected from 50% to 90% RH. The data show no signs of additional kinetic limitations to mass flux during droplet evaporation. Thus, the experimental hygroscopic response of sodium chloride can be modelled using the Kulmala equation .[82]The experimental data in Figure 4.5a compares well with data from the aerosol inorganic-organic mixtures function groups activity coefficients (AIOMFAC) model.

The hygroscopic response of lactose monohydrate in Figure 4.5b clearly shows signs of an additional limitation to the mass flux of water during evaporation. The data are collected in six different experiments, ranging from 50% RH to 90% RH. The values of MFS are seen to increase up to the equilibrium curve for lactose monohydrate on data below 70% RH. The high viscosity of the droplet decreases bulk phase diffusional mixing and kinetically limits the mass flux.[87] The highest MFS values of the final three lactose data sets best fit the extended aerosol thermodynamics model (E-AIM) data. The comparison between E-AIM and experimental data indicates the peaks of each data set are the true values. A kinetic limitation is also seen in the hygroscopic measurements of trehalose and benzalkonium chloride (BC) presented later in this chapter.
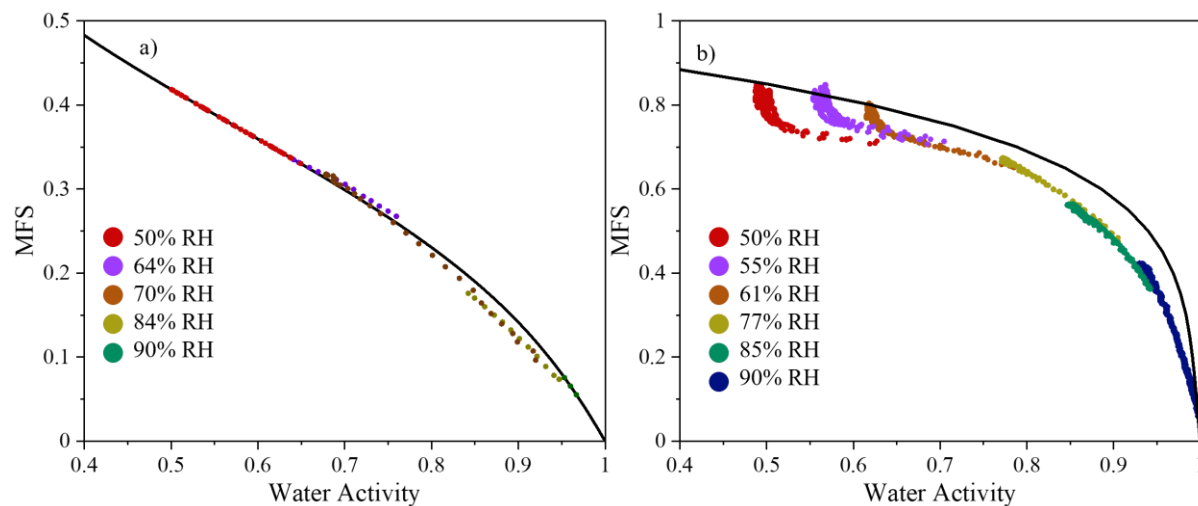
Figure 4.5. Hygroscopic growth curves for a) sodium chloride, non-viscous, and b) lactose, viscous, as a function of MFS vs water activity. Black lines are model data using E-AIM and AIOMFAC for sodium chloride and lactose, respectively.

The limitation of bulk-phase diffusion is thoroughly explained in Chapter 2, although an interpretation of the theory can be seen in Figure 4.6. Initially, it appears that both droplets, sodium chloride and lactose, have equilibrated with the gas phase at 50% RH, 293 K. However, on considering the fine changes in size that can be observed for the aqueous lactose droplet, a continuing decrease in radius is

identifiable after 30 s. The droplet retains more water than if only gas-phase diffusion limited, thus the MFS in Figure 4.5 is underestimated as the RH is lowered. In the lowest RH data sets in Figure 4.5, the MFS appears to fall below the line before. As further water is lost, the MFS increases up to the equilibrium curve. It is clear from the hygroscopic response of lactose that once the droplet is fully equilibrated then the MFS value is correct. Thus, when working with viscous compounds the intermediate hygroscopic data, i.e., when the MFS is underestimated, are ignored. Instead, only the final data points of the droplet evaporation profile are used. Additionally, each droplet data set can be used to identify the time at which the radius is no longer decreasing.
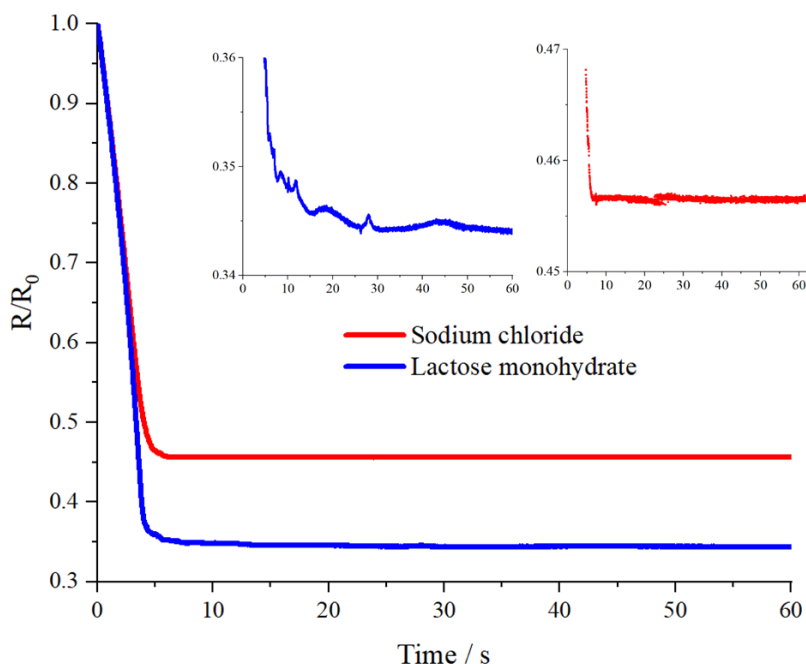
Figure 4.6. Evaporation of ~25 µm radius, 0.05 mass fraction lactose monohydrate and sodium chloride droplets at 52.5% RH, plotting radius over initial radius (R/R0) versus time. At low RHs, lactose monohydrate becomes viscous and water evaporation is bulk-phase diffusion limited.

It is possible to use the Stokes-Einstein equation, Equation 2-48, to determine the relationship between diffusion and viscosity. Subsequently, the diffusional mixing time can be calculated using Equation 2-49 after determining the diffusion coefficient from Stoke-Einstein. Parameterisations for a range of systems as a function of RH from Song et al.[50] were used to determine the length of time that each droplet must be levitated for to ensure water activity equilibration.

It should be noted that there is an additional source of error associated with the molar refraction mixing rule, which is used to parameterise the density and correct for the refractive index of an evaporating droplet. The error can lead to an under or over estimation of the droplet radius during the first stage of hygroscopic analysis. However, extensive work by Marsh et al. found that the error to be so small that it falls within the RH error of the CK-EDB.[48] Therefore, error of the molar refraction rule is not considered in this thesis.

4.3   Hygroscopicity of Binary Aqueous Aerosol

The deposition fraction of an inhaled aerosol in the lung is dependent on the aerosol radius.[92] Thus, a detailed understanding of droplet size dynamics is needed to predict and control where a droplet will deposit. The desired location of the drug is dependent on the disease being treated – respiratory or system circulatory.[95] Thus, improving the reproducibility of targeted site delivery will improve the efficiency and efficacy of administering drugs via oral inhalation.

In this section, the hygroscopicity of a range of excipients and APIs used in drug delivery to the lungs is explored. Additionally, the experimental measurements are compared with predictions from the AIOMFAC model, where possible. All experimental measurements were carried out on a CK-EDB, and the data were analysed using the LabVIEW programme outlined in Chapter 3. Due to the dependence of particle deposition on particle size, the hygroscopic response of substances will be presented using RGF rather than MFS. The RGF is defined as the ratio of wet to dry particle radius.

4.3.1   Hygroscopicity of Excipients used in Drug Delivery to the Lungs

The CK-EDB has already been used and validated for use in the hygroscopic measurements of inorganic salts[39] and sugars[104,110]. In this chapter hygroscopic measurements of additional components will be presented and compared with model data. The CK-EDB approach and corresponding AIOMFAC model are not always in agreement for complex compounds with little literature data. However, the CK-EDB has been validated and is a robust approach for determining the hygroscopic response of a new compound. This section explores the hygroscopic response of compounds used in SMI/nebuliser, DPI and MDI formulations.

Hygroscopicity of Pharmaceutical Salts in SMI and Nebuliser Formulations

A selection of salts, sugars and non-volatile compounds were chosen due to their role in nebulisers and SMIs formulations. Sodium chloride is a well understood compound within the literature. There have been many publications on the physicochemical properties of NaCl, such as hygroscopicity and crystallisation.[39,122] Thus, it makes a good model system, which is used throughout this project to explore poorly understood particle dynamics. Additionally, it is used in this chapter to validate the use of the CK-EDB for hygroscopic measurements on new substances. The hygroscopic response of NaCl, inferred from experimental data collected on the CK-EDB, is shown in Figure 4.7a. The RGF as a function of water activity is compared to model data from Clegg et al.,[73] simulated using the E-AIM model.[72] The model and experimental data are in very good agreement, validating the use of the CK-EDB for new substances and the accuracy of E-AIM for modelling the hygroscopic response of NaCl. For organic components, AIOMFAC is a thermodynamic model that calculates the activity coefficients

of different chemical species in a mixture.[72] The model distinguishes between two levels of functional group classifications: main groups and subgroups. As sodium chloride is made of only two ions, it is simple system to predict a hygroscopic response. Sodium chloride is used by patients with cystic fibrosis as it helps produce sputum from the mouth which aids lung function.[123] It is administered by a nebuliser, where the salt is in aqueous form. The desired location of deposition is the upper and lower airways, which ranges from the throat to the lungs. In the upper airway, particles of >2.5 µm radius will deposit via impaction and in the deep lung (lower airway), droplets of 0.5 to 2.5 µm radius will deposit via sedimentation.[124] For example, a saline droplet generated by a nebuliser with a MFS of 0.05 and initial radius of 1µm at 50% RH and 293 K will have a dry radius of 0.288 µm. Upon inhalation into the upper airway, 99% RH, the saline droplet will experience a radial growth factor of ~5. Thus, the final droplet size prior to deposition will be 1.44 µm, which is within the size range of deposition for the target location.

Ethylenediaminetetraacetic acid disodium salt dihydrate (EADD) is an excipient used in the Respimat® device, where it acts as a chelator of divalent cations, preserving the drug mixture.[26] Respimat® is an aqueous nebuliser (SMI) device that is used in drug delivery to the lungs, it is described thoroughly in Section 4.5. In this section the hygroscopic properties of each of its three components - two excipients and one drug - will be discussed. The API can vary between formulations, while the excipients, EADD and benzalkonium chloride (BC) remain constant. The hygroscopic response of EADD is shown in Figure 4.7. It can be inferred from Figure 4.7a that EADD is less hygroscopic than NaCl, i.e., a particle of the same dry radius will result in a smaller wet radius at 99% RH, 293 K. Following the example set out above, an EADD dry particle of radius 0.288 µm will grow to a droplet of radius 0.729 µm (2.56×0.288). A particle of less than 1 µm is more likely to travel through the upper airway and deposit in the deep lung. The particle dynamics of EADD could determine where the droplet will deposit, based on the desired target location for treatment.
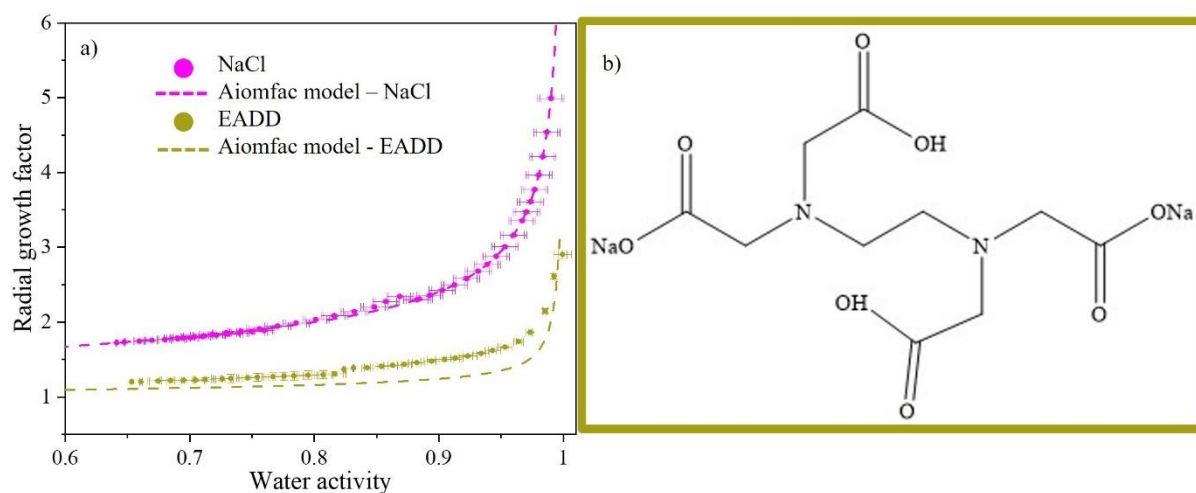
Figure 4.7. Hygroscopic response of excipients used in drug formulations, compared to model data at 293 K. a) Salts - NaCl and EADD compared to AIOMFAC.[72] b) Molecular structure of EADD.

The experimental data of EADD is compared with simulated data from AIOMFAC, where the salt is not found in the predefined list of organic components.[72] Thus, the molecular structure of the compound, shown in Figure 4.7b, was used to define the individual subgroups. AIOMFAC underestimated the RGF as it is not possible to include Na^+ ions with defined organic subgroups, a limitation of the AIOMFAC model. Thus, some uncertainty with the simulation is expected when dealing with such molecules. In the case of EADD, the model has slightly underestimated the hygroscopicity. The CK-EDB measurements presented in Figure 4.7b could be used to help refine AIOMFAC groups to represent disodium salts.

Hygroscopicity of Pharmaceutical Disaccharides in DPI formulations

DPI formulations consist of large, course carrier particles mixed with micronized drug particles. The micronized drug particles are attached to the large carrier particles, which are commonly α-lactose monohydrate or trehalose.[125] A typical drug to carrier mass ratio is 1:67.5,[126] where the carrier particles are on the radial size range of 25-50 µm and the drug particles on the radial size range of 0.5-2.5 µm.[127] The drug particles must be in that size range to achieve deep lung deposition. If dispersed without a carrier they would experience poor flow and molecular cohesion. Thus, a large, coarse carrier particle is needed to improve flow dispersion and drug deposition efficiency. A key property of a drug carrier is that it has low hygroscopicity, for two reasons. Firstly, it ensures the particle size dynamics are minimal, allowing for a high deposition fraction in target location. Secondly, it reduces the risk of physical and chemical instability of drug and carrier.[128] Thus, understanding the hygroscopic response of carrier particles is essential to developing a formulation that will have a good aerosol performance, where the drug particles deposit in the desired location. Figure 4.8a shows the hygroscopic response of lactose and trehalose, a chemically similar carrier to lactose. At 99% RH, conditions in the upper airway,

the growth factors of both sugars in aqueous solution droplets are ~ 2.5. Given that the size of a dry carrier particle, generated from a DPI, is around 25 - 50 µm, upon inhalation this particle would grow to 62.5 – 125 µm. Particle growth assumes that the dried particle fully deliquesces before deposition, which is likely given the high-water activity of the gas phase and the amorphous state of the carrier particle.[87] The large lactose carrier will impact in the airway, while the drug particles are dispersed from the surface of the carrier by the energy of the inspired flow.[125] The low hygroscopic properties of the carrier are vital to ensure that the drug particles are not exposed to significant water molecules that could prevent deep lung penetration. Additionally, if the carrier is holding on to too much water the adhesion forces between carrier and drug strengthen, leading to drug agglomeration on the carrier. Excessive adhesion forces may lead to upper airway deposition of the drug, reducing the efficiency and efficacy of DPI inhalation.
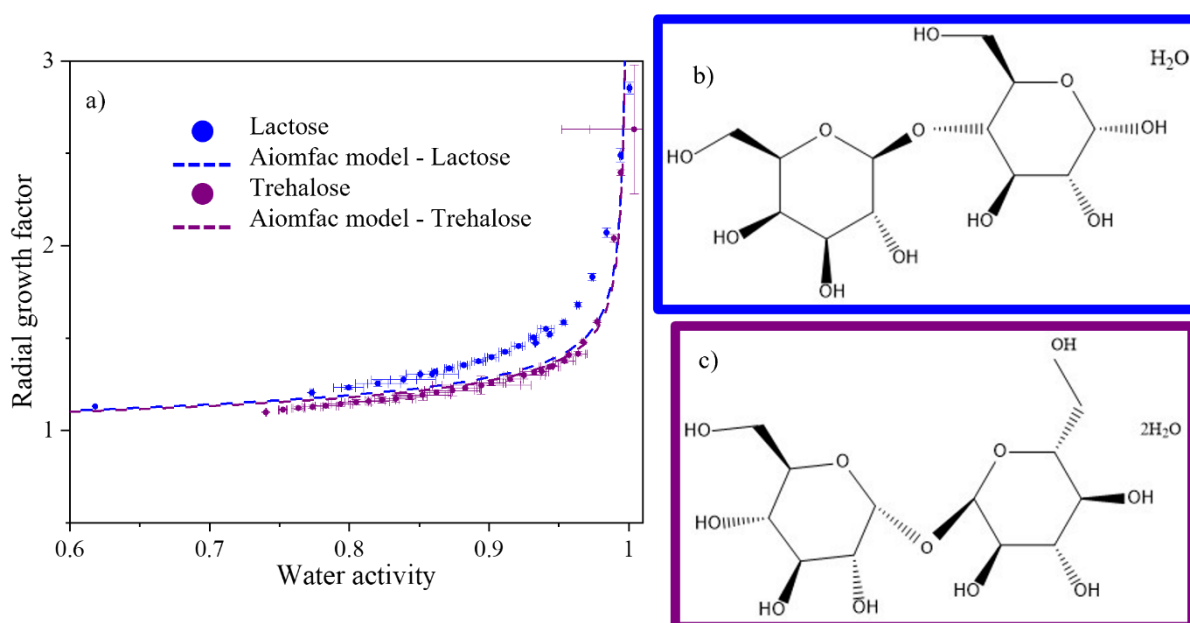
Figure 4.8. Hygroscopic response of disaccharides used in drug delivery to the lungs at 293 K. a) Lactose monohydrate and trehalose dihydrate, compared with AIOMFAC simulation. b & c) Molecular structure of both compounds in a).

The hygroscopic response of lactose and trehalose were modelled using AIOMFAC. The molecular structure of each excipient is shown in Figures 4.8 b&c, highlighting that they have the same chemical composition but different molecular structure. The model is not able to consider isomerism, therefore, the lactose and trehalose models overlay, and both fit the experimental data of trehalose. The model data of lactose underestimates the hygroscopicity. It could be that the positional isomerism of a compound's subgroups is influential in its hygroscopic response. It is possible that the position of the OH groups in lactose allow for easier interactions with water molecules, increasing its hygroscopicity above that of trehalose.

The transition from chlorofluorocarbon (CFC) to hydrofluoroalkane (HFA) propellants in MDIs posed many challenges for the pharmaceutical industry. HFAs could not directly substitute for CFC propellants, as previous APIs and devices were not compatible with HFA formulations. Thus, significant effort was required to develop new devices and new formulations. In particular, there has been an increased effort to discover components that can be added to the HFA drug formulation to match the previous chemical and physical properties of MDIs.[93] A key performance attribute of an MDI is the aerodynamic particle size distribution (APSD) of the delivered aerosol. It was found that adding a non-volatile component, glycerol, to a drug formulation, increase the residual particle APSD.[129] Additionally, it was found that glycerol improves the aerosolisation and deglomeration of micronized drug particles, allowing for better deposition in the deep lung.[130] Thus, understanding the particle size dynamics associated with inhaling a glycerol droplet is vital to improving the efficiency of HFA formulations in MDIs. The hygroscopic response of glycerol is shown in Figure 4.9a. The simulation from AIOMFAC fits the experimental data very well. There is a slight deviation at a high-water activity, where the largest error is seen. Upon actuation of an MDI, the propellant evaporates off prior to inhalation, commonly resulting in a water/glycerol droplet with inclusions of API. It is vital that the size range of the final droplets are < 2.5 µm to ensure a high deposition fraction in the deep lung. For example, any glycerol droplets with a dry radius larger than 1 µm, at 99% RH, will grow to > 2.5 µm and deposit in the upper airway. The final size of an inhaled glycerol particle is calculated using the hygroscopic growth curve of glycerol in Figure 4.9a, where RGF is equal to ~2.5 at 99% RH.

An example of the mass transport dynamics of an aqueous-glycerol droplet is given in Figure 4.9d, in which data is simulated using the hygroscopic response curve in Figure 4.9a. All droplets have an initial MFS of 0.8 at 48% RH, ambient conditions, and varying initial radii (0.5, 1, 1.14 & 1.5 µm). Upon inhalation, the glycerol droplets experience a rise in RH to 99% RH. The International Commission on Radiological Protection (ICRP) produced a whole lung deposition model. It states, for a healthy, fit, male, that within 1 s of inhalation, aerosol will reach the deep lung. In the deep lung, particles of radial size 0.5 to 2.5 µm will deposit.[113] The droplets with initial radii of 0.5, 1 & 1.14 µm all have an equilibrated size of less than or equal to 2.5 µm, i.e. likely to deposit in the deep lung. The latter is the largest initial droplet radius, held at RH 48 %, that will deposit in the deep lung. In the case of a droplet with initial radius larger than 1.14 µm, deposition in the upper airway will occur. It is also important to consider the time taken to reach equilibrium. In all 4 cases in Figure 4.9c, the final radius is reached within the inhalation time frame set out by ICRP, 1.64 s.[32] However, the largest droplet, with an initial radius of 1.5 µm, is still growing after 1 s (time taken to reach the deep lung). Dynamic droplet simulations of pharmaceutically relevant aerosol, based on experimental hygroscopic data, have potential to improve the efficiency of drug delivery to the lungs. Figure 4.9d is an example of how

droplet growth simulations can be used to determine the particle engineering required prior to inhalation, i.e., in the case of an MDI, the water/glycerol droplets must not exceed 1.14 µm to ensure a high deposition fraction, thus high efficiency.

The amount of API suspended in the glycerol/water droplet is negligible, and thus has little effect on the particle size dynamics during inhalation. However, the hygroscopic properties often ternary mixtures, API-excipient, and excipient-excipient, are explored in the next section. AIOMFAC could not be used to model BC due to the complex chemical formula and molecular structure, shown in Figure 4.9d. The additional Cl⁻ ion cannot be included in the model, whilst organic subgroups are being defined. Additionally, the general formula is shown in Figure 4.9d, however the adjoining carbon chain can range in length, which cannot be accounted for with AIOMFAC.
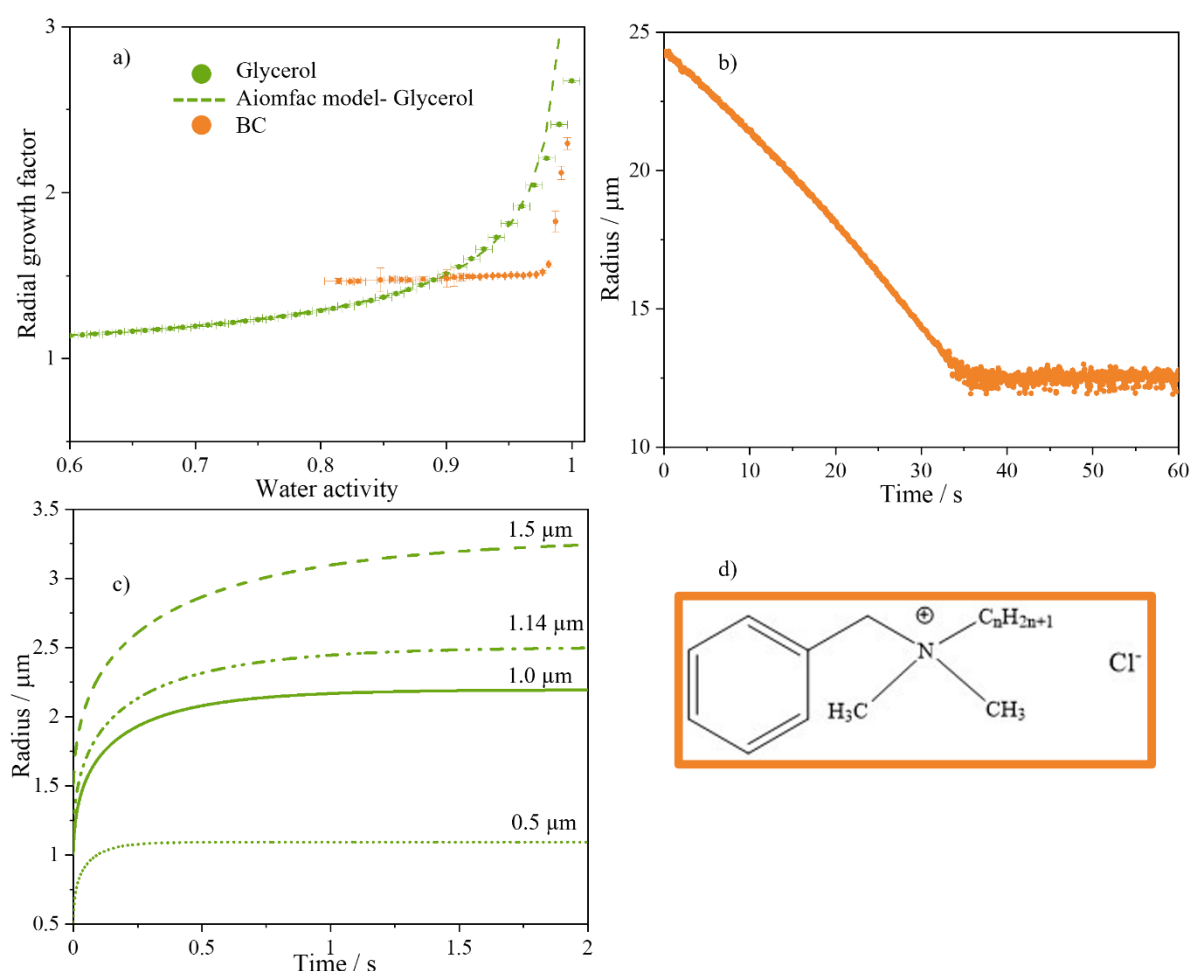
Figure 4.9. Hygroscopic response of non-volatile components used in drug delivery to the lungs at 293 K. a) Glycerol, compared with AIOMFAC, and BC. b) A BC droplet evaporation profile at 90% RH, data at equilibration appears non – homogeneous. c) Glycerol droplet growth as a function of time at 99% RH with different starting radii, initial MFS 0.8 at 48% RH. Molecular structure of BC is a mixture of alkyl-dimethylammonium chlorides of general formula d), where n ranges from 8 to 16.

The hygroscopic response of BC is shown in Figure 4.9a by the orange data. It is an unusually shaped hygroscopicity curve, where an increase in RGF is only seen after 0.98 a_w. Prior to an increase in RGF, a constant RGF between 0.78 and 0.98 a_w is observed. The high RH increase in RGF does not match the characteristics of the final RGF at a water activity close to one. A RGF of 2.3 at a a_w of 0.998 indicates that a substance only weakly hygroscopic but still able to absorb some water. Often, if the substance is relatively hygroscopic, e.g., glycerol, the increase in RGF as a function of aw will be more gradual, as seen by the green data points although a rapid increase is always seen as aw approaches 1. When considering BC, it appears that there is an additional limitation to mass flux and/or formation of a non-homogenous particle. A single droplet of BC at 90% RH is shown in Figure 4.9b. The light scattering shows a non-homogenous droplet at the equilibrated radial size. Non-homogeneity is inferred from irregular or erratically scattered light, for which the geometric optics approximation is inaccurate.

The data in Figure 4.9b appear irregularly scattered between 30 and 60 s, indicating non-homogeneity. BC is a viscous liquid in its pure form at 293 K. BC is known to be very soluble in water and so it can be assumed that it is fully miscible. However, the data clearly show signs of non-homogeneity, perhaps suggesting that solid structures are forming, such as a surfactant layer. Droplets containing surfactant structures, such as micelles, would have the characteristics of an inclusion droplet, often described as a "snow globe". An inclusion droplet produces irregular phase functions, which were observed during analysis of BC phase functions. As the RH increases, the surfactant and micelle concentrations reduce. Dilution of the surfactant removes the micelles; however it is highly likely that there will be a monolayer of surfactant residing on the surface. A surface layer is likely to remain as the hydrophobic tails of the surfactant tend to be at the droplet surface pointing towards the gas phase. A monolayer at the surface will result in an enrichment of surfactant on the surface compared with that in the bulk. Thus, the droplet is not homogenously mixed or isotropic, instead the centre of the droplet would be more dilute than the surface. Although the light scattering of the BC droplet produce phase functions with characteristics of a homogenous droplet, it is more likely to be non-homogenous. Thus, the hygroscopic curve cannot be used to predict size dynamics of an aqueous BC droplet. However, BC behaves very differently when mixed in a 1 to 1 ratio with EADD, replicating the formulation of Respimat®. The hygroscopicity of a EADD and BC mixture is discussed in Section 4.4.2.

4.3.2 Hygroscopicity of APIs used in Drug Delivery to the Lungs

Hygroscopic Response of Mannitol and Tobramycin

Mannitol is used in the treatment of cystic fibrosis, with the same desired outcome as inhaled NaCl. It is used to clear secretions from the airways by increasing mucocilary clearance.[131] Additionally, it is used to diagnose asthma - the procedure is called bronchial challenge test and checks if a patient has

difficulty breathing.[132] In the treatment of cystic fibrosis a DPI is used, where the mannitol is often spray or freeze dried prior to storage.[133] Rapid drying techniques often result in amorphous particles,[134] which have much faster dissolution rates than crystalline particles.[87,135] Therefore, it is important to understand the size dynamics of a liquid droplet, which forms prior to deposition due to quick dissolution.

The hygroscopic response of mannitol is presented in Figure 4.10a, orange. At a water activity of 0.998 (akin to conditions of the deep lung), mannitol has an RGF of 2.811, e.g. a particle of dry radius 1 µm would grow to a wet radius of 2.8 µm at 99.8% RH. The size dynamics of mannitol droplets with varying initial radius (0.5, 1.0, 1.2 & 1.5 µm) at 48% RH are shown in Figure 4.10b. The hygroscopic growth curve in Figure 4.10a was used to determine an MFS of 0.83 at 48% RH, ambient conditions, for a mannitol droplet. The droplets experience an increase in RH up to 99% RH, where data are plotted over 2 s, the time taken for droplets to reach the deep lung.[32] It is shown that droplets of starting size less than or equal to 1.2 µm will remain under the radial size threshold of 2.5 µm and reach the deep lung. On the other hand, droplets of starting radial size 1.5 µm grow to over 3 µm within 2 s, thus depositing via impaction prior to the deep lung.

Tobramycin is an aminoglycoside antibiotic used to treat various types of bacterial infections and is commonly administered using a nebuliser, SMI or DPI.[92] The hygroscopic response of tobramycin is shown in Figure 4.10, green. Tobramycin is less soluble than mannitol and often micronized and attached to large carrier particles for use in DPIs.[136] Thus, tobramycin is more likely to deposit in a non-homogeneous state than an aqueous droplet. In the case of an aqueous tobramycin droplet, the hygroscopic growth will be less than a mannitol droplet of equivalent size. Tobramycin has a RGF of 2.23 at 99.8% RH compared with 2.81 for mannitol.
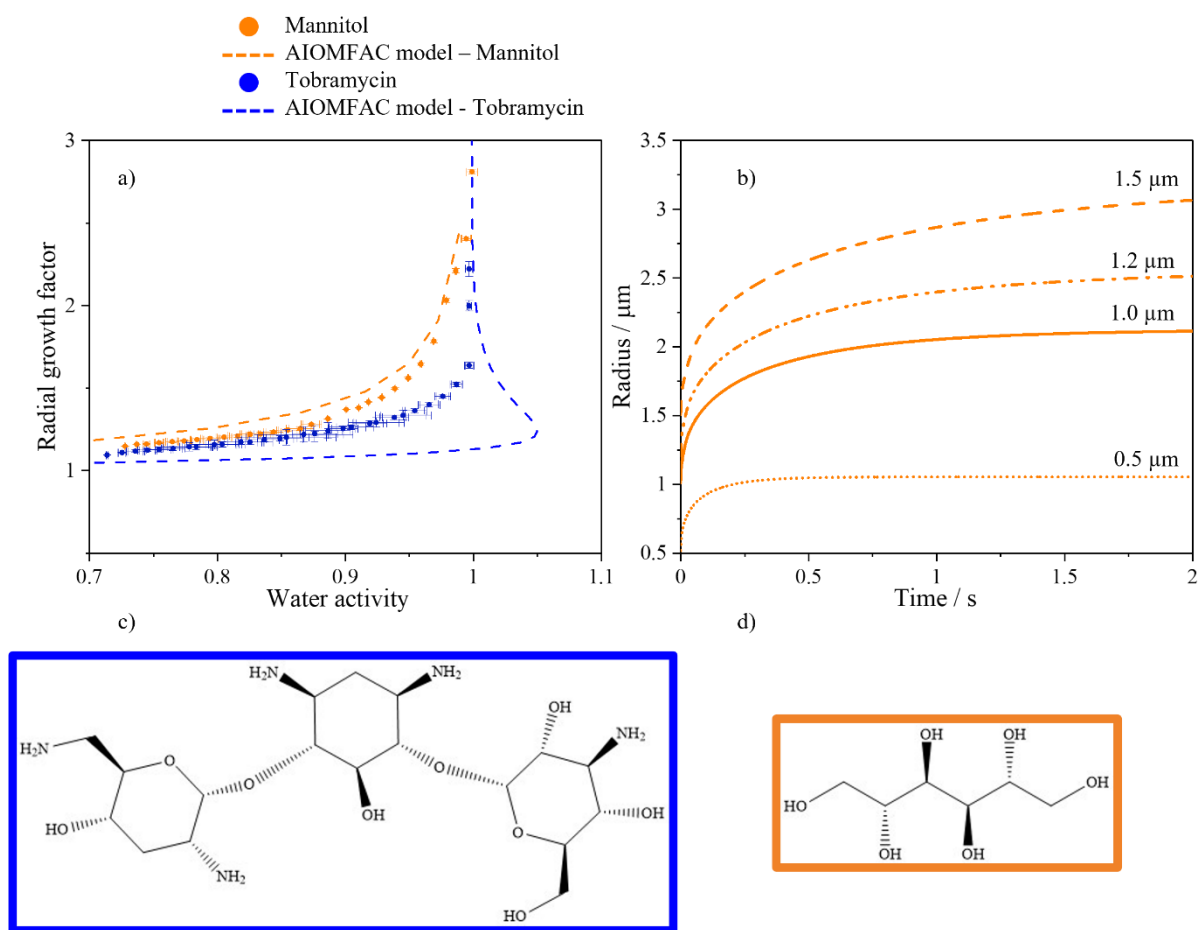
Figure 4.10. Hygroscopic response of two APIs used in drug delivery to the lungs at 293 K. a) Mannitol, orange, and Tobramycin, blue, both compared with AIOMFAC. b) Mannitol droplet growth as a function of time at 99% RH with different starting radii, initial MFS 0.83 at 48% RH. c) Molecular structure of Tobramycin. d) Molecular structure of Mannitol.

The molecular structure of tobramycin and mannitol allowed for hygroscopic response simulation using AIOMFAC. Figures 4.10c&d highlight the presence of only organic subgroups, which can all be found in AIOMFAC. The simulation of the hygroscopic response of mannitol is slightly overestimated by the model, although parts of the curve fall within the error bars of the experimental data. However, AIOMFAC underestimated the hygroscopicity of tobramycin as well as calculating values of water activity that fall outside the physical boundary. The error associated with the model could be due to the many complex subgroups associated with model, e.g., amines and cyclohexane rings.[48] The hygroscopicity of these functional groups is not well understood in the literature. Thus, molecules such as tobramycin could be used to widen the applicability of AIOMFAC.

Hygroscopic Response of Salbutamol Sulphate, Tiotropium Bromide, and Ipratropium Bromide

Salbutamol sulphate (SS), tiotropium bromide (TB) and ipratropium bromide (IB) are all bronchodilators. They are used to make breathing easier by relaxing the muscles in the lungs and

widening the airways (bronchi). Salbutamol sulphate is used in DPIs, MDIs and nebulisers. In the latter, SS is in aqueous form, so hygroscopicity becomes an influential factor in the deposition fraction. Additionally, SS commonly forms an amorphous or crystalline particle when spray dried,[137] thus dissolution and deposition of a liquid droplet is likely. Haddrell et al. found that SS has a DRH of ~78%, significantly lower than the RH of the lung.[92] Thus, it is likely that crystalline SS particles generated from DPIs and MDIs are liquid droplets prior to deposition. In this case, hygroscopicity governs the final size of the droplet and the location of deposition. The hygroscopic response of SS is shown in Figure 4.11a, red data. At an RH of 99.3% SS has a RGF of 2.9, i.e., a droplet with a dry radius of 1 µm will grow to an equilibrated size of 2.9 µm. Upon inhalation, SS must reach the bronchi in the deep lung for a high deposition efficiency. Thus, droplets must have a dry particle radius of less than 0.86 µm in order to remain under the 2.5 µm threshold and deposit in the deep lung. Droplets larger than 2.5 µm will deposit in the upper airways via impaction and reduce the deposition efficiency.

Spray drying TB and IB solutions often leads to a crystalline particle. When administering TB or IB using DPIs or MDIs dissolution dynamics control the physical state of the final particle, influencing drug delivery efficiency.[137] Hygroscopicity, however, is influential when TB and IB are administered using an aqueous based device, including a nebuliser such as Respimat®. The droplet dynamics associated with the formulation of the Respimat® device are discussed thoroughly in Section 4.5. The RGF as a function of water activity for TB and IB are shown in Figure 4.11a, green and purple data respectively. The hygroscopic response of TB and IB is less than that of SS within mid to high range RHs (80-95%). However, as the RH increases to saturation, >99% RH in the lung, the RGF of all three APIs tends to ~3. The mass flux of water in TB and IB droplets in Figure 4.11a is limited only by gas phase diffusion, a key assumption of the Kulmala model.[82] In other words, aerosol growth during inhalation is dependent on the availability of water vapour in the gas phase, i.e. the lungs. In a nebulised aerosol plume the high particle count may limit the amount of water vapour available to each droplet, thus reducing aerosol growth.[92] Nerbrink et al., estimated the number of saline droplets present in a nebulised aerosol whose hygroscopic growth will be limited by the availability of water vapour.[138] The number concentration of saline droplets was estimated as a function of the aerosol median diameter. Their estimations are based on the total mass of water required for growth of all saline droplets at a given starting radius, and the total mass of water vapour in the lungs. Haddrell et al. estimated the droplet number concentration for a set of 4 nebulisers,[92] using data published by Reisner et al.[139] For example, at an RH of 98% aerosol number concentrations from commercial nebulisers were not above the threshold lines, i.e. aerosol growth should be unaffected by the available mass of water. However, at an RH of 90%, particle concentrations of all tested nebulisers fell above the line. In this case it is likely that water availability will determine the rate and magnitude of mass flux during inhalation, i.e. theoretically there is not enough water in the gas phase to sustain the aerosol growth expected from the associated hygroscopic response.[92] Although such estimations are not calculated in this thesis, water

vapour availability should be considered when considering hygroscopic components administered using a nebuliser.
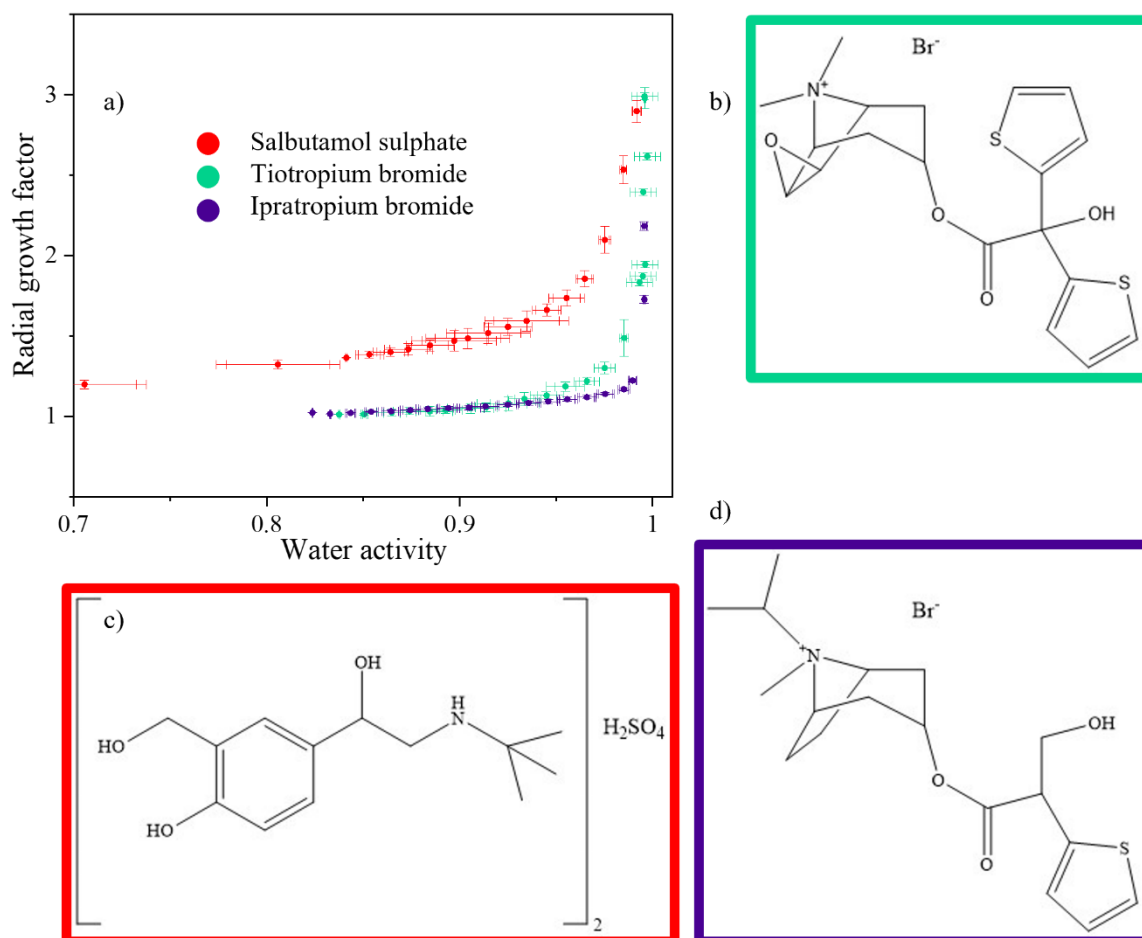
Figure 4.11. Hygroscopic response of three APIs used in drug delivery to the lungs at 293 K. a) Salbutamol sulphate, red, tiotropium bromide, green, and ipratropium bromide, purple. b) Molecular structure of tiotropium bromide. c) Molecular structure of salbutamol sulphate. d) Molecular structure of ipratropium bromide.

The molecular structures of TB, SS and IP are given in Figure 4.11 b, c, and d, respectively. The APIs contain inorganic ions, e.g., Br^-, which cannot be included with the organic subgroups in the AIOMFAC model. Thus, the model was not used to simulate the hygroscopic response of the components. The difference in chemical composition between TB (b) and IP (d) could be the reason for an increase in hygroscopicity, respectively. The additional thiophene and O^- present in Figure 4.11b could account for the ability of TB to hold on to more water molecules at a high-water activity than IB.

4.4 Hygroscopicity of Ternary Aqueous Aerosol

Inhaled drug formulations often consist of an API, excipient, and solvent/propellant. In an MDI for example there is always an API, solvent, and propellant. The propellant commonly makes up about 83% by mass of the formulation, solvent 13-15% and API 2-3%.[10] It is becoming more favourable for the addition of a non-volatile excipient, such as glycerol, to improve the aerosol performance of the drug formulation.[10] The concentration of glycerol in the formulation is ~1%, and always less than the concentration of the API. Upon actuation of an MDI, the propellant and solvent (often ethanol) evaporate almost instantly, leaving a cooled droplet which leads to rapid water condensation onto the droplet. At this point, a liquid droplet containing the API and excipient is formed, a ternary aqueous aerosol. Additionally, in the case of a DPI, the large carrier particle and micronized drug will deliquesce in the wet lung and form a ternary aqueous aerosol, if solubility allows. Therefore, it is important to understand how a mixture of two components in a liquid droplet affects the overall hygroscopic response.

4.4.1 Hygroscopicity of an Excipient with an API in an Aqueous Droplet

The determination of the hygroscopic response of a mixture containing multiple solute components requires an alternative method to parameterise the density and refractive index. The molar refraction rule discussed in Chapter 3 was extended to account for ternary aqueous aerosol.[48,106] The hygroscopic response of NaCl and SS mixtures are shown in Figure 4.12. The blue data are a mixture of 1:1 (NaCl:SS), a mass ratio, and the black data are 2:1. It is shown that an increase in NaCl concentration increases the hygroscopicity of the mixture. The additive behaviour of NaCl and SS could be used to create formulations of specific hygroscopicity. The equilibrated size of a ternary droplet in the humid lung (>99% RH) could be controlled, resulting in size dependent, targeted deposition and efficient drug delivery. The hygroscopicity of the 1:1 mixture appears to fall slightly closer to SS than NaCl. It is possible that the hygroscopicity slightly tends to SS due its larger molecular size, 337.39 vs 58.44 g/mol.[48]
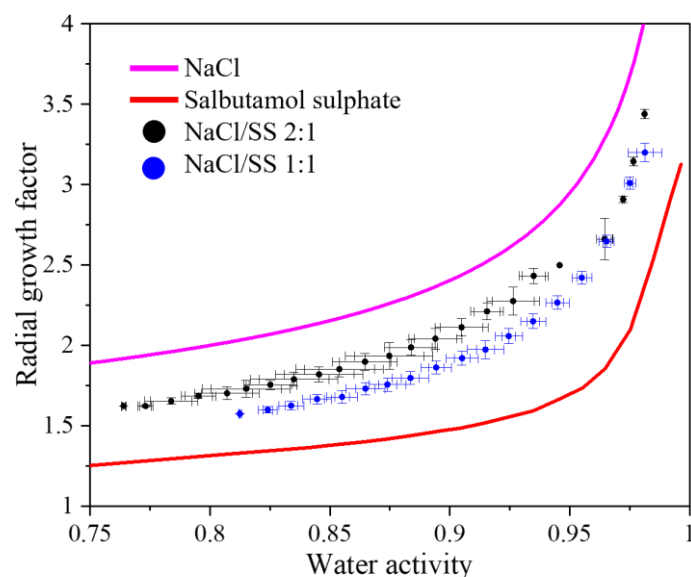
Figure 4.12. The hygroscopic response of NaCl and SS mixture, 1:1 and 2:1 mass ratio, compared with the hygroscopic curves of the individual components.

4.4.2 Hygroscopicity of an Excipient and Excipient in an Aqueous Droplet

The hygroscopic response of a ternary mixture containing EADD and BC was investigated to better understand the particle size dynamics associated with the Respimat® nebuliser. The formulation consists of BC, EADD, API and water. The API concentration is negligible and the mass concentration ratio of BC to EADD is 1:1. The hygroscopic curve of the mixture of the two excipients is shown in Figure 4.13. It is evident from Figure 4.13 that the hygroscopic response of BC/EADD in terms of RGF appears to be lower than that of pure EADD. However, the hygroscopicity of the mixture appears to tend to that of EADD, the more hygroscopic component. It is possible that the non-ideal interactions are due to complex charge interactions between the components, such as deprotonation.
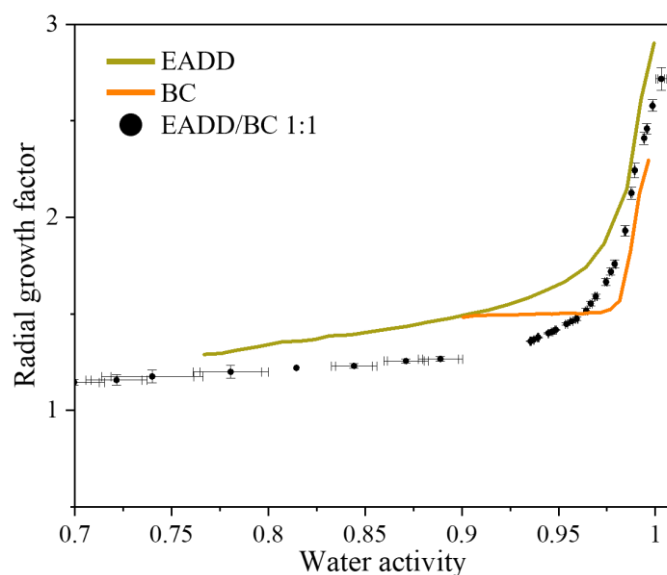
Figure 4.13. The hygroscopic response of a mixture containing two excipients, EADD and BC, 1:1 mass ratio.

In Section 4.3.2 it was discussed that the hygroscopic curve of BC cannot be used to infer droplet size dynamics. The component is thought to be non-homogeneously mixed throughout the droplet at high water activities, while micelles form at lower water activities. Interestingly, when BC is mixed with EADD, the hygroscopic response appears to follow a more traditional hygroscopic curve shape. The curve tends to a RGF of 1 from 0.9 aw downwards. The presence of EADD could prevent the formation of a saturated mono layer at the surface, thus the formation of micelles. In this case, the droplet would be homogenously mixed and a hygroscopic response inferred.

4.5   Simulations of Cascade Impactor Measurements for the Respimat® Device

A simulation for a cascade impactor has been developed that accounts for the dynamic change of aerosol during transport. The simulation includes droplet evaporation or condensation depending on the sampling relative humidity. Often, standard cascade impactor measurements do not include the hygroscopic response of particles or have an undefined RH.[28] The model is based on single particle measurements of hygroscopic response for aerosols formed from the Spiriva Respimat ® solution. This project is in collaboration with researchers from Bath University and Nanopharm: Dr. William Ganley and Prof. Rob Price. The single aerosol measurements and simulation data were carried out at BARC, while the bulk cascade impactor measurements were carried out at Bath University. A description of the methods and processes that were required to simulate a cascade impactor measurement is described here, as well as a comparison between simulated (BARC) and experimental (Bath) cascade impactor measurements.

The model was developed on LabVIEW, using the mass flux equations discussed in Chapter 2.[108] The cascade impactor simulator can produce aerosol radius as a function of time, size distribution as a function of time and deposition fraction of aerosol at varying size stages. The cascade impactor simulator has a user-friendly interface, with many input variables that can be chosen by the user. In this section, simulated data is compared against experimental data, where the environmental conditions, size distribution and initial concentration are the same. The outcome of the results indicate that the model could be used to simulate other aqueous based drug formulations. Additionally, the results show the value in understanding and quantifying the hygroscopic response of pharmaceutically relevant aerosol.

4.5.1   Introduction to the Formulation Delivered by Respimat ®

Drug delivery via the lungs offers instant respiratory relief by targeted site delivery of bronchodilators. Little is known about the physicochemical processes that an aerosol experiences upon generation and on inhalation, processes which are important for predicting both the deposition site of the drug and its physical state at deposition.

With typical delivery devices (MDIs, and DPIs), it is common that only 10-20% of the available drug is delivered to the lung.[140] The MDI, which requires a propellant, produces particles that travel fast and often deposit on the oropharynx; the aerosolisation and delivery of the DPI is dependent on the inspiratory flow of the patient, which is compromised when treating a respiratory disease. There is a need for delivery devices that can resolve these major disadvantages. Respimat® is a new propellant free, multi-dose inhaler developed by Boehringer Ingelheim that is mechanically actuated. The Respimat device can be used to deliver a dose of an API either in an aqueous or ethanolic solution, depending on solubility. Studies on an aqueous solution of fenoterol and an ethanolic solution of flunisolide delivered from a Respimat device have shown that the desired fine particle fractions (< 1 µm radius) are approximately 81% for the ethanolic mixture and only 66% for the aqueous formulation.[33] A potential reason for a higher percentage of fine particles from an ethanol mixture could be due to fast evaporation kinetics of an ethanol droplet, causing a significant decrease in the droplet diameter. This rapid loss of solvent causes the temperature of the droplet to decrease and could, if in a humid environment, lead to rapid water condensation.[31] Figure 4.14 compares the difference in evaporation kinetics of water and pure ethanol droplets at 82-90% RH, resulting in different time-dependent radii, as would be experienced during an inhalation into a humid lung.
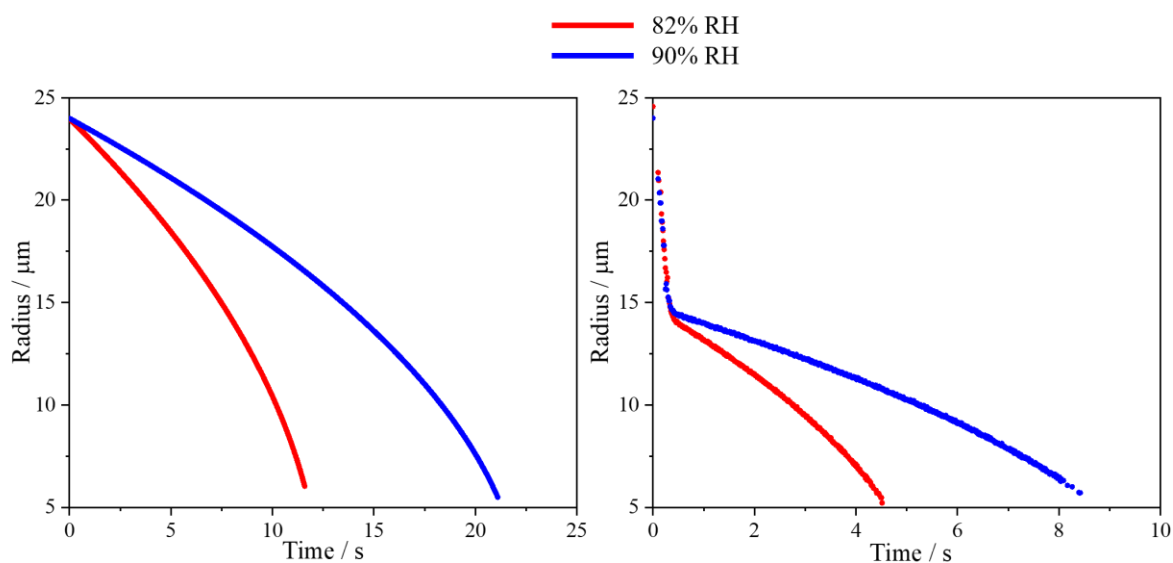
Figure 4.14. Evaporation kinetics of individual droplets at ~82%(red) and ~90%(blue) RH for water (left) and ethanol (right) droplets at 293 K. In the latter, the rapid evaporation of ethanol and the evaporative cooling that results, leads to rapid water condensation. After <1 s, the droplet is no longer composed of ethanol but of water.

The aim of this work is to aid further improvements of drug deposition efficiency. To do this, a better understanding of the physicochemical processes occurring from generation to inhalation are needed to optimise drug delivery via the lungs. These processes can be explored using the results of the cascade impactor simulator. Presented here are the deposition profiles of an aqueous solution of Respimat, where tiotropium bromide is the API. The modelled data is compared to the experimental data of a polydisperse population using the same solution and device. A cascade impactor collects the deposition fraction data of a plume of aerosol, with a known size distribution, at each stage of the 'lung' dependent on the particle size.[141] However, little is known about the dynamics of a particles at each stage within the impactor and relating the sampled distribution to the initial distribution is not trivial, particularly if the aerosol experiences changes in RH on passage through the impactor. This project aims to understand the dynamics of a single particle in a range of environmental conditions using experimental methods, which can then be applied to a cascade impactor simulator to ensure the physicochemical processes are considered when calculating the deposition fraction during an inhalation.

4.5.2. Simulating Droplet Dynamics using Hygroscopic Response Measurements

This project combined the experimental results of a cascade impactor with the simulated results from a cascade impactor model, providing a comprehensive view of the processes occurring when Spiriva Respimat® is used to deliver a dose of TB to the lung. In order to model the particle size dynamics of a plume of aerosol of known size distribution, the hygroscopic properties of the substance must be known. The CK-EDB was used to determine the hygroscopic properties of individual components of Spiriva

Respimat and the complete mixture. The hygroscopic growth curves are presented in Section 4.3. From these measurements, a comprehensive model can be developed that fully accounts for the water content and size changing dynamics that the aerosol can be expected to undergo on passage through the NGI. This is then used to inform the cascade impactor simulations.

The Spiriva Respimat produces a 2.5 µg dose of TB per actuation. The formulation contains an additional two excipients: BC and EADD, which both have concentrations of 1.8% by weight in an aqueous solution. The concentration of TB is extremely low, ~0.002% by weight, and can be neglected from the parameterisation of the aerosol hygroscopicity and, thus, from the dynamic cascade impactor simulation. The experimental work was carried out using a Next Generation Impactor (NGI) including the TB in the commercial formulation for the Respimat device.

The hygroscopic curve of BC/EADD mixture allows for simulation of individual droplet dynamics which can then be applied to a size distribution. During droplet evaporation simulation, the initial radius is set to vary over the size range determined from an experimental size distribution, in this case 0.1 to 20 µm diameter. The concentration of a Respimat droplet was calculated to be 3.6 g/L. The concentration was determined by the comparison between an evaporation profile of a Respimat droplet and the kinetics file of the BC/EADD mixture. The initial droplet radius, initial concentration, initial RH, bulk size distribution and average droplet size are the key input variables into the cascade impactor model. In this example, the RH was set to 90%, at 293 K, largest droplet diameter is 20 µm, smallest droplet is 0.1 µm and average droplet diameter is 9 µm. For comparison purposes, the input variables were consistent with experimental measurements performed at Bath University. Simulated Respimat droplets ranging from 0.1 to 20 µm diameter are shown in Figure 4.15a, with a size resolution of 500 nm. The droplet evaporation profiles are used to determine the evolving size distribution as a function of time. Figure 4.15b shows three size distribution curves at 0, 1 and 2 s. It should be noted that the model assumes a normally distributed size distribution, where the size range is controlled based on experimental size distribution measurements. The relative abundance, %, is a product of the particle size bin width, i.e., the size resolution and calculated as the particle fraction at each size bin width. The size bin widths are different between measurements at BARC and Bath University, thus only relative comparisons in size distribution can be made. In figure 4.15b the size resolution is 500nm. At 2 s the aerosol plume has reached stage 3 of the impactor, where the limit is set at 9 µm. Thus, any droplets larger than 9 µm are removed from the size distribution and labelled by the model as deposited. Simulating the size distribution as a function of time is the key to simulating the deposition within a cascade impactor.
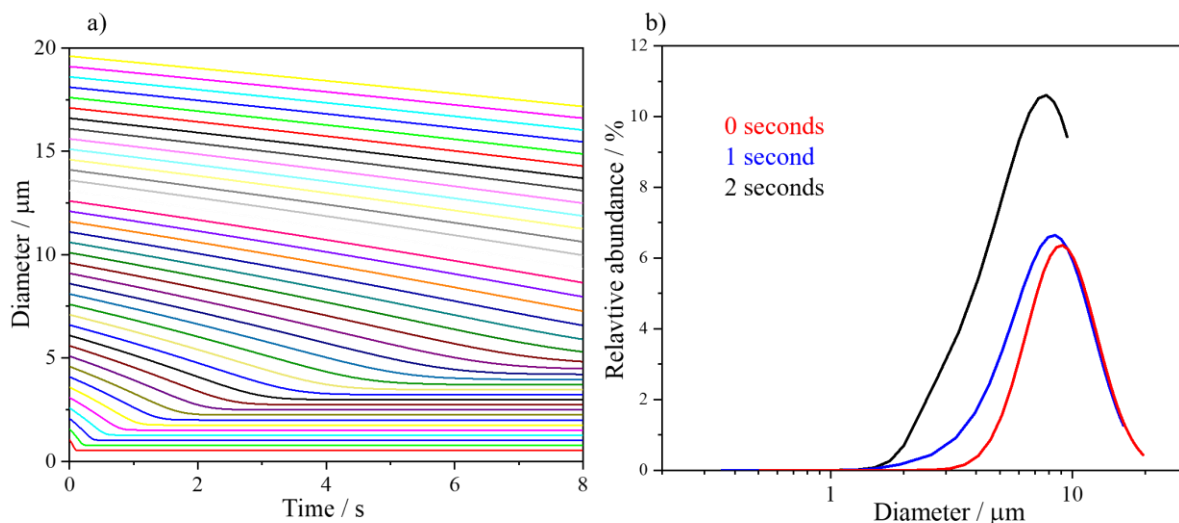
Figure 4.15. a) Multiple Respimat droplets simulated using the cascade impactor simulator, initial diameter ranging from 0.1 to 20 µm. b) Size distribution as a function of time, inferred from the droplet dynamics in a) and the impactor stage sizes. Relative abundance is equal to the relative number of particles at each size bin width.

The size distribution as a function of time in Figure 4.15b is based on the mass flux properties of the individual droplets shown in Figure 4.15a. The mass flux properties are known from the hygroscopic response determined in Figure 4.10.

4.5.3. Simulating Cascade Impactor Deposition

The hygroscopic curve of the aqueous ternary mixture of EADD and BC is reported as a radial growth factor as a function of water activity in Figure 4.13. The droplet size dynamics as a function of water activity can be combined with the size distribution data at a given RH. The size distribution of the aerosol plume will change as a function of time and RH due to evaporation of the individual droplets. As an aerosol plume travels through a cascade impactor, the droplets experience a change in size, thus changing the size distribution, shown in Figure 4.15b. In order to simulate the droplet dynamics over a relevant size range, an accurate size distribution of the initial Respimat aerosol plume is needed. Ganley et al. at Bath University produced a size distribution of particles directly after actuation in ambient conditions using a Spraytec particle size analyser. Additionally, a size distribution curve in drier conditions, ~30% RH, was collected at BARC. Figure 4.16 shows two size distribution curves collected in ambient (a) and below ambient conditions (b), a peak at about 9 µm is seen. The relevant size range taken forward into the cascade impactor simulations was 0.1 to 20 µm diameter. The size distribution collected by Ganley et al. clearly shows a bimodal distribution, albeit at a low abundance. The data collected at BARC show signs of irregular symmetry at the lower size range. It is possible that as the

BARC data were collected at a lower RH the water kinetics effect the size distribution, i.e., the larger droplets are losing radius over a short time. It was noted earlier that the model assumes a normal size distribution, however the experimental size distribution in Figure 4.16 of Respimat appears to be bimodal. The second mode in the experimental distribution is between 0.1 and 1 µm, thus it is assumed to have a negligible impact on the overall aerosol mass. Additionally, the second mode could be due to ambient RH conditions. To confirm this, a measurement of size distribution in dry air must be carried out. It should be noted that the size distributions collected at BARC and Bath University have different particle size bin widths. The size of the bin width affects the intensity of the relative abundance. In Figure 4.16b the size resolution is higher and the intensity of the peak height at ~9 µm is lower than in Figure 4.16a.
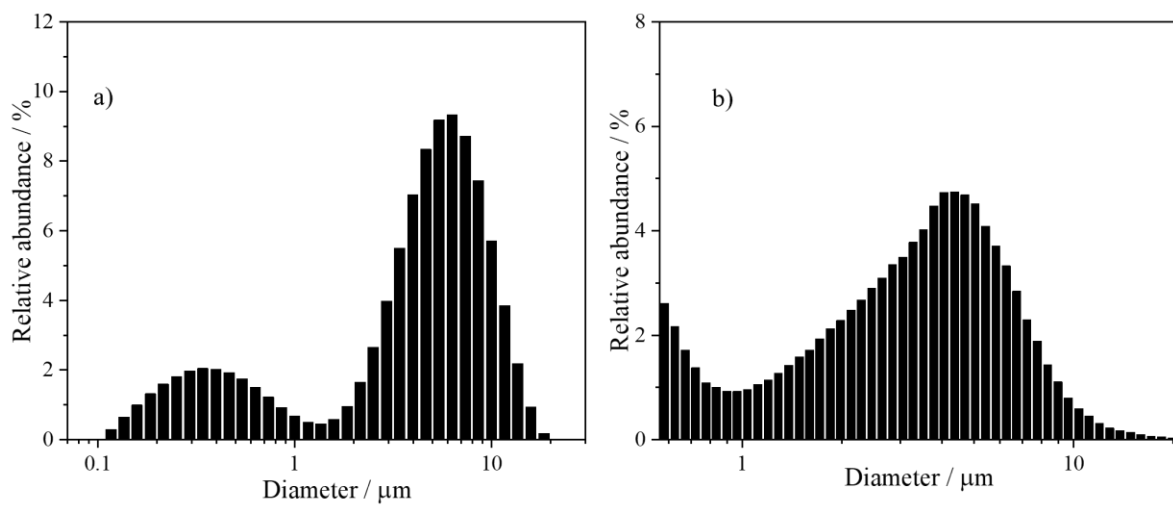
Figure 4.16. a) Size distribution of Respimat collect at Bath University by Ganley et al. in ambient conditions. b) Size distribution of Respimat collected at BARC in below ambient conditions. The graphs were used to determine the radial size range inputted into the cascade impact, 0.06 to 9 µm.

The data from the NGI was nominally collected at ~100% RH, but it is unlikely that this is fully accessible by the experimental measurement. Thus, it was deemed appropriate to run the cascade impactor simulator at a slightly lower RH, 90%. Figure 4.17 shows how the simulated and measured deposition profiles compare; the simulation accurately reproduces the bimodal distribution, where a high number of fine particles are present. The stage cut-off between each stage ranges from 0.53µm to 11.7 µm, where stage 0 includes the mouthpiece and throat. The NGI results show a large dose deposition in the early stages of the impactor, where the diameter ranges from 2-6 µm and there is low deposition in the range of 0.8-2 µm. At the lowest stage, 0.54 µm, there is an increase in particle mass deposition, indicating that Spiriva Respimat produces a significant number of smaller particles. It is possible that some initially larger particles have decreased in diameter as water evaporates and they collect in the lower stages. Integration of the curves in Figure 4.17 will result in the total mass of the

deposited dose. Further RHs will be compared in the future, along with other API formulations delivered from the Respimat device, including salbutamol sulphate, ipratropium bromide and various ethanolic mixtures.
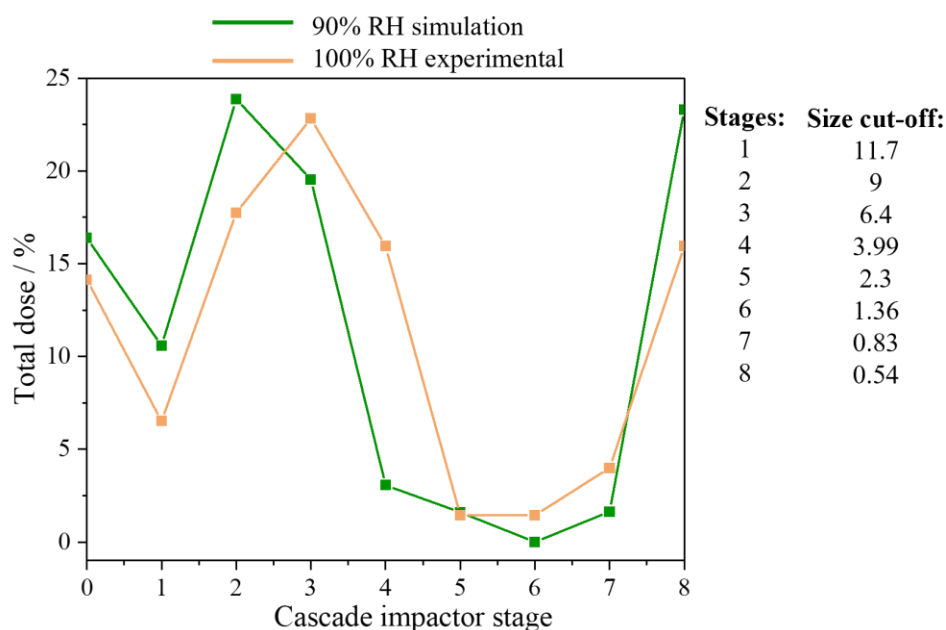
Figure 4.17. Simulated cascade impactor measurements compared with data collected on an NGI, at 90% and 100% RH, respectively.

The Respimat device has potential to be used for additional APIs, such as SS and IP. The hygroscopic properties of each API are shown in Figure 4.11. Therefore, with knowledge of the size distribution for each formulation, the cascade impactor simulator can also be applied to SS and IP formulations. The simulation will give an insight into the particle deposition as a function of relative humidity, time, and initial size distribution. Predicting and controlling deposition fraction is key to improving the efficiency and efficacy of drug delivery to the lungs. The size distributions of Respimat containing SS and IP are shown in Figure 4.18 and can be inputs to the simulator in the same way as described above.
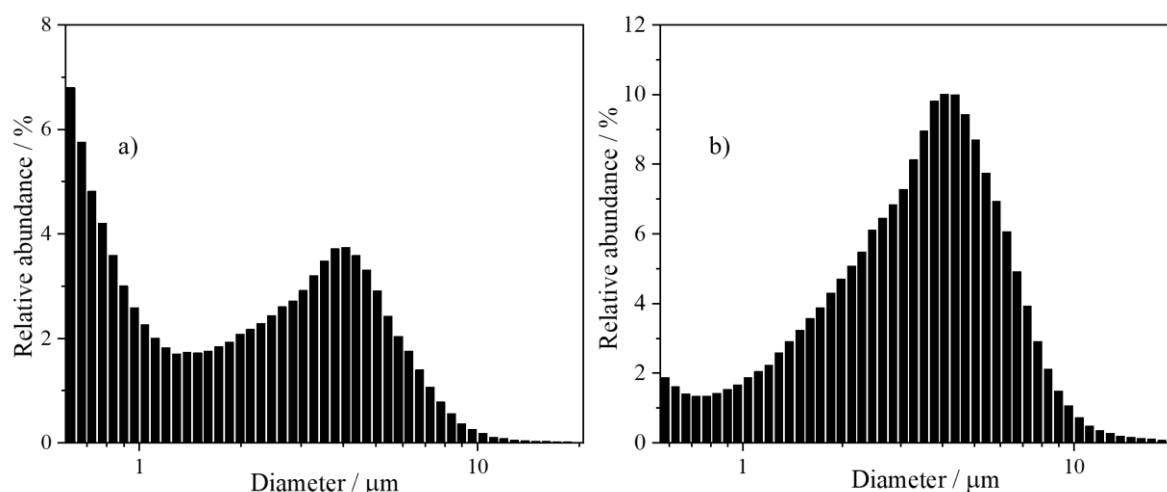
Figure 4.18. a) Size distribution of Respimat with SS as the API. b) Size distribution of Respimat with IP as the API. Both were recorded at 40% RH, 293 K.

The performance of an inhalation device and optimisation of the dynamic processes occurring from generation to inhalation are crucial for improving drug delivery to the lungs. As an aerosol droplet travels from ambient conditions (~45% RH ~20 °C) to lung conditions (~99.5% RH 37.5°C), it can significantly change in size due to the net flux of water, thus changing the deposition mechanism and site. Cascade impactors help to explore the deposition fraction of a cloud of particles as they travel through stages of varying sizes. However, little of the hygroscopic properties of an aerosol are considered when working with impactors. This work demonstrates that a cascade impactor simulator can model the deposition fraction of Spiriva Respimat at high RH, with good agreement to experimental data using an NGI. The simulator uses droplet kinetics to model the change in particle size as a function of time, where the initial size deposition and RH can be controlled. This new method of simulating cascade impactor measurements will be applied to a range of API formulations and systems, as the relative hygroscopic growth curves are produced.

4.6   Chapter 4: Summary

In this chapter experiments were performed using the CK-EDB measurement technique. The instrument was used to measure the hygroscopic response of pharmaceutically relevant aerosol. An introduction of hygroscopicity and drug delivery to the lungs was given in Section 4.2. A description of how to take hygroscopicity measurements on an EDB was given, explaining how to determine the RH of gas phase with a probe droplet. The hygroscopic response of binary aqueous droplets containing APIs and excipients were presented in Section 4.3. Next, the hygroscopic properties of more complex ternary droplets containing API & excipient and excipient and excipient were explored. It was shown that APIs tend to have a low hygroscopic response compared to an inorganic salt, such as NaCl. The hygroscopic

curves of excipients and APIs were compared to AIOMFAC where possible. In some cases, experimental and model data matched very well, in others the fit was poor. It was discussed that a poor fit could be due to the complex molecular structure of the components.

In section 4.5 the Respimat device was introduced. It is an aqueous based nebuliser that is used to treat a range of respiratory diseases, with the API TB. Collaborators at Bath University and Nanopharm collected bulk data on the deposition fraction using an NGI. The work in this thesis used experimental data on individual aerosol dynamics, along with size distribution data, to simulate the deposition fraction within a cascade impactor. The results of experimental and simulator were compared and matched well. The model could be used in the future with other APIs that are administered using Respimat.

Chapter 5

Single Particle Measurements of the Dynamics of MDI Formulations

This study aims to examine the aerosol dynamics occurring during generation and inhalation of particles formed from a metered dose inhaler (MDI) formulation. An electrodynamic balance (EDB) was used to take single particle measurements of a particle formed from an MDI formulation, with and without a non-volatile excipient (NvE) present. This chapter focuses on how a NvE influences aerosol microphysics, including the dependence on relative humidity (RH), and has implications for in vitro aerosol characterisation under standard laboratory conditions. The dynamics of particle size change and phase state were measured for single particles in the aerosol phase. The aerosol particles were formed from combinations of glycerol, ethanol, and beclomethasone dipropionate (BDP). Although present in some licensed propellant-driven inhalers, the effect of NvE on aerosol generation and dissolution is unclear. Drug release is a critical step in controlling the availability of poorly soluble inhaled drugs. The study shows that NvEs affect particle maturation after generation by modifying particle size, phase state and particle morphology. The observed physical changes due to NvEs are different at very high RH compared to intermediate RH typical of ambient laboratory conditions. The delay of drug release from deposited particles produced by MDI provides a mechanism for controlling the release of drug from inhaled aerosol formulations. Results collected at BARC are compared to bulk phase measurements collected by collaborators at Kings College London (KCL).

5.1 Introduction to Particle Engineering Associated with an MDI Formulation

Drug delivery via the lungs is a common way to treat a range of respiratory diseases. For an inhaled drug to be effective, it must be deposited at the preferred site of action in the lung where it will undergo dissolution in the lung lining fluid before subsequent absorption across the lung epithelial tissue.[142] Prior to deposition, the aerosols delivering the drug to the lungs experience dynamic changes in size and composition that are influenced by the local environmental conditions. As aerosol exits the nozzle of an MDI device, the propellant hydrofluoroalkane (HFA) rapidly evaporates from the droplets. Rapid evaporation quickly changes the size and composition of the remaining drug particles. Indeed, an improved understanding of dynamic particle processes can likely impact on our understanding of the disposition of the drug formulation when it finally deposits in the lung lining fluid.[143] Further, the deposited fraction in the lung is dependent on particle size, which can be dependent on the extent of interaction of the aerosol with water vapour and the water transport kinetics experienced by the particle during generation and inhalation.[144]

Typical formulated mixtures for pressurised metered dose inhalers (pMDI) include the active pharmaceutical ingredient (API), a co-solvent (commonly ethanol), and a volatile propellant.[93] Following the phase out of the ozone-depleting chlorofluorocarbon (CFC) propellants at the beginning of the 21st century, NvEs were incorporated into HFA solution pMDIs to match the pharmacokinetics of new reformulations to existing products. These excipients served to modulate the aerodynamic particle size distribution of the newer solution products in a successful attempt to match the pharmaceutical properties and clinical profile of the CFC predecessor.[145,146] The presence of excipients is thought to decrease the rate of HFA evaporation, and increase droplet diameter after actuation.[147] A reduced rate in HFA evaporation has been recorded when MDIs are actuated into humid, warm environments.[148] Measurements of the aerosol size dynamics during evaporation of HFA propellant are very difficult. Droplet sizes and velocities close to the nozzle experience rapid changes, causing difficulties for optical measurements. HFA evaporation occurs over an extremely short time scale, < 0.5 s.[147] For the first time, an adapted EDB was used to measure HFA evaporation and subsequent water kinetics.

MDIs are the most popular device for delivering drug to the lungs, and up until 1996 CFCs were used as the propellant.[9] The United Nations introduced the Montreal Protocol in 1987 which created a need to find alternatives to CFCs. Depletion of the stratospheric ozone has been linked to the use of CFCs for many years. Since the Montreal Protocol there has been a need for scientific research to develop a propellant with the same delivery efficiency, but environmentally friendly. HFAs were identified as a suitable alterative, but their physico-chemical properties differ significantly. Therefore, extensive research and testing programmes are needed to demonstrate the safety and efficiency of using HFA in MDIs.

Influence of NvEs on Particles Formed by An MDI Formulation

Non-volatile excipients can modify particle microphysics, the physical chemistry, and the dissolution of aerosol from solution pMDIs.[93] There has been much research into pMDI solution formulations of beclomethasone dipropionate (BDP),[149] a corticosteroid used in the treatment of asthma, the molecular structure of BDP is shown in Figure 5.1. Recent research has highlighted some differences in *in vitro* biopharmaceutics that suggest non-volatile excipients in these formulations may exhibit unintended effects on drug disposition. To illustrate, Freiwald et al. compared two HFA formulated BDP MDI products, Qvar® and Sanasthmax®, that both contained ethanol but differed in the presence of glycerol, a non-volatile, size modifying agent.[149] Using a simple dialysis model, they demonstrated differences in the release of drug from lung tissue to perfusate between the two formulations. Grainger et al. also

observed differences in the *in vitro* dissolution and absorptive transfer across epithelial cell layers for Qvar® and Sanasthmax®.[150] It was shown that these formulations produced aerosols with different aerodynamic and geometric particle size distributions which would account for the observed differing disposition. However, a follow-on study in which two test formulations were created to exhibit identical aerosol properties but differ only in the presence of non-volatile excipient glycerol,[151] also reported differences in dissolution profiles and drug cell layer permeability.[151] These findings point to a possible effect on drug kinetics that is attributable to the presence of non-volatile excipient in the formulation.
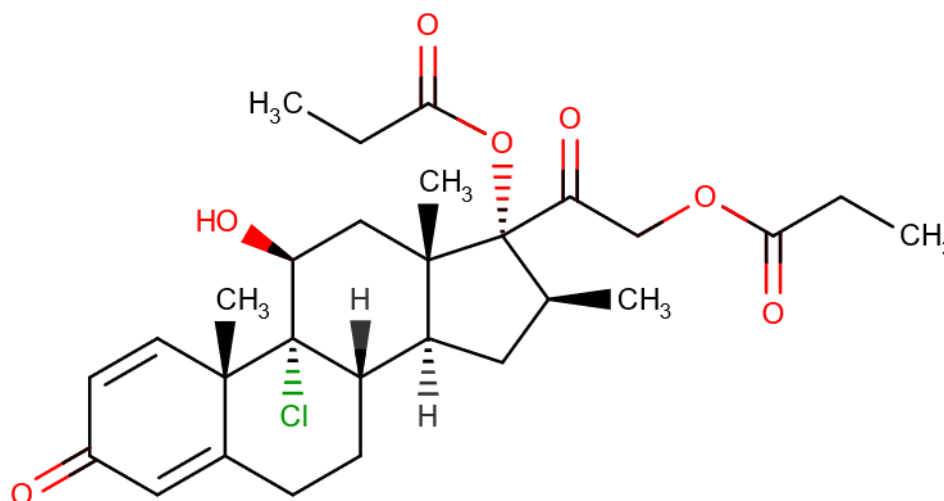
Figure 5.1. Molecular structure of beclomethasone dipropionate (BDP).

The particle microphysics during aerosol generation, evaporation and condensational growth occur on the same time scale as inhalation, where air residence times range between 2 and 5 s depending on the patients breathing capabilities.[118] Bulk phase dissolution, which dictates drug release into the body after deposition onto the lung wall, occurs on the scale of minutes to hours depending on the solubility of the compound.[152] One objective of this project was to use an EDB to collect data on the drying and dissolution kinetics of the BDP/glycerol mixtures in the aerosol phase. Such studies provide unique insights into the phase and size of the inhaled particles prior to deposition, the point at which bulk phase dissolution measurements commence. With these techniques, the full timeline of the inhaled drug can be explored, from generation, to inhalation, onto lung deposition and drug pharmacokinetics.

The results presented in this chapter determine the effect of two NvE in solution MDI formulations on the dissolution of emitted aerosols. Single particle measurements, modelling of particle dynamics and measurements drug dissolution in lung lining fluid are used to explore the effect of NvEs in MDIs.

Specific objectives were to:

- Study BDP aerosol particle processing in the presence of glycerol and ethanol as a NvE and co-solvent, respectively, using single particle measurements to explore excipient effects on size and phase state dynamics.
- Evaluate the impact of relative humidity (0, 45, 100%) on BDP particle development. Compare how aerosols form and measure under laboratory conditions correspond to aerosols inhaled by patients.

5.2   Measurements of MDI Aerosol

A single particle measuring technique was used to explore the drying and dissolution kinetics of aerosol particles formed from BDP-ethanol solutions, one containing glycerol and one without. To reliably generate single droplets for study, measurements were taken using solutions without the propellant HFA-134a. Given the volatility of HFA-134a, the propellant would be expected to evaporate within 0.004 s for droplets <10µm,[29] which is considerably faster than the evaporation of the co-solvent (<0.2 s).[31] Thus, although the droplets were not formed from an exact pMDI formulation, the evaporation of the co-solvent can be expected to play the more critical role in governing the aerosol microphysics on the timescale of 0.1-10 s studied here. The non-volatile components in each of the test solution consisted of drug (BDP) and a NvE. In this study, each solution will be referred to by the proportion of NvE in the non-volatile component. There were two BDP solutions tested in the aerosol phase: "glycerol 0%" (0% glycerol and 100% BDP constituting non-volatile component) and "glycerol 50%" formulation (50% glycerol and 50% BDP constituting non-volatile component) where the percentage of glycerol is expressed as a mass percentage (%w/w) of the non-volatile component. The glycerol absent formulation is made up of 97.5% (w/w) ethanol, i.e. 97.5% ethanol and 2.5% BDP, and the glycerol containing formulation 95% (w/w) ethanol, 2.5% BDP and 2.5% glycerol.

A comparative-kinetics electrodynamic balance (CK-EDB) was used to measure the dynamics of droplets formed from each solution when exposed to dry and saturated relative humidity (RH) at 20°C.[153] A detailed description of the EDB is given in Chapter 3. A specialised EDB was used for measurements at supersaturated conditions, >100% RH. This is achieved by creating a temperature gradient within the chamber and the addition of a water reservoir to the bottom electrode, the wet gas flow passes over the reservoir and becomes saturated prior to entering the chamber. Time-dependent crystallisation profiles (particle radius and phase) of droplets formed from the 0% glycerol and 50% glycerol BDP solutions were analysed using custom-written phase analysis software. A detailed description of the phase analysis software is given in Chapter 3. The characteristics of the phase functions can be used to assign the physical state of a particle.[111] The form of the phase function at each time point is used to assign the particle to one of the following morphologies:[111] an homogenous droplet,

a droplet containing inclusions, a droplet with a core/shell concentration gradient profile or a crystalline/non-spherical particle based on the regularity of the peaks. An example of water evaporation from a saline droplet on an EDB is shown in Figure 5.2a. The associated phase functions of a homogenous droplet and a droplet containing inclusions are shown in Figure 5.2 b & c, respectively. In the case of a crystalline particle, the angularly resolved light scattering pattern is erratic and no radial sizing can be collected from the phase functions. A good fit of both quadratic and polynomial function to the top of the peaks in a phase function is assigned homogenous. A droplet is said to contain inclusions when the angular peak spacings are regular, but the intensities are irregular, and the quadratic fit is poor (<0.98). A detailed description of using phase analysis for identify particle morphology is explained in Chapters 3 & 6.
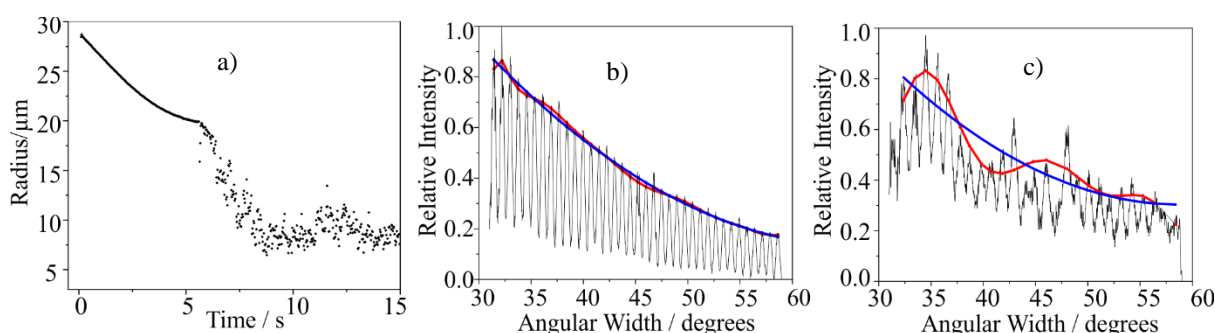
Figure 5.2. a) Radius of evaporating saline droplet as a function of time in dry air, resulting in a crystalline particle. b) Phase function of homogenous data point. c) Phase function of inclusion data point. Red line – quality of fit of polynomial function. Blue line – quality of fit of quadratic function. Functions fitted to the peak intensity maxima.

To collect aerosol particles for off-line analysis, a different electrodynamic trap was used to prepare particles, matching the environmental conditions (RH and temperature) of the aerosol dynamics experiments performed in the EDBs. This specialised trap is known as controlled electrodynamic levitation and extraction of bioaerosol onto a substrate (CELEBS). A detailed description of the instrument can be found in Chapter 3 and in the literature .[66,67,154] CELEBS consists of two ring electrodes, with droplets prepared by the droplet-on-demand generators discussed previously. Again, the charged droplets were captured within the trap before deposition onto a substrate after drying. The advantage of this form of trap is that a population of droplets (~30) can be manipulated simultaneously and then deposited, allowing samples consisting of many hundreds or thousands of monodisperse particles to be collected for post-analysis, with all following the same drying processes at the same RHs studied in the single aerosol particle dynamics measurements. These particles were then transported in petri dishes and taken for scanning electron microscopy (SEM) imaging, where their morphologies were analysed and compared to the particles collected from the PreciseInhale (see below). The particles were held for about 2 mins to ensure complete equilibration, before depositing on a statically charged petri

dish below. Particle samples were collected for two environmental conditions, broadly defined as rapid crystallisation (drying at 0% RH) and slow crystallisation (drying at 85%RH) to match the evaporation profiles measured in the EDB studies at 293 K. This was carried out for glycerol 0% and glycerol 50% BDP solutions.

5.1.3 Bulk Phase Measurements for an MDI Formulation

All bulk phase measurements discussed in this chapter were collected by colleagues at KCL. Their data are included in this thesis to draw relevant comparisons between bulk and aerosol phase measurements. They used several different sizing and dissolution techniques which are briefly outlined here. Additionally, colleagues from Chiesi formulated all the MDI canisters for both the aerosol and bulk phase measurements. Actuators and MDI valves with 63 µL fill chambers were provided by Bespak Ltd. The drug, beclomethasone dipropionate, and ethanol were supplied by Sigma Aldrich and HFA 227 (1,1,1,2,3,3,3-heptafluoropropane) were supplied by Mexichem Fluor. Solvents were of analytical grade Sigma Aldrich.

The proportional relationship between the MMAD of an HFA-134a solution aerosol population (µm) and the non-volatile component, n (%w/w), has been empirically derived:[145]

$$MMAD_{134} \approx 2.31 \; n^{1/3}$$

<div align="right">Equation 5 - 1</div>

In previous work,[151] formulations were designed to vary in the content of non-volatile excipient but produce similar aerodynamic size distribution by modifying the propellant, the actuator orifice geometry and metering volume. In this study, a series of five formulations for glycerol were designed using similar principles to produce similar APSD containing varying ratios between non-volatile excipient and drug.

BDP content % w/w	NvE Glycerol content % w/w	Ratio between NvE content and BDP content	NvE as a percentage of non-volatile component %
0.35	0	0:100	0
0.35	0.04	10:90	10

0.35	0.09	20:80	20
0.35	0.15	30:70	30
0.35	0.23	40:60	40
0.35	0.35	50:50	50

Table 5.1. Composition for glycerol test formulations.

Parameters such as the actuator geometry, propellant concentration and metering chamber were kept the same between formulations. Physical similarities of the device and formulation allowed for consistency in the desired fine particle fraction (proportion of particle population below 1 µm in radial size) obtained from each inhaler.[155] To prepare each formulation, the required amount of BDP powder was dissolved in ethanol and glycerol or isopropyl myristate was added to the bulk solution. The drug solutions were transferred to 19 mL aluminium cans which were then fitted with 63 µL metering valves. After crimping to specification, the cans were filled with the HFA 134a propellant to required mass. Cans were stored at 20˚C.

Each can was fitted with a 0.30 mm orifice diameter Bespak actuator and fired into an Anderson Cascade Impactor for aerodynamic characterisation. The total sampling flow rate was 28.3 L/min. A United States Pharmacopeia (USP) metal throat induction port was attached to the Anderson cascade impactor (ACI) to simulate throat geometry. BDP quantification was by UPLC/MS using a Waters Acquity UPLC. After quantification, the data was processed and analysed with Copley scientifics inhaler testing software (CITDAS). The metered dose, delivered dose, mass deposited per ACI stage, fine particle dose, fine particle fraction and mass median aerodynamic diameter (MMAD) were determined from the cascade impactor data.

Particles were collected from each of the test formulations via the PreciseInhale® (Inhalation Sciences, Stockholm Sweden) which was fitted with a USP induction Port No 1 to simulate throat geometry. The PreciseInhale has been used in *in vivo* studies for accurate dosimetry of inhaled formulation to animals[156] and for particle collection in dissolution studies.[157] Each inhaler was actuated into the 300 mL holding chamber with a 9-stage Marple cascade impactor attached to the outlet. All intermediate impactor stages were removed and BDP particles were deposited using a flow rate of 61.8 L/min on the last stage where a glass cover slip was placed. All evaluation of the pMDI formulations were conducted at ambient humidity and temperature, typically 32% RH and 22°C. To evaluate particle morphology, the particle-containing cover slips were imaged using a SEM.

For dissolution testing, particles were deposited on a glass microfibre filters grade GF/F using the same operating procedures described above. The filters were attached to watch-glass and transferred to a USP

2 dissolution apparatus containing surfactant (0.25% w/v) in a phosphate buffer solution. The paddle speed was 50 rpm and temperature was 37 ˚C. Samples were withdrawn over the course of an hour and replaced with equal volumes of fresh dissolution medium. BDP quantification in the samples was by HPLC.

Data from aerodynamic characterization of inhalers for both excipients were subjected to statistical analysis using the 2-way ANOVA (GraphPad Prism 8.0) to test for significance where differences were considered significant when p value < 0.05.

5.1.4   Comparing Aerosol and Bulk Phase Measurements of an MDI Formulation

The aim of this project is to bring together aerosol phase measurements, with a short time scale, and bulk phase measurements, with a longer time scale, of physical properties of an MDI formulation and the individual components. Developing an understanding of the full story, generation through to drug transport to the body, will facilitate development and selection of the initial MDI formulation. A schematic of the aerosol and bulk phase measurements presented here is shown in Figure 5.3. The aerosol phase measurements were carried out in BARC and liquid/bulk phase measurements carried out in KCL.
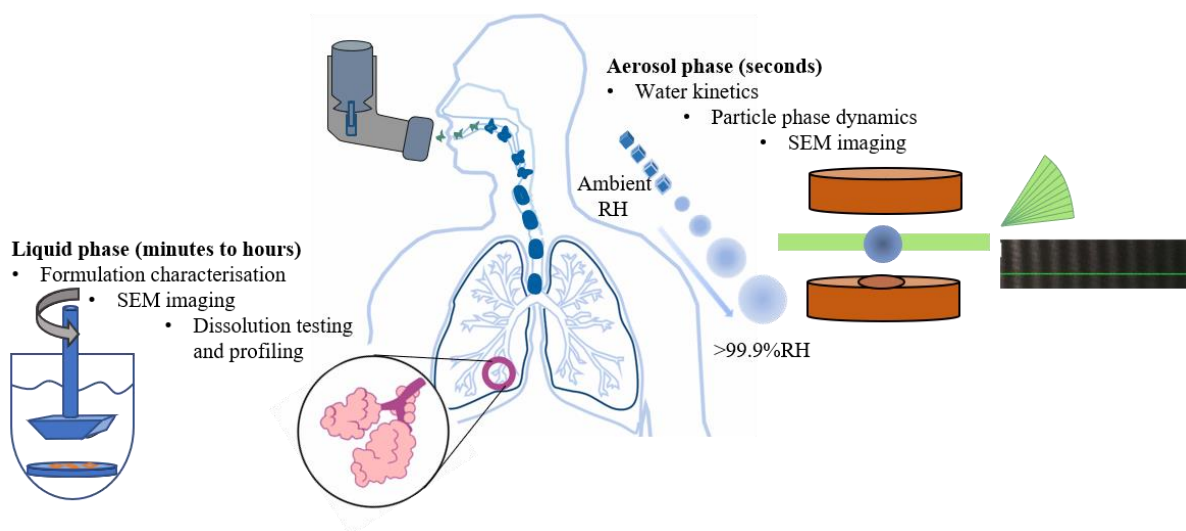
Figure 5.3. Illustration of the study objectives, detailing the relevance of *in vitro* techniques of aerosol and liquid phase procedures and measurements.

The aerosol phase measurements explore the particle dynamics occurring from generation to inhalation and through to deposition by simulating the exposure to changes in gas phase RH and probing the relevant timescales. The time scale for dynamical processes to change particle phase, moisture content

and composition prior to deposition is up to ~3 s, based on the internal commission on radiological protecting (ICRP) model.[116] Following deposition, bulk phase dynamics govern the pharmacokinetics affecting drug transport to the body. Bulk phase measurements of dissolution, replicating drug absorption by the lung wall, occur on the time scale of minutes to hours. It is vital to understand the particle size and phase prior to deposition.[158,28] The physicochemical properties of a deposited particle influence the bulk phase dissolution dynamics.

5.2.   Evaporation Kinetics of MDI Components

The results in this chapter are presented and discussed in two key sections: evaporation and crystallisation kinetics (i.e., the factors affecting the formation of the aerosol sampled for dissolution measurements) followed by dissolution/water uptake kinetics both in the bulk solution and aerosol phase in Section 5.3. Each section consists of a combination of aerosol phase and bulk phase measurements to develop a comprehensive understanding of the complete timeline, and the connection between aerosol microphysics and drug dissolution. Initially, aerosol phase measurements were used to identify the drying kinetics of each of the components individually followed by binary and then tertiary systems. Although these measurements are necessarily limited to studying the dynamics of individual droplets, they can be expected to provide insight into the rapid evolution in particle size, composition, and phase during the generation of aerosol from the pMDI and prior to sampling by the ACI or onto filter paper.

5.2.1   Evaporation Kinetics of Glycerol, Ethanol and Glycerol & Ethanol Droplets

Glycerol is referred to as a NvE in the context of pharmaceutical inhalers used by patients. However, glycerol in deposited particles evaporates over longer time periods (minutes to hours) that particles may experience during analysis, e.g., aerosol dissolution and imaging studies. Additionally, glycerol evaporation must be considered when storing drug formulations, as often formulations containing glycerol are stored in ambient or dry conditions for day, months, and years before use. To provide insight into the rate of glycerol loss, measurements were made of the evaporation rate of pure glycerol droplets at varying RH (0%, 40%, 85% and 95%). All measurements were performed on an EDB at 293 K over timescales consistent with the bulk phase measurements of this work. The percentage mass loss of glycerol as a function of time, in hours, is presented in Figure 4.a. Within 3 hours a glycerol droplet loses 93% of its mass under dry conditions, 37% in ambient conditions (45% RH) and 4% in humid conditions (85% RH). At 95% RH the mass loss is negligible, however these conditions are very

unlikely in storage or during bulk analysis measurements. The different rates of mass loss at different RH reflect the equilibrium moisture composition with varying RH. An increase in RH results in a decrease in glycerol concentration in the droplet, causing a reduction in component vapour pressure and, thus, mass flux. For example, a glycerol containing droplet collected and held for 2 hrs in ambient conditions will lose ~20% in mass prior to analysis. In a mixture droplet, the loss of glycerol is likely to affect the morphology, chemical stability, and crystallinity.[155] Therefore, when holding glycerol mixtures for use in analysis or storage of pharmaceutics, the timescale and RH must be considered in accordance with the data in Figure 5.4a.

The rate of evaporation of individual ethanol droplets was studied at a range of high RHs, 86% to 90%, using an EDB. Gregson et al. previously reported that a pure ethanol droplet is transformed into a pure water droplet by evaporation in a humid atmosphere, typically in <0.5 s.[31] After that time, the droplet evaporates at a rate consistent with a composition equal to that of pure water.[31] Measurements of the evaporation profiles of ethanol droplets at an RH from 86% to 90% are shown in Figure 5.4b. The initial radius of each droplet was ~25 µm, which is extrapolated using the linear relationship of ethanol evaporation within 0.2 s. The particle size reduces over approximately 1 s to ~17.5 µm. A decrease in radius corresponds to ethanol transferring into the gas phase, while evaporative cooling leads to condensation of water and the formation of a water droplet. Thereafter, the water droplet trapped at 90% RH evaporates at the slowest rate, whereas the droplet at 86% RH evaporates more rapidly. Differences in water evaporation rates reflect the differences in the degree of water saturation in the gas phase. The availability of water affects the gradient in gas phase concentration driving the diffusional transport of water away from the droplet. These measurements show that the process of ethanol evaporation (and indeed any propellant) is rapid and leads to water condensation due to substantial evaporative cooling. However, the timescale for significant changes in mass and composition is sub second, compared to the timescale of hours for change in glycerol composition.
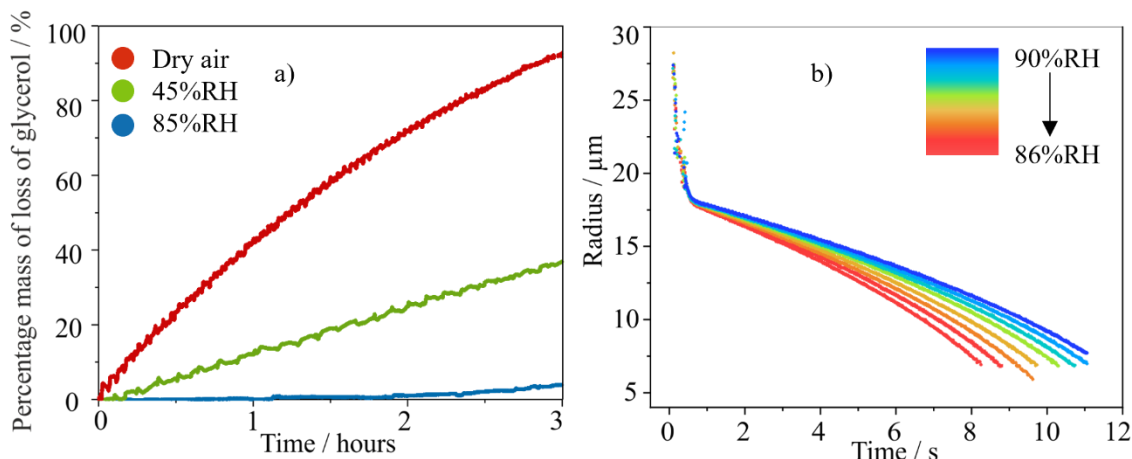
Figure 5.4. a) Experimental evaporation profiles of a glycerol droplet at 0%, 45% and 85% RH. b) Evaporation profiles of ethanol droplets at 86% to 90% RH. An abrupt change in the slope at 0.2 s indicates when the droplet has transformed to an almost pure water.

The evaporation of binary component droplets of glycerol and ethanol was measured to characterise the behaviour of the solvent compositions used in the pMDI formulations. As for the individual components, the evaporation was measured in dry, ambient, and high RH conditions. Specifically, the EDB was used to trap individual droplets and measure evaporation profiles at RHs of 0%, 40%, 85% and 95% relative humidity. The evaporation profiles of a droplet at each RH are shown in Figure 5.5. The binary mixture, investigated under dry and wet conditions, is 95% w/w ethanol and 5% w/w glycerol. However, the same mixture could not be used at 45% RH as the final droplet was too small to produce enough fringes in the phase function to accurately characterise the droplet size. It is well known that water and glycerol are fully miscible,[159] therefore the phase functions should always be consistent with an homogenous state. Thus, a higher concentration of glycerol was used to increase the final droplet size and to probe any dynamic changes in the phase state, 90% w/w ethanol & 10% w/w glycerol.
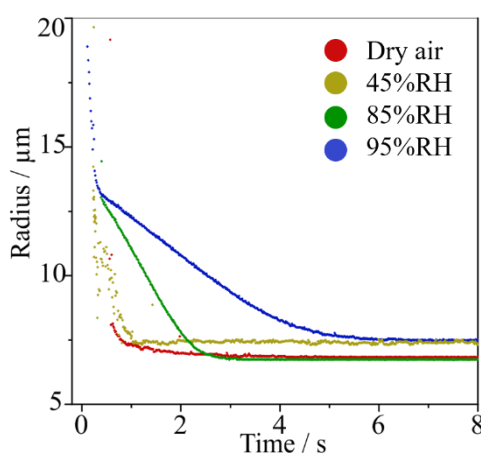
Figure 5.5. Evaporation kinetics of a mixed droplet of glycerol and ethanol at 0%, 45%, 85% and 95% RH, 293 K

139

In dry and ambient conditions there was no visible abrupt change in evaporation gradient in the time dependence of droplet size. Rapid evaporation with no subsequent water evaporation is a consequence of the low water activity in the gas phase and the limited extent of water condensation on to the evaporating droplet. The evaporation kinetics are consistent with the evaporation of ethanol and result in an almost pure glycerol droplet forming within 1 s. In humid conditions, at RHs of 85% and 95%, an abrupt change in evaporation gradient is seen at a size of ~13 µm consistent with a droplet composed of water and glycerol. The competing factors of the loss of latent heat and the warming of water condensation result in a similar abrupt change in evaporation gradient whether the RH is wet (85%) or very wet (95%). Once ethanol evaporation is complete, the reduction in particle size is governed by the evaporation of water. At 95% RH the mass loss of water from after the abrupt change in evaporation gradient until 1 s is 52%, whereas at 85% RH the mass loss of water from the droplet is 25%RH.

The measurements for individual and binary solvent mixtures show that when aerosol droplets are inhaled into a high RH environment, they absorb considerable water. The rate of water evaporation is determined by the surrounding RH and glycerol content. The co-solvent evaporates completely on timescales of <1 s. The high RH of the airways will mean that the rate of loss of water will be slow and particles will contain water throughout a typical inhalation/exhalation cycle to the point of deposition. On these timescales, the fraction of glycerol lost by evaporation will be minimal. When particles are generated under laboratory conditions (i.e., intermediate RH) for measurement of aerodynamic particle size distribution or dissolution testing, they will continue to lose glycerol over a timescale of hours. Formulations containing glycerol will retain considerable water in equilibrium with the surrounding RH which will be lost at a rate determined by the rate of loss of glycerol.

5.2.2. Evaporation Kinetics of a Propellant, Ethanol and Glycerol Mixed Droplet

An evaporation profile of an MDI droplet is shown in Figure 5.6. The droplet consists of 1% glycerol, 13% ethanol and 86% HFA. The concentration of each component in the droplet presented here is frequently used in the pharmaceutical industry. An MDI used by a patient will also contain an API, however the concentration of an API is negligible when considering the impact on the aerosol microphysics. For experimental purposes, droplets containing only propellant, co-solvent and a non-volatile excipient were examined. The process of measuring droplet dynamics of an MDI droplet in an EDB is extremely complex. An outline of the system and techniques used is explained in Chapter 3.

Due to the extreme boiling point of HFA, -26.3 °C, evaporation is rapid. The effect of droplet evaporative cooling on water condensation is shown in Figure 5.4b. with the example of ethanol. In a

humid environment, water from the gas phase condenses on to the cooled droplet as ethanol evaporates rapidly.[31] In the case of an MDI droplet, HFA evaporation is quicker than that of ethanol. In Figure 5.6. it is shown that after HFA evaporation, 0.01 s, an ethanol, glycerol, and water mixed droplet remains. Following, ethanol evaporation, 0.2 s, results in the formation of a glycerol and water binary droplet. Water condensation can be inferred to occur during both ethanol and HFA evaporation. Figure 5.4b suggests a pure ethanol droplet with starting radius 27 µm converts to a pure water droplet of size 17 µm at 90% RH. An HFA/ethanol/water/glycerol droplet of 27 µm starting size in Figure 5.6 transitions to a water/glycerol droplet of 14 µm. The data suggests that the amount of water condensing onto the particle is similar during ethanol and HFA evaporation. HFA evaporation is quicker than ethanol, leading to a larger reduction in droplet temperature. However, a larger reduction in droplet temperature does not appear to increase the amount of water condensing on. Therefore, it is suggested that condensation on to a cooled droplet, after ethanol or HFA, is gas phase diffusion limited rather than droplet temperature dependent. Once the propellant and co-solvent have evaporated, the size dynamics of the droplet are governed by the hygroscopicity of glycerol. The final radial size of the droplet is determined by the equilibrium between the water activity in the droplet and the RH of the gas phase. In Figure 5.6. the droplet appears to equilibrate at a radial size of ~8 µm. Assuming the concentration and hygroscopic response of an API is negligible, during actuation of an MDI any droplets of starting size 27 µm or larger will be too large for deep lung deposition. Therefore, water uptake during volatile component evaporation must be considered when predicting lung deposition. The data show that the droplet experiences a sudden size change of about -15 µm (HFA and ethanol evaporation). Rapid evaporation is followed by a further size change of about -6 µm (water evaporation). Similar droplet dynamics can be expected during inhalation of a plume of MDI droplets.

Solvent	HFA – 134a	Ethanol	Water	Glycerol
Boiling point	-26.3 °C	78 °C	100 °C	290 °C
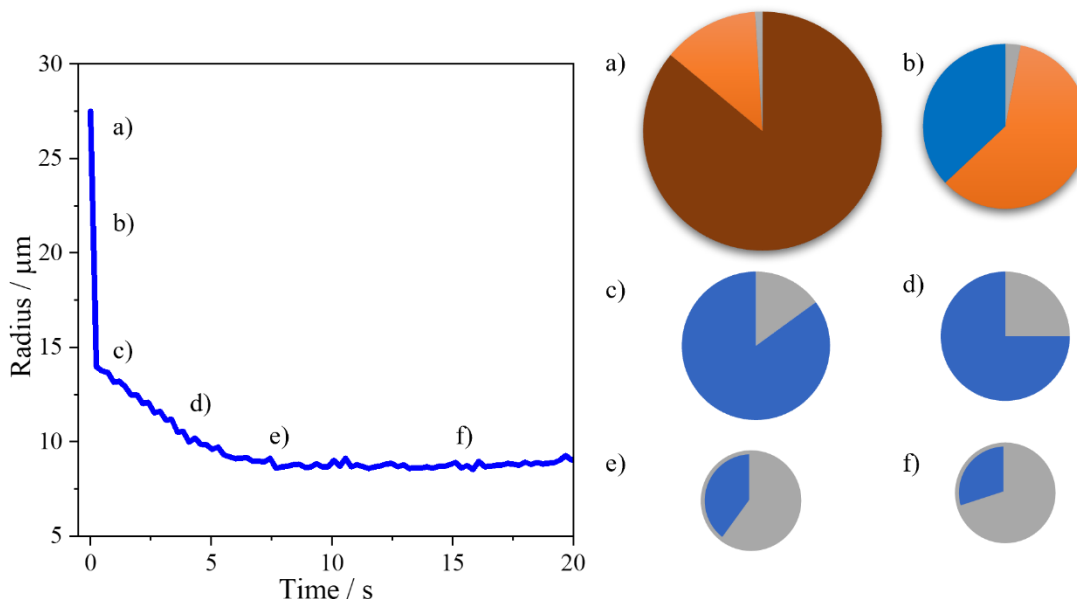
Figure 5.6. Evaporation of a droplet from an MDI canister made up of 1% glycerol, 13% ethanol and 86% HFA. Measured using an advanced EDB "single particle levitation at saturated humidity" (SPLASH) at 90% RH, 293 K.[2]

Often water condensation, and subsequent droplet dynamics, is overlooked when measuring deposition fraction.[28] The data presented here clearly show that water condensation kinetics on evaporatively cooled MDI droplets have a significant impact on the final size and should be considered in future lung models and cascade impactor measurements. Upon the evaporation of ethanol and HFA, the droplet will experience rapid cooling due to the transfer of energy away from the droplet, leading to a reduction in the saturation vapour pressure of water at the droplet surface. Gregson et al. found that in certain conditions (>45% RH), water from the gas phase will condense on to a cooled droplet after ethanol evaporation.[31] The rate of the %volume change of the droplet depends on the change in droplet temperature and the water availability in the gas phase. A consistent %volume change above a set RH could be a contributing factor to the inefficiencies observed with in vivo MDI research, as the actual final size is not what would be seen in a cascade impactor measurement taken in ambient conditions.

5.2.3. Evaporation, Condensation and Phase Behaviour of BDP, Glycerol and Ethanol Droplets at Varying RH

Measurements were made over 70-80 s to cover the kinetic events that can be expected during a patient inhalation event, or the laboratory measurements of aerosol properties reported in Sections 5.3.2 and

5.3.3. Measurements were made for each formulation and RH combination for 10-20 droplets. Representative individual droplet measurements are presented in Figure 5.7. Phase functions are included in the presentation of the evaporation profiles below to identify the points of a phase transition. Based on the single and binary component studies, the initial rapid decrease in radius can be attributed to the evaporation of ethanol, which occurs at approximately the same rate independent of relative humidity and starting composition, is complete within 0.2 s from droplet generation and causes concomitant condensation of water vapour from the surround vapour phase via evaporative cooling, except under conditions of dry air.[31]

The kinetics of a glycerol 50% formulation containing BDP is shown in Figure 5.7a with the measurement performed under dry conditions, <5% RH. Unlike measurements with ethanol and glycerol alone or as a binary solution, glycerol 50% is observed to form a droplet containing solid inclusions. The final radius of the droplet appears to be ~1/2 of the initial droplet size when held in dry air. It is likely that BDP inclusion crystals are suspended within a semi-spherical glycerol droplet. A droplet containing inclusion particles can be inferred from the change in the angular light scattering profile. The phase function retains uniformly distributed diffraction peaks, but with significant noise in light scattering intensity.[111] In comparison, glycerol 0% in dry air is shown in Figure 5.7b. The droplet has a smaller final radius due to the absence of glycerol, with a morphology that more closely represents a spherical particle. The rapid drying rate leads to a particle of compact shape, with a composition that is just BDP.

The ethanol evaporation and concomitant water condensation kinetics were measured at an RH 45% to represent typical air humidity in a laboratory setting. Within 20 s, glycerol 50% formed a droplet with inclusions and glycerol 0% formed a crystalline particle. In Figure 5.7c the water activity of the gas phase is 0.45. In ambient conditions a glycerol 50% droplet contains BDP inclusions suspended in a glycerol/water mixture. Consistent with Section 5.2.1, water condenses onto the droplet as the ethanol evaporates and subsequently evaporates within the first ~18 s. The particles persist as BDP inclusions within a liquid glycerol droplet beyond the measurement time of 80 s as the loss of glycerol is slow.[143] Glycerol 0% forms a droplet containing inclusions, shown in Figure 5.7d, consisting of water and undissolved BDP particles. After 18 s, once the water activity of the droplet has equilibrated with that of the gas phase, the BDP particles agglomerate to form a solid crystal and the particle contains no water. It should be noted that the size measurements reported have large uncertainty (± 1.5 µm) in Figures 5.7 c&d, a consequence of the inhomogeneity in particle phase and composition and the associated challenges of interpreting the phase function. However, the focus here is on establishing the timescale for the evaporation kinetics and the resulting phase state.

At 85% RH, Figures 5.7 e&f, particles generated by the glycerol 50% and glycerol 0% formulations showed similar behaviour to those at 45% RH but with noticeable differences attributable to the higher humidity. Both formulations formed droplets containing an aqueous component; notably, the wet size of the glycerol-containing formulation was larger at 85% than 45%. Both formulations produced initial signatures indicating spherical liquid droplets containing BDP crystal inclusions. Then, after a water loss phase, which was slower at 85% RH compared to 45%, the particle became predominantly crystalline. The particle in Figure 5.7e from the glycerol formulation formed crystallised BDP and retained glycerol over the period of measurement.

At 95% RH, Figures 5.7 g&h, droplets from both formulations remained spherical in shape with inclusions, presumably of BDP. The light scattering phase functions were considerably less noisy than those at lower RH, suggesting an almost homogeneous particle despite the inclusions. The angularly resolved fringes can be tracked and host droplet sizes of glycerol 50% and glycerol 0% estimated. The presence of glycerol in Figure 5.7g lead to a larger equilibrated droplet size due to the hygroscopic growth of glycerol. However, the droplet formed from the glycerol-free solutions also remains spherical with the presence of inclusions. To retain water, even at such high RH, some of the BDP must be solubilised within the aqueous phase. Water retention is consistent with previous measurements of the hygroscopic growth of BDP particles which suggest BDP particles have a growth factor of 1.2 at ~95 % RH.[158] The small variation in the equilibrated particle size over long period (<1 $\Box$m) reflects the very slow mass transport of water in the vicinity of saturation RH. Additionally, it is likely there is a slow upward drift in RH when making measurements under conditions of extremely elevated RH, and possibly also slow dissolution of BDP inclusions into a BDP/aqueous solution droplet.
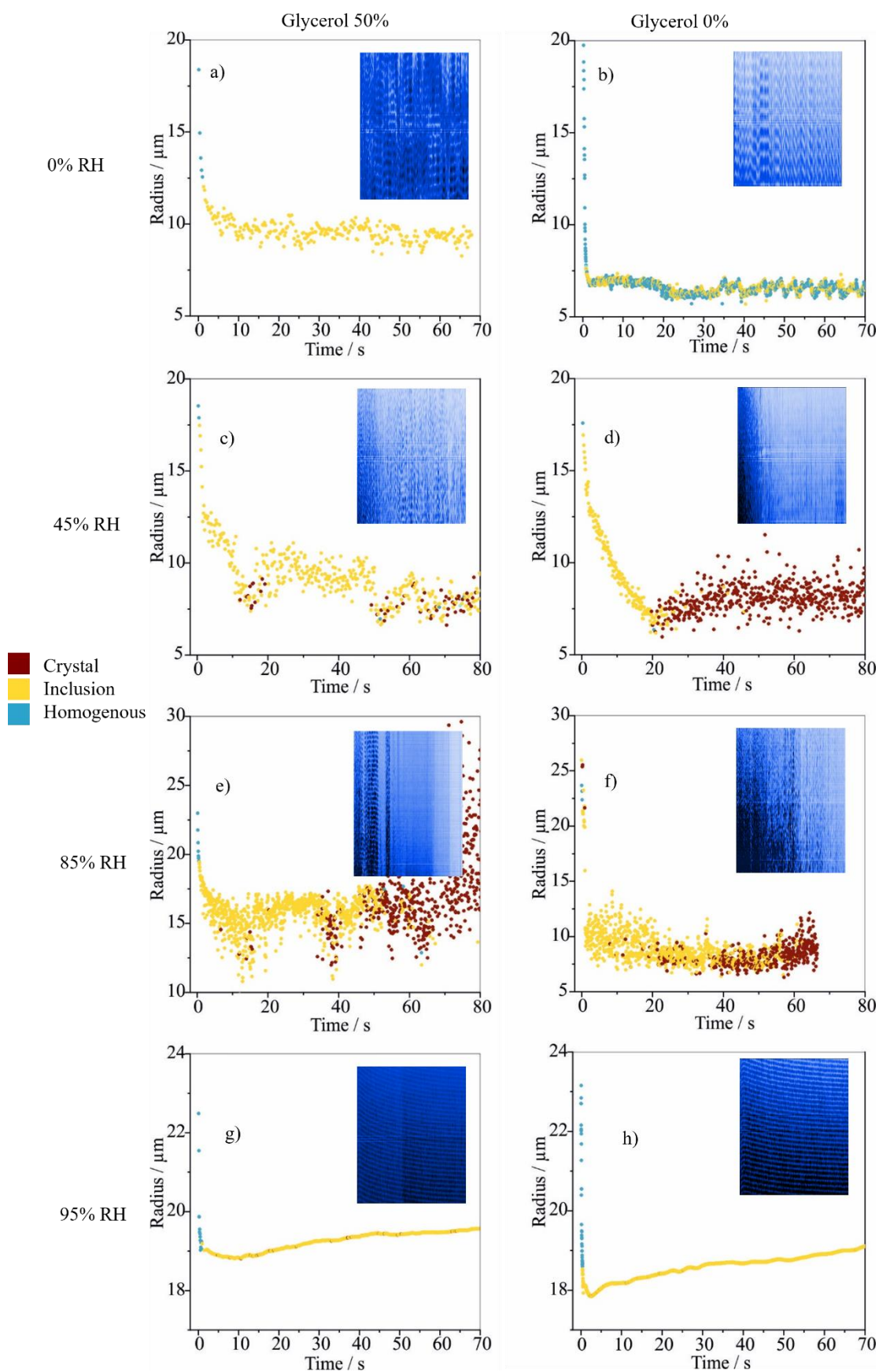
Figure 5.7. The evaporation of ethanol and condensation of water on droplets with compositions of glycerol 50% (left column) and glycerol 0% (right column) at varying RH: dry air (0%RH, a&b),

ambient conditions (45%RH, c&d), humid conditions (85%, e&f) and wet conditions (95%, g&h). The phase of the particle is identified at every time point: homogenous (blue), inclusions (yellow) and crystalline (dark red).

At RHs below 95% RH both the glycerol 0% and glycerol 50% exhibit signs of crystallisation, where a droplet that once contained inclusions appears to form a solid crystal. In the case of glycerol 0% at 85% RH an inclusion droplet is formed after the process of ethanol evaporation and water condensation. However, the BDP particles come together if given enough time to form a thermodynamically favourable state, a crystal. Plasticisation can be seen for glycerol 50%, however the timescale of crystal formation is longer. It is possible that due to the presence of glycerol, the BDP inclusion particles diffuse slower throughout the bulk phase of the droplet and therefore take longer to form an ordered state. MDI formulations often include an insoluble API, it is expected that, similar to BDP, these non-hygroscopic drugs will not fully dissolve even at high RHs. Instead, an inclusion droplet containing undissolved drug particles will form. The inclusion droplet formed during inhalation has potential to transform to a solid crystal prior to deposition if the particles have diffused to form an ordered state within the time scale, e.g. ~8 s. Crystallisation would have significant impact on the pharmacokinetics of the drug. In the case of BDP, at high RH and within 70 s, the BDP particles in Figure 5.7 do not form a crystal, with or without the presence of glycerol.

The measurements in Figure 5.7. are examples of observations seen when analysing multiple droplets. A collation of all data from the individual measurements of glycerol 0% at 95% RH is provided in Figure 5.8. to show the reproducibility of the droplet measurements in Figure 5.7. The outcome of this work is to explore particle dynamics of an MDI formulation, rather than absolute size changes. Therefore, a fair representation of each formulation at each RH is displayed in Figure 5.7.
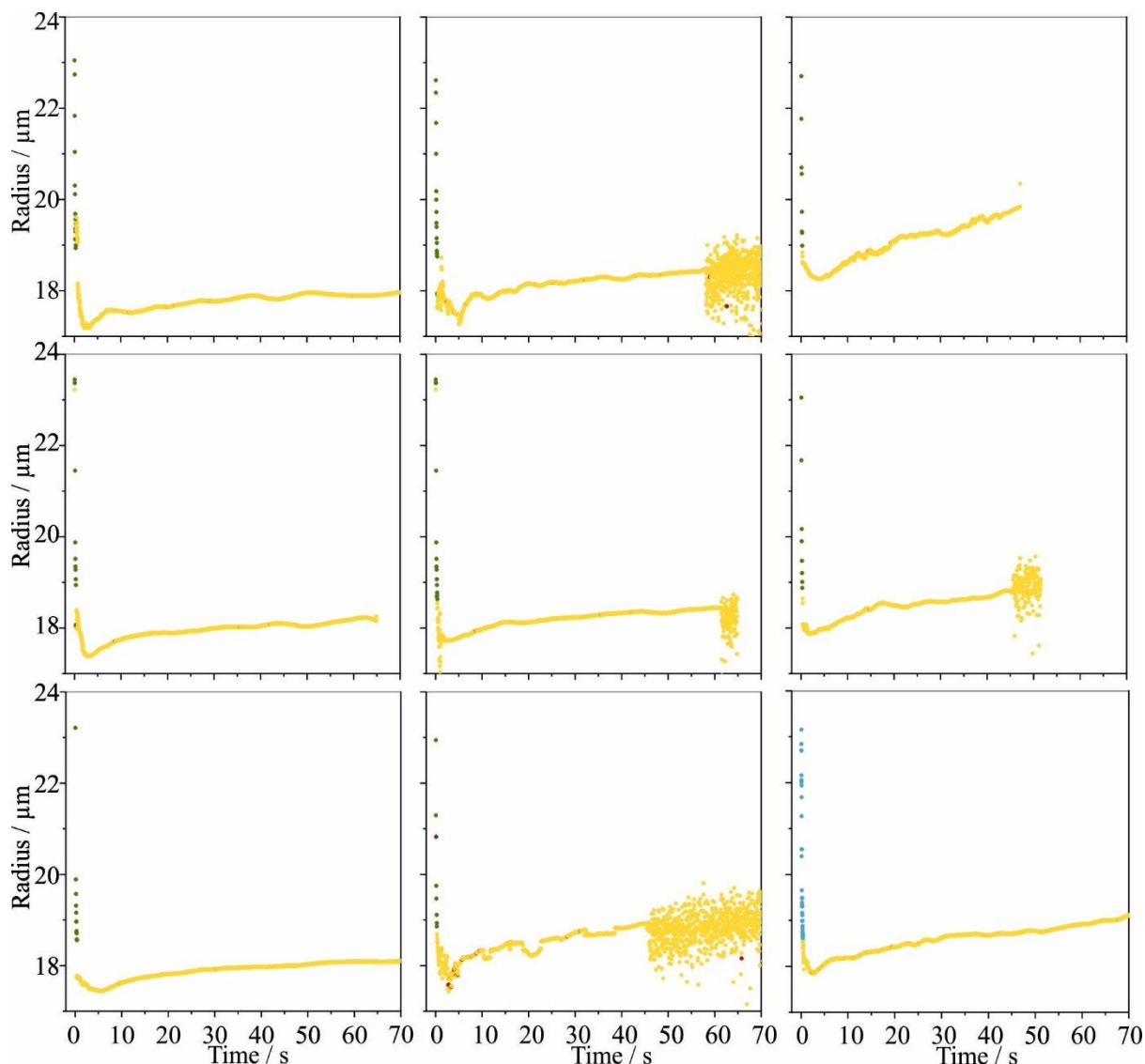
Figure 5.8. Droplet profiles of glycerol 0% formulation at 95%RH, collected on an EDB. An inclusion droplet was formed in every case with a similar final size. Peak tracking was used to correct for radius size. Note, noisy data points were not able to be corrected due to considerably more erratic light scattering. Bottom right figure is presented in the main text, Figure 5.7, as a fair representation of the phase dynamics for this formulation and conditions.

Kinetic measurements of the two formulations at 95%RH show a significantly larger final radius than that of the particles at 85%. Figures 5.7. g&h highlight a unique process: droplet growth following the initial abrupt change in the evaporation and after water condensation. Following the initial water uptake, the droplet appears to grow to 117% of the droplet volume after the abrupt gradient change following ethanol evaporation. Droplet growth after water uptake is seen for both formulations. However, Figure 5.7g indicates that a glycerol containing droplet experiences a larger increase in radius, which is as expected given glycerol's hygroscopic properties. In all other cases the final radius is less than the radius of the newly formed aqueous droplet. To explore the process of droplet growth after ethanol evaporation

measurements were taken for binary droplets of ethanol and glycerol at a range of concentrations. The droplet dynamics were measured on an EDB in ambient conditions, 45% RH, and humidified conditions, 95% RH. The evaporation and condensation kinetics of ethanol/glycerol droplets are shown in Figure 5. 9. The profiles show a water/glycerol droplet, originally an ethanol droplet with a w/w concentration of 20% glycerol, grows in humid conditions. Therefore, the effect of glycerol concentration on droplet growth in humid conditions must be considered when formulating a mixture for MDI use.   No water/glycerol droplet growth is seen for any other w/w glycerol concentration at 95% RH or 45% RH.
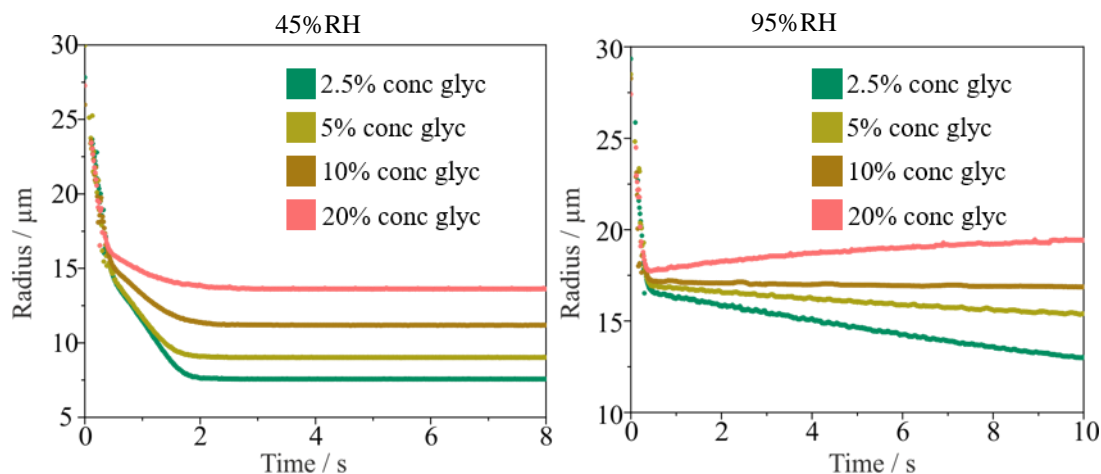
Figure 5.9. Ethanol and glycerol droplets of varying concentration trapped in ambient and wet conditions.

In conclusion, aerosol droplets generated by pMDIs from the formulations containing glycerol as a NvE will likely have solid BDP inclusions within host glycerol droplets with a water content governed by the RH to which they are exposed. At intermediate RHs, BDP inclusions may aggregate to form a particle that significantly departs from sphericity. A similar picture emerges for formulations without glycerol, with water replacement of the volatile solvents occurring on short timescale driven by evaporative cooling. BDP will be dispersed as insoluble inclusions within an aqueous droplet that loses water at a rate governed by the surrounding RH. At very high RH, as encountered in the lungs, the water content may persist for timescales longer than inhalation/exhalation and BDP will be present in the form of solid inclusions with some dissolved within the aqueous phase of the inhaled aerosol.

5.2.4. Morphology of Dried BDP, Glycerol and Ethanol Particles

Samples of particles matured under the wet (85% RH) and dry (0% RH) conditions for single particle measurement were collected and analysed by SEM for glycerol 0% and glycerol 50% formulations. CELEBS was used to levitate multiple droplets (10-30) until crystallisation occurred,[66] which was ~1 minute for droplets held in wet conditions. After crystallisation the particles were then deposited onto a glass slip and taken for SEM imaging. It was not possible to access the very high RHs studied in

Section 5.2.1 as CELEBS could not capture and sample large numbers of particles for SEM analysis, so an upper limit of RH of 85% was used to explore the affect that wet conditions have on the resulting particle structure and shape. The images in Figure 5.10. complement the drying profiles in Figure 5.7. by showing the morphology of particles formed under the kinetics dictated by the different environments. It is well known that particle chemistry and morphology influence dissolution rates.[160] The single particle analysis showed that BDP particles will crystallise due to its low aqueous solubility at any RH as ethanol is rapidly replaced by water generating supersaturated conditions.

Representative SEM images for glycerol 0% and glycerol 50% formulations in dry air and 85% RH are shown in Figure 5.10. In dry air ethanol evaporates rapidly without water condensation, whereas at 85%RH, ethanol evaporates rapidly but with water condensation and subsequent water evaporation. The SEM images show broadly similar structures in different conditions when the formulation contain glycerol but differ for the formulations without glycerol. When formed in dry air, it is suggested that the presence of glycerol, Figure 5.10.a, gives structural integrity to the particle morphology leading to the formation of a spherical particle. SEM images in Figure 5.10b suggest that the BDP inclusion particles diffuse to the edge of the droplet during evaporation, resulting in a uniformed spherical, hollow shell. The shell in Figure 5.10b appears to be made of many smaller inclusion crystals and is larger than that of Figure 5.10a due to the higher RH. At elevated RH, the water partitioned into the glycerol phase during drying remains volatile and is lost from the particle on exposure to the high vacuum in the SEM analysis, leading to particles that have some buckling deformation. However, once again the BDP shell is apparent.

A uniform shell is not observed when evaporation is rapid, i.e., dry air, and glycerol is not present. The undissolved particles suspended in a droplet do not have time to diffuse to the edge and form an ordered structure. Rapid evaporation and crystallisation results in the formation of a fragile crystal in Figure 5.10c. Upon deposition compact, fragmented particles in Figure 5.10c are formed from the rapid drying (loss of ethanol) of the glycerol-free formulation. Figure 5.10d shows a buckled BDP particle with no glycerol present. Without glycerol, the particles formed under both dry and humid conditions are much smaller, appear brittle and show considerable deformation on SEM analysis, although the shell can again be assumed to be formed from BDP. Large particles that appear deflated in the SEM are formed when the glycerol-free formulation is dried at elevated RH. The deflated particles in Figure 5.10d reflect the collapse under vacuum conditions. Deflation occurs during analysis of a porous structure due to the acquisition and loss of water during particle maturation.

Generally, NvE content together with any resultant change in particle morphology, was the only variable expected to affect the dissolution rate of BDP from these formulations. Glycerol containing droplets appear to be more structurally stable once dried. SEM images show that glycerol 0% droplets

have shrivelled as they were exposed to vacuumed conditions, however glycerol 50% has kept a spherical structure.
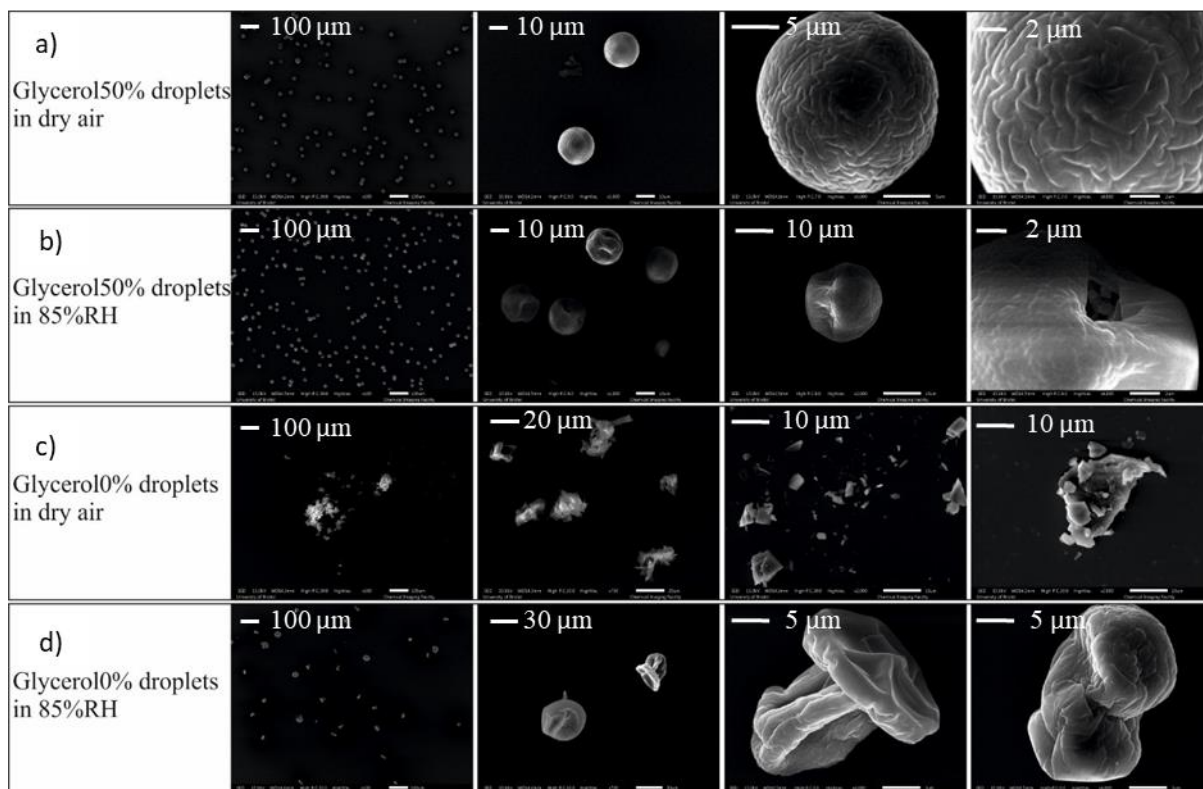
Figure 5.10. SEM images of 0% glycerol & 50% glycerol BDP particles collected on CELEBS in dry air and 85% RH, 293 K.

The rationalisation of morphologies in Figure 5.10. can be seen to be broadly consistent with the drying measurements presented in Fig. 5.7, but differs from that of Lewis et al. 2014,[151] where the replacement of evaporating ethanol by condensing water is not considered. Images in Figure 5.10 can be compared to particles collected under laboratory conditions where intermediate RH persists in studies using similar formulations and inhalers formulated for this study.[150,151] The particles collected by KCL, Grainger et al. and Lewis et al., Figure 5.11, show similar morphologies to particles observed in SEM images at BARC. However, the particles shown in Figure 5.11. appear more porous and less spherical than in Figure 5.10. Grainger et al. found that the glycerol absent BDP particles had some crystallinity, whereas glycerol containing BDP particles were amorphous.[150] They characterised crystallinity using powder X-ray diffraction. The particles corresponding to 0% glycerol formulations in Figure 5.11 appear more like the particles formed in 0% RH than 85% RH in Figure 5.10. Whereas the particles corresponding to 50% glycerol in Figure 5.11 exhibit a consistent morphology that is observed for glycerol-containing particles at high, low, and intermediate RH.
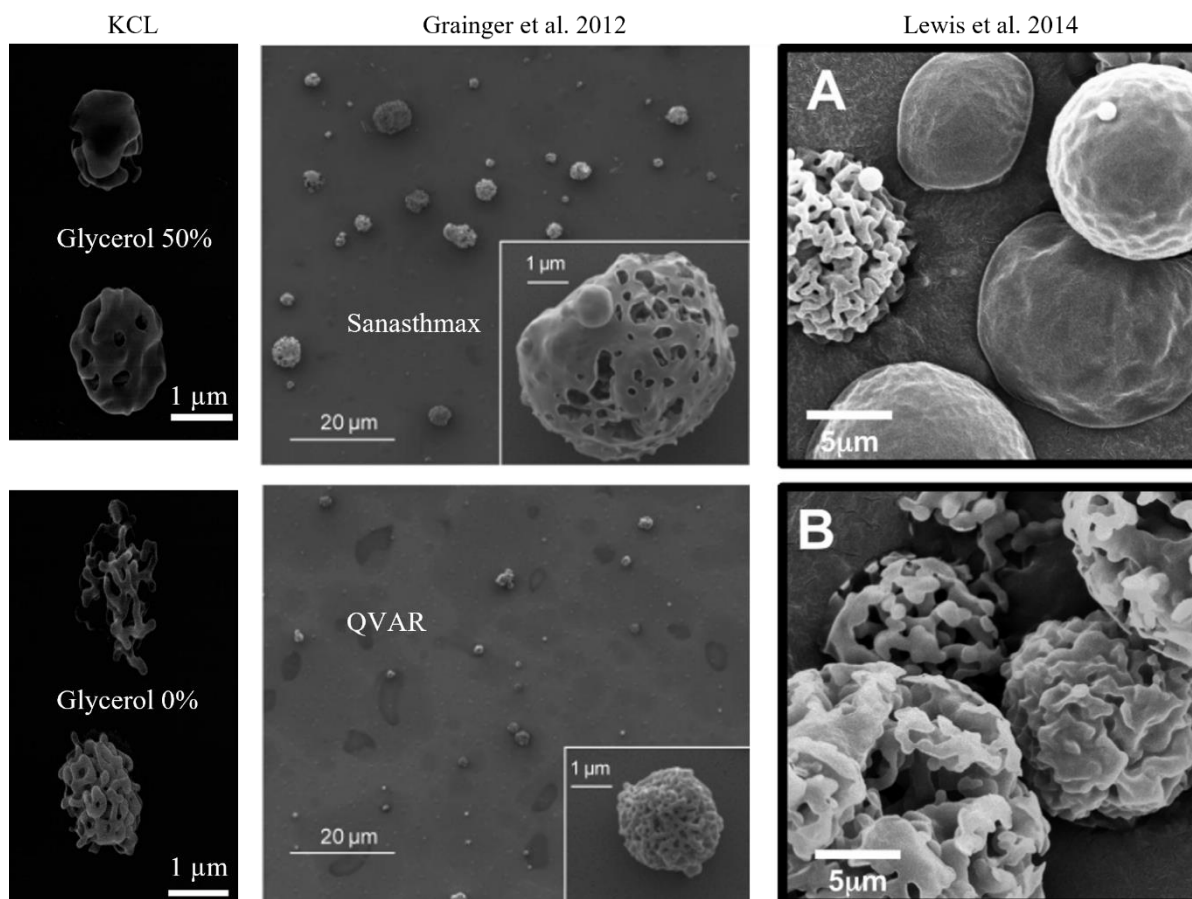
Figure 5.11. SEM images of glycerol 0% and 50% collected in ambient conditions at KCL. SEM images collected by Grainger et al. of BDP formulations generated from different inhalers: Sanasthmax (glycerol present) and QVAR (no glycerol).[150] Lewis et al. collected BDP particles with (A) and without (B) glycerol.

5.3. Aerosol Phase and Bulk Phase Dissolution Measurements of an MDI Mixture

The results in this section explore the dissolution dynamics of an MDI droplet in the aerosol phase compared with the bulk phase. Single particle measurements were carried out using SPLASH in super saturated conditions. Bulk phase dissolution measurements were carried out using a beaker and stirrer technique. Additionally, a cascade impactor was sued to collect a size distribution of an MDI mixture containing BDP. The results in Section 5.3. are representative of the inhalation processes occurring after the particle dynamics discussed in Section 5.2. Upon deposition, within ~2-5 s, bulk phase dissolution governs the efficiency of drug transport around the body, as well as the phase state of the deposited particle.

Formulation manufacture in this study took a Quality-by-Design (QbD) approach to the process where careful selection of components and device parameters was employed to achieve desired effects on

formulation performance.[158] For inhaled drugs like BDP that are poorly soluble in water, the absorption into lung tissue which is the preferred site of action may be dissolution rate limited.[161] If systemic targets are desired, then the dissolution rate may become an indirect predictor of onset of action of the active component. So, dissolution may be a key quality attribute to contribute to clinical behaviour of inhaled drugs.[162,163] Additionally, it has been suggested that where dissolution testing of inhaled formulations may not be directly predictive of *in vivo* behaviour, there is likely merit in using it to distinguish between formulations like the ones in this study that may have different release profiles.[142] Therefore, to determine how drug disposition may be affected by NvEs inhaled formulations dissolution profiling was selected as an indirect, *in vitro* measure of *in vivo* performance.

5.3.1. Water Condensation Kinetics on an MDI Formulated Particle in a Saturated Gas Phase

Experiments were conducted with glycerol-ethanol-BDP solutions (glycerol 50% and glycerol 0%) in supersaturated humidity using a specialised EDB, SPLASH. The aerosol phase dissolution profiles for BDP droplets are shown in Figure 5.12. No dissolution for either glycerol 0%, a, or glycerol 50%, b, is seen. Phase analysis shows erratic light scattering and no sizing is available. Figure 5.12. indicates that the BDP particles do not dissolve prior to deposition in the lung or in a cascade impactor.

The final sizes of particles in Figure 5.12 are much smaller than those in Figure 5.7. There are three possible reasons for a difference in final particle size for measurements taken on an EDB compared with SPLASH. Firstly, as mentioned above, the data presented here do not show absolute size changes but rather indicate particle dynamics. Therefore, it could be that the trapped particles in Figures 5.12 and 5.6 are of the same size, but erratic light scattering has given he impression of a large radial difference. Secondly, plasticisation is a crystallisation process described in Chapter 4. Plasticisation occurs when amorphous particles take up water, allowing space for the solute ions to rearrange and a form a more thermodynamically stable crystalline state. The plasticisation RH of non-soluble compounds is often close to the deliquescence RH (DRH), >99% RH in the case of BDP.[164] Therefore, it is possible that in saturated conditions an amorphous BDP particle will take up water and begin crystallisation. Upon formation of a crystalline BDP particle, further size or phase dynamics will be limited as dissolution of a crystal is much slower than that of an amorphous particle. Unlike the amorphous particle in Figure 5.7, a crystalline particle will not grow until dissolution commences. Figure 5.12. indicates that no dissolution is seen for 100 s for both glycerol 0% and glycerol 50% formulations in saturated RH. Finally, a difference in particle size between EDB and SPLASH data could be due to the solutions used for each measurement. The measurements in Figure 5.7. were carried out within 3 weeks after receiving the vials from KCL, thus the mixture is assumed to still contain 97.5%

ethanol. However, in the case of the SPLASH measurements in Figure 5.12, there was an interim period of a couple of months. It could be that some ethanol had evaporated from the solutions, thus increasing the concentration of BDP. A change in formulation is likely to have impacted the final residual size. However, dissolution dynamics of a BDP particle will not be affected by a decrease in ethanol concentration.
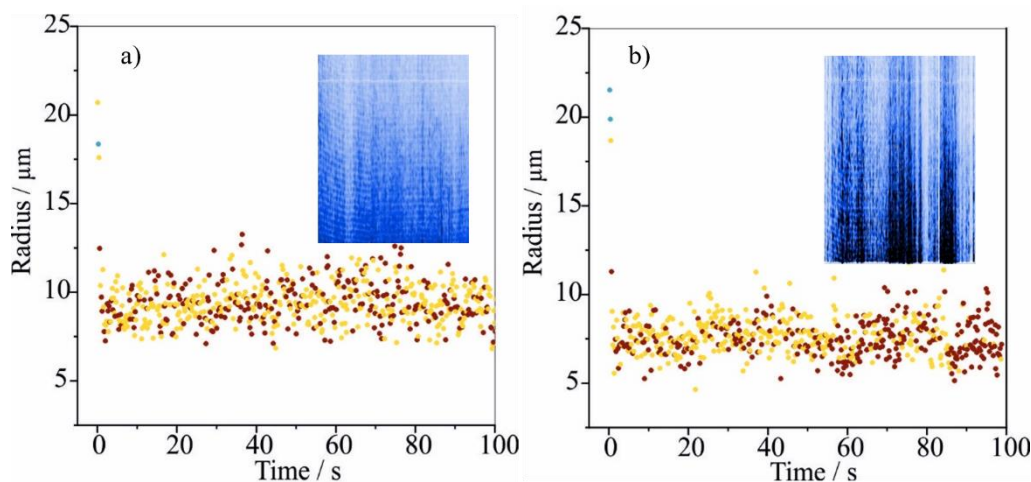
Figure 5.12. Glycerol 0% and glycerol 50% at >100% RH on SPLASH, a) & b) respectively.

Dissolution is a result of the deliquescence process, which is a first order phase transition of the solid to a saturated solution.[42] Deliquescence is prompted at a well-defined RH that depends on the temperature and the properties of the substance.[99] Once this RH is reached, the thermodynamically favoured phase is the aqueous solution phase, commencing dissolution. The crystalline solid surrounded by water molecules is favourable when the RH is below the DRH (deliquescence relative humidity). Non hygroscopic solids can resist dissolution even when the RH is above 100%. The total amount of dissolved solid is a function of its solubility in water, mass and droplet volume.[165] BDP is a poorly water-soluble drug, 1.6×10^{-4} g/L.[166]

5.3.2. MDI Aerosol Characteristics Measured on a Cascade Impactor

The work presented in Sections 5.3.2 and 5.3.3 was carried out by colleagues at KCL, it is included in this chapter to draw comparisons between aerosol phase and bulk phase measurements. The MDI formulations were designed to deliver 250 µg of BDP with each actuation. The difference in the formulations came from the varying amount of glycerol incorporated, all other components were identical. In addition to the 5 formulations manufactured, a formulation with 0% excipient was created to contain only BDP, ethanol and HFA 134a i.e. without a non-volatile excipient. The aerosol particle size distribution as determined from cascade impaction is shown in Figure 5.13. Within particle size distributions in Figure 5.13., with increasing NvE%, there is trend of decreasing amount of BDP in

lower stages of the ACI. Figure 5.13. indicates that the presence of NvE increases the proportion of drug particles with larger aerodynamic size dimensions.
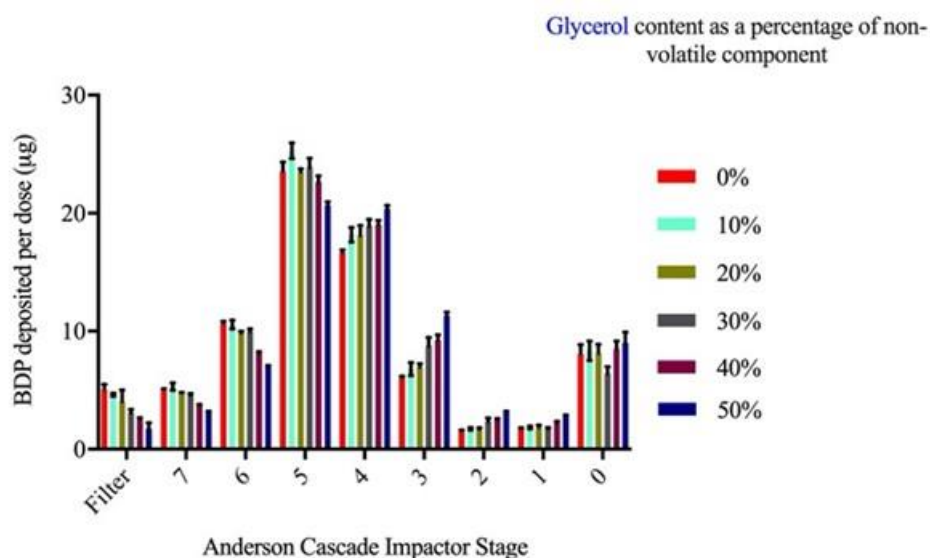
Figure 5.13. ACI stage deposition profile for glycerol/BDP formulations. Values = mean ± SD from n=3 cascade impaction measurement. Collected by colleagues at KCL.

To investigate a possible relationship between particle morphology as affected by excipient, and in vitro dissolution rate, the aerosol particles collected for dissolution were examined using SEM. The particles which form after the evaporation of volatile excipients (HFA-134a and ethanol) were roughly spherical with varying surface textures between the excipients (Figure 5.11 KCL). The glycerol containing formulations had a distinctly different surface topologies which appeared to smooth with increasing amount of glycerol in the formulation. As described previously, the glycerol 0 and 50% particles have similar appearances to with those in Figure 5.11 in dry air. More than a 1:5 glycerol:BDP ratio was required before the excipient conferred a smooth surface.

It is shown that glycerol containing droplets reach a larger final radius than glycerol absent droplets at a range of relative humidities. A larger final size is due to the water retention properties of glycerol.[167] During a standard inhalation, in a very humid lung, little to no glycerol will evaporate and therefore a stable droplet size will be seen. Interestingly, increasing volume fraction of NvE appears to slightly reduce the amount of drug particles in smaller size ranges and increase, in almost proportional fashion, the amount of larger drug particles.

5.3.3. Dissolution of an MDI Formulation in The Bulk Phase

Dissolution profiles of test formulations were measured with the process of deposition on to filter paper by Precise Inhaler followed by transfer to a USP 2 rotating apparatus. The dissolution profiles were calculated over time by measuring the change in BDP concentration of the solution within the apparatus. Dissolution times were obtained for all test formulations and comparisons between them were made. All profiles in Figure 5.14 appear to follow a first-order kinetics with dissolution rate of BDP reducing over time, regardless of percentage of excipient present in the formulation. There appears to be an inverse relationship between the amount of non-volatile excipient present in the formulation and the dissolution rate of BDP from the formulation. The 0% excipient dissolution rate exceed all the formulation containing glycerol. In general, the trend is towards slower amount of BDP release with increasing NvE content in the pMDI formulation.
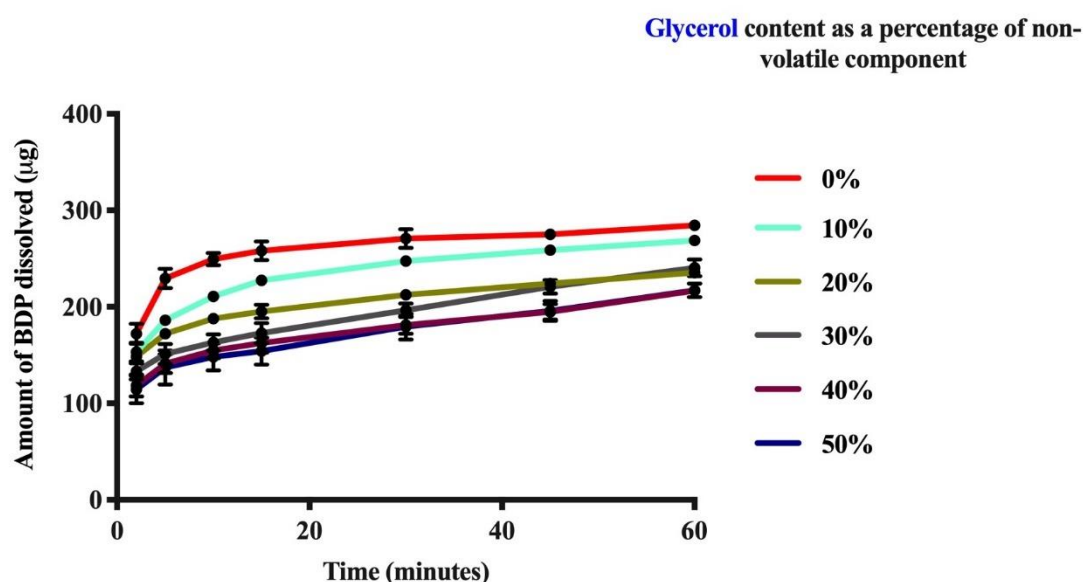
Figure 5.14. Bulk phase dissolution profiles of glycerol 0% up to glycerol 50%. Collected by colleagues at KCL.

The rate of dissolution decreased with increasing non-volatile excipient content. A dose-dependent relationship is suggested to be due to process of particle formation prior to dissolution (*in vitro*) or prior to deposition (*in vivo*). Upon release of the formulation from the inhaler and following evaporation of propellant and then ethanol, if there is significant water availability, water molecules will condense on to the droplet. Following condensation a BDP inclusion aqueous droplet will form,[31] with or without glycerol depending on the formulation. A droplet containing inclusion particles is seen to occur for all droplets held at 45%RH and upwards in Figure 5.7. Additionally, a binary droplet containing glycerol and BDP inclusion is formed when glycerol 50% is held in dry air. It is suggested that the BDP particle

is coated with the glycerol in Figures 5.10 and 5.11, which could prevent water molecules readily detaching BDP ions. Slow detachment of ions will also slow the dissolution rate. In comparison the glycerol-free formulation forms a more porous BDP particle, which leads to a higher surface area and a reduced dissolution rate. As previously mentioned, with molecules like BDP that tend to dissolve slowly, there is an increased risk of dose depletion due to mucocilary clearance mechanisms before an optimal amount of drug has dissolved and is absorbed into the lung tissue.[11] Thus, dissolution rate may be delayed by the presence of excipient. A decrease in dissolution rate will extend the residence time of drug in the lumen. Extended exposure could have far-reaching consequences in terms of lung tissue concentration for locally acting drugs, and total bioavailability for drugs intended for extra-lung effects.

5.4   Chapter 5: Summary

This chapter introduced a common formulation used in MDIs. Aerosol phase and bulk phase measurements of all components were carried out to better understand the particle dynamics occurring during inhalation. The inclusion of an NvE in an MDI formulation was discussed, highlighting the physicochemical reasons why glycerol is often added to an MDI mixture. Single particle measurements, using an EDB, were carried out to explore the size dynamics of individual components and as a mixture. It was shown that as a droplet rapidly cools as a consequence of ethanol or HFA evaporation, water condenses on to the droplet. The inflexion point was found to be dependent on the droplet temperature and water availability in the gas phase. After 82% RH the %volume change from ethanol to water becomes constant. A constant mass flux can lead to growth of a particle a very high relative humidities, or high solute concentration. After water condensation the droplet dynamics are governed by the water kinetics and the hygroscopicity of the API and excipient, if present.

Evaporation kinetics of glycerol were discussed, often evaporation of an NvE is overlook due to the low volatility. However, evaporation must be considered when carrying out laboratory measurements or storing MDI formulations. The morphology of dried BDP particles, with and without glycerol, were discussed. The SEM images between KCL and BARC matched well, however the particles collected by KCL appeared more spherical and more porous. All glycerol containing particles appeared to have a more stable and less porous structure.

It was shown that BDP does not fully dissolve under any conditions in the aerosol phase within a 4-minute time frame. Therefore, it is likely to deposit on the lung surface as a non-homogenous droplet, potentially partial dissolution will take place. Additionally, in high RHs an inclusion, or amorphous, particle can transition to a more thermodynamically stable crystalline state. In the bulk phase, there was an inverse relationship between the amount of non-volatile excipient present in the formulation and the dissolution rate of BDP from the formulation. Cascade impactor measurements show that glycerol

containing droplets reach a larger final radius than glycerol absent droplets at a range of relative humidities.

Chapter 6

Dynamic Measurements of Crystallisation and Dissolution of Individual Suspended Particles

Aerosols transform between physical phases as they respond to variations in the environmental conditions. There are many industries that depend on these dynamic processes of crystallisation and dissolution, and a better understanding of water evaporation and condensation on an aqueous droplet in the aerosol phase could improve the efficacy for applications such as drug delivery to the lungs. The effectiveness of drug delivery to the lungs is largely governed by the size dependent deposition fraction and the pharmacokinetic properties of deposited particles. This chapter aims to better understand the phase state of the particle upon deposition. Here, a single particle measuring technique is used to explore the crystallisation and dissolution dynamics of a model system, sodium chloride. The physical and environmental factors that influence the dynamics of crystal formation from a saline droplet and the kinetics of water adsorption onto a dried particle are examined. The drying relative humidity (RH) is shown to impact the physical properties of the dried particle. When a saline droplet was injected into an airflow at an RH close to efflorescence RH (ERH) an individual, single crystal formed. Whereas, when a compositionally equivalent saline droplet was injected into dry air a salt crystal made of multiple crystalline particles was formed. The crystal shape, morphology, and surface area were all found to affect the dissolution dynamics of the dried particle. Crystallisation and dissolution measurements of an active pharmaceutical ingredient (API), salbutamol sulphate, and an excipient, lactose monohydrate, were also explored. The dissolution rate of an amorphous particles was found to be faster than that of crystal particles. The results provide insight into the dynamic behaviour of drug particles upon inhalation from a dry powder inhaler (DPI).

6.1   Introduction to Crystallisation and Dissolution of particles in Drug Delivery to the Lung

6.1.1   Water Kinetics During Droplet Evaporation and Condensation in Drug Delivery to the Lung

The presence of water in air influences the physical and chemical properties of aerosol particles.[168] The moisture content in air can impact on the physical state, size and chemical structure of an aerosol particle.[87] Spray or freeze drying techniques are often used to produce dried particles from solution droplets ready for human consumption, where the most common industries include food or pharmaceutical production.[169] The process of spray drying can form amorphous or crystalline particles;

depending on the solute properties, rapid water evaporation can form amorphous particles whereas slower evaporation can lead to the formation of an energetically more stable crystalline form.[170] Amorphous particles are seen as an ideal formulation for drug delivery to the lungs when quick dissolution is required. Amorphous particles are often used in pharmaceutics for devices such as DPIs. However, amorphous particles are much less resilient to variations in environmental conditions, particularly RH.[171] By contrast, crystalline aerosol particle often show slower dissolution once a threshold RH is achieved, with an induction time as water first adsorbs to a particle surface.[170]

The dissolution of solid particles in the aerosol phase, i.e. the uptake of water vapour by dried particles to form a solution droplet, has implications on the efficacy of drug delivery to the lungs.[172,173] The deposition fraction and location of particles delivered to the lungs are dependent on particle size and the particle phase state at the point of deposition influences the pharmacokinetics.[174] A greater understanding and control over the dissolution kinetics of solid particles during inhalation may afford opportunities to improve the efficacy of an inhaled aerosolised mixtures.[95] Although there has been much research regarding the condensation kinetics of water on amorphous aerosol particles,[87] there is limited literature on the condensation and dissolution of crystalline particles in a humid environment.[152]

The response of a crystalline aerosol system to RH is governed by the efflorescence – deliquescence cycle, distinct for different chemical systems; consider the process for sodium chloride (NaCl) in Figure 6.1a. The radial growth factor (RGF) is calculated as the ratio of the wet radius to the dry radius, where the dry radius relates to a sphere-equivalent of dried pure solute while the wet radius is the equilibrium size the particle will adopt at a given RH. Efflorescence, the formation of a crystal on de-humidification and drying, occurs when the water activity in the solution droplet phase falls below a certain critical value and the solute can no longer be held in a metastable solution. Deliquescence, transformation from solid to a saturated aqueous solution phase, occurs when water molecules adsorb onto the surface of a solid until complete dissolution; this process occurs at a well-defined RH dependent on the substance. The concentration of the solution droplet at the deliquescence RH (DRH) is equivalent to the solubility limit of the substance in the bulk phase, known as the saturation limit. An aqueous sodium chloride droplet will crystallise once the RH is less than or equal to 45% RH, and will deliquescence at an RH of 75%, water activity 0.75.

The four key stages of the deliquescence process for a sodium chloride particle are shown in Figure 6.1b. When the ambient RH is below the DRH, water interacts with the solid particle via adsorption. Sodium chloride can absorb 2-3 monolayers of water at an RH < DRH before bulk dissolution is seen.[43] As the RH increases, more water adsorbs onto the solid surface via capillary condensation until the RH of the gas phase is higher than the DRH, at which point a solute saturated film forms around the solid. The film is the basis of the continued deliquescence water condensation process as it has a lower vapour

pressure that that of pure water. The water in the saturated film has a lower thermodynamic activity relative to water in the gas phase, providing the driving force for continued water condensation onto the particle until complete dissolution and equilibration with the water activity, RH, of the gas phase.[43]

Experimental examples of three different evaporation profiles of a NaCl droplet using the electrodynamic balance (EDB) are shown in Figure 6.1c. The droplets are dried producing physically different particles. At 50% RH NaCl remains in solution and forms a droplet equilibrated with the gas phase. At 40% RH and 0% RH there is not enough water present to keep NaCl in solution and thus a crystal particle is formed. The saline droplets have a starting radius of 20 to 22.5 µm, where their final size depends on the water activity of the gas phase and initial droplet solute concentration. The starting mass fraction of solute (MFS) of NaCl equilibrating at 50% RH is 0.1, where the water activity in the starting droplet is 0.93. Whereas the MFS of droplets at 40% and 0% RH is much higher, 0.2. A droplet with a high initial MFS will equilibrate at a larger radius compared to that at a lower MFS at similar RH. Additionally, the rate of evaporation is also affected by the initial MFS and RH. The droplet at 40% RH begins to equilibrate at about 16 µm compared to 11 µm for the droplet at 50% RH. Sodium chloride effloresces at a water activity of 0.45 or below, Figure 6.1a, droplets in Figure 6.1c have crystallised. The rate of crystal nucleation, according to classical nucleation theory, increases with increasing degree of solution supersaturation (lower RH, in this case).[175]

By contrast, the water uptake profiles of a dried sodium chloride crystal when the RH is elevated to 95% RH (blue), 80% RH (red) and 95% RH (green) are shown in Figure 6.1d. There are two particles introduced to a humidified gas flow (95% RH), one profile is condensation of a liquid droplet and the other dissolution of a dried particle. The dissolution profiles begin from sodium chloride crystals of 6 µm, red, and 7.5 µm, green. The crystal dissolution profiles show a lag period between time after RH switch (t=0 s in Figure 6.1d) and time until homogenous. This thesis investigates the factors affecting the dissolution lag, such as RH, crystal size and crystal morphology. The blue curve shows a condensation profile of a saline droplet from starting radius 10 µm at 95% RH with droplet growth limited by gas phase diffusion, where water uptake is spontaneous after an increase in RH but governed by the rate of mass transport in the gas phase.[88] The liquid droplet introduced to 95% RH in Figure 6.1d equilibrates at a radius dependant on the solute mass and RH.[39]. In the case of a liquid droplet, condensation leads to equilibration. However, in the case of water uptake by a dried crystal, the dissolution process is influenced by additional limitations It is suggested that dissolution commences after an induction period of capillary condensation, where a saturated film forms at the particle's surface.[42] The induction period shown in Figure 6.1. and dissolution dynamics of dried particles are discussed in this chapter.
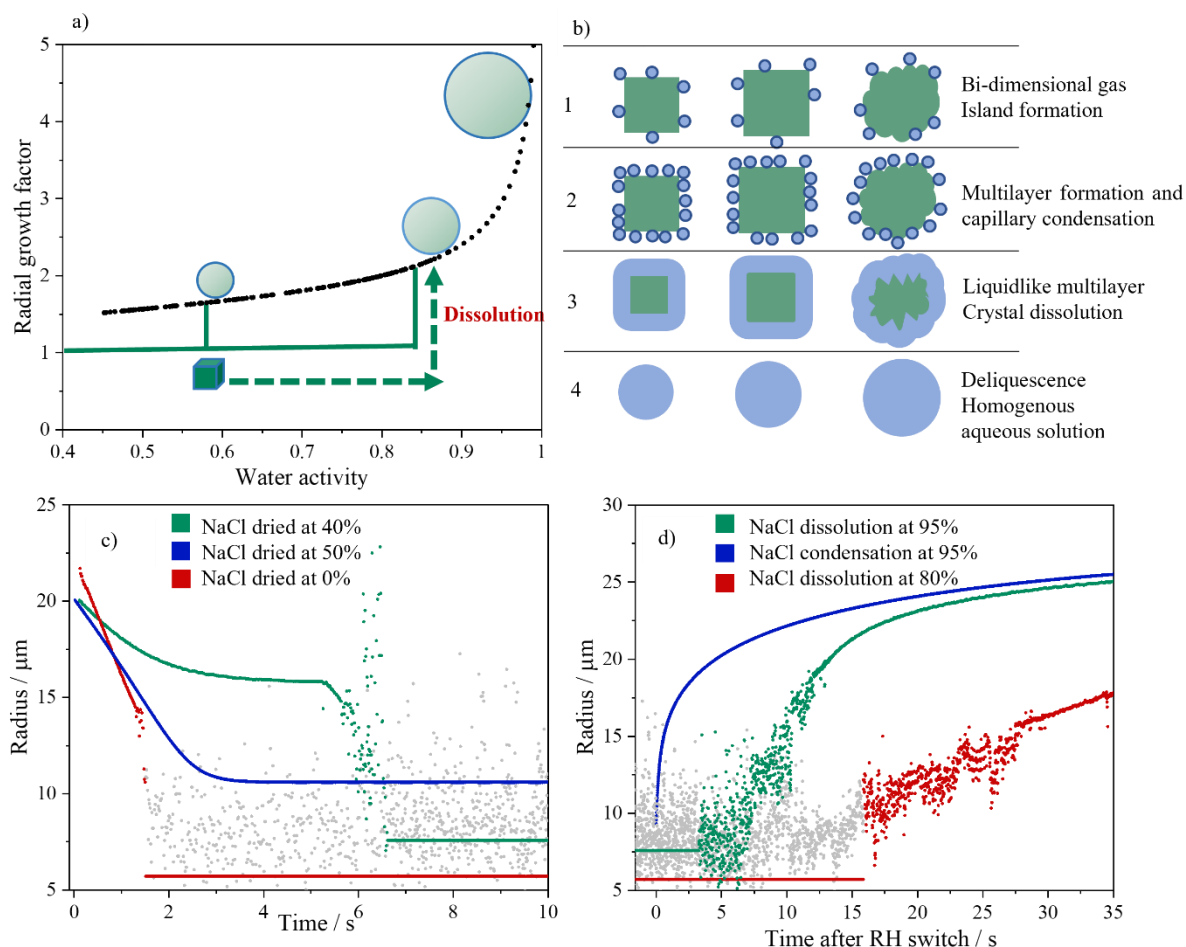
Figure 6.1. a) The hygroscopic growth curve of sodium chloride, highlight efflorescence and deliquescence. b) Diagram of the deliquescence process. c) Experimental evaporation profiles of sodium chloride droplets 40%, 50% and 0% RH. d) Experimental dissolution profiles of dried sodium chloride particles at 95% and 85% RH. As well as experimental condensation profile at 95% RH.

The aim of this work is to identify physical properties and environmental conditions that influence the crystallisation and dissolution processes of inorganic and pharmaceutically relevant aerosol. Control of dissolution is shown to be possible, and the dissolution kinetics of a well characterized crystalline particle, sodium chloride, in the aerosol phase are explored using a single particle measuring technique. The dissolution and crystallisation kinetics are compared between crystal and amorphous particles.

6.1.2   Measurements of Dried Particles and Dissolution with an EDB

Studies of the crystallisation of sodium chloride droplets are reported first, followed by the dissolution kinetics of the dried particles with varying environmental conditions. The capability provided by the

EDB to rapidly change the RH in the gas phase from very low RH (e.g. dry) to very high (>90% RH) allows a droplet to be dried until the point of crystallisation, and then switched to above the DRH to observe the dissolution kinetics and how they depend on the evaporation and crystallisation step.[96] The dissolution and condensation rates were explored by changing factors such as the initial drying conditions, the dissolution RH, and crystal surface area and morphology by varying the concentration of solute in the initial droplets generated by the droplet on demand (DoD) generator. As an example, the water evaporation kinetics and condensation kinetics of three saline droplets are compared in Figures 6.1 c&d respectively. In this figure, we compare the evaporation and condensation of water via a homogenous aqueous droplet (50% RH) and salt crystals prepared from drying at low RH (0%) and an RH just below the efflorescence humidity (40% RH).

In all measurements, the distinct character in the light scattering profile can be used to characterise the physical state of the trapped particle. Four different droplet/particle phase states (spherical/homogenous droplet, droplet containing inclusions, droplet with core-shell/concentration gradient and crystalline particle) have distinct scattering patterns.[111] The point of crystallisation is identified by a transition between identifiable scattering patterns. Using the plots in Figure 6.2, the exact timeline of the phase change can be retrieved. The regularity in the angular separation between the peaks in the phase function are expressed in terms of relative standard deviation (RSD) of the average angular separation.[111] A thorough description of the method of phase analysis using light scattering is described in Chapter 3. Next, the angular variation of each peak is fitted with polynomial and quadratic curves, which provided correlation coefficients of the polynomial and quadratic fits. These three parameters were used in the morphology assignment for each time frame.[111] As an example, the polynomial fit, RSD value and radius are presented as a function of time for a single particle in Figure 6.2. Consistent with our previous work which examined over one million phase functions recorded from particles of a variety of known morphologies, if the RSD value is greater than 0.4 then the particle can be characterised as inhomogeneous.[111] The polynomial fit can be used to determine when the particle transitions from an inclusion droplet to a crystal, or vice versa.[111] A detailed description of phase function analysis is outlined in Chapter 3.
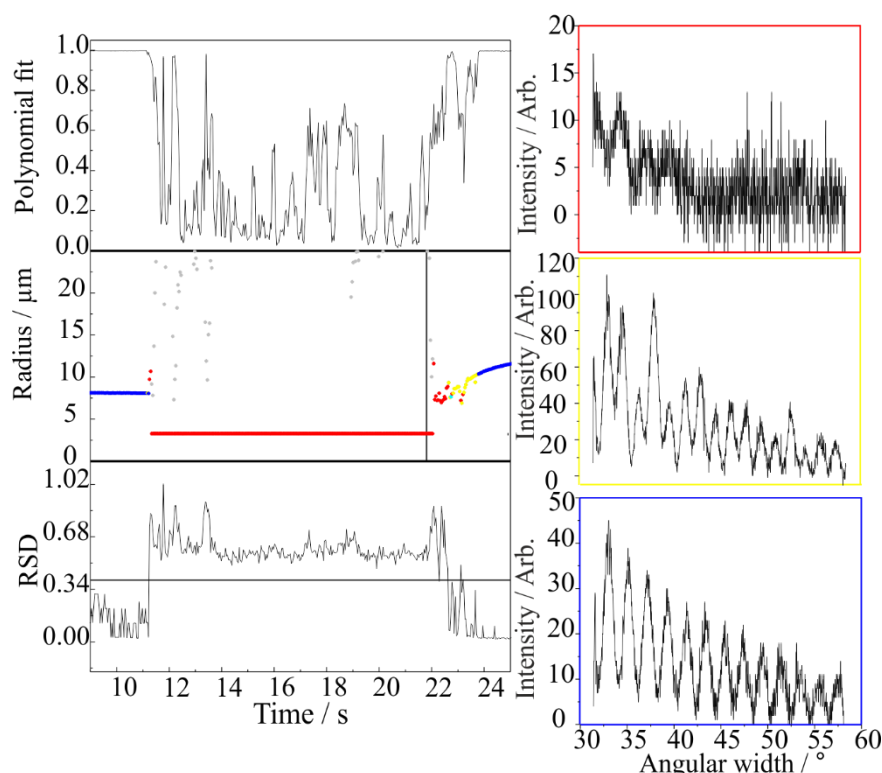
Figure 6.2. The polynomial fit (top) and RSD value (bottom) for all phase functions during droplet lifetime (middle) were used to distinguish between inclusion, crystalline and homogenous phases. Above an RSD value of 0.35 (horizontal black line) the particle was characterised as non-homogeneous. The RH was switched from dry air to wet (90% RH) at the time indicated by the vertical black line, ~20.9s, in panel. The particle transitions from crystalline, before switch, to inclusion and homogenous, after switch. The phase functions in the red, yellow, and blue boxes are examples of a crystalline, inclusion and homogenous phase function, respectively.

6.2   Dynamic Crystallisation of Aqueous Aerosol on an EDB

Crystallisation kinetics of NaCl and other pharmaceutically relevant aerosol were measured using an EDB. Crystallisation and dissolution, measurements do not require comparative kinetics unlike work in Chapter 4. Thus, only one droplet on demand dispenser was required, the sample. Control of the RH was the most important aspect in this work and extreme conditions were reached to truly replicate inhalation. An inhaled drug generated from a DPI is stored in dry conditions, 0% RH, and subsequently introduced to an ambient environment, 45% RH, prior to inhalation. In this section factors affecting the water kinetics during crystallisation are explored, such as the drying conditions.

6.2.1 Changing Rates of Water Evaporation During Crystallisation of Sodium Chloride

Individual saline droplets of known composition were trapped in the EDB at RHs in the range from dry (2%) to the efflorescence RH (45%). The angularly scattered light patterns were analysed using the phase analysis software described in Chapter 3. The phase of the particle at times during evaporation was identified as homogenous, inclusion or crystalline. Estimates of the dry radii of each particle, shown by the horizontal red lines in Figure 6.3, were calculated from the starting radius and concentration using the following equations,

$$DV\ (g) = \frac{SC\left(\frac{g}{ml}\right) \times SV\ (ml)}{CD\left(\frac{g}{ml}\right)}$$

$$DR\ (\mu m) = 1000 \times \left(\left(\frac{DV}{\Pi}\right) \times \left(\frac{3}{4}\right)\right)^{\frac{1}{3}}$$

where *DV* is the dry volume (g), *SC* is the starting concentration, *SV* is the starting volume (ml), *CD* is the crystal density (g/cm^3, 2.165 g cm^{-3} for sodium chloride) and DR (µm) is the dry radius. The estimation of the dry radius assumes a homogeneous spherical shape, an unlikely morphology for a sodium chloride crystal. However, *DR* allows for relative comparison of dry sizes between all droplets. Additionally, the dry mass of sodium chloride was subsequently estimated from the dry radius which gave an absolute measurement.

The saline droplets in Figure 6.3a, b&c were exposed to different drying conditions which led to varying crystallisation rates. In all environments drier than 45%RH, the efflorescence RH, the droplet surface recedes as water evaporates into the gas phase. At a critical supersaturation point achieved at the droplet surface (a critical supersaturation of ~2, i.e. a concentration of twice the solubility limit),[122] NaCl particles nucleate to form inclusions within the remaining solution.[122] Eventually, the crystals grow as water continues to evaporate and the suspension of undissolved crystalline particles merge to form a single dry particle. However, the time taken for a droplet to transform to a dried crystal differed depends on the environmental conditions.

The rates of water evaporation from a saline droplet at different RHs are compared in Figure 6.3. At an RH of 2% the water evaporation was most rapid, an inclusion droplet was formed within ~2 s and a crystal within 2.5 s, shown in Figure 6.3a. However, at an RH of ~40%, i.e., close to efflorescence RH,

the evaporation is much slower. The evaporation profiles in Figures 6.3 b&c differ from that seen with crystallisation in dry air. The droplet first equilibrates with the gas phase moisture content, Figure 6.3c, and a crystal spontaneously forms after some delayed time.[122] It is important to note that the time taken for crystallisation at 40% RH ranged from ~6 s (Figure 6.3b), to ~20 s (Figure 6.3c). A variation in crystallisation time was explored by Gregson et al. and they found it is likely due to the stochastic nature of crystal nucleation.[176] Additionally, in the drying conditions of 40% RH, it is more likely that a single nucleation site is formed, to be contrasted with the likely formation of multiple nucleation sites at lower RHs. These differences likely lead to different dry particle morphologies, and this can be confirmed by SEM imaging.[89]

The crystallisation of an aqueous sodium chloride droplet at 2% RH is shown in Figure 6.3a. Despite repeating over times, there appeared to be little variation in the timings of crystallisation. The droplet remains homogenous during drying for the first second, i.e., all the NaCl is in aqueous form. At the point of efflorescence, a droplet containing inclusions, partially undissolved sodium chloride crystals, is formed. After a further 0.5 s crystal formation is observed. The dry radius of the crystals in Figure 6.3 are indicated by the red horizontal line. The dry radius is calculated using the Equations 6.1 and 6.2. The starting concentration for each droplet remained constant, 171.2 g/L. In reality the calculated dry radius can be assumed to be smaller than the actual crystal radius. This is due to the likelihood of voids and inefficient backing between different crystals forming the composite particle.

Figures 6.3 b & c show crystallisation of two separate droplets at 40% RH, b shows a shorter "equilibration" time than c. Nucleation is a stochastic process, leading to some variation in the timing of crystallisation when only one nucleation site was involved. Once a region in the droplet has nucleated crystals, there are two competing rates of processes that follow. There is the rate of growth and spread of that crystal to other regions droplet, led by the heterogeneous nucleation rate of NaCl, competing with the rate that another region in the droplet will also undergo homogeneous nucleation. In the 40% RH case, the final particles were single crystals, suggesting that heterogeneous nucleation and spread of the first crystal nucleus to the rest of the droplet was the dominate mechanism of crystallisation, taking place before other homogeneous nucleation sites formed.[122] On the other hand, a droplet in lower RHs is expected to have a more rapidly rising surface concentration of NaCl and thus more likely to have formed multiple nucleation site, resulting in a particle with more, smaller crystals. As the crystallisation rate, which was governed by the abundance of nucleation sites, differs between Figures 6.3 a & b & c, it is proposed that the final crystal morphology will differ depending on the crystallisation RH.
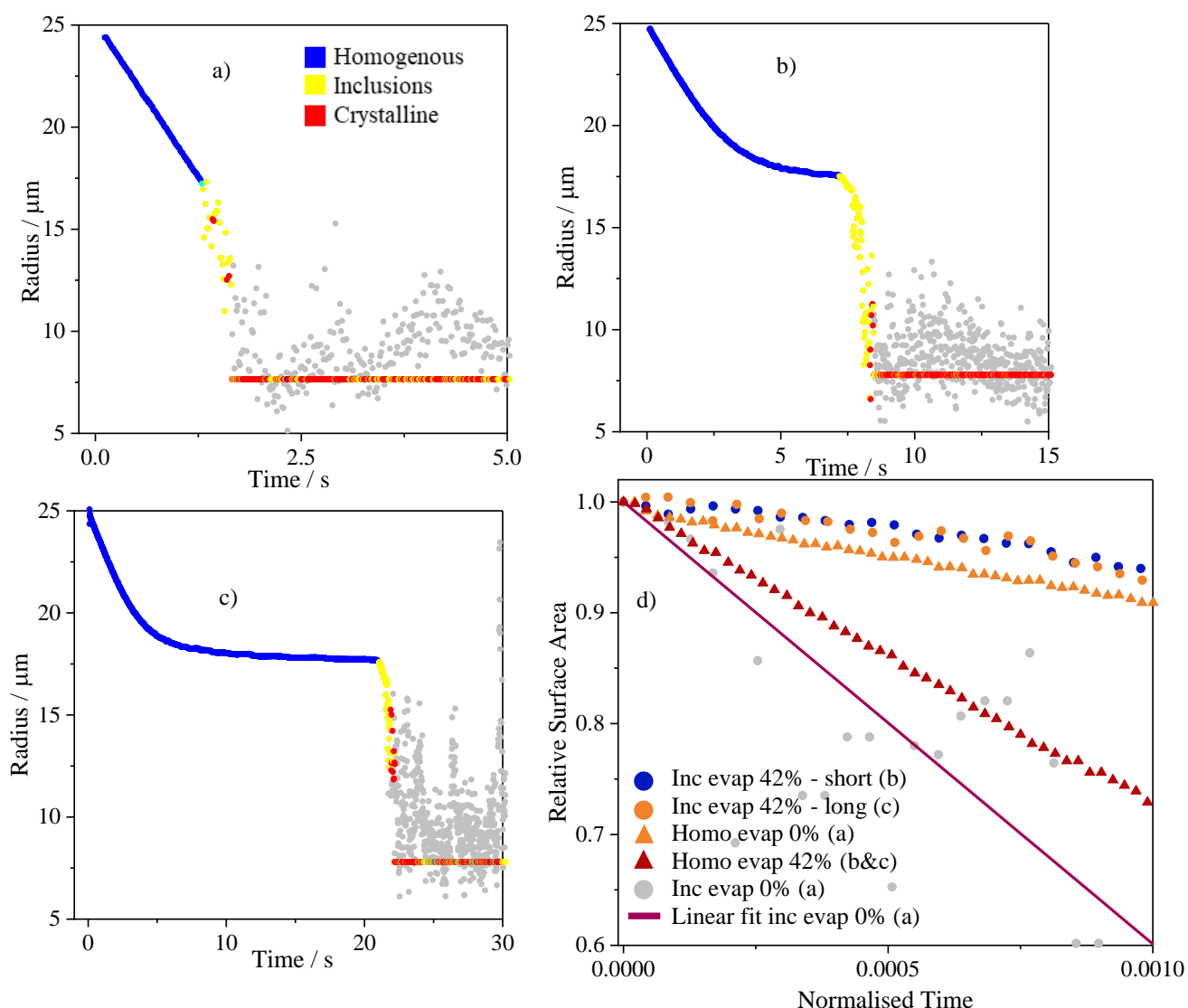
Figure 6.3. Crystallisation of sodium chloride at varying RHs. a) an example of faster crystallisation with multiple nucleation sites at <5% RH, b & c were slower crystallisation with a single nucleation site at ~40% RH. d) shows faster water evaporation for the inclusion phase of the process, additionally the overall evaporation rate was faster at low RH, where $y = r^2/r0^2$ and $x = t/r0^2$.

The crystallisation profile can be split into two key phases: the homogenous phase and the droplet containing inclusions evaporation phase. It was found that as the drying RH decreases the rate of water evaporation during phase one increases. The rate of water evaporation at different RHs in phase one is shown in Figure 6.3d. The homogeneous evaporation data collected at 0% RH indicates a quicker evaporation rate than homogenous data collected at 42% RH. Water evaporation increases the concentration of sodium chloride, leading to the second phase. As the concentration increases it eventually becomes too high for the salt to remain in solution, leading to crystallisation of NaCl. Nucleation of NaCl causes the formation of an inclusion droplet. The evaporation rates of water in the

second phase are shown in Figure 6.3d. The evaporation of water of a droplet containing inclusions at 40% RH is slower than that from a droplet containing inclusions in dry air. The evaporation rate is controlled by the diffusional gradient in the gas phase and is determined by the difference in water activity between the gas phase and droplet.

The enthalpy of crystallisation for NaCl is the reverse of enthalpy of dissolution ($\Delta H_{dissolution}$ (NaCl) $= + 3.9$ kJ mol^{-1}). During crystallisation, energy in the form of heat is released, resulting in a negative enthalpy change. Thus, in a finite volume droplet where the internal conduction of heat is faster than conduction and convection with the gas phase, the droplet temperature increases. An increase in droplet temperature enhances the water evaporation rate.[169] Once the onset of nucleation and crystal growth is identified from the light scattering, the rate of water evaporation appears to more than double. The rate of water evaporation, $\frac{dr}{dt}$, is equal to:

$$\frac{dr}{dt} = \frac{d\left(\frac{r^2}{r0^2}\right)}{d\left(\frac{t}{r0^2}\right)}$$

Equation 6 - 3

where *r* and *t* are radius and time, respectively.

From Figure 6.3c it can be inferred that the evaporation rate of the homogenous phase is equal to $\frac{dr1}{dt1} = -6.08$. After formation of a droplet containing inclusions, phase 2, the evaporation rate is equal to $\frac{dr2}{dt2} = -13.9$. It is known that differences in evaporation rates between phases will be different for other substances. For example, an API with a higher dissolution enthalpy than 3.9 kJ mol^{-1} would experience a larger increase in droplet temperature during crystallisation. The droplet temperature would increase more than that of NaCl, thus the rate of water evaporation would be faster during phase 2, while assuming all environmental conditions are constant.

As stated in the previous section, particle morphology and shape are governed by the evaporation kinetics during crystallisation.[177] Understanding and controlling the evaporation process allows control over the final morphology of the particle. Managing physical properties of dried particles provides an important route to assess the impact of particle morphology on inhalation processes such as dissolution.

6.2.2 Formation of Mono and Poly Sodium Chloride Crystals

During crystallisation there are two key competing processes that govern the kinetics and rate of crystal formation. The competing rates are the nucleation rate and the rate of crystal growth. If the nucleation rate is slow only one crystal forms and nucleation of more crystals is out competed by the crystal growth rate, resulting in a single/mono crystal. If the nucleation rate is high multiple crystals form and can out compete crystal growth. In the 40% RH case in Figure 6.4a, the final particles were mono crystals. A mono crystal suggests that heterogeneous nucleation and crystal growth of the first crystal nucleus to the rest of the droplet was the dominate mechanism of crystallisation. Thus, formation of a mono crystal took place before other homogeneous nucleation sites formed.[122] On the other hand, a poly crystal in Figure 6.4b is formed during the rapid drying events that occur in dry air. A poly crystal may lead to a rising surface concentration of sodium chloride and thus more likely to form multiple nucleation site. The dry masses of the final dry crystalline NaCl particles are equal in Figure 6.4 a & b.

At an RH of < 5% the rate of water evaporation up to formation of a droplet containing inclusions was higher than when at an RH of 40%. When the RH is close to the ERH, water evaporation is slow. Thus, it was more likely that there is an individual nucleation site which forms a single cubic crystal, described here as a mono crystal.[177] This was seen consistently in SEM images that were taken after the collection of crystal samples from the falling droplet column (FDC). When the RH is close to 0%, the increased water evaporation rate leads to multiple nucleation sites forming crystals that then grow competitively. Thus, this induces the formation of multiple crystals in the same droplet, described here as a poly crystal. Figure 6.4a shows the final morphology of a mono NaCl crystal that was dried under ambient conditions, slow water evaporation. Figure 6.4b shows the formation of poly NaCl crystals that were formed under dry conditions, ~0% RH, fast water evaporation.
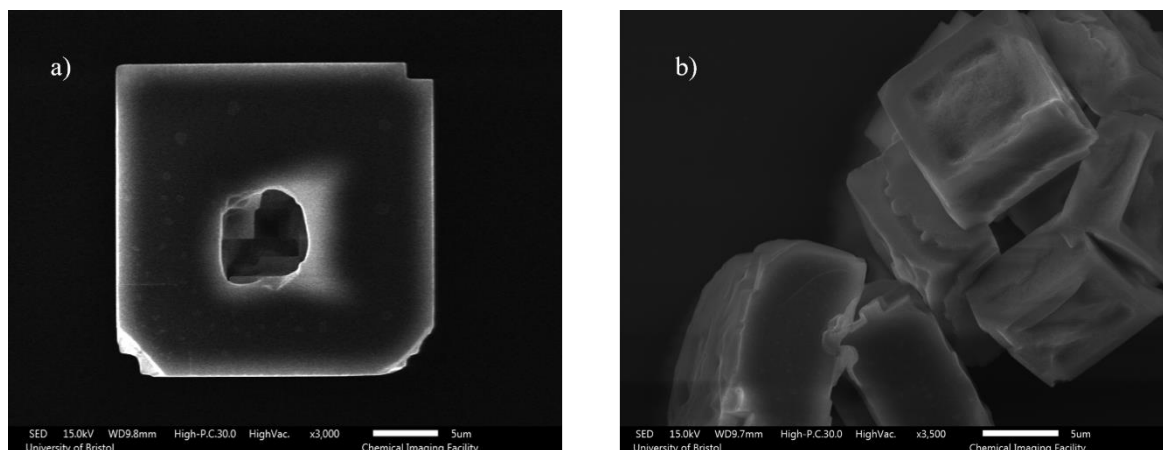
Figure 6.4. a) SEM image on a mono NaCl crystal, formed in ambient conditions, 40% RH. b) SEM image of a poly NaCl crystal formed in dry conditions.

The crystallisation rate differs between Figures 6.3 a&b&c. It is shown in Figures 6.4 a&b that the final crystal morphology differs depending on the crystallisation RH. A difference in crystal morphology will affect factors such as the surface area, density, and shape. The resulting question is then whether variations in the crystallisation process affect the dissolution rate upon rehydration of the crystal.

6.2.3 Drying Kinetics of Lactose Monohydrate

Lactose monohydrate is an ideal carrier for DPIs, due to its physical and chemical properties.[137] These include low density, dried particles are spherical, flowability, low toxicity and chemical stability. The hygroscopic response of lactose is described in Chapter 4. In this chapter, "lactose" is used as an abbreviation of lactose monohydrate. A large, coarse carrier particle is used to transport small, micronized drug particles into the deep lung. Lactose particles are commonly prepared by spray drying, usually producing amorphous or crystalline particles.[178] The amorphous nature of spray dried lactose is a great benefit to DPI development. The amorphous state of carriers is known to increase stability of drugs and the effectiveness of delivering drugs to the lung, where the drug absorbs efficiently into the blood circulation.[178] Further understanding of the drying kinetics of individual particles is needed to better understand the drying kinetics of polydisperse aerosol during spray drying.

An EDB was used to explore the evaporation kinetics of aqueous lactose droplets. The drying kinetics to form a lactose particle are shown in Figure 6.5a. The phase analysis software used to assign morphology to particles identifies a droplet containing inclusions at ~2.2 s. Figure 6.5b is an example of a phase function assigned to a droplet containing inclusions. Although the phase analysis software indicates formation of a droplet containing inclusions, it can be assumed that there is only residual water present, thus an amorphous particle has formed. Additionally, no phase functions consistent with an

irregular non-spherical particle were observed during drying measurements of lactose. Assignment of a droplet containing inclusions requires some level of homogeneity, which is observed in amorphous particles.[103] Work by Wu et al. found that amorphous lactose particles are spherical.[178] Thus, the particle formed in Figure 6.5a is identified as an amorphous lactose particle.
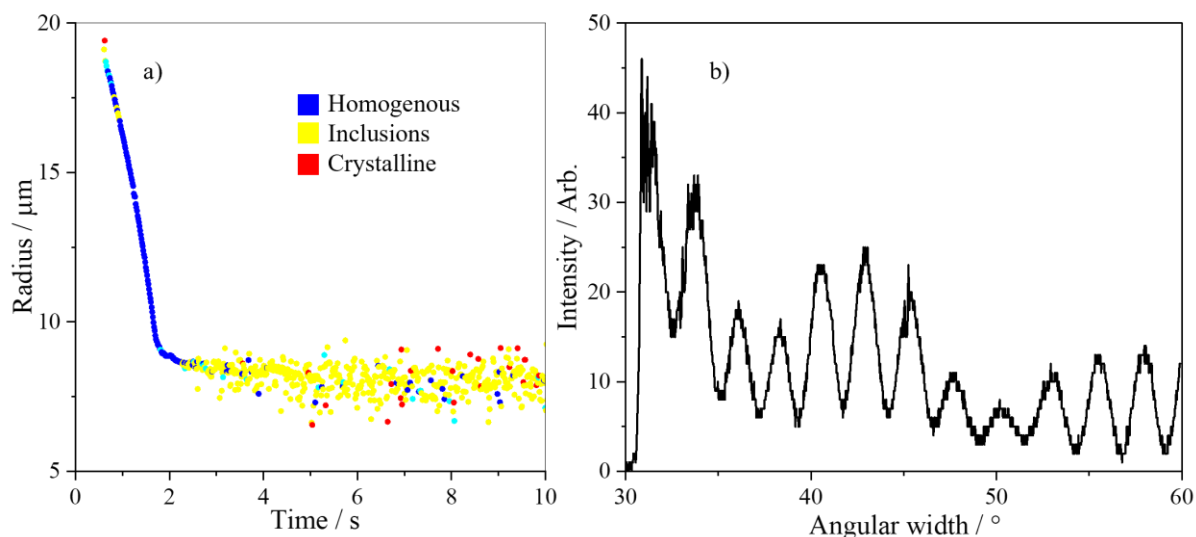
Figure 6.5. a) Formation of an amorphous lactose particle on the EDB. b) An individual phase function of a dried lactose particle, assigned by phase analysis software as "inclusion".

An important phenomenon affecting spray dried amorphous particles is plasticisation.[179,179] During rapid drying techniques, crystallisation can be suppressed by the appropriate selection of drying conditions.[179] However, once the spray dried amorphous materials are exposed to a higher equilibrium relative humidity, water sorption can lead to crystallisation. The increased water content allows the solute ions to form an ordered, more thermodynamically preferable state. As well as acting as a plasticisation agent, water can change the surface of the dried particles, and induce adhesion or agglomeration. Therefore, it is important to study the crystallinity transformation of spray dried amorphous particle. Research on plasticisation can then be used to determine storage conditions of DPI formulations. Wu et al., found crystallinity transformation of spray dried lactose occurred in samples stored at 43% RH for 3 days. Therefore, amorphous lactose stored in ambient conditions for 3 days prior to DPI actuation will be inhaled as a crystal, resulting in less efficient drug delivery. They found no additional changes in crystallinity at day 7, indicating that no further change occurred during the extended storage.[178] An example of plasticisation of an amorphous particle is given in the next section.

6.2.4 Drying Kinetics of a Sodium Chloride and Salbutamol Sulphate Mixture

Salbutamol sulphate (SS) is a common bronchodilator API used to treat asthma and chronic obstructive pulmonary disease (COPD). SS is often administered using a DPI. Similar to lactose, formulations containing SS are commonly produced using rapid trying techniques, such as spray or freeze drying.[180]

Chawla et al. found that spray drying formulations of SS resulted in spherical particles of correct aerodynamic diameter to deposit in deep lung, 1 µm to 5 µm.[181] Additionally, they found that spray drying does not chemically alter SS, although a reduction in crystallinity of the micronized drug particles was observed.[181] Gorny et al. and Littringer et al. found that spray drying SS resulted in amorphous particles.[182,4] The stability of amorphous particles poses a challenge for DPI formulations. It is possible for amorphous particles, in the presence of water, to recrystallise to the more thermodynamically stable crystalline state. Zellnitz et al. found that the recrystallisation rate of SS is a non-linear function of temperature and RH.[164] They carried out studies of crystallisation at 25 and 35 °C and a range of RHs, 60, 70, 80, 90 %. An increase in RH resulted in an increase in crystallisation rate. At 60 % RH after 12 h SS particles remained amorphous, however samples changed optically. At RHs above 60% SS amorphous particles are found to recrystallise. In this section the plasticisation rate of an SS and NaCl mixture are explored to compare with crystallisation of pure SS amorphous particles. NaCl is a common inorganic salt that is used in the pharmaceutical industry.

Plasticisation measurements were carried on an EDB, where near instantaneous switching between RHs is possible. An aqueous tertiary droplet of NaCl and SS, identical to the solutions described in Chapter 4, was exposed to dry conditions in the EDB. The droplet was trapped in dry air and held until an amorphous particle had formed, ~10 s. At this point, the RH increased to 40%. The experiment was reproduced multiple times and the data presented in Figure 6.6 demonstrate the observed trends. In the case of the 1:1 mixture, an amorphous particle transformed to a crystal within ~ 3 s of switching the RH from dry to 40%. The plasticisation of an amorphous SS/NaCl particle, mass ratio 1:1, is shown in Figure 6.6a, where the black horizontal line indicates the time of the RH switch. An example of a phase function collected during the amorphous phase and before crystallisation is shown in Figure 6.6b. Additionally, an example of a phase function consistent with that of a crystalline particle is shown in Figure 6.6c. As before, phase functions indicating a droplet containing inclusions can instead be assumed to represent the formation of an amorphous SS/NaCl particle. Amorphous particles exhibit a certain level of homogeneity, as do droplets containing inclusions, with some residual water.
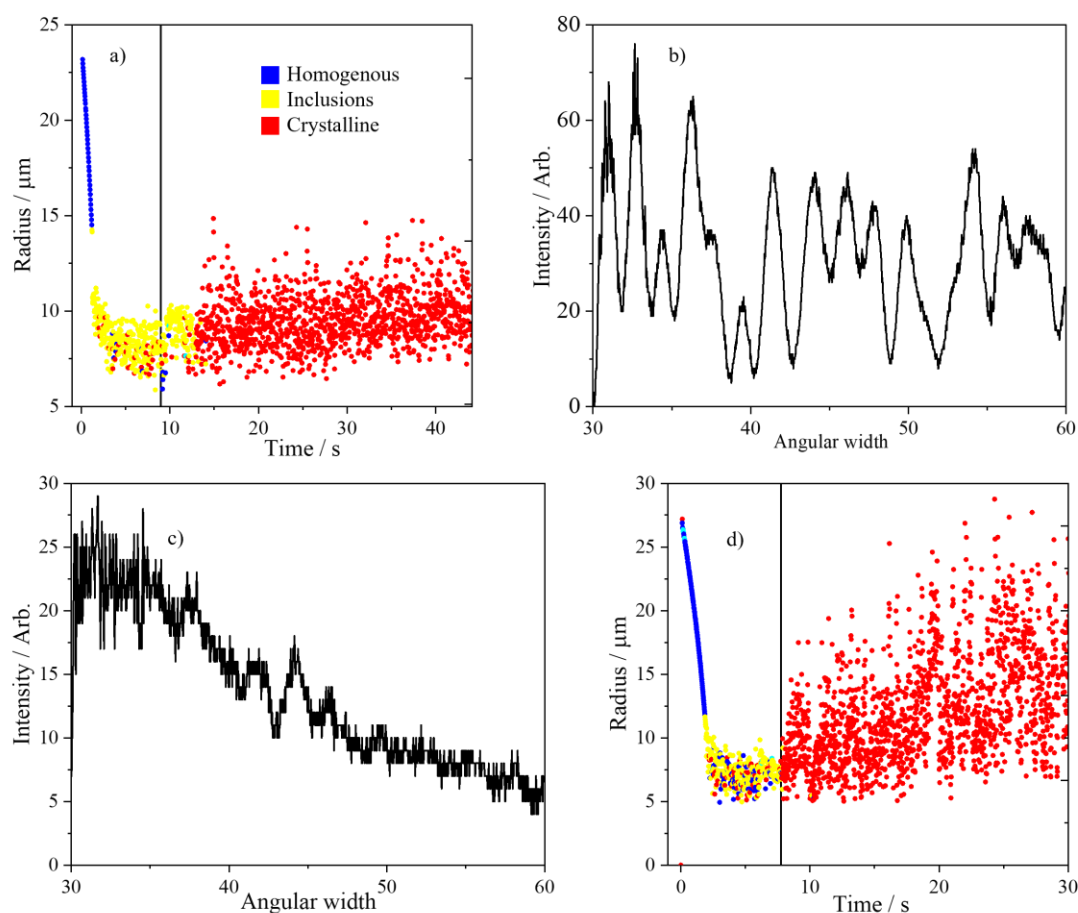
Figure 6.6. a) Plasticisation dynamics of a dried amorphous SS/NaCl 1:1 particle, dry air to 40% RH. b) & c) An example of phase functions in a) for amorphous particle data (yellow) and crystalline particle data (red). d) Plasticisation dynamics of a dried amorphous SS/NaCl 1:2 particle, dry air to 40% RH, crystallisation is instantaneous.

In the case of the SS/NaCl mixture mass ratio 1:2 the transformation from amorphous to crystalline is immediate with the RH switch. It appears that the presence of additional NaCl, which crystallises in pure form at 45% RH, increases the plasticisation rate. Figure 6.6d shows the plasticisation dynamics of a 1:2 SS/NaCl droplet held in dry air and switched to 40 % RH Bulk phase diffusion of solutes is a limiting factor of the plasticisation rate. There are two reasons why an increase in NaCl allows for an increase in bulk phase diffusion, and thus an increase in the rate of plasticisation. Firstly, NaCl is more hygroscopic than SS, see Chapter 4. Thus, if there is more NaCl present then more water is likely to adsorb onto the amorphous particle. Plasticisation relies on the addition of water to allow the movement of ions into a preferred crystal state. If there are more water molecules present then the solute ions are able to diffuse more freely, increasing crystallisation rate. Secondly, in the case of the 1:2 mixture there is a high concentration of NaCl ions to SS ions. Therefore, interactions of NaCl ions with each other will become more common, increasing the nucleation rate.

6.3   Dissolution Kinetics of Dried Particles Formed within the EDB

6.3.1   Changing Rates of Condensation Rate During Dissolution of Dried Sodium Chloride Particles at 95% RH

The first step in exploring the timescale for dissolution of NaCl in the aerosol phase is to form crystals of a particular morphology and size using the EDB, as described in Section 6.2.1. A dried crystal is formed within the EDB and the RH is switched to 95% RH.[87,96] In this section the dissolution dynamics of NaCl are explored. After the switch, water adsorbs onto the crystal and dissolution begins. Complete deliquescence leads to the formation of an aqueous sodium chloride droplet. Transitions in the light scattering phase function from particle are used to estimate the times at which the particle transformed from homogenous to crystalline and back to homogenous. The changes in phase functions were used to explore the dissolution rate, and to further identify the changes in the phase state of the particle. Under "sink conditions", sufficient solvent is present for the solute to be fully dissolved. Typically 5 to 10 times greater volume of media is used in respect to the saturation point at which dissolution would slow.[172] It was important to have the upper RH well above the DRH of NaCl (75%) when exploring dissolution dynamics without the limitation of water availability in the gas phase.

The complete crystallisation and dissolution profile of a NaCl droplet of initial concentration 171.2 g/L is shown in Figure 6.7a. A trapped aqueous NaCl droplet crystallises in the EDB once the water activity of the droplet fell below 0.45, within ~ 2 s. Approximately 5 s after crystallisation, the RH is switched to the upper RH, ~95%; the time of the switch is indicated by the black vertical line. Once the RH is above the DRH, 75%, water condenses onto the particle. After sufficient water adsorption the crystal particle dissolves and form an aqueous NaCl droplet.[183] However, the scattered phase function from the particle, Figure 6.7a, indicates that it remains crystalline for ~5 s before any phase or size change is seen, described as a dissolution lag period. After the dissolution lag period, phase functions indicate than a droplet containing inclusions forms. Particle size can be extracted using peak tracking analysis, albeit with slightly less accuracy than for a homogenous droplet, ±50 nm.[111]
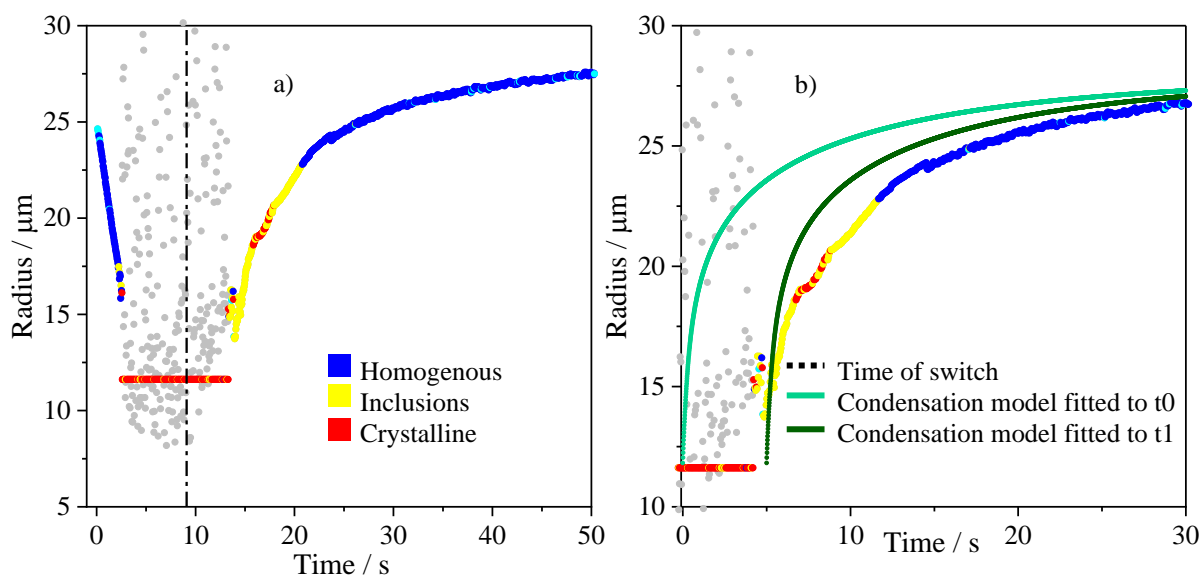
Figure 6.7 a) Crystallisation and dissolution of sodium chloride. b) Dissolution profile compared with modelled simulations of condensation, a solely gas-diffusion limited process.[82] An aqueous droplet of sodium chloride is trapped in dry air until crystallisation, after which the RH is switched (time = dashed black line) to the upper flow, 95% RH. The Kulmala model is fitted at t0 (light green), time of switch, and t1(dark green).

It is known that water molecules adsorb onto the surface of an NaCl crystal particle before the RH is above or equal to 75%, the DRH. Below the DRH, water condensation leads to the formation of multilayers around the crystal particle in the range 50% < RH < 75%,.[184] Once the RH is above 75% detachment of ions can commence. Lanaro et al. found that the initial stage is the detachment of the most exposed ions located on edges, i.e., corners or edges.[172] The ions at corners and edges have the weakest bond energies so are more readily removed than ions on flat surfaces.[172] Prior to reaching the DRH the rate of water adsorption onto the crystal surface increases with RH. Vapour continues to condense on to the surface until the RH of the gas phase is higher than the DRH. At this point, a film made up of a saturated solution of NaCl forms around the surface of the particle.[183] Vapour condensation and formation of a saturated film are the basis of deliquescence. A lower vapour pressure relative to that of pure water occurs due to the formation of the film on the surface of the NaCl particle.[98] It is described in literature that once the edges and corners have been consumed, the crystal becomes more spherical. From then on, the shape does not change until the final stage of dissolution.[172] Langlet et al. produced a time sequence of environmental scanning electron microscopy (ESEM) images showing the dissolution of NaCl at RH > DRH.[184] The sequence followed the steps detailed in Figure 6.1b; firstly, they found that the surface of the crystal becomes more smooth. Followed by a crystal encased by a saturated NaCl film, resulting with the formation of a perfectly spherical droplet.[184] Additionally, Wise

et al. observed water uptake on the surfaces of NaCl before the DRH.[185] The formation of a saturated film when RH > DRH is the initial stage, phase one; ions begin detaching from the edges and corners once sufficient water molecules from the gas phase have adsorbed onto the dried particle.

The second phase of dissolution starts once a droplet containing inclusions has formed. At this stage ultra-fine solute particles, that have detached from the primary particle, are encompassed within an aqueous droplet. In this thesis, such droplet is described as a "snow globe".[111] The phase of a droplet containing inclusions lasts ~7 s in Figure 6.7a, where there was a change in radial size of more than 10 µm. After the formation of a droplet containing inclusions the uniformity in the progression of peak intensities transitions from something irregular to a more consistent fall in intensity with increase in scattering angle. Thus, estimates of the droplet size can resume. However, it should be noted that sizing of a droplet containing inclusions is less accurate than a homogenous, aqueous droplet.[111] A saline droplet is formed once enough water molecules condense onto the inclusion droplet and dissolve the fine particles. The concentration of NaCl decreases until the water activity inside the droplet is equal to that of the gas phase, ~0.95.[88] Equilibration of water activity between droplet and gas phase governs the final size of the particle. In Figure 6.7a & b the droplet equilibrates once the radius is ~27 µm. It is important to note that water molecules impart energy in the form of latent heat as they condense onto the droplet. The transfer of energy acts to heat the droplet, however there is competition for the droplet to maintain equilibrium with the gas phase temperature via conduction.[82]

To better understand the kinetic limitations during the dissolution process, simulations from a condensation model can be compared to the data, shown in Figure 6.7b. The Kulmala condensation model,[82] which assumes net water flux is gas-diffusion limited only, is compared to the experimental data in Figure 67.b. The model is set with the same starting dry radius and final RH. The dark green line is fitted from t=0 s, i.e., time when the gas flow is switched to 95% RH. The light green line is fitted from the start time of the second stage of dissolution, i.e., once a droplet containing inclusions is formed. The experimental data show a much slower growth rate than the condensation simulation. A difference in radius dynamics between experimental and model data indicates that there are additional limitations to gas phase diffusion within the experimental data. The model assumes size dynamics are limited only by gas phase diffusion and heat transport, up to a change in temperature of ±3 K. A potential limitation during the second stage of dissolution is the need to form a complete monolayer around the particle prior to ion detachment. The proposed limiting factor of monolayer formation is based on the Langmuir isotherm of water adsorption. As well as a molecular dynamics simulation of NaCl dissolution. [186,172]The Langmuir isotherm presents the surface coverage, Θ, as:

$$\Theta = \frac{bp}{1 + bp}$$

where p is the partial pressure of the gas being adsorbed and b is constant specific to the surface material and temperature. The main assumption of Equation 6-4 is that water adsorption leads to a single layer, which is as expected in the aerosol phase.[184] Knowledge of the parameters for Equation 6-4 will further our understanding on the surface coverage during the first phase.

Once the adsorption layer has formed it could be stabilised due to the attractive interactions between the water and NaCl molecules. Strong interactions between solute and solvent reduces the chemical potential of the adsorbed phase with respect to bulk liquid,[187] an example of the Kelvin effect. The chemical potential of water, and thus, the vapour pressure, is greater at a convex surface and lower at a concave surface, compared to that at a flat surface. It is suggested here, based on SEM images in Figure 6.4, that a cubic crystal of NaCl has at least one flat face. Section 6.2.2 shows that a rapid formation of a NaCl crystal is more likely to have concave spaces between the poly crystals.

The second phase of dissolution is water condensation onto an aqueous surface during dissolution of droplet containing inclusions particles. To better understand the second phase of the dissolution process, the Kulmala model is compared to the homogenous experimental data, i.e., independent of the induction lag period. Figure 6.7b indicates that rate of growth of the inclusion droplet to reach the final size is slower than that of a homogenous droplet starting at the same concentration. An increase in droplet temperature, due to condensation, could potentially slow the rate of further ion detachment. On the other hand, the condensation of water vapour onto the droplet from the high RH gas phase will deposit energy to the droplet in the form of latent heat. The competition between the endothermic dissolution and exothermic condensation may account for the slower rate of droplet growth compared to that of the model. In addition to gas-phase diffusion, the dissolution rate of the crystalline phase may also be limited by bulk-phase diffusion.[88] At low water activities the viscosity of a NaCl droplet could slow the diffusional mixing of the solute, kinetically limiting the partitioning of water between the gas and aerosol phase.[122,51]

6.3.2. Complete Dissolution Dynamics of a Dried Sodium Chloride Particle Close to Deliquescence RH

The rate of complete dissolution increases as the RH rises above the DRH.[42] At RHs close to the DRH, the deliquescence process can be extremely slow,[42] taking hours before the system reaches homogenous equilibrium. Van Campen et al. modelled and experimentally studied the kinetics of moisture uptake in

singe components deliquescent solid systems and reported a decrease in dissolution timescale as RH approaches DRH[99] The aim of this work is to explore the effect that RH has on the dissolution timescale of dried NaCl crystals.

An EDB was used to measure the time taken for a NaCl crystal to dissolve, whilst varying the upper RH. The experiment was performed 15 times at each upper RH, ranging from 76% RH to 95% RH at intervals of ~2% RH. The average time until homogeneity was observed and assessed for each droplet, 15-20 droplets per data point in Figure 6.8c. The time of homogeneity was recorded using the RSD and polynomial fit parameters discussed in Chapter 3 and Figure 6.2. The uncertainty in the x-axis represents the potential fluctuation in RH, which is ±0.5%. As an example, NaCl droplet of starting concentration 171.2 g/L, was trapped in the EDB at an RH of ~0%, Figure 6.7. The droplet crystallised within ~2 s, after which the gas flow was switched to the upper RH. An example of a dissolution dynamics profile for a NaCl crystal at 76% RH is shown in Figure 6.8a. The RH in Figure 6.8a is 1% higher than the DRH of NaCl, ensuring that the RH never fluctuated below 75% RH during the measurement, based on an RH of ±0.5%.[39] The light scattering from the trapped particle in Figure 6.8a produced phase functions of crystalline characteristics for ~50 s after the RH switch. Once the particle has taken up sufficient water, a droplet containing inclusions forms at the beginning of the second phase. At 76% RH the second stage lasted for ~100 s, compared with ~10 s for an RH of 95% in Figure 6.7a. After ~2 mins the particle fully dissolves and the equilibrated size is governed by the water activity of the gas phase, 0.76. Thus, a smaller final droplet forms at 76% RH compared to 95%. A longer dissolution lag period at 76% RH indicates that the RH of the gas phase is a limiting factor to the dissolution time. The overarching aim here is to study the dissolution kinetics at an RH close to the DRH. Necessarily this will be the case for poorly soluble APIs when inhaled even at the high RHs of the lung.[183]

In the pharmaceutical literature sink conditions are described as when water availability is no longer a limiting factor of the dissolution rate.[42] An example droplet of the next dissolution profile, 78% RH, in this experiment is shown in Figure 6.8b. The first stage of dissolution is the time up to the first identification of inclusions within a host droplet with some size change but no phase change. In first stage of dissolution phase functions appear erratic due to the presence of a crystalline particle. At 76% RH the dissolution lag period is ~40 s at compared with ~10 s at 78% RH. The second phase of dissolution, once a droplet containing inclusions has formed and through to the equilibrated final homogeneous droplet size, lasts around 40 s at 78% RH compared with 100 s at 76% RH. It is proposed that this is due the capacity of the liquid phase to absorb dissolving ions. The difference between dissolution rates at 76% and 78% RH is the difference between the water activity at the surface of the crystal and at the droplet boundary, creating a significant water activity gradient. Figure 6.8c shows that

once the RH reaches 88% then the dissolution lag time is constant, ~8 s. At 88% RH it is assumed that there are sufficient water molecules present to form a mono layer and water uptake is gas phase diffusion limitation. Previous work has suggested that the detachment of ions will only begin once a layer of water has formed around the crystal; my findings are in agreement with this stage of the dissolution process.[184]
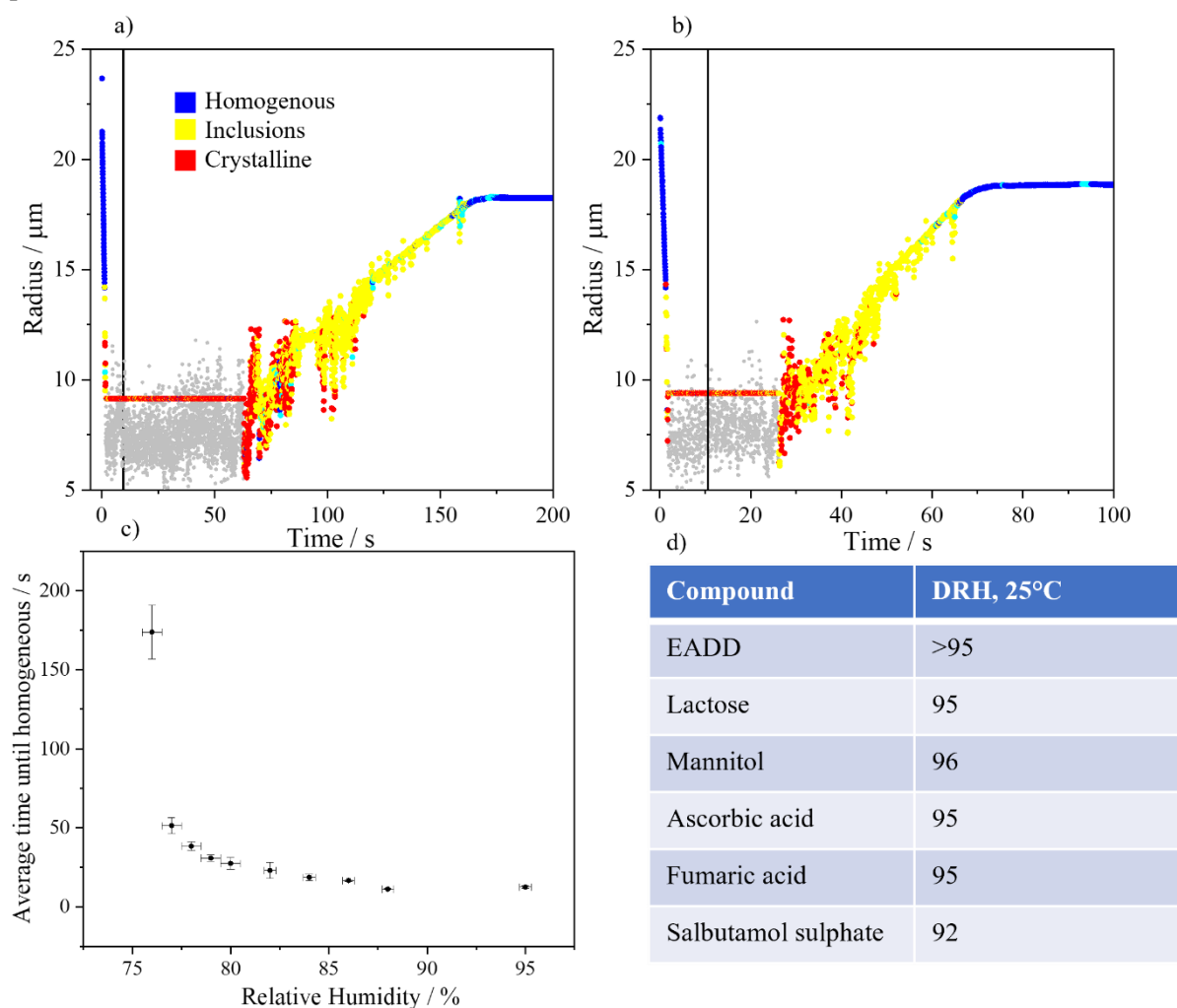
Figure 6.8. Exploring the dependence of dissolution dynamics of a crystalline NaCl particle on the water availability in the gas phase. All NaCl crystals dried under the same conditions, 0% RH. a) Dissolution dynamics at 76% RH. b) Dissolution dynamics at 78% RH. c) Average time until homogenous as a function of upper RH. Each data point in c) is an average of 15-20 dissolution profiles. d) A table of compounds and their associated DRH.[183] Time of switch is denoted by vertical black line in a) and b).

Figure 6.8 highlights the impact on dissolution dynamics when an environmental RH is close to the DRH. Many APIs and excipients that are frequently used in the treatment of respiratory diseases have a DRH above 90%, a list of common compounds is shown in Figure 6.8d.[97,53] Inhaled drugs and excipients will experience an RH of >99% in the airways and lung. In the case of lactose monohydrate,

a well-used drug carrying excipient, it has a DRH of 95%, only 4% lower than the surrounding RH. To put into perspective, Figure 6.8c indicates that an NaCl crystal will dissolve ~24 s slower at 79% RH than >88% RH. Given that an average breath is ~4 s, if the time and RH relationship were like that of NaCl, none of the excipients or APIs in Figure 6.8d would dissolve prior to deposition. Partially or undissolved drug formulations will have an impact on the subsequent pharmacokinetics and thus the efficiency of the drug delivery.[188] The kinetic limitation induced by a difference between the water activity in the saturated solution and the RH of the gas phase should be taken into account when performing deposition fraction measurements of drug formulations.

6.3.3 Dependence of Dissolution Dynamics on Surface Area and Crystal Mass of Sodium Chloride Crystal

The final objective is to explore any relationship between the surface area and the mass of the crystalline particle and the time for dissolution. It is predicted that an increase in crystal mass or surface area will increase the time taken for complete dissolution. Experiments were performed at RH 95%, to ensure the RH was not a limiting factor in the measured dissolution time of crystals of varying mass or surface area. To achieve a range in dry mass, 2-27 ng, the starting concentration, g/L, was varied and starting radial size of the droplets, µm. The pulse signals sent to a micro dispenser can be tailored to produce droplets of a different starting radius, about 20-32 µm, and, thus, dried mass. A further range in crystal mass was achieved by varying the initial concentration of the aqueous droplet, 50–370 g/L. Overall, it was possible to achieve a range in dry crystal mass of 2-28 ng. The dry mass was converted into surface area of a mono or poly crystal, μm^2, to determine which were a better predictor of dissolution time, providing a range of 500-4000 μm^2.

In addition to varying the crystal mass the experiment was performed at two different RHs, drying the droplets at RHs of ~2% and ambient, ~40%. As mentioned previously in Section 6.2.2, it is possible to control the morphology of a NaCl crystal by subjecting the initial aqueous droplet to specific drying conditions. This technique was used to produce crystals of different surface area whilst keeping the dry mass constant. To explore the morphology of the crystals a FDC was used, which was used to collect a large sample of dried NaCl crystals, which were then analysed using SEM. The environmental conditions were set to dry air, ~2%RH, and ambient, ~40%. The droplets were produced as a steady stream using a micro-dispenser at the same pulse conditions as the kinetic measurements on the EDB. A gas flow was used to control drying conditions, enabling the formation of mono crystalline particles and poly crystals which are formed when drying in dry or ambient air, respectively. To estimate the surface area of particles formed under different drying conditions SEM imaging was used. SEM images

shown previously in Figure 6.4 indicate that a mono crystal appears to have a slab shape and has roughly two equal square surfaces on top and bottom, surrounded by four rectangular sides. Figure 6.9 shows that formation of a mono crystal is reproducible and all crystals appear uniform in shape. SEM images indicate that the poly crystals have an average of 5 slabs per composite particle, where the dimensions of each slab are the same as that of a mono crystal. It was found that intra connection between the poly crystals were on corners and edges only. Based on the corner and edge connections, the total surface area of a poly crystal is taken as the sum of the surface area of each inclusion crystal. The shape and size of the crystals in Figure 6.9a at each drying condition are seen to be reproducible, which is as expected when using a micro-dispenser at constant pulse settings and a solution of the same concentration. The black data points in Figures 6.9 b & c were dried slowly and thus forming a mono slab crystal, whereas the red data points are poly crystals and were dried rapidly. Each data point is an average of the corresponding data set, where each data set is made up of repeats, 8-15 droplets under identical conditions. The uncertainty refers to the standard deviation from the average time, crystal mass (Figure 6.9b) and surface area (Figure 6.9c).
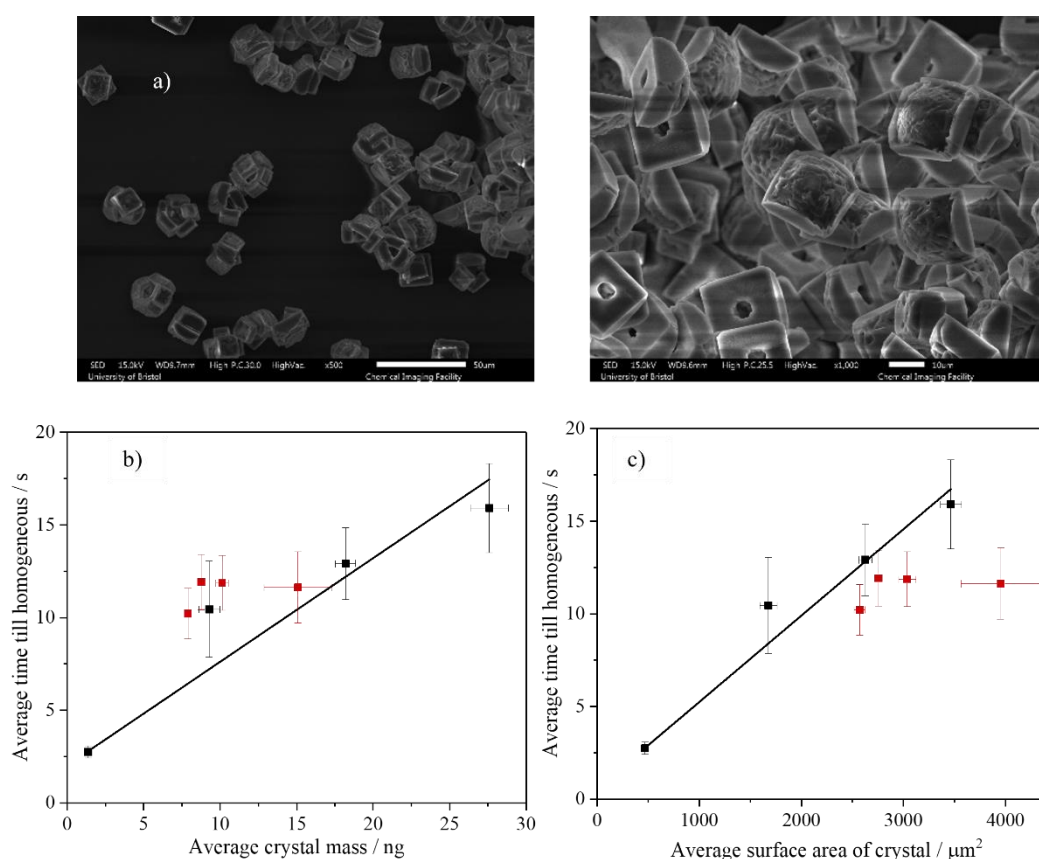

Figure 6.9. a) SEM images of sodium chloride mono and poly crystals produced from slow and rapid crystallisation respectively. b) Time until homogeneous as a function of dry crystal mass. c) Time until homogeneous relative to surface area of a crystal, calculated from the dry mass. b & c show a comparison between poly (red) and mono (black) crystals with dissolution time.

The data in Figure 6.9b support the hypothesis that there is a relationship between crystal mass and dissolution time. As the crystal mass increases the time taken to fully dissolve also increases which is as expected. A large crystal slab has a greater number of ions on the corners and edges than a small slab. Therefore, the ions of a larger slab take longer to be detached. Once all weakly held ions have been detached it is thought that a sphere shape forms, where all ions are held by the same strength bonds, leading to the final and complete stage of dissolution.[172,189] In addition, Briese et al., found that smaller crystals, >75 nm, show less tendency to form a step edge, potentially slowing down the dissolution process further.[190] Lanaro et al. suggest that dissolution is made of three key stages: detachment of most exposed ions (corners and edges), fixed rate regime after edges are removed and rapid dissolution once the crystal reaches a "stability limit".[172] It is suggested here that as the mass of NaCl increases as do the number of exposed ions. Therefore, it is expected that the time scale of the first phase of dissolution will increase with mass. After detachment of all exposed ions, it is likely that a spherical crystal is formed,[172] leading to stage two of dissolution, where a fixed rate regime is experienced. Stage 2 is likely to have little impact on the dissolution rate for varying dry mass as all ions are attached equally and are removed until complete dissolution. Crystal mass appears to be a good indicator of dissolution time. A linear fit of the mono crystal data shows a clear upward trend, whereas the poly crystal data points deviate slightly.

It has been shown here that crystal mass is a good indicator of dissolution time. Figure 6.9c shows a similar relationship between average surface area and dissolution time. The linear fit of the mono crystals also shows a clear upward trend. However, the relationship of surface area and poly crystal dissolution data deviates further from the linear trend. The surface area estimates are deduced from the crystal mass and the SEM images in Figure 6.4. Therefore, it is not possible to separate the two, rather highlight that they are both good indicators of dissolution time for mono crystals. As mass increases for a mono crystal so does the surface area. However, preliminary data in Figure 6.9b at a crystal mass of ~10 ng indicate some difference in the dissolution time between poly and mono crystals of equivalent mass. The average time until dissolution for a mono crystal of dry radius 6.2 µm is 10.4 s, whereas the average time for a poly crystal of the same dry radius is 12.1 s. Interestingly, this is the opposite to what is observed in the bulk phase. Typically, solids dissolve faster in a solvent bulk if the solid is broken up to increase the surface area. Alongside the increasing linear relationship between surface area and dissolution time, poly crystals are made up of an average of 5 slabs. A longer dissolution timescale for poly crystals, of the same dry mass as an equivalent mono crystal, could be due to a larger surface area. The process of ion detachment will take longer if the there is more surface for the water layer to cover. Additionally, it could be that as a poly crystal has a larger area of corners and edges, the time taken for the ions to be removed from these areas naturally takes longer.[172]This data suggests that an increase in surface area is a factor in controlling the detachment of the most exposed ions, prior to stage 2 of

dissolution. Thus, dissolution time increases with surface area. More data is needed to confirm whether poly crystals, of the same mass, take longer to dissolve than a mono crystal.

Assumptions have been made during the calculation of the surface area for poly crystals, most significant being that the crystal is formed of 5 slabs. It is possible that this is the reason why the poly crystal data in Figure 6.9c appear to deviate from the linear trend of increasing dissolution time for increasing mass. A change to the number of slabs that make up a poly crystal would have significant impact on the total surface area, and thus its relationship with dissolution time. In Figure 6.9c there is one polycrystal data point that lies far from the trend line (surface area, SA, ~4000µm^2). The droplets at that data point were formed using a starting solution of high concentration, to ensure a large dry mass. It has been found that a high initial concentration leads to fewer nucleation sites, and therefore lower number of inclusions in the poly crystal.[176] If a reduce number of inclusions crystals were the case it would indicate that the number of slabs in this data set were lower than the assumed 5. Data in Figure 6.9 show that a lower number of assumed slabs for the data set with a high crystal mass would fit better to the trend line made by the mono crystals in Figure 6.9c. It is possible to use dry mass or surface area as an indicator of dissolution time for a crystal. However, the data show that this is more reliable if the morphology consists of a single crystal.

It is important to study the relationship between mono crystals and poly crystals with time until complete dissolution. The physicochemical difference between mono and poly crystals could affect the efficiency of powdered formulations used pharmaceutics. In drug delivery to the lungs, aerosol formulations are often produced using a spray dryer technique; where the droplets experience rapid evaporation.[191] The drying conditions and initial concentration affect the morphology of the dried particles, and thus the surface area. Spray drying is well known for producing engineered amorphous particles. The main advantage of the spray drying is the ability to produce particles in specific size ranges, which is vital for drug inhalation where deposition is size-dependent.[191] Amorphous particle formation is not always the case, in situ crystallisation has been found to produce crystalline sucrose.[192] Additionally, a one-step crystallisation approach employed to spray drying has been used to produce crystalline lactose particles.[179] Data in Figure 6.9 show that the drying conditions of each particle formation technique affect the evaporation rate, number of nucleation sites and therefore the surface area of the dried particle. In Figure 6.9c It is shown that as the surface area increases so does the dissolution time. If a drug solution is spray dried and forms poly crystals made from several inclusion crystals, it will have a different dissolution dynamic than a poly crystal of fewer inclusion particles. The data presented here compares the difference in dissolution dynamics between a mono crystal and poly crystal that averaged 5 inclusion particles. The poly crystals are calculated to have double the total

surface area, with an equivalent mass. The morphology of dried particles using different techniques and solutions could vary hugely. Variation in crystal morphology will affect the surface area of the particle and dissolution time. The efficiency of the drug delivered is heavily dependent on dissolution time. An increase in surface area is likely to increase the time taken for the drug to transfer into the blood stream and take the desired effect.[173]

6.3.4 Water Uptake of an Amorphous Lactose Monohydrate Particle

The drying kinetics of lactose are described in Section 6.2.3. It is explained that when an aqueous lactose droplet is exposed to dry conditions an amorphous particle formed. The drying conditions in this work replicate those in a spray dryer, a common technique used to produce inhalable drug formulations. The phase transition dynamics of an amorphous lactose particle to liquid droplet are shown in Figure 6.10. An aqueous lactose droplet is trapped in an EDB in dry air, ~2% RH, and held for ten seconds. At this point the gas flow is switched with the upper RH set at 90%. Unlike an NaCl crystal there is no lag period prior to water uptake and droplet growth, water uptake appears to be almost instant. There is a clear change in size and phase function characteristics within 0.4 s. The characteristics of the phase functions switch from that of an amorphous particle to a homogenous droplet. In the case of amorphous particles, continuous condensation is often observed, rather than the DRH dependent phase transition for crystalline particles.[87,193,194] The phase transition in Figure 6.10 appears to be more gradual than that of NaCl, supporting the theory of continuous condensation. However, the amorphous particle is held in dry air, where only residual water is present. Therefore, the particle does experience water uptake kinetics, where rate of formation of a liquid droplet is significantly quicker than for a crystal particle. There is some residual water available, it could be that remaining water increases the rate of water uptake. Molecules within an amorphous particle are held with weaker bonds than in a crystal and require less energy to detach. It could be that the rapid time scale of liquid droplet formation gives the appearance of instantaneous dissolution, i.e., continuous condensation.[87]

Upon formation of a homogenous droplet in Figure 6.10, subsequent condensational growth is governed by the hygroscopic properties of lactose. In Chapter 4 lactose is shown to have a low hygroscopic response, with a RGF of ~1.5 at 95% RH, compared to ~2.7 for NaCl at the same RH. Therefore, after complete dissolution of the dried particle, only a small size change from about 6 to 7 µm is observed. The efficiency of drug delivery to the lungs is reduce if the large drug carrier, commonly lactose, grows significantly in radius and takes up a lot of water. A change in size or addition of water negatively effects the deposition fraction and chemical stability of the drug, respectively. The work presented here shows that lactose fills the above criteria and explains why it is a suitable carrier particle.
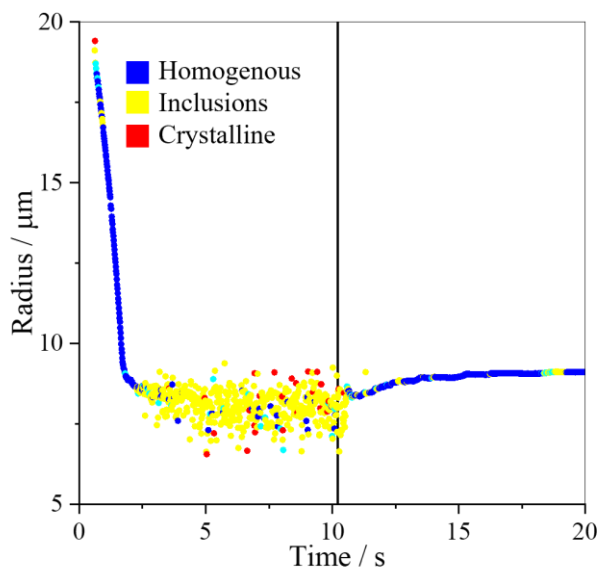
Figure 6.10. Dissolution profile of an amorphous lactose particle. RH switched dry to 90%.

6.3.5 Water Uptake of an Amorphous Salbutamol Sulphate Particle

The drying kinetics of SS are similar to that of lactose; rapid water evaporation in dry air leading to formation of an amorphous particle. In the treatment of respiratory diseases, an instant pharmacological effect is vital to ensure the patient is treated efficiently. Therefore, it is important that the inhaled amorphous drug particles remain amorphous or dissolve to form a liquid droplet. In this section the plasticisation effect of water is introduced, a process which enables the transformation of an amorphous particle to a more thermodynamically favourable crystal state. The plasticisation kinetics of SS are discussed in Section 6.2.4, which describes formation of a SS crystal at RHs between 70-90%.[164] Therefore, to ensure dissolution of an amorphous SS particle, rather than crystallisation, the upper RH must be above the RH required for recrystallisation of solute.

The transition of an amorphous SS particle to a liquid droplet is shown Figure 6.11. The drying conditions were set to ~2% RH, replicating the rapid evaporation experienced in a spray dryer. After ~6 s the gas flow is switched to the upper RH, 95%. Unlike lactose, there is a short lag of ~ 2 s before there is a change in size or characteristics of phase functions. At this point a homogenous, aqueous SS droplet is formed, where the final size is governed by the hygroscopic properties of SS. To ensure deep lung deposition inhaled particles must remain <2.5 μm in radius. The data in Figure 6.11 show that there is no change in size within 2 s, longer than the time taken to reach the deep lung according to ICRP.[116] Therefore, upon inhalation of an amorphous SS particle, up to 2.5 μm in radius, deep lung deposition is expected based on the data presented here.
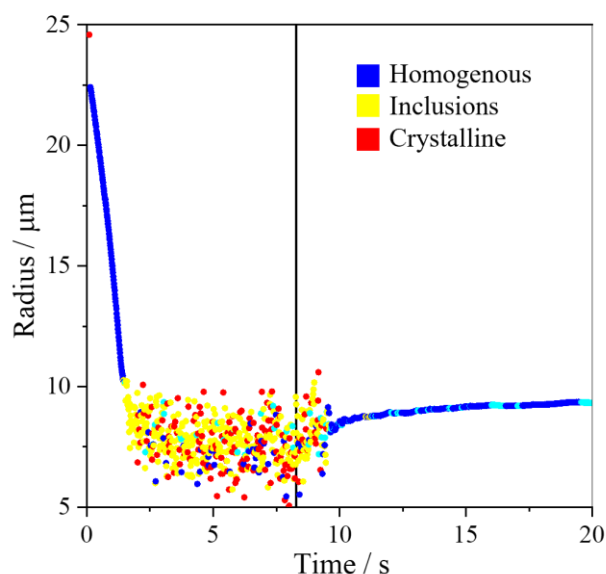
Figure 6.11. Dissolution profile of an amorphous SS particle. RH switched from dry to 95%.

6.4   Chapter 6: Summary

Advancing technologies in aerosol consumable industries require a better understanding of the physical processes that occur within a droplet system. The kinetics of efflorescence and deliquescence are key for exploring the phase transitions experienced by an aerosol as different environmental and physical conditions are experienced. Crystallisation is a common phase transition when drying solution droplets, in techniques such as spray drying, and dissolution is often seen when dried particles experience wet conditions, such as inhalation to the lung.[97,191] It was found that the rate of water evaporation during crystallisation of NaCl affected the dried crystal morphology; rapid evaporation was more likely to lead to poly crystals and slow evaporation was more likely to form a mono crystal. Following this, it was found that the difference in crystal morphology appeared to have an impact on the dissolution time. A poly crystal took longer to dissolve on average than a mono crystal of equivalent mass. However, further mass equivalent measurements are required to substantiate this finding. Additionally, it was found that the upper RH affected the complete dissolution time of a NaCl crystal. As the RH approached the DRH the average time until dissolution increased. The data show that onwards of 88% RH the time until dissolution was not limited by the RH, which was 13% higher than the DRH. Finally, it was shown that there were additional limitations during dissolution compared with gas-phase diffusion limited condensation. A lag period of ~5 s was experienced by the dried crystal before any phase or size change was observed. After which an inclusion droplet was formed prior to complete dissolution, which took no less than 12 s. In the pharmaceutical industry many API and excipient formulations are produced using spray driers, the data show that the drying conditions will cause a variation in the dried crystal morphology.[164] Additionally, API's DRH is often very higher, >90% RH. The findings in this chapter

indicate that these physical and environmental factors will affect the dissolution dynamics and thus the efficacy of the delivered drugs.[97]

A comparison between the crystallisation and dissolution kinetics of amorphous and crystal particles was made. Amorphous particles were formed on an EDB using similar drying conditions to that of a spray drier, rapid evaporation. In the case of lactose and SS rapid drying lead to the formation of an amorphous particle. It was shown that an amorphous particle can transform to a crystal particle with the addition of water molecules to the gas phase. An increase in RH from dry to 40% lead to plasticisation of a SS/NaCl mixture. Additionally, the dissolution dynamics of amorphous particles were found to be quicker than that of a crystal particle. There was no lag period during the transition from an amorphous particle to aqueous lactose droplet and a lag of only ~2 s for SS, compared to ~8 s for complete dissolution of a crystalline NaCl particle.

Chapter 7

Thesis Summary and Significant Conclusions

7.1   Summary

An introduction to the role of aerosol in the pharmaceutical industry was outlined in Chapter 1. A key factor in determining, predicting, and improving delivery of aerosolised drug mixtures via the lungs is the dependence of deposition location on particle size. The objective of this thesis was to study the dynamic processes of inhaled aerosol and their influence on particle size, phase state and morphology. The results in Chapters 4-6 provide significant conclusions on the dynamic processes prior to and during inhalation of particles produced by SMIs/nebulisers, MDIs and DPIs. The key aims were outlined in Chapter 1 and are as follows:

- Study the hygroscopic response of APIs, excipients and mixtures of APIs and excipients commonly used in drug delivery to the lungs in the treatment of respiratory diseases. Further, apply the hygroscopic response of a drug formulation to a deposition fraction simulator, replicating measurements of a cascade impactor.

- Develop an EDB to be used for measurements of the generation and inhalation of rapidly evaporating propellant (HFA) and co-solvent (ethanol) found in MDIs. Note: Low temperatures are required in the generation stage of measurements, followed by saturated conditions of the gas phase inside the chamber during droplet trapping.

- Combine aerosol phase and bulk phase measurements of particle dynamics of MDI formulations with and without an excipient. Explore the crystallisation and dissolution processes of MDI droplets and analyse dried particles using SEM.

- Investigate the dissolution dynamics of dried crystal particles, with a focus on the model system sodium chloride. Determine the variables effecting dissolution dynamics and to provide knowledge on how dissolution can be controlled and predicted in drug delivery to the lungs.

7.2   Significant Conclusions

The CK-EDB was used to levitate droplets and particles in order to determine the hygroscopic response of a substance. In addition, the CK-EDB was used to explore the crystallisation and dissolution kinetics of inhalable aerosol particles. CELEBS and the FDC were used to collect dried particles where the environmental conditions matched those of the kinetic measurements carried out on the CK-EDB. Dried particles were imaged using SEM. Lastly, a new EDB named SPLASH was designed, developed, and used to explore how particles and droplets react to a supersaturated gas phase.

The hygroscopic response of a range of pharmaceutically relevant compounds was determined using an EDB and presented in Chapter 4. A comparative kinetics method and the RH of gas phase was inferred with a probe droplet. The hygroscopic response of binary aqueous droplets containing APIs and excipients were presented in Section 4.3. Followed by the hygroscopic properties of more complex ternary droplets containing API with excipient and excipient with excipient. It was shown that APIs tend to have a low hygroscopic response compared to an inorganic salt, such as sodium chloride. Experimental hygroscopicity data on individual compounds, along with size distribution data, was used to simulate the deposition fraction within a cascade impactor. The results of experimental and simulated results were compared and matched well. It was shown that the model could be used in the future with other APIs that are administered using Respimat.

Aerosol phase measurements of particles generated from an MDI formulation containing propellant, API, co-solvent and with or without a NvE were presented in Chapter 5. The size dynamics and phase dynamics of individual components in an MDI formulation were explored using SPLASH. Single particle measurements showed that as a droplet cools rapidly, due to ethanol or HFA evaporation, water condenses on to the droplet. The %volume change after transition from HFA/ethanol droplet to a water droplet was found to be dependent on the droplet temperature and water availability in the gas phase. After 82% RH the %volume change from ethanol to water became constant. After water condensation the droplet dynamics were found to be governed by the water kinetics and the hygroscopicity of the API and NvE, if present. Dried samples of API/ethanol/NvE were collected using CELEBs for further SEM imaging analysis. The SEM images collected by colleagues at KCL and BARC matched well, however the particles collected by KCL appeared more spherical and more porous. All glycerol containing particles appeared to have a more stable and less porous structure. Aerosol phase measurements were compared with bulk phase measurements to better understand the particle dynamics occurring during inhalation (aerosol phase) and upon deposition (bulk phase). It was shown that BDP, the API in the formulation, does not fully dissolve under any conditions in the aerosol phase within a 4-minute time frame. Therefore, it is likely to deposit on the lung surface as a non-homogenous droplet, potentially partial dissolution will take place. In the bulk phase, there was an inverse relationship between the amount of NvE present in the formulation and the dissolution rate of BDP from the formulation. Cascade impactor measurements showed that glycerol containing droplets reached a larger final radius than glycerol absent droplets at a range of RHs.

Chapter 6 discussed the crystallisation and dissolution kinetics of the model system, sodium chloride. Crystallisation is a common phase transition when drying solution droplets, in techniques such as spray drying, and dissolution is often seen when dried particles experience humid conditions, such as inhalation to the lung.[97,191] It was found that the rate of water evaporation during crystallisation of NaCl affected the dried crystal morphology; fast evaporation was more likely to lead to poly crystals and slow

evaporation was more likely to form a mono crystal. It was found that the difference in crystal morphology appeared to have an impact on the dissolution time. A poly crystal took longer to dissolve on average than a mono crystal of equivalent mass. However, further mass equivalent measurements are required to substantiate this finding. Additionally, it was found that the upper RH affected the complete dissolution time of a NaCl crystal. As the upper RH decreased towards the DRH the average time until complete dissolution increased. The data showed that onwards of 88% RH the time until complete dissolution was not limited by the RH, which is 13% higher than the DRH (75% RH). It was found that there were additional limiting factors during dissolution compared with gas-phase diffusion limited condensation. A lag period of ~5 s was experienced by the dried salt crystal before any phase or size change was observed. After which a droplet containing inclusions was formed prior to complete dissolution, taking no less than 12 s. Often, API with excipient formulations are produced using spray driers, the data show that drying conditions cause a variation in the dried crystal morphology.[164] Additionally, API's DRH is often very high, >90% RH.[183] The findings in Chapter 6 indicate that these physical and environmental factors will affect the dissolution dynamics and thus the efficacy of the delivered drugs.[97]

A comparison between the crystallisation, dissolution and water uptake kinetics of amorphous and crystal particles was made. Amorphous particles were formed on an EDB using similar drying conditions to that of a spray drier, fast evaporation. In the case of lactose and SS fast drying lead to the formation of an amorphous particle. It was shown that an amorphous particle can transform to a crystal particle with the addition of water molecules to the gas phase acting as a plasticising agent. An increase in RH from dry to 40% lead to plasticisation of a SS/NaCl mixture. Additionally, the transition from an amorphous particle to a liquid droplet was found to be quicker than that of a crystal particle. There was no lag period during the phase transition of amorphous lactose to a liquid droplet and a lag of only ~2 s for SS, compared to ~8 s for a NaCl crystal.

7.3   Final Comments

Advancing technologies in aerosol consumable industries require a better understanding of the physical processes that occur within a droplet system. The measurements, simulations and analysis presented in this thesis contribute to the understanding of pharmaceutical aerosol dynamics during and prior to inhalation. In particular, the thesis separates the dynamic aerosol processes that occur during generation and inhalation for each of the four main delivery devices. Implications to the inhalable aerosol pharmaceutical industry are as follows:

- SMI/Nebulisers – Droplet size dynamics are governed only by the hygroscopic response of the substance, which increase in the very humid conditions within the lungs. Assuming that generated and inhaled droplets remain homogenous.

- MDI – Droplets generated from an MDI lose all HFA and ethanol within 0.2 s which significantly reduces temperature of the droplet. Prior to deposition, water condenses onto the cooled droplet, thus forming a non-homogeneous aqueous API particle.

- DPI – There is a lag period, longer than an average inspiration, prior to complete dissolution of a crystalline particle. An inhaled crystalline particle is likely to deposit in the lungs as a non-homogenous particle. Water uptake, and transition to a homogenous aqueous droplet, of amorphous particles is quicker, instantaneous in some cases. An inhaled amorphous particle is likely to deposit in the lungs as a homogenous aqueous droplet.

References

1. Patil, J. S. & Sarasija, S. Pulmonary drug delivery strategies: A concise, systematic review. *Lung India* **29**, 44–49 (2012).

2. Legh-Land, V., Haddrell, A. E., Lewis, D., Murnane, D. & Reid, J. P. Water uptake by evaporating pmdi aerosol prior to inhalation affects both regional and total deposition in the respiratory system. *Pharmaceutics* **13**, (2021).

3. Hickey, A. J. *Inhalation Aerosols: physical and biological basis for therapy*. (Marcel Dekker, 1996).

4. Littringer, E. M. *et al.* Spray Drying of Aqueous Salbutamol Sulfate Solutions Using the Nano Spray Dryer B-90-The Impact of Process Parameters on Particle Size. *Dry. Technol.* **31**, 1346–1353 (2013).

5. Widiyastuti, W. *et al.* Simulation and experimental study of spray pyrolysis of polydispersed droplets. *Cambridge Univ. Press* **22**, (2011).

6. Iskandar, F., Chang, H. & Okuyama, K. Preparation of microencapsulated powders by an aerosol spray method and their optical properties. *Adv. Powder Technol.* **14**, 349–367 (2003).

7. Nandiyanto, A. B. D. & Okuyama, K. Progress in developing spray-drying methods for the production of controlled morphology particles: From the nanometer to submicrometer size ranges. *Adv. Powder Technol.* **22**, 1–19 (2011).

8. Rogers, T. L., Johnston, K. P. & Williams, R. O. Solution-based particle formation of pharmaceutical powders by supercritical or compressed fluid CO_2 and cryogenic spray-freezing technologies. *Drug Dev. Ind. Pharm.* **27**, 1003–1015 (2001).

9. K.J., M. & G.P., M. Transition to CFC-free metered dose inhalers - Into the new millennium. *Int. J. Pharm.* **201**, 89–107 (2000).

10. Lewis, D. A. Intrinsic particle size distribution : A new metric to guide the design of HFA solution pMDIs. *Respir. Drug Deliv. Eur.* 1–10 (2013).

11. Labiris, N. R. & Dolovich, M. B. Pulmonary drug delivery. Part II: The role of inhalant delivery devices and drug formulations in therapeutic effectiveness of aerosolized medications. *Br. J. Clin. Pharmacol.* **56**, 600–612 (2003).

12. Newman, S. P., Pavia, D., Moren, F., Sheahan, N. F. & Clarke, S. W. Deposition of pressurised aerosols in the human respiratory tract. *Thorax* **36**, 52–55 (1981).

13. Crompton, G. K. Problems patients have using pressurized aerosol inhalers. *Eur. J. Respir. Dis.* **63**, 101–104 (1982).

14. Bennett, W. D. & Smaldone, G. C. Human variation in the peripheral air-space deposition of inhaled particles. *J. Appl. Physiol.* **62**, 1603–1610 (1987).

15. Newman, S P; Pavia, D; Garland, N; Clarke, S. W. Effects of various inhalation modes on the deposition of radioactive pressurized aerosols. *Eur. J. Respir. Dis.* **119**, 57–65 (1982).

16. Dolovich, M. Characterization of medical aerosols: Physical and clinical requirements for new inhalers. *Aerosol Sci. Technol.* **22**, 392–399 (1995).

17. Dolovich, M., Eng, P. & Ruffin, R. Clinical evaluation of a simple demand inhalation MDI aerosol delivery device. *Chest* **84**, 36–41 (1983).

18. Velaga, S. P. *et al.* Dry powder inhalers: An overview of the in vitro dissolution methodologies and their correlation with the biopharmaceutical aspects of the drug products. *Eur. J. Pharm. Sci.* **113**, 18–28 (2018).

19. Pedersen, S. Inhalers and nebulizers: Which to choose and why. *Respir. Med.* **90**, 69–77 (1996).

20. Dolovich, M. New propellant-free technologies under investigation. *J. Aerosol Med. Depos. Clear. Eff. Lung* **12**, (1999).

21. Newhouse MT & Kennedy A. Condensation due to rapid, large temperature (t) changes impairs aerosol dispersion from Turbuhaler (T). *Am. J. Respir. Cell Mol. Biol.* **161**, (2000).

22. Borgstrom, L., Bondesson, E., Moren, F., Trofast, E. & Newman, S. P. Lung deposition of budesonide inhaled via Turbuhaler®: A comparison with terbutaline sulphate in normal subjects. *Eur. Respir. J.* **7**, 69–73 (1994).

23. Pleasants, R. A. & Hess, D. R. Aerosol delivery devices for obstructive lung diseases. *Respir. Care* **63**, 708–733 (2018).

24. O'Callaghan, C. & Barry, P. The science of nebulised drug delivery. *Thorax* **52**, 31–31 (1997).

25. Van Dyke, R. E. & Nikander, K. Delivery of iloprost inhalation solution with the halolite, prodose, and I-neb adaptive aerosol delivery systems: An in vitro study. *Respir. Care* **52**, 184–190 (2007).

26. Dalby, R., Spallek, M. & Voshaar, T. A review of the development of Respimat® Soft Mist™ Inhaler. *Int. J. Pharm.* **283**, 1–9 (2004).

27. Dalby, R. N., Eicher, J. & Zierenberg, B. Development of Respimat® soft mist™ inhaler and its clinical utility in respiratory disorders. *Med. Devices Evid. Res.* **4**, 145–155 (2011).

28. Haddrell, A. E. *et al.* Pulmonary aerosol delivery and the importance of growth dynamics. *Ther. Deliv.* **8**, 1051–1061 (2017).

29. Stein, S. W. & Myrdal, P. B. The relative influence of atomization and evaporation on metered

dose inhaler drug delivery efficiency. *Aerosol Sci. Technol.* **40**, 335–347 (2006).

30. Ulrik, C. S. & Lange, P. Targeting small airways in asthma: Improvement in clinical benefit? *Clin. Respir. J.* **5**, 125–130 (2011).

31. Gregson, F. K. A. *et al.* Studies of competing evaporation rates of multiple volatile components from a single binary-component aerosol droplet. *Phys. Chem. Chem. Phys.* **21**, 9709–9719 (2019).

32. Bair, W. J. Human Respiratory Tract Model for Radiological Protection. *Health Physics* vol. 57 249–253 (1989).

33. ZIERENBERG, B. Optimizing the in Vitro Performance of Respimat. *J. Aerosol Med.* **12**, S-19-S-24 (2010).

34. Laube, B. L. *et al.* What the pulmonary specialist should know about the new inhalation therapies. *Eur. Respir. J.* **37**, 1308–1331 (2011).

35. Vinchurkar, S., Longest, P. W. & Peart, J. CFD simulations of the Andersen cascade impactor: Model development and effects of aerosol charge. *J. Aerosol Sci.* **40**, 807–822 (2009).

36. Timsina, M. P., Martin, G. P., Marriott, C., Ganderton, D. & Yianneskis, M. Drug delivery to the respiratory tract using dry powder inhalers. *Int. J. Pharm.* **101**, 1–13 (1994).

37. Craig, B. & Huffman, D. *Absorption and Scattering of Light by Small Particlestle*. (1983).

38. Mie, G. Articles on the optical characteristics of turbid tubes, especially colloidal metal solutions. *Ann. Phys.* **25**, 377–445 (1908).

39. Rovelli, G., Miles, R. E. H., Reid, J. P. & Clegg, S. L. Accurate Measurements of Aerosol Hygroscopic Growth over a Wide Range in Relative Humidity. *J. Phys. Chem. A* (2016) doi:10.1021/acs.jpca.6b04194.

40. Davies, J. F. Characterising The Impact Of Bulk, Surface And Gas-Phase Limitations On Mass Transport In Aerosol. (2014).

41. Löndahl, J. *et al.* Size-resolved respiratory-tract deposition of fine and ultrafine hydrophobic and hygroscopic aerosol particles during rest and exercise. *Inhal. Toxicol.* (2007) doi:10.1080/08958370601051677.

42. Mauer, L. J. & Taylor, L. S. Water-Solids Interactions: Deliquescence. *Annu. Rev. Food Sci. Technol.* **1**, 41–63 (2010).

43. Foster, M. C. & Ewing, G. E. Adsorption of water on the NaCl(001) surface. II. An infrared study at ambient temperatures. *J. Chem. Phys.* **112**, 6817–6826 (2000).

44. Tuckermann, R., Bauerecker, S. & Cammenga, H. K. IR-thermography of evaporating acoustically levitated drops. *Int. J. Thermophys.* **26**, 1583–1594 (2005).

45.   Yu, Y., Qiu, W. & Sun, L. Particle trapping for acoustic tweezers. *IEEE Int. Ultrason. Symp. IUS* **2**, 1533–1536 (2011).

46.   Tian, Y., Holt, R. G. & Apfel, R. E. A new method for measuring liquid surface tension with acoustic levitation. *Rev. Sci. Instrum.* **66**, 3349–3354 (1995).

47.   Ashkin, A. Acceleration and Trapping of Particles by Radiation Pressure. *Phys. Rev. Lett.* **24**, 156–159 (1970).

48.   Marsh, A. Hygroscopic Response and Reactivity of Compositionally Complex Aqueous-Organic Aerosol. (2018).

49.   Ashkin, A., Dziedzic, J. M. & Yamane, T. Optical trapping and manipulation of single cells using. *Nature* **330**, 769–711 (1987).

50.   Song, Y. C. *et al.* Measurements and Predictions of Binary Component Aerosol Particle Viscosity. *J. Phys. Chem. A* **120**, 8123–8137 (2016).

51.   Power, R. M., Simpson, S. H., Reid, J. P. & Hudson, A. J. The transition from liquid to solid-like behaviour in ultrahigh viscosity aerosol particles. *Chem. Sci.* **4**, 2597–2604 (2013).

52.   Cotterell, M. I. *et al.* Measurements of the evaporation and hygroscopic response of single fine-mode aerosol particles using a Bessel beam optical trap. *Phys. Chem. Chem. Phys.* **16**, 2118–2128 (2014).

53.   Davidson, N. *et al.* Measurement of the Raman spectra and hygroscopicity of four pharmaceutical aerosols as they travel from pressurised metered dose inhalers (pMDI) to a model lung. *Int. J. Pharm.* **520**, 59–69 (2017).

54.   Baldelli, A., Power, R. M., Miles, R. E. H., Reid, J. P. & Vehring, R. Effect of crystallization kinetics on the properties of spray dried microparticles. *Aerosol Sci. Technol.* **50**, 693–704 (2016).

55.   Baldelli, A., Boraey, M. A., Nobes, D. S. & Vehring, R. Analysis of the Particle Formation Process of Structured Microparticles. *Mol. Pharm.* **12**, 2562–2573 (2015).

56.   Hardy, D. A. *et al.* High time resolution measurements of droplet evaporation kinetics and particle crystallisation. *Phys. Chem. Chem. Phys.* **23**, 18568–18579 (2021).

57.   Haddrell, A. E., Davies, J. F., Yabushita, A. & Reid, J. P. Accounting for changes in particle charge, dry mass and composition occurring during studies of single levitated particles. *J. Phys. Chem. A* **116**, 9941–9953 (2012).

58.   Laucks, M. L., Roll, G., Schweiger, G. & Davis, E. J. Physical and chemical (RAMAN) characterization of bioaerosols-pollen. *J. Aerosol Sci.* **31**, 307–319 (2000).

59.   Heinisch, C., Wills, J. B., Reid, J. P., Tschudi, T. & Tropea, C. Temperature measurement of

single evaporating water droplets in a nitrogen flow using spontaneous raman scattering. *Phys. Chem. Chem. Phys.* **11**, 9720–9728 (2009).

60. Davis, E. J. Transport phenomena with single aerosol particles. *Aerosol Sci. Technol.* **2**, 121–144 (1982).

61. Wilson, H. A. XLII. A determination of the charge on the ions produced in air by Röntgen rays . *London, Edinburgh, Dublin Philos. Mag. J. Sci.* **5**, 429–441 (1903).

62. Paul, W. & Raether, M. Das elektrische Massenfilter. *Zeitschrift für Phys.* **140**, 262–273 (1955).

63. Wuerker, R. F., Shelton, H. & Langmuir, R. V. Electrodynamic containment of charged particles. *J. Appl. Phys.* **30**, 342–349 (1959).

64. Davis, E. J. & Ray, A. K. Single aerosol particle size and mass measurements using an electrodynamic balance. *J. Colloid Interface Sci.* **75**, 566–576 (1980).

65. Ray, A. K., Johnson, R. D. & Souyri, A. Dynamic Behavior of Single Glycerol Droplets in Humid Air Streams. *Langmuir* **5**, 133–140 (1989).

66. Fernandez, M. O. *et al.* Assessing the airborne survival of bacteria in populations of aerosol droplets with a novel technology. *J. R. Soc. Interface* **16**, (2019).

67. Oswin, H. P. *et al.* Measuring stability of virus in aerosols under varying environmental conditions. *Aerosol Sci. Technol.* **55**, 1315–1320 (2021).

68. Vehkamäki, H. & Riipinen, I. Thermodynamics and kinetics of atmospheric aerosol particle formation and growth. *Chem. Soc. Rev.* **41**, 5160–5173 (2012).

69. P. Atkins and J. De Paula. *Physical chemistry*. *Physical Chemistry* (Oxford University Press, Oxford, 2006). doi:10.1021/ed078p1173.

70. Murphy, D. M. & Koop, T. Review of the vapour pressures of ice and supercooled water for atmospheric applications. *Q. J. R. Meteorol. Soc.* **131**, 1539–1565 (2005).

71. Zuend, A., Marcolli, C., Luo, B. P. & Peter, T. A thermodynamic model of mixed organic-inorganic aerosols to predict activity coefficients. *Atmos. Chem. Phys.* **8**, 4559–4593 (2008).

72. Zuend, A. Aerosol Inorganic-Organic Mixtures Functional groups Activity Coefficients. http://www.aiomfac.caltech.edu/.

73. Clegg, S. L., Brimblecombe, P. & Wexler, A. S. Thermodynamic Model of the System H+-NH4+-Na+-SO42--NO3--Cl--H2Oat 298.15 K. **5639**, 2155–2171 (1998).

74. Sjogren, S. *et al.* Hygroscopic growth and water uptake kinetics of two-phase aerosol particles consisting of ammonium sulfate, adipic and humic acid mixtures. *J. Aerosol Sci.* **38**, 157–171 (2007).

75.   Köhler, H. The nucleus in and the growth of hygroscopic droplets. *Trans. Faraday Soc.* **32**, 1152–1161 (1936).

76.   Wexler, A. S. & Clegg, S. L. Atmospheric aerosol models for systems including the ions H+, NH4+, Na+, SO42−, NO3−, Cl−, Br− and H2O,. *J. Geophys. Res.* **107**, 3173–3185 (2002).

77.   Clegg, S. L., Brimblecombe, P. & Wexler, A. S. Thermodynamic model of the system H+-NH4+-SO42-NO 3--H2O at tropospheric temperatures. *J. Phys. Chem. A* **102**, 2137–2154 (1998).

78.   Clegg, S. L. E-AIM Home Page. http://www.aim.env.uea.ac.uk/aim/aim.php.

79.   Zuend, A., Marcolli, C., Peter, T. & Seinfeld, J. H. Computation of liquid-liquid equilibria and phase stabilities: Implications for RH-dependent gas/particle partitioning of organic-inorganic aerosols. *Atmos. Chem. Phys.* **10**, 7795–7820 (2010).

80.   Zuend, A. *et al.* New and extended parameterization of the thermodynamic model AIOMFAC: Calculation of activity coefficients for organic-inorganic mixtures containing carboxyl, hydroxyl, carbonyl, ether, ester, alkenyl, alkyl, and aromatic functional groups. *Atmos. Chem. Phys.* **11**, 9155–9206 (2011).

81.   Maxwell, J. C. & Niven, W. D. The scientific papers of James Clerk Maxwell. *Sci. Pap. James Clerk Maxwell* **2**, 1–802 (2011).

82.   Kulmala, M., Vesala, T. & Wagner, P. E. An Analytical Expression For the Rate of Binary Condensational Particle Growth. *Proc. R. Soc. A Math. Phys. Eng. Sci.* **441**, 589–605 (1993).

83.   Newbold, F. R. & Amundson, N. R. A model for evaporation of a multicomponent droplet. *AIChE J.* **19**, 22–30 (1973).

84.   Li, W. & Davis, E. J. Aerosol evaporation in the transition regime. *Aerosol Sci. Technol.* **25**, 11–21 (1996).

85.   Clarke, F. W., Thorpe, T. E. & Urbain, G. The Constitution and Fundamental Properties of Solids and Liquids. **2046**, (1916).

86.   Aerosol, A. N. D. *Interactions Between Fluid and Aerosol Particles*. *Topics in Current Aerosol Research* vol. 1 (1971).

87.   Rothfuss, N. E., Marsh, A., Rovelli, G., Petters, M. D. & Reid, J. P. Condensation Kinetics of Water on Amorphous Aerosol Particles. *J. Phys. Chem. Lett.* **9**, 3708–3713 (2018).

88.   Davies, J. F., Haddrell, A. E., Miles, R. E. H., Bull, C. R. & Reid, J. P. Bulk, surface, and gas-phase limited water transport in aerosol. *J. Phys. Chem. A* **116**, 10987–10998 (2012).

89.   Tsapis, N., Bennett, D., Jackson, B., Weitz, D. A. & Edwards, D. A. Trojan particles: Large porous carriers of nanoparticles for drug delivery. *Proc. Natl. Acad. Sci.* **99**, 12001–12005

(2002).

90. Kwamena, N. A. & Reid, J. P. Aerosols. (2021).

91. Reid, J. P. & Sayer, R. M. Heterogeneous atmospheric aerosol chemistry: laboratory studies of chemistry on water droplets. *Chem. Soc. Rev.* **32**, 70–79 (2003).

92. Haddrell, A. E. *et al.* Dynamics of aerosol size during inhalation: Hygroscopic growth of commercial nebulizer formulations. *Int. J. Pharm.* **463**, 50–61 (2014).

93. Myrdal, P. B., Sheth, P. & Stein, S. W. Advances in Metered Dose Inhaler Technology: Formulation Development. *AAPS PharmSciTech* **15**, 434–455 (2014).

94. Jubaer, H. *et al.* On the importance of droplet shrinkage in CFD-modeling of spray drying. *Dry. Technol.* **36**, 1785–1801 (2018).

95. Labiris, N. R. & Dolovich, M. B. Pulmonary drug delivery. Part I: Physiological factors affecting therapeutic effectiveness of aerosolized medications. *Br. J. Clin. Pharmacol.* **56**, 588–599 (2003).

96. Gregson, F. K. A., Robinson, J. F., Miles, R. E. H., Royall, C. P. & Reid, J. P. Drying and Crystallization of Evaporating Sodium Nitrate Aerosol Droplets. *J. Phys. Chem. B* **124**, 6024–6036 (2020).

97. Mauer, L. J. & Taylor, L. S. Deliquescence of pharmaceutical systems. *Pharm. Dev. Technol.* **15**, 582–594 (2010).

98. Zografi, G. Hydrogen Bonding i n Water. **14**, 1905–1926 (1988).

99. van Campen, L., Amidon, G. L. & Zografi, G. Moisture sorption kinetics for water-soluble substances I: Theoretical considerations of heat transport control. *J. Pharm. Sci.* **72**, 1381–1388 (1983).

100. van Campen, L., Amidon, G. L. & Zografi, G. Moisture sorption kinetics for water-soluble substances II: Experimental verification of heat transport control. *J. Pharm. Sci.* **72**, 1388–1393 (1983).

101. van Campen, L., Amidon, G. L. & Zografi, G. Moisture sorption kinetics for water-soluble substances III: Theoretical and experimental studies in air. *J. Pharm. Sci.* **72**, 1394–1398 (1983).

102. Davis, E. J. Electrodynamic Levitation of Particles. *Aerosol Meas. Princ. Tech. Appl. Third Ed.* 417–434 (2011) doi:10.1002/9781118001684.ch19.

103. Zheng, F., Laucks, M. L. & Davis, E. J. Aerodynamic particle size measurement by electrodynamic oscillation techniques. *J. Aerosol Sci.* **31**, 1173–1185 (2000).

104. Davies, J. F., Haddrell, A. E., Rickards, A. M. J. & Reid, J. P. Simultaneous analysis of the

equilibrium hygroscopicity and water transport kinetics of liquid aerosol. *Anal. Chem.* **85**, 5819–5826 (2013).

105. Haddrell, A. E., Davies, J. F., Yabushita, A. & Reid, J. P. Accounting for changes in particle charge, dry mass and composition occurring during studies of single levitated particles. *J. Phys. Chem. A* **116**, 9941–9953 (2012).

106. Cai, C. *et al.* Comparison of methods for predicting the compositional dependence of the density and refractive index of organic-aqueous aerosols. *J. Phys. Chem. A* **120**, 6604–6617 (2016).

107. Jain, N. K. & Roy, I. Effect of trehalose on protein structure. *Protein Sci.* **18**, 24–36 (2009).

108. Kulmala, M., Vesala, T. & Wagner, P. E. An analytical expression for the rate of binary condensational particle growth: Comparison with numerical results. *J. Aerosol Sci.* **23**, 133–136 (1992).

109. Vesala, T., Kulmala, M. & Olin, M. Condensation and evaporation of binary droplets with internal mass transfer. *J. Aerosol Sci.* **21**, S7 (1990).

110. Marsh, A. *et al.* Accurate representations of the physicochemical properties of atmospheric aerosols: when are laboratory measurements of value? *Faraday Discuss.* (2017) doi:10.1039/C7FD00008A.

111. Haddrell, A., Rovelli, G., Lewis, D., Church, T. & Reid, J. Identifying time-dependent changes in the morphology of an individual aerosol particle from its light scattering pattern. *Aerosol Sci. Technol.* **53**, 1334–1351 (2019).

112. Chen, X., Ma, R., Zhong, W., Sun, B. & Zhou, X. Numerical study of the effects of temperature and humidity on the transport and deposition of hygroscopic aerosols in a G3-G6 airway. *Int. J. Heat Mass Transf.* **138**, 545–552 (2019).

113. Haddrell, A. E., Davies, J. F. & Reid, J. P. Dynamics of Particle Size on Inhalation of Environmental Aerosol and Impact on Deposition Fraction. *Environ. Sci. Technol.* (2015) doi:10.1021/acs.est.5b01930.

114. Hofmann, W. Modelling inhaled particle deposition in the human lung-A review. *J. Aerosol Sci.* **42**, 693–724 (2011).

115. Rostami, A. A. Computational modeling of aerosol deposition in respiratory tract: A review. *Inhal. Toxicol.* **21**, 262–290 (2009).

116. YEH, H. & SCHUM, G. Models of human lung airways and their application to inhaled particle deposition. *Bull. Math. Biol.* **42**, 461–480 (1980).

117. Chan, C. K., Liang, Z., Zheng, J., Clegg, S. L. & Brimblecombe, P. Thermodynamic properties

of aqueous aerosols to high supersaturation: I—measurements of water activity of the system na+−cl−−no−3−so2−4−h2o at ∼ 298.15 k. *Aerosol Sci. Technol.* **27**, 324–344 (1997).

118. Broday, D. M. & Georgopoulos, P. G. Growth and deposition of hygroscopic particulate matter in the human lungs. *Aerosol Sci. Technol.* **34**, 144–159 (2001).

119. Ariyananda, P. L., Agnew, J. E. & Clarke, S. W. New techniques Aerosol delivery systems for bronchial asthma. 151–156 (1996).

120. Zhu, S., Kato, S., Murakami, S. & Hayashi, T. Study on inhalation region by means of CFD analysis and experiment. *Build. Environ.* **40**, 1329–1336 (2005).

121. Petters, M. D. & Kreidenweis, S. M. A single parameter representation of hygroscopic growth and cloud condensation nucleus activity-Part 3: Including surfactant partitioning. *Atmos. Chem. Phys.* **13**, 1081–1091 (2013).

122. Gregson, F. K. A., Robinson, J. F., Miles, R. E. H., Royall, C. P. & Reid, J. P. Drying Kinetics of Salt Solution Droplets: Water Evaporation Rates and Crystallization. *J. Phys. Chem. B* **123**, 266–276 (2019).

123. Özçelik, U. *et al.* Sodium chloride deficiency in cystic fibrosis patients. *Eur. J. Pediatr.* **153**, 829–831 (1994).

124. Costa, A. *et al.* The formulation of nanomedicines for treating tuberculosis. *Adv. Drug Deliv. Rev.* **102**, 102–115 (2016).

125. Pilcer, G., Wauthoz, N. & Amighi, K. Lactose characteristics and the generation of the aerosol. *Advanced Drug Delivery Reviews* (2012) doi:10.1016/j.addr.2011.05.003.

126. Larhrib, H., Zeng, X. M., Martin, G. P., Marriott, C. & Pritchard, J. The use of different grades of lactose as a carrier for aerosolised salbutamol sulphate. *Int. J. Pharm.* **191**, 1–14 (1999).

127. Feeley, J. C., York, P., Sumby, B. S. & Dicks, H. Determination of surface properties and flow characteristics of salbutamol sulphate, before and after micronisation. *Int. J. Pharm.* **172**, 89–96 (1998).

128. Hickey, A. J. & Martonen, T. B. Behavior of Hygroscopic Pharmaceutical Aerosols and the Influence of Hydrophobic Additives. *Pharmaceutical Research: An Official Journal of the American Association of Pharmaceutical Scientists* vol. 10 1–7 (1993).

129. Magnussen, H. Budesonide modulite®: Improving the changeover to CFC-free treatments. *Respir. Med.* **97**, 1–3 (2003).

130. Stank, K. & Steckel, H. Physico-chemical characterisation of surface modified particles for inhalation. *Int. J. Pharm.* **448**, 9–18 (2013).

131. Nevitt, S. J., Thornton, J., Murray, C. S. & Dwyer, T. Inhaled mannitol for cystic fibrosis.

Cochrane Database Syst. Rev. **2020**, (2020).

132. Spector, S. Use of mannitol inhalation challenge in assessment of cough. *Lung* **188**, 99–103 (2010).

133. Tingting, P. *et al.* Nanoporous mannitol carrier prepared by non-organic solvent spray drying technique to enhance the aerosolization performance for dry powder inhalation. *Sci. Rep.* **7**, 1–11 (2017).

134. Chiou, D. & Langrish, T. A. G. Crystallization of amorphous components in spray-dried powders. *Dry. Technol.* **25**, 1427–1435 (2007).

135. Pan, X., Julian, T. & Augsburger, L. Increasing the dissolution rate of a low-solubility drug through a crystalline-amorphous transition: A case study with indomethicin. *Drug Dev. Ind. Pharm.* **34**, 221–231 (2008).

136. Islam, N. & Cleary, M. J. Developing an efficient and reliable dry powder inhaler for pulmonary drug delivery - A review for multidisciplinary researchers. *Med. Eng. Phys.* **34**, 409–427 (2012).

137. Corrigan, D. O., Corrigan, O. I. & Healy, A. M. Physicochemical and in vitro deposition properties of salbutamol sulphate/ipratropium bromide and salbutamol sulphate/excipient spray dried mixtures for use in dry powder inhalers. *International Journal of Pharmaceutics* vol. 322 22–30 (2006).

138. Nerbrink, O. L., Pagels, J., Pieron, C. A. & Dennis, J. H. Effect of humidity on constant output and breath enhanced nebulizer designs when tested in the EN 13544-1 EC standard. *Aerosol Sci. Technol.* **37**, 282–292 (2003).

139. Reisner, C. *et al.* Characterization of aerosol output from various nebulizer/compressor combinations. *Ann. Allergy, Asthma Immunol.* **86**, 566–574 (2001).

140. Newman, S. P. Pesignrinciples of Metered-Dose Inhaler D. *Respir. Care* **50**, 1177–1190 (2005).

141. Sham, J. O. H., Zhang, Y., Finlay, W. H., Roa, W. H. & Löbenberg, R. Formulation and characterization of spray-dried powders containing nanoparticles for aerosol delivery to the lung. *Int. J. Pharm.* **269**, 457–467 (2004).

142. Forbes, B. *et al.* In Vitro Testing for Orally Inhaled Products: Developments in Science-Based Regulatory Approaches. *AAPS J.* **17**, 837–852 (2015).

143. Su, Y. Y., Marsh, A., Haddrell, A. E., Li, Z. M. & Reid, J. P. Evaporation Kinetics of Polyol Droplets: Determination of Evaporation Coefficients and Diffusion Constants. *J. Geophys. Res. Atmos.* **122**, 12,317-12,334 (2017).

144. Myrdal, P. & Angersbach, B. Pulmonary Delivery of Drugs by Inhalation. *Modif. Drug Deliv. Technol. canisevapo Ed.* 553–562 (2013) doi:10.3109/9781420045260-42.

145. Ganderton, D. *et al.* Modulite®: a means of designing the aerosols generated by pressurized metered dose inhalers. *Respir. Med.* **96**, S3–S8 (2002).

146. Woodcock, A., Acerbi, D. & Poli, G. Modulite® technology: Pharmacodynamic and pharmacokinetic implications. *Respir. Med.* **96**, S9 (2002).

147. Martin, A. R., Kwok, D. Y. & Finlay, W. H. Investigating the evaporation of metered-dose inhaler formulations in humid air: Single droplet experiments. *J. Aerosol Med. Depos. Clear. Eff. Lung* **18**, 218–224 (2005).

148. Fink, J. B., Dhand, R., Duarte, A. G., Jenne, J. W. & Tobin, M. J. Aerosol delivery from a metered-dose inhaler during mechanical ventilation: An in vitro model. *Am. J. Respir. Crit. Care Med.* **154**, 382–387 (1996).

149. Freiwald, M. *et al.* Monitoring the initial pulmonary absorption of two different beclomethasone dipropionate aerosols employing a human lung reperfusion model. *Respir. Res.* **6**, 1–13 (2005).

150. Grainger, C. I. *et al.* Critical Characteristics for Corticosteroid Solution Metered Dose Inhaler Bioequivalence. *Mol. Pharm.* **9**, 563–569 (2012).

151. Lewis, D. A. *et al.* Towards the bioequivalence of pressurised metered dose inhalers 1: Design and characterisation of aerodynamically equivalent beclomethasone dipropionate inhalers with and without glycerol as a non-volatile excipient. *Eur. J. Pharm. Biopharm.* **86**, 31–37 (2014).

152. Siepmann, J. & Siepmann, F. Mathematical modeling of drug dissolution. *Int. J. Pharm.* **453**, 12–24 (2013).

153. Davies, J. F., Haddrell, A. E. & Reid, J. P. Time-resolved measurements of the evaporation of volatile components from single aerosol droplets. *Aerosol Sci. Technol.* **46**, 666–677 (2012).

154. Fernandez, M. O., Thomas, R. J., Oswin, H., Haddrell, A. E. & Reid, J. P. Transformative Approach To Investigate the Microphysical Factors Influencing Airborne Transmission of Pathogens. *Appl. Environ. Microbiol.* **86**, e01543-20-e01543-20 (2020).

155. Buttini, F. *et al.* Differences in physical chemistry and dissolution rate of solid particle aerosols from solution pressurised inhalers. *Int. J. Pharm.* **465**, 42–51 (2014).

156. Selg, E. *et al.* Dry powder inhalation exposures of the endotracheally intubated rat lung, ex vivo and in vivo: The pulmonary pharmacokinetics of fluticasone furoate. *J. Aerosol Med. Pulm. Drug Deliv.* **26**, 181–189 (2013).

157. Gerde, P. *et al.* DissolvIt: An in Vitro Method for Simulating the Dissolution and Absorption

of Inhaled Dry Powder Drugs in the Lungs. *Assay Drug Dev. Technol.* **15**, 77–88 (2017).

158. Farkas, Á. *et al.* Experimental and computational study of the effect of breath-actuated mechanism built in the NEXThaler® dry powder inhaler. *Int. J. Pharm.* **533**, 225–235 (2017).

159. Saleh, J., Dubé, M. A. & Tremblay, A. Y. Effect of soap, methanol, and water on glycerol particle size in biodiesel purification. *Energy and Fuels* **24**, 6179–6186 (2010).

160. Mosharraf, M. & Nyström, C. The effect of particle size and shape on the surface specific dissolution rate of microsized practically insoluble drugs. *Int. J. Pharm.* **122**, 35–47 (1995).

161. Franek, F. *et al.* Ranking in Vitro Dissolution of Inhaled Micronized Drug Powders including a Candidate Drug with Two Different Particle Sizes. *Mol. Pharm.* **15**, 5319–5326 (2018).

162. Riley, T. *et al.* Challenges with developing in vitro dissolution tests for orally inhaled products (OIPs). *AAPS PharmSciTech* **13**, 978–989 (2012).

163. Floroiu, A., Klein, M., Krämer, J. & Lehr, C. M. Towards standardized dissolution techniques for in vitro performance testing of dry powder inhalers. *Dissolution Technol.* **25**, 6–18 (2018).

164. Zellnitz, S., Narygina, O., Resch, C., Schroettner, H. & Urbanetz, N. A. Crystallization speed of salbutamol as a function of relative humidity and temperature. *Int. J. Pharm.* **489**, 170–176 (2015).

165. Shulam, M., Jacobson, M., R, C. & R, S. Dissolution behavior and surface tension effects of organic compounds in nucleating cloud droplets. **23**, 60–65 (1996).

166. Sahib, M. N. *et al.* Solubilization of beclomethasone dipropionate in sterically stabilized phospholipid nanomicelles (SSMs): Physicochemical and in vitro evaluations. *Drug Des. Devel. Ther.* **6**, 29–42 (2012).

167. Cai, C. *et al.* Organic component vapor pressures and hygroscopicities of aqueous aerosol measured by optical tweezers. *J. Phys. Chem. A* **119**, 704–718 (2015).

168. Butler, J. R., Mitchem, L., Hanford, K. L., Treuel, L. & Reid, J. P. In situ comparative measurements of the properties of aerosol droplets of different chemical composition. *Faraday Discuss.* **137**, 351–366 (2007).

169. Vehring, R., Foss, W. R. & Lechuga-Ballesteros, D. Particle formation in spray drying. *J. Aerosol Sci.* **38**, 728–746 (2007).

170. Walton, D. E. & Mumford, C. J. The morphology of spray-dried particles. The effect of process variables upon the morphology of spray-dried particles. *Chem. Eng. Res. Des.* **77**, 442–460 (1999).

171. Vehring, R. Pharmaceutical particle engineering via spray drying. *Pharm. Res.* **25**, 999–1022 (2008).

172. Lanaro, G. & Patey, G. N. Molecular dynamics simulation of nacl dissolution. *J. Phys. Chem. B* **119**, 4275–4283 (2015).

173. R.U., A., M.I., U., M., A., R., K. & N., V. The lung as a route for systemic delivery of therapeutic proteins and peptides. *Respir. Res.* **2**, 198–209 (2001).

174. Heyder, J. Deposition of Inhaled Particles in the Human Respiratory Tract and Consequences for Regional Targeting in Respiratory Drug Delivery. *Proc. Am. Thorac. Soc.* **1**, 315–320 (2004).

175. Sear, R. P. Quantitative studies of crystal nucleation at constant supersaturation: Experimental data and models. *CrystEngComm* **16**, 6506–6522 (2014).

176. Sear, R. P. Nucleation: Theory and applications to protein solutions and colloidal suspensions. *J. Phys. Condens. Matter* **19**, (2007).

177. Robinson, J. F., Gregson, F. K. A., Miles, R. E. H., Reid, J. P. & Royall, C. P. Nucleation kinetics in drying sodium nitrate aerosols. 1–10 (2019).

178. Wu, L. *et al.* Studies on the spray dried lactose as carrier for dry powder inhalation. *Asian J. Pharm. Sci.* **9**, 336–341 (2014).

179. Chiou, D. & Langrish, T. A. G. A comparison of crystallisation approaches in spray drying. *J. Food Eng.* **88**, 177–185 (2008).

180. Alhusban, F. A. & Seville, P. C. Carbomer-modified spray-dried respirable powders for pulmonary delivery of salbutamol sulphate. *J. Microencapsul.* **26**, 444–455 (2009).

181. Chawla, A., Taylor, K. M. G., Newton, J. M. & Johnson, M. C. R. Production of spray dried salbutamol sulphate for use in dry powder aerosol formulation. *Int. J. Pharm.* (1994) doi:10.1016/0378-5173(94)90132-5.

182. Gorny, M., Jakobs, M., Mykhaylova, V. & Urbanetz, N. A. Quantifying the degree of disorder in micronized salbutamol sulfate using moisture sorption analysis. *Drug Dev. Ind. Pharm.* **33**, 235–243 (2007).

183. Mauer, L. J. & Taylor, L. S. Deliquescence of pharmaceutical systems. *Pharm. Dev. Technol.* **15**, 582–594 (2010).

184. Langlet, M. *et al.* Kinetics of dissolution and recrystallization of sodium chloride at controlled relative humidity. *KONA Powder Part. J.* **29**, 168–179 (2011).

185. Wise, M. E., Buseck, P. R., Martin, S. T. & Russell, L. M. Water uptake by nacl particles prior to deliquescence and the phase rule. *Aerosol Sci. Technol.* **42**, 281–294 (2008).

186. Romakkaniemi, S., Hämeri, K., Väkevä, M. & Laaksonen, A. Adsorption of water on 8-15 nm NaCl and (NH4)2SO4 aerosols measured using an ultrafine tandem differential mobility

analyzer. *J. Phys. Chem. A* **105**, 8183–8188 (2001).

187. Stöckelmann, E. & Hentschke, R. A molecular-dynamics simulation study of water on NaCl(100) using a polarizable water model. *J. Chem. Phys.* **110**, 12097–12107 (1999).

188. Lewis, D. A. *et al.* Towards the bioequivalence of pressurised metered dose inhalers 1: Design and characterisation of aerodynamically equivalent beclomethasone dipropionate inhalers with and without glycerol as a non-volatile excipient. *Eur. J. Pharm. Biopharm.* **86**, 31–37 (2014).

189. Zasetsky, A. Y., Sloan, J. J. & Svishchev, I. M. Dissolution of solid NaCl nanoparticles embedded in supersaturated water vapor probed by molecular dynamic simulations. *J. Phys. Chem. A* **112**, 3114–3118 (2008).

190. Briese, L., Arvidson, R. S. & Luttge, A. ScienceDirect The effect of crystal size variation on the rate of dissolution – A kinetic Monte Carlo study. *Geochim. Cosmochim. Acta* **212**, 167–175 (2017).

191. Shakiba, S., Mansouri, S., Selomulya, C. & Woo, M. W. In-situ crystallization of particles in a counter-current spray dryer. *Adv. Powder Technol.* **27**, 2299–2307 (2016).

192. Shastry, A. V. & Hartel, R. W. Crystallization during drying of thin sucrose films. *J. Food Eng.* **30**, 75–94 (1996).

193. Chemistry, A., Discussions, P. & Mikhailov, E. Mass-based hygroscopicity parameter interaction model and measurement of atmospheric aerosol water uptake. *Atmos. Chem. Phys. Discuss.* **11**, 30877–30918 (2011).

194. Robinson, C. B., Schill, G. P. & Tolbert, M. A. Optical growth of highly viscous organic/sulfate particles. *J. Atmos. Chem.* **71**, 145–156 (2014).